

# **Characterisation of a New Nanostructured Aluminium Alloy and Piston Design for Internal Combustion Engines**

By

Habibullah Adil



A thesis submitted in partial fulfilment of the requirements of the award of

Doctor of Philosophy

March 2023



## **Abstract**

The ever growing concerns over toxic engine emissions, sustainability and global warming put the automotive industry under immense pressure to reduce pollution and improve the efficiency of internal combustion engines. The lighter the mass of a vehicle the lower the energy required to propel it and potentially the lower the emissions that will ensue. Also, reducing piston mass affects piston and ring assembly frictional losses and therefore engine efficiency. This trend in the automotive industry motivates desire for new lighter materials such as the nanostructured aluminium alloy used in this research.

The aim of this research was to characterise a new nanostructured aluminium alloy and use heat treatment to optimise its mechanical properties for application as a lightweight engine piston material. The hardness of the new alloy at T6 was 35% higher than that corresponding to Al-2618 that is used for the test engine piston in this project. The high temperature tensile tests carried out at piston operating temperature showed that the new alloy had 1.09–1.82 times higher strengths than that of Al-2618 depending on the test temperature. In addition, the new alloy also had higher strengths than other aluminium alloys used in piston applications.

The design approach used in this work was to reduce piston mass using topology optimisation without affecting the external envelope and the shape of the combustion chamber. The new piston's mass was 218.35 grams which was 16.38% lighter than the original piston with mass of 261.13 grams. The final machined piston turned out to be slightly heavier than the final optimised piston design. This was due to the coating and also some modifications needed to make the design machinable. However, the final machined piston was still 13.5% lighter than the original piston.

The new piston was more fuel efficient than the original piston at higher speeds and lower torques. At a speed of 3000 rpm, the new piston was on average 2.04% more fuel efficient at all torques values. Overall, the new piston had higher volumetric efficiency compared to the original piston, but at higher engine speed of 6000 rpm and higher torque the new piston had lower volumetric efficiency. To ultimately determine whether the new lightweight piston would generate any sizeable difference in engine performance and/or efficiency across the wider engine running envelope, further work is needed.

## **Acknowledgements**

First of all and foremost, I would like to express my sincere gratitude to my supervisors, Dr. Shpend Gerguri, Prof. John Durodola, Dr. Fabrizio, Bonatesta and Prof. Fernando Audebert for their excellent and infinite guidance, help, encouragement and patience through this PhD project.

I would also like to extend my thanks and acknowledge the contributions made by the following people during this project.

- Mike Hartman, technical advice and help with the use of stress laboratory to carryout heat treatments, material preparation and optical microscopy.
- Prof. Fabiana Saporiti from the University of Buenos Aires, advice and technical assistance with high temperature tensile tests.
- Charles Bokor, for technical assistance with engine testing.
- Dr. James Brought (Oxford Brookes University) and Javier Faig (University of Buenos Aires) for their help with use of scanning electron microscope.
- The whole of the Oxford Brookes workshop team, for their help with cutting the test specimen and welding the engine mount.
- RSP Technology, for the provision of the alloy used in this work.

I am indebted to the Universities of Buenos Aires and Oxford for allowing me to use their facility to carry out high temperature tensile tests and X-ray diffraction analyses.

Finally, I would like to thank my family and friends for their support and encouragement throughout the time that I was working on this project.



## **Publications**

**Comparative Study and Evaluation of Two Different Finite Element Models for Piston Design** (Published in *Journal of Engineering Research and Application*, ISSN : 2248-9622 Vol. 9, Issue 3 (Series -V) March 2019, pp23-37)

**Microstructure and Mechanical Properties of an Al-Mg-Si-Cu Alloy for High Temperature Application** (Submitted to *Journal of Engineering Materials and Technology*)

**Evolution of Materials for Internal Combustion Engines Pistons** (Accepted in *International Journal of Research and Review*)

**Application of a Nanostructured Aluminium Alloy in Internal Combustion Engine Pistons for Mass Reduction** (Submitted to *International Journal of Automotive Engineerin*)

**Word Count = 35,131**

## Table of Contents

Abstract.....	I
Acknowledgements.....	II
Publications.....	III
List of Figures.....	X
List of Tables.....	XIX
List of Abbreviations.....	XXI
List of Symbols.....	XXV
Chapter 1: Introduction.....	1
1.1. Background.....	1
1.1.1. Project motivation and Research Gap.....	4
1.2. Aim and objectives of the project.....	5
Chapter 2: Literature review and background theory.....	7
2.1. Introduction.....	7
2.2. Internal combustion engines (ICEs) piston.....	7
2.3. Piston design aims and evolution over time.....	8
2.3.1. Piston design considerations.....	8
2.3.2. Piston design evolution.....	8
2.4. Piston's material requirements.....	9
2.5. Piston material evolution and development.....	11
2.5.1. Conventional aluminium alloys.....	11
2.5.2. Nanostructured aluminium alloys or super alloys.....	12
2.6. Strengthening mechanisms in aluminium alloys.....	14
2.7. Rapid solidification of aluminium alloys.....	14
2.7.1. Melt spinning.....	15
2.8. Heat treatment background theory.....	16
2.9. Engine loadings on piston.....	16
2.9.1. Mechanical loads.....	17
2.9.1.1. Combustion pressure.....	17
2.9.1.2. Inertial force due to acceleration.....	18
2.9.1.3. Lateral force.....	19
2.9.2. Thermal loads.....	20
2.9.2.1. Heat transfer between the combustion gas and the piston crown.....	21

2.9.2.2. Heat transfer between compression ring and cylinder .....	22
2.9.2.3. Heat transfer between ring lands, piston outer skirt and the cooling oil .....	22
2.9.2.4. Heat transfer between the piston under-crown and inner walls of the piston skirt and the cooling oil .....	23
2.9.2.5. Heat transfer between the engine cylinder and cooling water jacket .....	24
2.10. Summary .....	25
Chapter 3: Research methodology and thesis structure .....	26
Chapter 4: Microstructural characterisation of nanostructured aluminium alloy RSA Al-612 .....	29
4.1. Introduction .....	29
4.2. Microstructural characterisation and sample preparation.....	29
4.2.1. Sample preparation .....	30
4.2.1.1. Step 1: Sectioning .....	30
4.2.1.2. Step 2: Mounting.....	30
4.2.1.3. Step 3: Grinding .....	31
4.2.1.4. Step 4: Polishing .....	31
4.3. Microscopic analyses .....	32
4.3.1. Optical microscopy.....	32
4.3.1.1. Homogeneity of the alloy and particle analyses .....	33
4.3.2. Scanning electron microscopy .....	39
4.3.2.1. Secondary electron (SE) and back scatter (BS) modes .....	39
4.3.2.2. Energy dispersive spectroscopy (EDS).....	40
4.3.2.3. SEM results .....	40
4.4. Heat treatment for T6 determination.....	44
4.4.1. Heat treatment methodology .....	44
4.4.2. Heat treatment results for T6 condition .....	46
4.5. Microstructural stability heat treatments.....	48
4.5.1. Microstructural stability results .....	49
4.6. Tensile tests results and fracture surface analysis.....	51
4.6.1. Tests at elevated temperatures .....	52
4.6.2. Tests at room temperature after 100 hours of use .....	54
4.6.3. Fracture surface analyses of tensile specimen .....	56
4.7. Compression test results and fracture surface analyses .....	59
4.7.1. Fracture surface analyses of compression specimen.....	61
4.8. X-Ray diffraction (XRD) analysis .....	63

4.9. Suitability of the new alloy for piston application and comparison with existing aluminium alloys .....	64
4.10. Summary .....	66
Chapter 5: Piston design, finite element analysis and manufacturing.....	67
5.1. Introduction .....	67
5.2. Piston finite element methodology .....	67
5.3. Piston finite element modelling .....	69
5.3.1. Geometric constraints and contacts in the FE models.....	70
5.3.2. Scope of the piston FEA and assumptions .....	73
5.3.3. Reverse engineering of the current piston.....	74
5.3.4. Required material properties for piston FEA .....	75
5.4. Determination and application of engine loads on piston .....	76
5.4.1. Consideration of mechanical loads .....	76
5.4.1.1. Combustion pressure.....	77
5.4.1.2. Inertial force/acceleration .....	78
5.4.1.3. Lateral force .....	79
5.4.2. Consideration of thermal loads .....	80
5.4.2.1. Heat transfer between the combustion gas and piston crown .....	81
5.4.2.2. Compression ring heat transfer coefficient .....	82
5.4.2.3. Heat transfer between ring lands and piston outer skirt and the cooling oil .....	83
5.4.2.4. Heat transfer between the piston under-crown and inner walls of the piston skirt and the cooling oil.....	84
5.4.2.5. Cooling jacket heat transfer coefficient .....	84
5.5. FEA results of the baseline piston.....	85
5.5.1. Critical load cases .....	86
5.5.2. Results.....	87
5.5.2.1. Mesh convergence analyses .....	88
5.5.2.2. Temperature distribution in Piston.....	93
5.5.2.3. Maximum principal stress distribution in piston.....	94
5.5.2.4. Plastic strain distribution in piston.....	95
5.5.2.5. Piston directional deformations.....	96
5.5.2.6. Fatigue life .....	100
5.6. New lightweight piston design.....	101
5.6.1. Design approach to reduce piston mass and limitations due to the existing engine components .....	101

5.6.2 Topology optimisation for piston mass reduction.....	103
5.6.2.1 Limitations of topology optimisation in Ansys.....	103
5.6.2.2. Topology optimisation methodology and results .....	103
5.6.3. Piston design optimisation by inspection.....	105
5.7. Manufacturing of the new piston design.....	111
5.7.1. Challenges encountered with piston design and manufacturing .....	114
5.8. Summary .....	114
Chapter 6: Engine testing and results.....	116
6.1. Introduction.....	116
6.2. Engine test methodology.....	116
6.3. Engine test scope and limitations.....	116
6.4. Engine test preparation .....	117
6.4.1. Choice/selection of dynamometer .....	117
6.4.2. Mount design .....	118
6.4.3. Coupling with dynamometer.....	118
6.4.4. Electrical wiring harness and cranking.....	120
6.4.5. Exhaust system and lambda sensor .....	120
6.4.6. Cooling system.....	121
6.4.7. Crank position location system .....	122
6.4.8. Torque, speed and fuel measuring systems .....	123
6.4.9. Installation and Calibration of in-cylinder pressure sensor.....	124
6.4.10. Installation and calibration of air intake pressure sensor, temperature and carburettor ..	125
6.4.11. Other engine test considerations .....	126
6.5. Modifications required for the accommodation of new piston in the test engine .....	126
6.6. Comparison of the original and new engine configurations .....	127
6.7. Tests results with original and new pistons .....	131
6.7.1. Test results at 3000 rpm.....	132
6.7.2. Test results at 4500 rpm .....	136
6.7.3. Test results at 6000 rpm .....	139
6.8. Summary .....	142
Chapter 7: Discussion .....	143
7.1. Introduction.....	143
7.2. Microstructure of the alloy.....	143
7.3. Heat treatments .....	145

7.4. Mechanical properties, deformation and fracture behaviour .....	146
7.5. Strength contribution of different strengthening mechanisms.....	149
7.5.1. Particle strengthening.....	149
7.5.2. Grain boundary strengthening.....	151
7.5.3. Dislocation-dislocation interaction strengthening.....	152
7.5.4. Solid solution strengthening.....	153
7.6. Finite element analysis of the original piston .....	153
7.7. Finite element analysis of the new lightweight piston and implementation of the new piston in the engine with existing components .....	157
Chapter 8: Conclusions and further work .....	158
8.1. Conclusions.....	158
8.1.1. Overall research findings .....	158
8.1.2. Critical review of piston material evolution.....	158
8.1.3. Characterisation of the new alloy for piston applications and its comparison with existing piston alloys .....	159
8.1.4. Finite element modelling of the original & new piston and manufactured pistons .....	160
8.1.5. Engine performance with new configuration.....	161
8.1.6. Novel contribution of the research.....	162
8.2. Further work.....	162
8.2.1. Application of the new alloy in diesel engine piston and other high temperature applications .....	162
8.2.2. Tensile tests at higher strain rates and determination of other mechanical properties at various temperatures .....	163
References.....	164
Appendix A.....	172
Appendix A.1. Averaged artificial aging results for all the test temperatures .....	172
Appendix A.2. Scatter in artificial aging results for all the test temperatures .....	175
A.2.1. 140 °C .....	175
A.2.2. 160 °C .....	176
A.2.3. 165 °C .....	177
A.2.4. 170 °C .....	178
A.2.5. 175 °C .....	179
A.2.6. 180 °C .....	180
Appendix A.3. 2D engineering drawings of test specimen.....	181
Appendix A.4. XRD reference cards .....	183

A.4.1. XRD card for Mg <sub>17</sub> Al <sub>12</sub> crystal structure.....	183
A.4.2. Aluminium (Al).....	184
A.4.3. XRD cards for Mg <sub>2</sub> Si crystal structure .....	184
Appendix B .....	189
B.1. Engine technical data: Engine tightening torques and piston life .....	189
B.2. Pressure on the cylinder head nuts .....	190
B.3. Engineering drawings of the different engine components .....	191
B.4. Material properties for FEA .....	201
B.4.1. Connecting rod and gudgeon pin.....	201
B.4.2. Cylinder block .....	202
B.4.3. Cylinder threaded studs and nuts.....	204
B.5. Instantaneous combustion gas temperature and heat transfer coefficient .....	205
B.5.1. 6000 RPM .....	205
B.5.2. 7000 RPM .....	206
Appendix C .....	208
Appendix C.1. Dynamometer specification and torque, power speed curves.....	208
Appendix C.2. 2D engineering drawings of engine mount and other components .....	209
Appendix C.3. In-cylinder pressure sensor specification.....	215
Appendix C.4. Calculation for cutting the bar .....	215
Appendix C.5. Tabulated engine results .....	216
Appendix D .....	218
Appendix D.1. Failure mechanisms in new lightweight piston .....	262
D.1.1. Lack of lubrication caused by fuel flooding due to excessive use of choke .....	262
D.1.2. Less cylinder deformation due to lower coolant temperature .....	263
Appendix D.2. Checklist for new piston assembly and testing.....	266
D.2.1. Assembly, disassembly and piston installation .....	266
D.2.2. Just before testing the engine .....	267
D.2.3. During engine operation.....	267

## List of Figures

<b>Figure 1.1.</b> Proportion of piston friction loss in a Toyota representative 2 litre, inline 4-cylinder, gasoline engine .....	2
<b>Figure 1.2.</b> A schematic of different forces acting on a piston of an internal combustion engine .....	2
<b>Figure 1.3.</b> Representative piston tilting motion of an engine .....	3
<b>Figure 1.4.</b> Development of the specific piston mass .....	4
<b>Figure 2.1.</b> A piston from an old combustion engine .....	7
<b>Figure 2.2.</b> A reverse engineered CAD model of the test engine's piston .....	9
<b>Figure 2.3.</b> Schematic of melt spinning and subsequent processes .....	16
<b>Figure 2.4.</b> Geometry of the crank-mechanism .....	17
<b>Figure 3.1.</b> Flowchart diagram of the research methodology.....	26
<b>Figure 4.1.</b> The rotary grinder used in this project .....	31
<b>Figure 4.2.</b> Specimen dryer with the polished sample .....	32
<b>Figure 4.3.</b> An image of the finished polished sample .....	33
<b>Figure 4.4.</b> An image of the new alloy's microstructure taken with light microscope .....	34
<b>Figure 4.5.</b> Semi-processed microstructure image of the new alloy in ImageJ .....	34
<b>Figure 4.6.</b> Particles numbered by ImageJ .....	35
<b>Figure 4.7.</b> Particle volume fraction across the sample's cross section .....	36
<b>Figure 4.8.</b> Average 3D particle size across the bar's cross section .....	37
<b>Figure 4.9.</b> Particle distribution of all the observed particles .....	38
<b>Figure 4.10.</b> Hardness test results along the bar's cross section of the as-received material .....	39
<b>Figure 4.11.</b> SEM image used for bulk EDS analysis .....	41
<b>Figure 4.12.</b> EDS spectrum of the bulk material in as-received state .....	41
<b>Figure 4.13.</b> SEM image of the alloy's microstructure in SE mode .....	43
<b>Figure 4.14.</b> SEM image of the alloy's microstructure in BS mode .....	43



<b>Figure 4.15.</b> EDS spectrum of a large particle in as-received state .....	43
<b>Figure 4.16.</b> Material cutting plan for the heat treatment .....	45
<b>Figure 4.17.</b> Heat treatment methodology diagram to determine T6 .....	46
<b>Figure 4.18.</b> T6 heat treatment results after removing the samples from furnace .....	47
<b>Figure 4.19.</b> T6 heat treatment results a week after removing the samples from furnace ....	47
<b>Figure 4.20.</b> Solid solution results for the reused heat treated samples .....	48
<b>Figure 4.21.</b> Microstructural stabilisation heat treatment methodology diagram .....	49
<b>Figure 4.22.</b> Microstructural stability results after removing the samples from furnace .....	50
<b>Figure 4.23.</b> Microstructural stability results a week after removing the samples from Furnace .....	50
<b>Figure 4.24.</b> A picture of the flat dogbone specimen used for the tensile tests .....	52
<b>Figure 4.25.</b> a) Test setup for the high temperature tensile tests. b) Alignment of the sample in the slot .....	52
<b>Figure 4.26.</b> Tensile test results at various temperatures .....	53
<b>Figure 4.27.</b> Deformed flat dogbone specimens .....	53
<b>Figure 4.28.</b> Yield strength comparison of Al-2618 and the new alloy at a range of tensile test temperatures .....	54
<b>Figure 4.29.</b> Tensile test results after 100 hours of use at the relevant temperatures .....	55
<b>Figure 4.30.</b> Yield strength comparisons of the new alloy during operation and after 100 hour of use .....	55
<b>Figure 4.31.</b> SEM images of the fractured samples tested at a) room temperature (T6) and b) 350 °C.....	56
<b>Figure 4.32.</b> Zoomed in SEM images of the fractured samples tested at a) room temperature T6 and b) 350 °C.....	57
<b>Figure 4.33.</b> SEM image of the fractured face of the specimen tested in room temperature (T6) .....	58
<b>Figure 4.34.</b> EDS spectrum of the large particle in the fractured face of the sample	

tested in room temperature .....	58
<b>Figure 4.35.</b> SEM image of the fractured face of the sample tested at 350 °C.....	59
<b>Figure 4.36.</b> EDS spectrum of the large particle in the fractured face of the sample tested at 350 °C .....	59
<b>Figure 4.37.</b> Test fixture used for the compression tests .....	60
<b>Figure 4.38.</b> Compression test results of the new alloy for samples cut from the extruded bar in two different directions .....	61
<b>Figure 4.39.</b> SEM image of the fractured face of the sample in extrusion direction .....	62
<b>Figure 4.40.</b> EDS spectrum of the large particle in the sample tested in extrusion direction .....	62
<b>Figure 4.41.</b> SEM image of the fractured face of the sample tested in transverse direction .....	63
<b>Figure 4.42.</b> EDS spectrum of the large particle in the sample tested in transverse direction .....	63
<b>Figure 4.43.</b> Diffractograms of the samples in two different heat treatment conditions .....	64
<b>Figure 4.44.</b> Yield strength comparison of different aluminium alloys .....	65
<b>Figure 4.45.</b> Ultimate tensile strength comparison of different aluminium alloys .....	65
<b>Figure 4.46.</b> Temperature and mass distributions of KTM 450 XCF .....	66
<b>Figure 5.1.</b> Methodology flowchart for the piston finite element analysis .....	68
<b>Figure 5.2.</b> Model 1 assembly for the piston finite element analysis .....	70
<b>Figure 5.3.</b> Model 2 assembly for the piston finite element analysis .....	70
<b>Figure 5.4. a)</b> Application of the cylindrical support on pin-connecting rod interface .....	71
<b>b)</b> Definition of the cylindrical support according to the Ansys Workbench™ manual .....	71
<b>Figure 5.5.</b> Application of the boundary conditions to FE model 2 .....	72
<b>Figure 5.6.</b> Contacts between the cylinder-mounting studs, cylinder and washers .....	73
<b>Figure 5.7.</b> A reverse engineered CAD model of the test engine's piston .....	74
<b>Figure 5.8.</b> A representation of the crank slider mechanism and the piston mechanical	

loads .....	77
<b>Figure 5.9.</b> The in-cylinder pressure traces of the test engine at different engine speeds .....	77
<b>Figure 5.10.</b> Application of in-cylinder pressure to the FE models 1 and 2 .....	78
<b>Figure 5.11.</b> Piston accelerations of the test engine at different engine speeds .....	78
<b>Figure 5.12.</b> Application of the acceleration to FE models 1 and 2 .....	79
<b>Figure 5.13.</b> Lateral forces of the test engine at different engine speeds .....	80
<b>Figure 5.14.</b> Application of the lateral forces to FE models 1 and 2 .....	80
<b>Figure 5.15.</b> Application of gas heat transfer coefficient to the piston crown and cylinder in FE models 1 and 2 .....	82
<b>Figure 5.16.</b> Application of the heat transfer coefficients to the compression ring in the FE models 1 and 2 .....	83
<b>Figure 5.17.</b> Application of the heat transfer coefficients to the rings lands and piston outer skirt in the FE models 1 and 2 .....	83
<b>Figure 5.18.</b> Application of the heat transfer coefficients to the piston under-crown and inner walls of piston skirt in the FE models 1 and 2 .....	84
<b>Figure 5.19.</b> Application of the heat transfer coefficient to the cooling jacket in FE model 2 .....	85
<b>Figure 5.20.</b> Mesh convergence analyses at crown for both FE models .....	88
<b>Figure 5.21.</b> Mesh convergence analyses at the pin hole for both FE models .....	89
<b>Figure 5.22.</b> Maximum principal stresses in piston crown over an entire engine cycle at 6000 rpm .....	92
<b>Figure 5.23.</b> Maximum principal stresses in piston pin hole over an entire engine cycle at 6000 rpm .....	92
<b>Figure 5.24.</b> Piston temperature distributions in both FE models .....	93
<b>Figure 5.25.</b> Temperature distribution in cylinder in model 2 .....	93
<b>Figure 5.26.</b> Maximum principal stresses in piston in model 1 .....	94

<b>Figure 5.27.</b> Maximum principal stresses in piston in model 2 .....	95
<b>Figure 5.28.</b> Plastic strain in piston in model 1 .....	95
<b>Figure 5.29.</b> Plastic strain in piston in model 2 .....	96
<b>Figure 5.30.</b> Piston deformation graphs in X directions for both FE models .....	97
<b>Figure 5.31.</b> Piston deformation plots in X directions for both FE models .....	97
<b>Figure 5.32.</b> Piston deformation graphs in Y directions for both FE models .....	98
<b>Figure 5.33.</b> Piston deformation plots in Y directions for both FE models .....	98
<b>Figure 5.34.</b> Piston deformation graphs in Z directions for both FE models .....	99
<b>Figure 5.35.</b> Piston deformation plots in Z directions for both FE models .....	99
<b>Figure 5.36.</b> Pin deformation plots in Z direction in both FE models .....	100
<b>Figure 5.37.</b> Fatigue strength of Al-2618 at different temperatures .....	100
<b>Figure 5.38.</b> Features and regions of piston that we were left unmodified .....	102
<b>Figure 5.39.</b> Exclusion regions (red) for the piston optimisation .....	104
<b>Figure 5.40.</b> Optimised piston design from the topology optimisation analysis .....	104
<b>Figure 5.41.</b> Maximum principal stresses in the piston crown due to incremental material removal .....	107
<b>Figure 5.42.</b> Maximum principal stresses in pin hole due to incremental material removal .....	107
<b>Figure 5.43.</b> Maximum temperature changes in piston due to incremental material removal .....	108
<b>Figure 5.44.</b> Deformation changes in piston due to incremental material removal .....	108
<b>Figure 5.45.</b> Piston deformation graphs in X directions for original and new pistons .....	109
<b>Figure 5.46.</b> Piston deformation graphs in Y directions for original and new pistons .....	109
<b>Figure 5.47.</b> Piston deformation graphs in Z directions for original and new pistons .....	110
<b>Figure 5.48.</b> Comparison of original and new piston designs .....	111
<b>Figure 5.49.</b> Pictures of the available material before upset forging .....	112

<b>Figure 5.50.</b> Pictures of the upset forged billets .....	112
<b>Figure 5.51.</b> FE results after the suggested changes were made .....	113
<b>Figure 5.52.</b> Pictures of the machined pistons.....	113
<b>Figure 5.53.</b> Picture of the coated piston .....	114
<b>Figure 6.1.</b> Flow chart of the engine test methodology .....	116
<b>Figure 6.2.</b> A CAD model of engine mount assembly .....	118
<b>Figure 6.3.</b> Pictures of the coupling shaft with universal joint used in this project .....	119
<b>Figure 6.4.</b> a) A picture of the standard sprocket for the test engine. b) A picture of the modified sprocket .....	119
<b>Figure 6.5.</b> Installation of the boss on exhaust pipe for lambda sensor .....	121
<b>Figure 6.6.</b> A picture of the exhaust system and support fixture used for the test engine ...	121
<b>Figure 6.7.</b> Representation of the crankshaft extension for the encoder installation .....	122
<b>Figure 6.8.</b> Encoder assembly mounted on the engine .....	122
<b>Figure 6.9.</b> FMS 1000 fuel weigher system used in this research .....	123
<b>Figure 6.10.</b> A screenshot of the FMS 1000 control .....	124
<b>Figure 6.11.</b> a) Sensor mounted modified spark plug. b) Electronic circuitry for the pressure sensor .....	125
<b>Figure 6.12.</b> Air inlet modification to allow for the sensor installation .....	126
<b>Figure 6.13.</b> Pictures of modified crankshaft assembly .....	127
<b>Figure 6.14.</b> Comparisons of various performance indicators for original and new pistons at 3000 rpm <b>a)</b> BSFC vs. MFRair <b>b)</b> BSFC vs. torque <b>c)</b> volumetric efficiency vs. torque <b>d)</b> volumetric efficiency vs. MFRair <b>e)</b> peak pressure vs. MFRair .....	135
<b>Figure 6.15.</b> Comparisons of various performance indicators for original and new pistons at 4500 rpm <b>a)</b> BSFC vs. MFRair <b>b)</b> BSFC vs. torque <b>c)</b> volumetric efficiency vs. torque <b>d)</b> volumetric efficiency vs. MFRair <b>e)</b> peak pressure vs. MFRair .....	138
<b>Figure 6.16.</b> Comparisons of various performance indicators for original and new pistons at 6000 rpm <b>a)</b> BSFC vs. MFRair <b>b)</b> BSFC vs. torque <b>c)</b> volumetric efficiency vs. torque <b>d)</b> volumetric efficiency vs. MFRair <b>e)</b> peak pressure vs. MFRair .....	141
<b>Figure 7.1.</b> Yield strength comparison of two different piston aluminium alloys vs. the new alloy .....	148

<b>Figure A.1.</b> T6 heat treatment results for all the test temperatures after removing the samples from the furnace .....	173
<b>Figure A.2.</b> T6 heat treatment results for all the test temperatures a week after removing the samples from the furnace .....	174
<b>Figure A.3.</b> Scatter in the 140 °C heat treatment results after removing the samples from the furnace .....	175
<b>Figure A.4.</b> Scatter in the 140 °C heat treatment results a week after removing the samples from the furnace .....	175
<b>Figure A.5.</b> Scatter in the 160 °C heat treatment results after removing the samples from the furnace .....	176
<b>Figure A.6.</b> Scatter in the 160 °C heat treatment results a week after removing the samples from the furnace .....	176
<b>Figure A.7.</b> Scatter in the 165 °C heat treatment results after removing the samples from the furnace .....	177
<b>Figure A.8.</b> Scatter in the 165 °C heat treatment results a week after removing the samples from the furnace .....	177
<b>Figure A.9.</b> Scatter in the 170 °C heat treatment results after removing the samples from the furnace .....	178
<b>Figure A.10.</b> Scatter in the 170 °C heat treatment results a week after removing the samples from the furnace .....	178
<b>Figure A.11.</b> Scatter in the 175 °C heat treatment results after removing the samples from the furnace .....	179
<b>Figure A.12.</b> Scatter in the 175 °C heat treatment results a week after removing the samples from the furnace .....	179
<b>Figure A.13.</b> Scatter in the 180 °C heat treatment results after removing the samples from the furnace .....	180
<b>Figure A.14.</b> Scatter in the 180 °C heat treatment results a week after removing	

the samples from the furnace .....	180
<b>Figure A.15.</b> A 2D engineering drawing of flat dogbone specimen for tensile tests .....	181
<b>Figure A.16.</b> A 2D engineering drawing of the cylindrical specimen for the compression tests .....	182
<b>Figure A.17.</b> XRD reference card for $Mg_{17}Al_{12}$ crystal structure .....	183
<b>Figure A.18.</b> Aluminium XRD reference card .....	184
<b>Figure A.19.</b> XRD reference card for $Mg_2Si$ crystal structure .....	186
<b>Figure A.20.</b> XRD reference card for $Mg_2Si$ crystal structure .....	188
<b>Figure B.1.</b> The recommended torque for the cylinder mounts and nuts .....	189
<b>Figure B.2.</b> The recommended service life for the original piston .....	190
<b>Figure B.3.</b> A 2D engineering drawing of the connecting rod small end for the piston FEA .....	192
<b>Figure B.4.</b> A 2D engineering drawing of the cylinder mounts for the piston FEA .....	193
<b>Figure B.5.</b> A 2D engineering drawing of the cylinder liner and casing for the piston FEA .....	194
<b>Figure B.6.</b> A 2D engineering drawing of the gudgeon pin for the piston FEA .....	195
<b>Figure B.7.</b> A 2D engineering drawing of the washer for the piston FEA .....	196
<b>Figure B.8.</b> A 2D engineering drawing of the original piston for the piston FEA .....	198
<b>Figure B.9.</b> A 2D engineering drawing of the new piston for the piston FEA .....	200
<b>Figure B.10.</b> A picture of the cylinder block for the test engine .....	203
<b>Figure B.11.</b> Instantaneous combustion gas temperature for one engine cycle at 6000 rpm .....	205
<b>Figure B.12.</b> Instantaneous combustion heat transfer coefficient for one engine cycle at 6000 rpm .....	206
<b>Figure B.13.</b> Instantaneous combustion gas temperature for one engine cycle at 7000 rpm .....	206

<b>Figure B.14.</b> Instantaneous combustion heat transfer coefficient for one engine cycle at 7000 rpm .....	207
<b>Figure C.1.</b> The torque and power speed curves of Schenck, type W130 dynamometer used in this project .....	209
<b>Figure C.2.</b> A 2D engineering drawing of the engine mount .....	210
<b>Figure C.3.</b> A 2D engineering drawing of the upright plate .....	211
<b>Figure C.4.</b> A 2D engineering drawing of the engine aligning plate .....	212
<b>Figure C.5.</b> A 2D engineering drawing of the engine representation .....	213
<b>Figure C.6.</b> An exploded view of the engine mount assembly setup .....	214
<b>Figure D.1.</b> Fuel flooded piston .....	262
<b>Figure D.2.</b> Cylinder deformation in X direction (along pin direction) with coolant temperature of 80 .....	264
<b>Figure D.3.</b> Cylinder deformation in Y direction (perpendicular to pin direction) with coolant temperature of 80 °C .....	264
<b>Figure D.4.</b> Cylinder deformation in X direction (along pin direction) with coolant temperature of 120 C .....	265
<b>Figure D.5.</b> Cylinder deformation in Y direction (perpendicular to pin direction) with coolant temperature of 120 °C .....	265



## List of Tables

<b>Table 4.1.</b> Bulk elemental analysis results of the alloy in as-received state .....	42
<b>Table 4.2.</b> Averaged bulk elemental analyses results of the alloy in as-received state .....	42
<b>Table 4.3.</b> Elemental analysis results of the large particle in as-received state .....	44
<b>Table 4.4.</b> Averaged elemental analyses results of the large particle in as-received state .....	44
<b>Table 5.1.</b> Mechanical properties of the two piston alloys .....	75
<b>Table 5.2.</b> The test engine specification .....	76
<b>Table 5.3.</b> Reciprocating components masses .....	79
<b>Table 5.4.</b> Engine cooling oil properties and other relevant data .....	81
<b>Table 5.5.</b> Mean gas heat transfer coefficient and temperature values for two different engine speeds .....	81
<b>Table 5.6.</b> Heat transfer coefficient values of the compressing ring .....	82
<b>Table 5.7.</b> Heat transfer coefficient values of the ring lands and outer piston skirt .....	83
<b>Table 5.8.</b> Heat transfer coefficient values of the piston under-crown and the inner walls of the piston skirt .....	84
<b>Table 5.9.</b> Mechanical loads values in the maximum combustion load case at 6000 rpm .....	86
<b>Table 5.10.</b> Stresses in both FE models with various interface treatments .....	87
<b>Table 5.11.</b> Mesh convergence analyses results for the non-critical parts .....	89
<b>Table 5.12.</b> Mesh refinement at the pin hole for both FE models .....	90
<b>Table 5.13.</b> Different contact formulations for both FE models .....	90
<b>Table 5.14.</b> Piston stresses in critical areas for the critical load cases .....	91
<b>Table 5.15.</b> Descriptions of the material removal steps for manual piston optimisation .....	106
<b>Table 5.16.</b> Stresses of first optimised piston and after the suggested changes for machining .....	113

<b>Table 7.1.</b> Summary of various strengthening mechanisms contribution .....	148
<b>Table B.1.</b> Mechanical properties of AISI 8620 steel used in the connecting rod and pin of the test engine .....	202
<b>Table B.2.</b> Mechanical properties of aluminium alloy 356-T6-T-T61 used in the cylinder block of the test engine .....	204
<b>Table B.3.</b> Mechanical properties of stainless steel 316 used in studs and nuts of the test engine .....	205
<b>Table C.1.</b> Performance specification of Schenck, type W130 dynamometer used in this project .....	208
<b>Table C.2.</b> Performance specification of the in-cylinder pressure sensor used in this project .....	215
<b>Table C.3.</b> Averaged engine test results in two configurations at engine speed of 3000 rpm.....	216
<b>Table C.4.</b> Averaged engine test results in two configurations at engine speed of 4500 rpm.....	217
<b>Table C.5.</b> Averaged engine test results in two configurations at engine speed of 6000 rpm.....	217

## List of Abbreviations

Abbreviation	In Full
1D	One Dimensional
2D	Two Dimensional
3D	Three Dimensional
AFR	Air Fuel Ratio
Al	Aluminium
ASM	American Society for Metals
ATS	Anti-Thrust Side
BC	Boundary Condition
BCC	Body Centre Cubic
BDC	Bottom Dead Centre
BS	Back Scatter
BSFC	Brake Specific Fuel Consumption
C	Carbon
CA	Crank Angle
CAD	Crank Angle Degree
CAD	Computer Aided Design
CGI	Compact Graphite Iron
CNC	Computer Numerical Control
Comp.	Compression
CTE	Coefficient of Thermal Expansion
Cu	Copper
Dyno	Dynamometer
ECU	Electronic Control Unit
ED	Extrusion Direction
EDS	Energy Dispersive Spectroscopy
EDX	Energy-Dispersive X-ray Spectroscopy
eV	Electron Volt
FCC	Front Centre Cubic
FE	Finite Element

FEA	Finite Element Analysis
F1	Formula One
FGM	Functionally Graded Material
FMS	Fuel Measuring System
G	Gram
GP	Grand Prix
H	Hour
HCP	Hexagonal Closed Pack
Hp	Horse Power
H-P	Hall-Petch
HSE	High Speed Engine
HT	Heat Treatment
HTC	Heat Transfer Coefficient
HTZ	High Temperature Zirconia
HTO	High-Temperature Oxidation
HV	Hardness Vickers
IC	Internal Combustion
ICE	Internal Combustion Engine
IM	Industrial Metallurgy
IMS	Industrial Methylated Spirit
J	Joule
K	Kelvin
Kg	Kilogram
kW	Kilo Watt
L	Litre
M	Metre
MA	Mechanical Alloying
MAS	Micro-Alloyed Steel
Mg	Magnesium
MMC	Metal Matrix Composite
MPa	Mega Pascal
MPS	Mean Piston Speed

MW	Mega Watt
MPa	Mega Pascal
N	Newton
NASA	National Aeronautics and Space Administration
NCI	Nodular Cast Iron
Nm	Nano Metre
NS	Nanostructured
Nu	Nusselt Number
O	Oxygen
Pa	Pascal
Pr	Prandtl Number
Re	Reynold's Number
rpm/RPM	Revolution Per Minute
RS	Rapid Solidified/Solidification
RT	Room Temperature
SE	Secondary Electron
sec	Second
SE	Secondary Electron
SEI	Secondary Electron Imaging
SEM	Scanning Electron Microscopy
SEM	Scanning Electron Microscope
Si	Silicon
SI	Spark Ignition
SPD	Sever Plastic Deformation
SSS	Supersaturated Solution
TBC	Thermal Barrier Coating
TDC	Top Dead Centre
Temp.	Temperature
TM	Trade Mark
TS	Thrust Side
UBA	University of Buenos Aires
UFG	Ultra-Fine Grained

UK	United Kingdom
US	United States
USA	United States of America
UTS	Ultimate Tensile Strength
V	Volt
W	Watt
XRD	X-ray Diffraction
YS	Yield Strength

## List of Symbols

Symbol	Description	Unit
A	Area	$m^2$
Ac	Cross-Sectional Area	$m^2$
A <sub>s</sub>	2D Particle Area	$\mu m^2$
b <sub>v</sub>	Burgers Vector	nm
b	Lubricating Oil Film	m
B	Engine's Bore	m
BSFC	Brake Specific Fuel Consumption	g/kW.hr
°C	Degree Centigrade	-
C	Coefficient of friction	-
C <sub>p</sub>	Specific Heat Capacity	kJ/(Kg.K)
d	Average Grain Size	nm
D	Nominal Bolt Diameter	m
D <sub>h</sub>	Hydraulic Diameter	m
D <sub>p</sub>	Precipitate Diameter	nm
D <sub>ps</sub>	3D Particle Size	$\mu m$
D <sub>s</sub>	Mean Planar Particle Diameter	nm
E	Young's Modulus	GPa
F	Force	N
F <sub>g</sub>	Gas Force	N
f <sub>v</sub>	Particle Volume Fraction	%
G	Shear Modulus	GPa
Gd	Gadolinium	
H	Heat Transfer Coefficient	$W/m^2 K$
h <sub>m</sub>	Mean Heat Transfer Coefficient	$W/m^2 K$
k	Locking Parameter	-
K	Thermal Conductivity	W/m.°C
k <sub>oil</sub>	Engine Oil Thermal Conductivity	W/m K
L	Connecting Rod Length	m

$L_{ps}$	Edge to Edge Planar Inter-Particle Spacing	nm
$L_f$	Lateral Force	N
$m$	Mass of Fuel or Air	g
$M_m$	Molar Mass of Fuel or Air	g/mol
$M$	Taylor Factor	-
$m_a$	Mass of Air	g
$m_f$	Mass of Fuel	g
$(m_a)_{act}$	Mass of Air Actual	g
$(m_f)_{act}$	Mass of Fuel Actual	g
$(\frac{m_a}{m_f})_{st}$	Standard/Stoichiometric Air Fuel Ratio	-
$m_B$	Reciprocating Components Mass	Kg
$\mu m$	Micro Meter	-
$n$	Combustion Product	mol
$N$	Engine Speed	rpm
$n_r$	Number of Revolution per Engine Cycle	-
$\eta_v$	Volumetric Efficiency	-
$P$	Pressure	Psi
$P_g$	Gas Pressure	Pa
$P_w$	Wetted Perimeter	m
$P_b$	Brake Power	
$\phi$	Equivalence Ratio	-
$\pi$	The Mathematical Constant = 3.1415...	-
$r$	Crank Offset/Radius	m
$R$	Universal or Ideal Gas Constant	J/mol K
$r_c$	Compression Ratio	-
$r_s$	2D Particle Radius	$\mu m$
$r_v$	3D Particle Radius	$\mu m$
$\rho$	Density	kg/m <sup>3</sup>
$\rho_d$	Dislocation Density	m <sup>-2</sup>
$\rho_a$	Air Density	kg/m <sup>3</sup>



$\rho_{oil}$	Oil Density	kg/m <sup>3</sup>
S	Engine Stroke	m
s	Sensitivity	V/Psi
$T_g$	Gas Temperature	K
T	Torque	Nm
$T_b$	Brake Torque	Nm
TEC	Thermal Expansion Coefficient	μm/m.K
$T_m$	Mean Gas Temperature	K
$\theta$	Crank Angle	Degree
UTS	Ultimate Tensile Strength	MPa
$U_{oil}$	Oil Flow Speed	m/sec
$\mu_{oil}$	Oil Dynamic Viscosity	kg/m.sec
V	Cylinder Volume	m <sup>3</sup>
$V_c$	Clearance Volume	m <sup>3</sup>
$V_d$	Displacement Volume	m <sup>3</sup>
$V_p$	Mean Piston Speed	m/sec
$V_t$	Engine's Total Volume	m <sup>3</sup>
v	Poisson Ratio	-
$\Omega$	Crank Angular Velocity	rad/sec
X	Piston Position	m
$\ddot{x}$	Piston's Acceleration	m/sec <sup>2</sup>
Y	Yttrium	-
YS	Yield Strength	MPa
$\alpha$	Dislocation Strengthening Efficiency	%
$\Delta\sigma_p$	Strengthening Contribution to Yield Stress Due to the Hard Particles	MPa
$\Delta\sigma_{gb}$	Strengthening Contribution to Yield Stress Due to the Grain Boundaries	MPa
$\sigma_0$	Lattice Frictional Stress	MPa

## Chapter 1: Introduction

### 1.1. Background

The automobile and motorsport industries are under immense pressure due to emission laws to reduce fuel consumption and alleviate the effects of global warming. Also there is a finite source of hydrocarbon supply which points towards possibility of depletion in the long term. One quarter of the crude oil consumed in Western Europe is used in transport sector, out of which 60% is used in private cars (Blackmore and Thomas, 1977). The Transport sector especially private transport is the largest contributor to emissions hence improvement in this sector will lead to a bigger reduction in global warming. Emissions reduction is the leading reason to improve engine efficiency. Fuel consumption economy is not only required in transport sector, but also in motor racing since frequent refuelling wastes valuable motor racing time. The time taken for refuelling could be the difference between winning and losing (Blackmore and Thomas, 1977).

The reduction in fuel consumption and improvement in engine performance can effectively be achieved by reducing losses in the engine. There are many types of losses in an engine and the most dominant are those caused by friction (Merkle, Kunkel and Wachtmeister, 2012). Engines and engine component investigations have shown that even today the best class engines harbour a frictional reduction potential of 20% (Schwaderlapp, Koch and Dohmen, 2000). It has been reported that the piston assembly is responsible for 30 – 40% (Kohashi *et al.*, 2013) or even 50% (Schwaderlapp, Koch and Dohmen, 2000) of the friction losses in an engine (Figure 1.1).

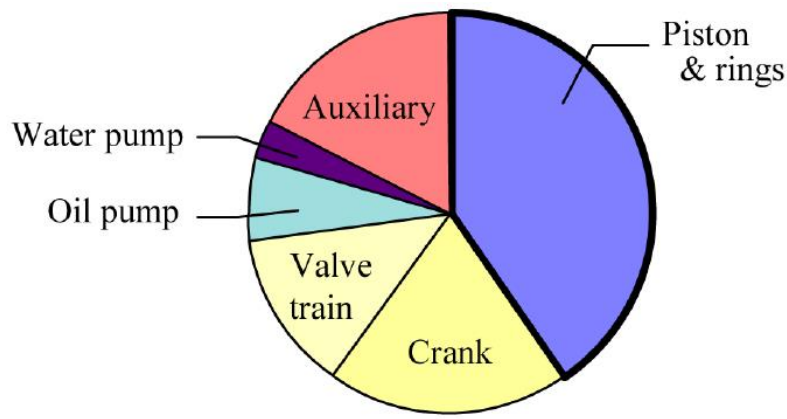


**Figure 1.1.** Proportion of piston friction loss in a Toyota representative 2 litre, inline 4-cylinder, gasoline engine (Kohashi *et al.*, 2013).

The piston assembly friction is caused by a phenomenon called piston lateral movement/secondary acceleration. In ideal world there should be no contact between piston and cylinder wall. However, the conversion of a piston's linear motion into the crankshaft's rotational motion and the piston tilt due to the connecting rod resisting the combustion gas pressure generates force components in the crank mechanism that press the piston against the cylinder wall as illustrated in Figure 1.2. This force is generally known as lateral force or connecting rod force.

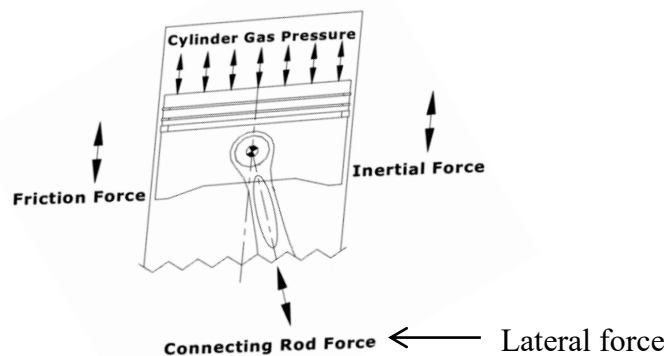


**Figure 1.2.** A schematic of different forces acting on a piston of an internal combustion engine (Nagar and Miers, 2011).

During the compression stroke the piston tilts towards the anti-thrust side (ATS) and during expansion/power stroke the high gas pressure forces the piston onto thrust side (TS) (see Figure 1.3). The secondary movement increases with engine speed and results in increased

secondary inertial forces hence the piston changes direction more frequently and causes the friction to increase (J and Agarwal, 2014). This reduces engine efficiency at higher speeds.

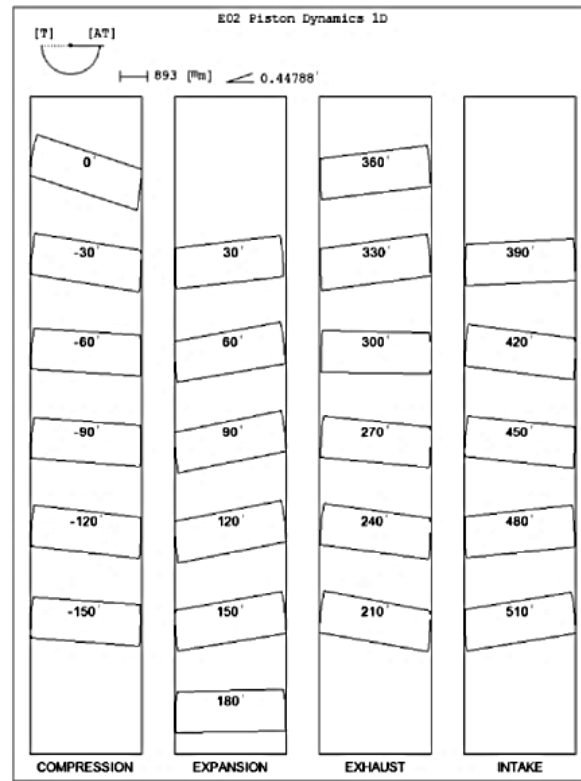


**Figure 1.3.** Representative piston tilting motion of an engine (J and Agarwal, 2014).

The lateral force is made of the components of gas and inertial forces (Norton, 2012) (See Section 2.9.1.3 and equation 2.3) and the inertial force is dependent on the oscillating mass, hence the lateral force is also dependent on the oscillating mass (see Section 2.9.1.3) . The oscillating masses include piston, pin, rings etc. The piston and the piston pin account for the greatest proportion of the oscillating mass. Any mass reduction undertaking must therefore start with these components. There has been great effort towards reducing the oscillating mass and reducing the piston mass is one of the approaches (Loureiro et al, 2010). Figure 1.4 shows the mass reduction trend of pistons with 0.4 – 0.6 L displacement for years 1992 – 1999.

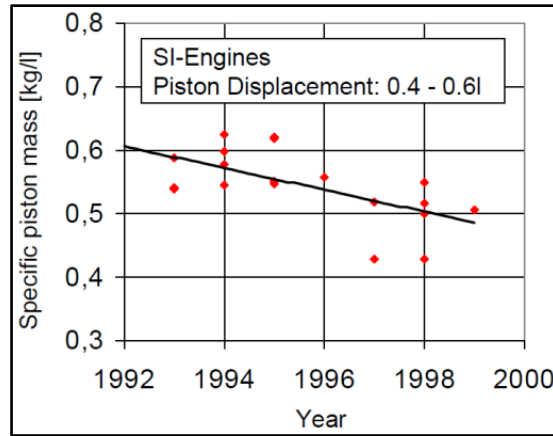


**Figure 1.4.** Development of the specific piston mass (Schwaderlapp, Koch and Dohmen, 2000).

### 1.1.1. Project motivation and Research Gap

The motivation of the project lies in the heat treatment characterisation and design evaluation of a new rapidly solidified (RS) aluminium alloy with improved mechanical properties for internal combustion engine pistons. The new alloy has lower density and higher strength at elevated temperatures than conventional aluminium alloys, making it an ideal piston material in internal combustion (IC) engines. The improved properties of the new alloy will enable engineers to design lightweight pistons with reduced mass.

The reduced piston mass will contribute to increased acceleration and speed of the engine hence improving engine's performance in terms of torque, power and fuel consumption. Reduced engine friction will not only enhance engine performance, but will also reduce piston wear therefore improves piston fatigue life and engine reliability (Winship, 1967).

Nanostructured aluminium alloys such as the one investigated in this project can be used in both types of engine, diesel and petrol. Due to higher compression ratios in diesel engines, there are higher demands on mechanical components and tend to be more robust and heavy; therefore the development of lighter and resistant alloys is also beneficial for those engines. However; the main interest is to use these in Otto cycle/petrol engines because they can operate faster than diesel and the inertial forces are significantly higher. The inertial forces

depend on the speed and mass; the lighter piston will therefore produce greater reduction in inertial forces in petrol engines. In petrol racing engines, the rotational speed can reach values of order of 20000 rpm compared to 6000 rpm limit posed by diesel engines. Furthermore, the trend of changing from diesel to petrol in small high speed engines will further encourage more efforts to be put into developing high temperature aluminium alloys.

As highlighted in this literature review Nanostructured aluminium alloys have attracted significant attention due to their superior mechanical properties at elevated temperatures and offer possibilities of numerous applications in internal combustion engines (ICEs). However, their use has not expanded into internal combustion engine applications and there is not much publically available research. Previous experiments, carried out at the University of Buenos Aires on similar material have shown promise in the use of such alloys for piston applications (Bonelli *et al.*, 2014). The research undertaken here is to explore and expand the applications of nanostructured aluminium alloys in ICE pistons using a newly developed nanostructured alloy as a case study.

## **1.2. Aim and objectives of the project**

The aim of the research is to characterise a new nanostructured aluminium alloy and use heat treatment to optimise its mechanical properties for application as a lightweight engine piston material. In order to achieve this aim, the following objectives were set.

- I. Review of literature on the development and characterisation of piston materials.
- II. Review of piston design methods using finite element analyses.
- III. Determine the T6 heat treatment and thermal stability conditions of the new alloy for optimum mechanical properties.
- IV. To review practices and standards for material testing and carry out the testing to determine the mechanical properties.

- V. Carry out new piston design using the new alloy's mechanical properties.
- VI. Review of practices and standards for engine testing and carry out engine tests in both configurations, with original and new pistons to determine the engine performance changes.

## **Chapter 2: Literature review and background theory**

### **2.1. Introduction**

This chapter highlights the function of pistons, design considerations and the evolution of piston design. The mechanical properties required for a piston design have been reviewed and the potential of using nanostructured aluminium alloys in pistons, and the work being undertaken in this area in the literature is reviewed. Furthermore, this Chapter specifies the mechanisms used to strengthen metals specifically the ones that contributed to the higher strength of the alloy investigated in this project. It also describes the production method used to produce the alloy. In addition, it describes the different types of engine loads that act on pistons and how they can be determined and implemented in finite element analysis (FEA) to design a piston.

### **2.2. Internal combustion engines (ICEs) piston**

Most internal combustion engines use piston (Figure 2.1) reciprocating back and forth or up and down in a cylinder (Pulkrabek, 2014). The piston is one of the most important components of an internal combustion engine and its design greatly affects the performance of an engine.



**Figure 2.1.** A piston from an old combustion engine (Robinson, 1964).



### **2.3. Piston design aims and evolution over time**

Piston design varies vastly depending on application and the type of engine. A lot of research has been devoted to this engine component than many others due to its importance (Robinson, 1964). A piston design is an engineering challenge due to the complex physics and uncertainty in its operating conditions. An improper piston design could increase friction and noise, leading to reduction in the engine's efficiency and life (Patel, Shah and Mourelatos, 2010).

#### **2.3.1. Piston design considerations**

The piston is one of the most critical components in an engine which transfers energy from the combustion of air-fuel mixture to the crankshaft through the connecting rod (Xu *et al.*, 2011). The piston is also one the most stressed components in an engine (Cha *et al.*, 2009). A piston must be designed to withstand an engine's thermal and dynamic loads and avoid structural failure, noise and skirt scuffing. It should also be light to minimise inertial loads, reduce friction and transmit heat (Cha *et al.*, 2009; Xu *et al.*, 2011). Reducing vibration and noise is a prime concern in passenger cars, but not that important in high performance racing engines where the piston design is driven by reducing friction to increase performance and efficiency (Taylor, 1985).

#### **2.3.2. Piston design evolution**

Piston design has evolved over time to match performance requirements. There are 3 basic types of piston designs as described by (Winship, 1967). The closed slotless type piston design is used in high performance engines such as motorbikes and has no slot between the piston's head and the skirt. It has little tolerance to variations in fits therefore requires precise machining. It also allows excellent heat flow and reduces the ring groove deflection due to the all-round support of the ring belt area (Winship, 1966; Winship, 1967).

The test engine used in this project is a KTM (450 XCF 2008) high performance motorbike engine which has a closed slotless type piston as can be seen in Figure 2.2. A geometrical 3D model of the piston was reverse engineered based on the actual piston which was scanned using a three dimensional (3D) laser scanner. The scanning of the piston was carried out by an external company called Central Scanning that used Comet L3D Blue Light Scanner. The scanner had measurement accuracy of 0.007 – 0.08 mm (7 – 80  $\mu\text{m}$ ) which was sufficient to capture all the external detailed features of the piston required for the piston design. For example, the valves clearances are normally within close dimensional tolerances and in the case of the test engine the cold valves clearances were 0.1 – 0.17 mm.

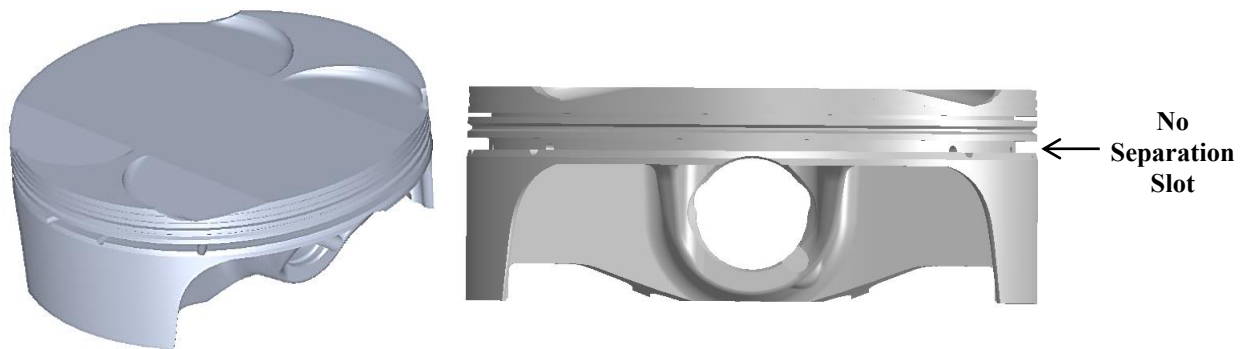


**Figure 2.2.** A reverse engineered CAD model of the test engine's piston.

An improved piston not only needs robust design, but also materials with better mechanical properties. Material requirements for piston applications are described below.

#### **2.4. Piston's material requirements**

The properties required for a piston can be best identified by considering the work a piston has to do. The very first function of a piston is to transfer the combustion gas energy to the crankshaft through the connecting rod, and to act as a seal against the combustion products and the engine oil in the crankcase. In addition, it must transmit the combustion heat to the atmosphere via the rings and the cylinder's cooling jacket. It must perform these functions as silently as possible, without breaking or distorting under the thermal and mechanical loads.

As much as possible, it should avoid changing shape and size under the influence of heat and mechanical loading. The piston must neither be eroded nor burnt by the combustion products and the wear should be kept to minimum (Schofield and Wyatt, 1946). Furthermore, the piston should be cheap as a material and not costly to produce (Rudnik *et al.*, 2003; GmbH, 2016).

A piston has to be strong enough to withstand the combustion pressures and the inertial forces generated by its own mass and the motion. The strength should be maintained throughout the piston's working temperatures range which lies between  $-30\text{ }^{\circ}\text{C}$  and  $300\text{ }^{\circ}\text{C}$  in the case of petrol engines and as high as  $350$  or  $400\text{ }^{\circ}\text{C}$  for diesel engines. The suitable piston material therefore should possess the following properties.

- A sufficiently high tensile, compression, creep and fatigue strengths at the operating temperature range.
- Should have low density to reduce the inertial loads.
- A high thermal conductivity to facilitate quick heat transfer to the neighbouring parts to avoid overheating which can weaken the piston and also to avoid detonation or pre-ignition of the air-fuel mixture. Detonation results in considerable power loss and further increases the stresses on an engine's components.
- Excellent bearing properties so that the friction between the piston and the cylinder wall can be as low as possible which will minimise the risk of engine seizure.
- A low thermal expansion coefficient to retain the shape and size, but high yield and creep strengths to avoid collapse under the loads at the operating conditions.
- It should not suffer large permanent growth and be sufficiently free from internal stresses to prevent distortion when heated (Schofield and Wyatt, 1946; GmbH, 2016).

## **2.5. Piston material evolution and development**

Performance and other requirements have changed material selection for pistons, starting with cast iron in the earliest engines to super alloys in the present. Other materials that have been experimented with and used in piston applications included magnesium alloys and various composites. However, the mostly commonly used alloys in small engine pistons are aluminium alloys which are described in more details below. Since this research is investigating the application of a new nanostructured aluminium alloys in pistons, the application of nanostructured aluminium alloys by other researchers is also given in later section.

### **2.5.1. Conventional aluminium alloys**

An aluminium piston design was first proposed in 1913 for the Kaiserpreis aero-engine, but it was rejected on the basis of its lower strength and melting point. It was believed that the material was not strong enough and would not withstand the combustion temperatures since the material's melting point is only 659 °C. Despite the low melting point and reduced hot strength, some designers still tried aluminium in search of lighter materials for the pistons. It was the discovery of age hardening (Section 2.8) by Alfred Wilm that enabled aluminium alloying to achieve higher strength. Aluminium alloy pistons were first fitted by Miller in a Peugeot for the 1914 GP. The car finished second in a 500 mile race in 1915 in Indianapolis and its sister car won in the same race in 1919. It was discovered by the early aluminium alloy piston users that the low melting point was irrelevant since an aluminium alloy had 4.5 times thermal conductivity of cast-iron and the heat could efficiently be passed to the cooled cylinder wall. The better thermal conductivity of aluminium alloys allowed the compression ratios to be raised without knocking thus improved the engine's performance. The piston's crown temperature was measured to be 200 °C lower than that of a cast iron piston (Taulbut 2001).

The improvement in materials processing and production technologies enabled new aluminium alloys with superior properties compared to conventional aluminium alloys to be developed. These alloys are termed super alloys (Section 2.5.2) and in this project, one such alloy is investigated for piston applications. The comparison of commonly used piston alloys and the new alloy is given in Section 4.9.

### **2.5.2. Nanostructured aluminium alloys or super alloys**

The conventional high-strength aluminium alloys are strengthened using various mechanisms such as grain size refinement, solid solution, artificial aging and others (Inoue, Kimura and Amiya, 2002) (see Section 2.6). However, to meet the higher tensile strength requirements at elevated temperatures; different strengthening techniques have been considered to produce aluminium-based nanostructured alloys. They can be produced using mechanical alloying (MA), severe plastic deformation (SPD), melt spinning etc. Secondary production processes such as extrusion or die compact are needed to produce the final bulk materials (Inoue, Kimura and Amiya, 2002; Asgharzadeh, Simchi and Kim, 2011). Several types of aluminium-based nanostructured alloys have been developed with the microstructures of nanometre-sized particles embedded in the aluminium matrix (Audebert, Mendive and Vidal, 2004; Galano *et al.*, 2010).

Earlier work on the feasibility of the aluminium-based nanostructured alloys in piston applications has been carried out by Bonelli *et al.* (2014) and Scrimshaw (2014) at the Universities of Buenos Aires and Oxford Brookes respectively. The study carried out by Scrimshaw (2014) mainly consisted of theoretical calculations including finite element modelling which concluded that a mass reduction of approximately 12% can be achieved when switch from the conventional Al-Si alloy (Al-4032) to a nanostructured aluminium alloy. The work carried out at the University of Buenos Aires (UBA) was based on the practical applicability of one the nanostructured hypereutectic aluminium alloys. The study

suggested that change in the piston material can result in gains in the engine's performance in terms of fuel consumption, torque and power (Bonelli *et al.*, 2014).

The Pacific Northwest National Laboratory Richland in the USA also worked from May 2011–May 2014 on the development of aluminium-based nanostructured alloys (Smith, 2012). The alloys were expected to have better tensile and fatigue strengths at elevated temperatures that can facilitate applications in heavy duty diesel engine pistons. The primary objectives were to evaluate the candidate high temperature and high strength aluminium based alloys that could be processed using rapid solidification methods, and establish cost-effective processing methods that can preserve the desired microstructure and properties through the consolidation and forming steps (secondary production processes) (Smith, 2012).

The candidate alloy selected for further development was Al-Fe alloy and the aim was to achieve strength in excess of 300 MPa at 300 °C. The project could not achieve the aforementioned target, but claimed to have achieved yield strength (YS) and ultimate tensile strength UTS of 244 and 261 MPa respectively. The alloy's strength was much better than the conventional aluminium alloys. It was also found that melt spinning followed by extrusion consolidation is a more cost-effective process to mass produce these materials than the mechanical alloying. It is not yet known if the project had tested any component for an application demonstration as planned. It was however clear that, the consolidation and extrusion processes needed further optimisation in order to eliminate porosity and improve high temperature properties (Smith, 2012).

The work undertaken in this doctoral programme is one more step towards the application of aluminium based nanostructured alloys in pistons. The nanostructured aluminium alloy under investigation in this project has been mass produced by RSP Technology in Netherlands using melt spinning followed by hot extrusion for the consolidation. The alloy

was developed by Prof. Fernando Audebert and his team at the Universities of Oxford and Benous Aires. The characterisation of the alloy is presented in Chapter 4 and the mechanical properties are compared with those of existing aluminium alloys used in piston applications.

## **2.6. Strengthening mechanisms in aluminium alloys**

It is crucial to understand the strengthening mechanisms in metals to develop new materials with better mechanical properties and to understand these mechanisms, it is important to understand the nature of dislocations and the role they play in the deformation processes of metals (Chandrasekaran, 2003; Callister and Rethwisch, 2011). Normally more than one of these techniques contribute towards the strengthening of an alloy (Callister and Rethwisch, 2011; Martin, 2012). The strengthening mechanisms that contribute to the higher strength of the alloy studied in this project are grain boundary, solid solution and precipitation or age hardening. More information about these strengthening mechanisms can be found in (Callister and Rethwisch, 2011; Bata and Pereloma, 2004; Gedeon, 2010; Martin, 2012; Ma *et al.*, 2014).

## **2.7. Rapid solidification of aluminium alloys**

It has been well known that grain size refinement is one of the metal strengthening mechanisms to improve the mechanical properties of polycrystalline metallic materials (Tellkamp, Lavernia and Melmed, 2001; Ma, 2006). A number of techniques (mechanical alloying (MA), severe plastic deformation (SPD) etc.) have emerged over the last two-three decades with the primary aim of grain reduction for processing metals and alloys in a bulk form.

Nanostructured (NS) and ultra-fine grained (UFG) aluminium alloys, and their composites have attracted significant attention during the last two-three decades due to their superior mechanical properties compared to conventional aluminium alloys hence offer interesting

possibilities related to many structural applications (Audebert, Mendive and Vidal, 2004; Galano *et al.*, 2010). The specific properties of interest include higher strength, lower density and higher temperature capabilities (Lewis *et al.*, 1984). NS materials owe their superior properties to their unique microstructure where the volume of grain boundary is significant, i.e. a 5 nm material has approximately 50% of its volume as grain boundaries (Han, Mohamed and Lavernia, 2003).

It is known that grain size can be controlled by controlling the rate of solidification from liquid phase or plastic deformation. The method of interest in this work is controlling the rate of solidification. The alloy under consideration was produced by a rapid solidification process called melt spinning described as follow.

#### **2.7.1. Melt spinning**

Since the introduction of rapid solidification of metallic melts by Duwez in 1960, many techniques and devices have been designed to produce alloys by rapid solidification. Amongst the techniques melt spinning is the most commonly used technique because of its relatively high cooling rates and suitability for high volume industrial manufacturing (Uzun, Karaaslan and Keskin, 2001; Abed, 2014).

A schematic representation of the melt spinning and subsequent processes to produce the final bulk material is given in Figure 2.3. In melt spinning, molten aluminium mixture is introduced onto a spinning copper wheel creating a puddle (Karpe *et al.*, 2009) (Figure 2.3a). The material is dragged out from the wheel in form of ribbons due to the relative motion of the wheel (Figure 2.3b) (Karpe, Kosec and Bizjak, 2012). The ribbons are then cut (Figure 2.3c) and compacted by hot extrusion into the final bulk material in a bar form (Figure 2.3d).



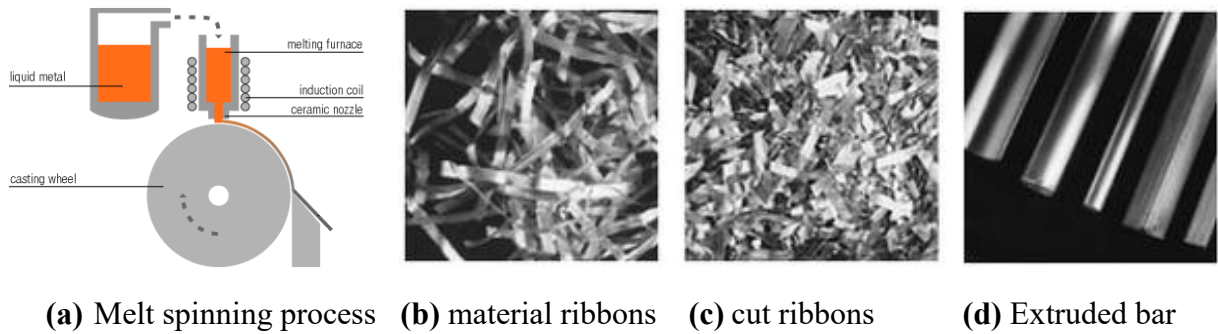


**Figure 2.3.** Schematic of melt spinning and subsequent processes (images courtesy of RSP Technology Netherlands)

## 2.8. Heat treatment background theory

Heat treatment in a general sense is the heating and cooling processes with the aim of changing the mechanical properties, the metallurgical structure or the residual stress state of metals or alloys. However, in the case of aluminium alloys, heat treatment is frequently used to increase the strength and hardness of the precipitation-hardenable wrought and cast alloys which are termed heat treatable alloys (American Society for Metals. Handbook, 1979; American Society for Metals. Heat Treating and American Society for Metals. Handbook, 1981).

Most of the commercial heat-treatable aluminium alloys contain combination of alloying elements hence exhibit multistage precipitation and undergo accompanying strength. Heat treatment to increase the strength of aluminium alloys is a three-step process; solution heat treatment, quenching and aging, and each of them is explained in detail in (American Society for Metals. Heat Treating and American Society for Metals. Handbook, 1981).

## 2.9. Engine loadings on piston

Determination of the engine loads on piston is required for designing piston using FEA. The two types of loads acting on piston are explained in detail below along with how they are determined and implemented in the FEA (Mahle, 2016).

### 2.9.1. Mechanical loads

These loads include, the cyclic loading on the piston due to

- Gas force from the combustion pressure.
- Inertial force from the oscillating motion of the piston.
- Lateral force from the support of the gas force by the inclined connecting rod, and the inertial force of the oscillating connecting rod.

The above loads at any given point during an engine operation can be determined using simple trigonometry and crank slider mechanism (Figure 2.4). In order to avoid neglecting any combination of these forces so called load cases-that may be critical, a practical number of appropriately selected points in time are analysed. These include primarily the points at which the individual components of the mechanical load reach a maximum (Mahle, 2016). The three different mechanical loads are individually described below.

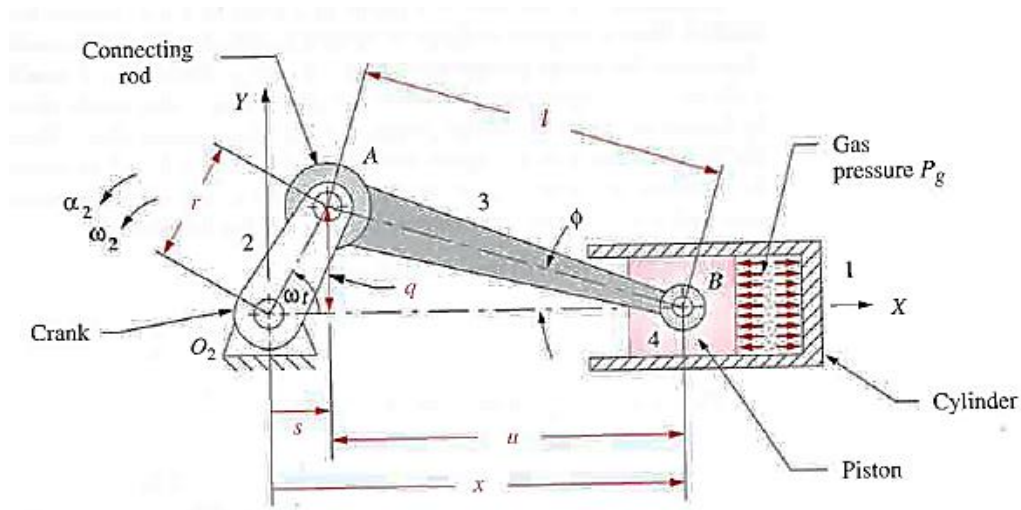


**Figure 2.4.** Geometry of the crank-mechanism (Norton, 2012).

#### 2.9.1.1. Combustion pressure

The combustion gas pressure of the air-fuel mixture on the piston is modelled as a pressure acting on the piston's crown and the pressure is applied over the entire piston's crown going down to the lower flank of the compression ring groove as suggested by Mahle (2016). The

force flow of the longitudinal force generated thus runs through the pin to the connecting rod small end (Mahle, 2016). For this project, the gas pressure was measured directly from the engine; the average pressure traces of the test engine at different engine speeds are given in the later chapters (Section 5.4.1.1).

### **2.9.1.2. Inertial force due to acceleration**

The oscillating motion of a piston in the cylinder generates accelerations that reach their maximums at the cylinder's dead centres. The accelerations are linearly dependent on the stroke-connecting rod ratio of the crank mechanism, and quadratically dependent on the engine speed. This means that inertial forces in an engine increase significantly at high speeds (Mahle, 2016) and makes the engine less efficient at higher speeds (Section 1.1).

The resulting acceleration is applied to the connecting rod by the piston, by means of the pin. In the FE model, the acceleration is applied globally to the piston assembly. The model is fixed in the axial direction at the connecting rod small end and the inertial force is applied as acceleration in Ansys Workbench<sup>TM</sup> (the computer package used for FEA in this project) (Mun Yao *et al.*, 2014; Mahle, 2016).

The simple geometry of the slider-crank mechanism (Figure 2.4) allows a very straightforward approach to the exact analysis of its slider's position, velocity and acceleration, using only plane trigonometry and scalar equations. The equation to determine the piston acceleration has been derived by (Norton, 2012) and is given in (2.1).

$$\ddot{x} = -r\omega^2(\cos \theta + \frac{r}{l}\cos 2\theta) \quad (2.1)$$

where  $\ddot{x}$ ,  $r$ ,  $\omega$ ,  $\theta$  ( $\omega t$ ) and  $l$  are the piston's acceleration ( $\text{m/sec}^2$ ), crank offset or crank radius (m), crank angular velocity (rad/sec), crank angle (rad) and the connecting rod length (m) respectively.

The crank radius ( $r$ ) is the distance between the crank pin and crank centre or half of the stroke. The crank angular velocity is related to the engine speed ( $N$ ) in revolution per minute (RPM) by equation (2.2)

$$\omega = 2\pi N/60 \quad (2.2)$$

### 2.9.1.3. Lateral force

The conversion of the piston's linear motion into the crankshaft's rotational motion generates force components in the crank mechanism that presses the piston against the cylinder wall. In the FEA, the lateral forces are transferred into the piston via the connecting rod small end and the pin. The piston then presses against the cylinder (Mahle, 2016).

The lateral force is made up of the components of the gas pressure force and the inertial force and can be determined using equation (2.3) (Norton, 2012).

$$L_f(\theta) = - (m_B \ddot{x} + F_g) \tan \phi \quad (2.3)$$

where  $m_B$  is mass of the reciprocating components (Kg) that include the piston, the pin and approximately one-third of the connecting rod's mass (Table 5.3).  $\phi$  is the angle that the connecting rod makes with the cylinder axis (Figure 2.4) and can be determined from equation (2.4) (Norton, 2012).

$$\sin \phi = \frac{r}{l} \sin \theta \quad (2.4)$$

$F_g$  is the gas force (N) and can be calculated from equation (2.5) (Norton, 2012).

$$F_g(\theta) = - \frac{\pi}{4} B^2 P_g(\theta) \quad (2.5)$$

where  $B$  and  $P_g$  are the engine's bore  $m$  and the gas pressure  $Pa$  respectively.

### 2.9.2. Thermal loads

The thermal load from the combustion of the air-fuel is also a cyclic load on the piston. It acts mainly during the expansion stroke on the combustion chamber side of the piston. During engine operation most of the piston mass reaches a quasi-static temperature during engine operation with limited cycle variation. Although there is no cycle variation, there is still significant variation of the quasi-static temperature within the piston (Mahle, 2016).

The heat transfer calculations require determination of the combustion gas temperature, but the gas temperature in the cylinder varies considerably depending on the state of the combustion. As an approximation, the ideal gas law described by equation (2.6) is used to determine the mean gas temperature indirectly from the in-cylinder pressure (Hohenberg, 1979).

$$T_g (\theta) = \frac{P (\theta)V(\theta)}{nR} \quad (2.6)$$

where  $P$ ,  $V$ ,  $n$ ,  $R$  and  $T_g$  are the in-cylinder pressure (Pa), cylinder volume ( $m^3$ ), combustion product (mole), universal or ideal gas constant (J/mol K) and the gas temperature (K) respectively. The momentary cylinder volume can be calculated using equation (2.7) (Pulkrabek, 2014).

$$V (\theta) = V_c + \left(\frac{\pi B^2}{4}\right) (l + r - x) \quad (2.7)$$

where  $V_c$  and  $x$  are the clearance volume ( $m^3$ ) and the piston position (m) respectively. The clearance volume can be obtained using equation (2.8) (Pulkrabek, 2014).

$$V_c = \frac{V_t}{(r_c - 1)} \quad (2.8)$$

where  $V_t$  is the engine's total volume ( $m^3$ ) and  $r_c$  is the compression ratio. The value of  $x$  in equation (2.7) in terms of the angular position ( $\theta$ ) can be determined using equation (2.9).

$$x = 1 - \frac{r^2}{4l} + r (\cos \theta + \frac{r}{4l} \cos 2\theta) \quad (2.9)$$

The product or mass of the combustion in moles can be calculated using equation (2.10).

$$n = m/M \quad (2.10)$$

where  $m$  and  $M_m$  are mass of the fuel or the air in grams and molar mass of the fuel or the air in g/mol respectively.

Having determined the combustion gas temperature the heat transfer between piston and its surroundings can be evaluated. Sections 2.9.2.1 to 2.9.2.5 explore the different areas of the piston where the heat transfer takes place.

#### ***2.9.2.1. Heat transfer between the combustion gas and the piston crown***

The transient heat transfer coefficient (HTC) of the hot gases can be obtained from one-dimensional thermodynamic analysis of the engine cycle. There are numerous models that have been put forward to determine the heat transfer coefficient of these gases inside the engine cylinder. The Hohenberg model described by equation (2.11) (Hohenberg, 1979) was used to determine the instantaneous heat transfer coefficient of the hot gases. The Hohenberg model was based on extensive experimental observations and showed agreement with test results which was obtained after detailed examination of the Woschni's model (Woschni, 1967) (Torregrosa, Olmeda and Romero, 2008).

$$h(\theta) = C_1 V(\theta)^{-0.06} P(\theta)^{0.8} T(\theta)^{-0.4} (V_p + C_2)^{0.8} \quad (2.11)$$

where  $h$ ,  $P$  and  $V_p$  are the heat transfer coefficient ( $W/m^2 K$ ), cylinder pressure (bar) and the mean piston speed (MPS) (m/sec) respectively.  $C_1$  and  $C_2$  are constants and their mean values

are 130 and 1.4 respectively, they have no units. The piston's mean speed (m/sec) can be determined using equation (2.12).

$$V_p = 2SN \quad (2.12)$$

where S and N are the engine stroke (m) and speed (rpm) respectively.

The simulation of quasi-static temperature distribution needs the mean heat transfer coefficient ( $h_m$ ) and the mean gas temperature ( $T_m$ ) values which can be obtained using equations (2.13) and (2.14) respectively (Sanli *et al.*, 2008).

$$h_m = \frac{1}{720} \int_0^{720} h(\theta) d(\theta) \quad (2.13)$$

$$T_m = \frac{1}{720 \times h_m} \int_0^{720} h(\theta) T(\theta) d(\theta) \quad (2.14)$$

#### **2.9.2.2. Heat transfer between compression ring and cylinder**

A significant amount of heat from the piston exits through the compressing ring which needs to be accounted for in the thermal modelling of a piston. The heat transfer coefficients are different for the upper and lower faces of the compression ring. Determining the real heat transfer coefficients for compression rings are complicated and beyond the scope of this work. The values used in this work were therefore taken from published literature (Mizuno *et al.*, 2009) (Section 5.4.2.2).

#### **2.9.2.3. Heat transfer between ring lands, piston outer skirt and the cooling oil**

The heat transfer to the lubrication oil film between the ring lands and the outer skirt through convection can be modelled as a laminar flow between two parallel plates as suggested by (Ahmed and Basim, 2009). To get the value of the heat transfer coefficient; the Nusselt number (Nu) should be found for the laminar flow between two parallel plates and it can be determined using equation (2.15) (Ahmed and Basim, 2009; Munyao *et al.*, 2014)

$$Nu = \frac{h D_h}{k_{oil}} = 8.235 \quad (2.15)$$

The heat transfer coefficient (h) is given by equation (2.16)

$$h = 8.235 \frac{k_{oil}}{D_h} \quad (2.16)$$

where  $k_{oil}$  and  $D_h$  are the thermal conductivity of oil (W/m K) and hydraulic diameter (m) respectively. Hydraulic diameter is determined as a function of the cross-sectional area of the plates per unit depth ( $A_c$ ) and the wetted perimeter ( $P_w$ ). Hydraulic diameter can be calculated using equation (2.17).

$$D_h = \frac{4 A_c}{P_w}; \quad A_c = 2b; \quad P_w = 2 \quad D_h = 4b \quad (2.17)$$

where  $A_c$ ,  $P_w$  and  $b$  are cross-sectional area of the plate per unit depth ( $m^2$ ), wetted perimeter (m) and the piston-cylinder gap (the lubricating oil film) (m) respectively.

#### ***2.9.2.4. Heat transfer between the piston under-crown and inner walls of the piston skirt and the cooling oil***

The piston's under crown has a very complex geometry due to the existence of the ribs and the pin boss where evaluations of the heat transfer coefficients are intricate. The piston's under crown is cooled by oil sprayed onto the underside of the piston. To model this cooling, the piston inner surface is assumed to be cylindrical, with diameter equal to the outer piston diameter, and the cooling oil moving along the inner surface of the cylinder is assumed to have a velocity equivalent to the mean piston velocity. This assumption is based on the Ditus-Boelter correlation which satisfies the turbulent forced convection heat transfer on a cylindrical surface (Ahmed and Basim, 2009). The correlation gives the Nusselt number which can be used to determine the heat transfer coefficient. The Ditus-Boelter correlation is described by equation (2.18) (Ahmed and Basim, 2009; Munyao *et al.*, 2014).



$$Nu = 0.023Re^{0.8}Pr^n \quad (2.18)$$

The Reynolds's and Nusselt's numbers can be determined using equations (2.19) and (2.20).

$$Re = \frac{\rho_{oil} U_{oil} D_h}{\mu_{oil}} \quad (2.19)$$

$$Nu = \frac{h_{oil} D_h}{k_{oil}} \quad (2.20)$$

Substituting equations (2.18) and (2.19) into equation (2.20) leads to equation (2.21) which can be used to determine the heat transfer coefficient.

$$h_{oil} = 0.023 D_h^{-0.2} k_{oil} \left( \frac{\rho_{oil} U_{oil}}{\mu_{oil}} \right)^{0.8} Pr^n \quad (2.21)$$

where Nu, Pr, Re,  $\rho_{oil}$ ,  $U_{oil}$ ,  $\mu_{oil}$ ,  $h_{oil}$  are Nusselt's number, Prandtl number, Reynold's number, oil density (Kg/m<sup>3</sup>), oil flow speed (m/sec), oil dynamic viscosity (kg/m.sec) and heat transfer coefficient of the oil (W/m<sup>2</sup>K) respectively. The value of the index n is 0.4, when the oil is being heated and 0.3 when the oil is being cooled (Munyao *et al.*, 2014).

and Pr number can be determined using equation (2.22)

$$Pr = \frac{\mu_{oil} C_p}{k_{oil}} \quad (2.22)$$

where  $C_p$  is the specific heat value of the cooling oil (kJ/(Kg.K)).

#### **2.9.2.5. Heat transfer between the engine cylinder and cooling water jacket**

The heat transfer coefficient of the combustion engine's cooling jacket has been determined experimentally for different engines and presented in literature. However, for the majority of spark ignition (SI) engines, the average value is 1480 (W/m<sup>2</sup>K) (Esfahanian, Javaheri and Ghaffarpour, 2006), which has been used in this work. The application of the heat transfer

coefficient between the engine cylinder and cooling water jacket in the FEA can be seen in later chapters (Section 5.4.2.5).

## **2.10. Summary**

A comprehensive literature survey was carried out on the development of materials for piston applications in internal combustion engines. The properties a material should possess to be used as a piston material were discussed with reference to the functions a piston performs. The materials that are under development and have the potential to become future piston materials were also highlighted. The different strengthening mechanisms, which contribute to higher strength of the alloy under investigation in this project, were described. Furthermore, the primary and secondary production processes to produce the alloy in bulk form were described in conjunction with strengthening mechanism they contribute to. The heat treatment procedure and background theory for optimising the mechanical properties of the as-received alloy were explained. Lastly, the different engine loads acting on pistons were presented along with how they can be determined and implemented in the finite element analysis (FEA) of pistons.

### Chapter 3: Research methodology and thesis structure

In order to achieve the aforementioned aim and objectives (Section 1.2), a research strategy was devised which is presented as a flow chart in Figure 3.1. The first phase was to carry out extensive literature review regarding the piston materials, material characterisation & testing, piston design & testing and engine testing. The main bulk of experimental work was carried out in three areas which were material characterisation, heat treatments & mechanical testing, piston design & finite element modelling and engine testing with original & new pistons.

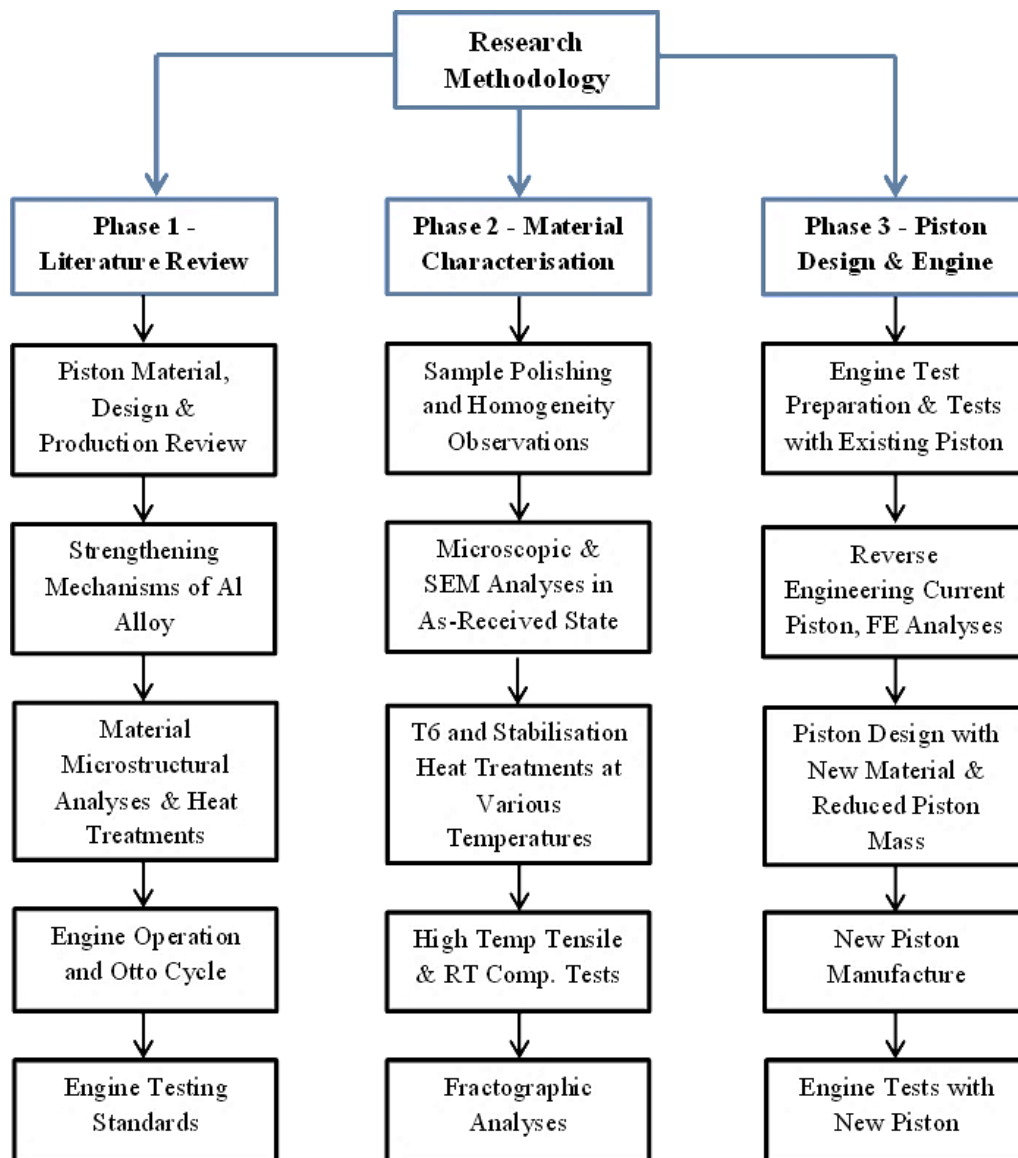


**Figure 3.1.** Flowchart diagram of the research methodology.

The different areas of the research methodology with respect to the thesis structure are given as the following:

An extensive literature review was carried out and some of the important and research related topics are summarised in Chapter 2. It started with the function of pistons, design considerations and the evolution of piston design. The mechanical properties required for a piston design were reviewed including the trends of use of materials for piston manufacture. The pros and cons of different piston materials were critically analysed and the potential of using nanostructured aluminium alloys in pistons and the work being undertaken in this area in the literature was reviewed.

The literature review also included reviewing the mechanisms used to strengthen metals specifically the ones that contributed to the higher strength of the alloy investigated in this research. It also describes the production method used to produce the alloy. The Chapter contains some background theory about the heat treatment of aluminium alloys. Furthermore, it describes the different types of engine loads that act on pistons and how they can be determined and implemented in finite element analysis (FEA) to design a piston.

The work carried out in Phase 2 of the research methodology is given in Chapter 4. It describes a list of mechanical tests and microscopic analyses carried out to characterise, assess the homogeneity and determine the strength of the alloy used in this research. To optimise the mechanical properties of the as-received material, heat treatment studies were undertaken to determine the T6 conditions where the alloy had the highest strength. Furthermore, fractographic analyses were performed using electron microscope to determine the failure modes. Finally, the yield and ultimate tensile strengths of the new alloy were compared with those of existing aluminium alloys used in piston applications.

Some of the practical work in Phase 3 of the research methodology is given in Chapter 5. FE analyses were carried out on existing piston using two different modelling techniques to determine the more realistic approach for new piston design. The chapter described the scope and the assumptions made in the FE analyses. The different thermal and mechanical loads on the piston were determined and a critical load case was also determined where the combinations of these loads are detrimental to the piston design. Based on the more realistic FE approach, critical load case and the new alloy's mechanical properties, a new lightweight piston was designed. The chapter also explains why topology optimisation could not be used to optimise the piston design parametrically. The design and manufacturing challenges of the new piston design are also described.

The experimental work of engine testing with original and new pistons from Phase 3 is given in Chapter 6. It explains the modifications made to the engine, auxiliary components design and installation of various sensors to prepare the engine for dynamometer testing according to the requirements in this project. It also describes the engine test methodology and engine performance parameters that needed to be measured. The engine test scope, test limitations and technical problems faced are highlighted. Furthermore, it talks about the modifications needed to the engine to accommodate the new piston. The engine tests results with original and new pistons are presented and compared to assess the changes in the engine's performance.

The experimental results and analyses are discussed in Chapter 7. Conclusions reached as a result of the research undertaken here and the recommendations for further work are discussed in Chapter 8

## **Chapter 4: Microstructural characterisation of nanostructured aluminium alloy RSA Al-612**

### **4.1. Introduction**

This work examined the microstructure of the as-received alloy to assess its homogeneity through the application of intrusive and nonintrusive techniques. Energy dispersive spectroscopy (EDS) analyses were performed to evaluate the chemical composition of the alloy. To optimise the mechanical properties of the as-received material, heat treatment studies were undertaken to determine the T6 conditions where the alloy had the highest strength. High temperature tensile tests at the piston operating temperature ranges were carried out to determine the strength values as a basis for the design of the piston. Furthermore, fractographic analyses were performed using scanning electron microscope to determine the failure modes. X-ray diffraction (XRD) analyses were also carried out to determine the phases present. Finally, the yield and ultimate tensile strengths of the new alloy were compared with those of existing aluminium alloys used in piston applications.

### **4.2. Microstructural characterisation and sample preparation**

The examination of microstructure is one of the principal means of evaluating alloys and products to determine the effects of various fabrication and thermal treatments. The most common applications of microstructural examinations to aluminium alloys are as follow (Callister and Rethwisch, 2011).

- To ensure the association between the properties and microstructure are properly understood.
- To predict the properties of materials once these relationships have been established.
- To determine whether a material has been correctly heat treated or not.

- To design alloys with new property combinations.
- To ascertain the mode of mechanical fracture (Callister and Rethwisch, 2011).

Microscopic examination is a very useful tool in the study and characterisation of materials and different microscopes such as optical, and electron microscopes are commonly used in microscopy (Cerri and Evangelista, 1999). The two types of microscopies used in this project are explained in Section 4.3.

A very detailed surface preparation was needed to reveal the important details of the microstructure; the preparation included grounding and polishing of the surface to give it a mirror like smooth finish using finer abrasive papers and powders (Callister and Rethwisch, 2011). The sample preparation method used in this project is described in the following section.

#### **4.2.1. Sample preparation**

The sample preparation involved the use of the following four steps.

##### ***4.2.1.1. Step 1: Sectioning***

A sample with dimensions of 60 x 8 mm (diameter and thickness respectively) was cut from the material bar and dry cutting was avoided since it generates heat which affects the microstructure and hardness (Voort, 2016) (American Society for Metals. Handbook and Mills, 1985).

##### ***4.2.1.2. Step 2: Mounting***

The sectioned sample is normally encapsulated, but it was not required for the optical microscopy analyses since the sample was large enough, while it was required for the scanning electron microscopy (SEM) in this project. Thermoplastic resin was used since it provided better edge retention, more chemically inert (Voort, 2016) and was readily available in the laboratory (American Society for Metals. Handbook and Mills, 1985).

#### **4.2.1.3. Step 3: Grinding**

The un-encapsulated sample was ground using a rotary grinder, Figure 4.1, to reduce the sample's surface roughness. Grinding was performed using a silicon carbide abrasive paper starting with the rough grit size of P240g followed by finer grit size of P320g. The sample was kept cooled with water to avoid overheating during grinding.



**Figure 4.1.** The rotary grinder used in this project.

#### **4.2.1.4. Step 4: Polishing**

The sample was polished to remove the surface scratches produced during the grinding stage. This was performed in two stages; rough and final polishing. Both polishing stages were carried out using a metal oxide [alumina ( $\text{Al}_2\text{O}_3$ ) mixed with diamond particles of different sizes] in powder form. The alumina was mixed with a water-based fluid/lubricant called Hyprez to make a paste. This lubricant helped to maintain the uniform dispersion of the diamond and improved the surface finish of the sample. When EDS analyses were carried out (Section 4.3.2.3), it was realised that a large portion of the particles have been dislodged from



the sample's surface. Ethylene glycol was used instead of Hyprez and it reduced particle dislodging.

The rough and final polishing stages were performed using 0.3 and 0.04  $\mu\text{m}$  alumina diamond paste on a nap cloth disk respectively (Cerri and Evangelista, 1999). Once the polishing was completed, the sample was wiped with industrial methylated spirit (IMS) and dried immediately using a specimen dryer (Figure 4.2) to ensure there were no stains left on the sample's surface.



**Figure 4.2.** Specimen dryer with the polished sample.

### **4.3. Microscopic analyses**

The two types of microscopic analyses carried out in this project are described below.

#### **4.3.1. Optical microscopy**

In this work, optical microscopy was used to determine homogeneity of the as-received material through particle analyses such as particle size and volume fraction across the bar's cross section. The methodology followed to carry out the aforementioned analyses is given in the following section.

#### ***4.3.1.1. Homogeneity of the alloy and particle analyses***

Homogeneity of the as-received alloy was investigated through non-intrusive (optical microscopy) and intrusive Vicker's Hardness tests techniques. A picture of the finished polished sample prepared in Section 4.2.1 can be seen in Figure 4.3. The aim of the non-intrusive investigation was to observe the microstructure to assess its uniformity or homogeneity. Pictures of the sample's surface were taken across the sample's cross-section at 2 mm distance as marked out in Figure 4.3 to observe and determine the particle size, volume fraction and distribution. The pictures were processed for further investigation using an open source computer programme called ImageJ.

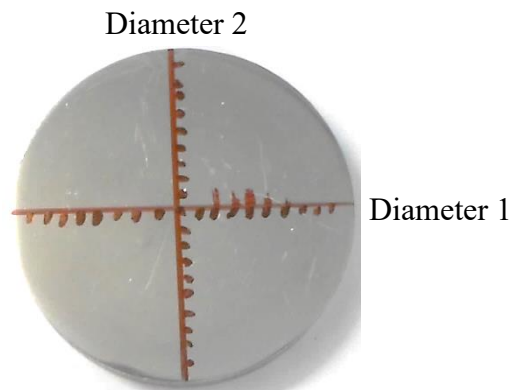


**Figure 4.3.** An image of the finished polished sample.

An image of the new alloy's microstructure taken with light microscope can be seen in Figure 4.4. The image was processed using ImageJ (image processing software) (ImageJ, 2023) to show the particles in black and the aluminium matrix in white (Figure 4.5). The software then numbered each of the particles in sequence starting from the top (Figure 4.6) for which it determined their surface areas assuming the particles as spheres. Furthermore, the software also calculated the ratio of areas covered in black vs. white to determine the particle volume fraction. Since the particles agglomerated (examples shown in red circles in Figure 4.4), they needed to be separated manually to determine the correct particle size. This was done through removing black pixels between the two particles using the tools provided in ImageJ software.

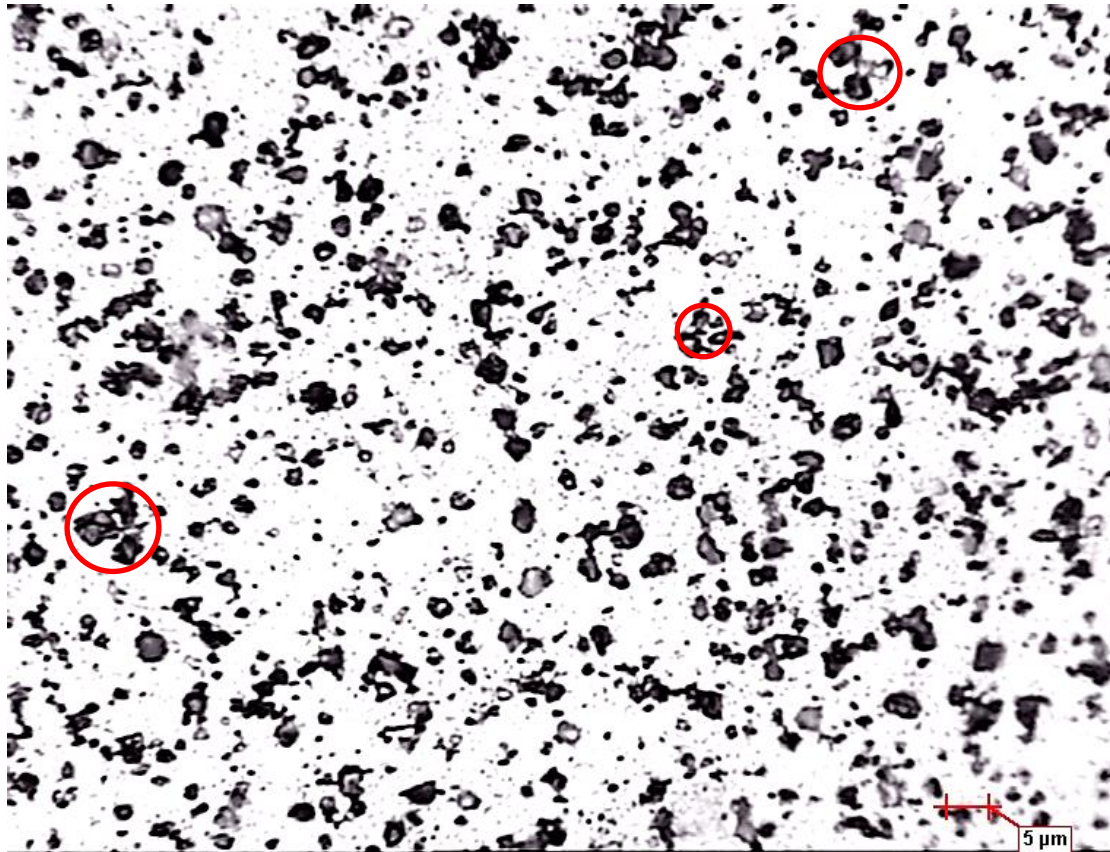


Figure 4.4. An image of the new alloy's microstructure taken with light microscope.

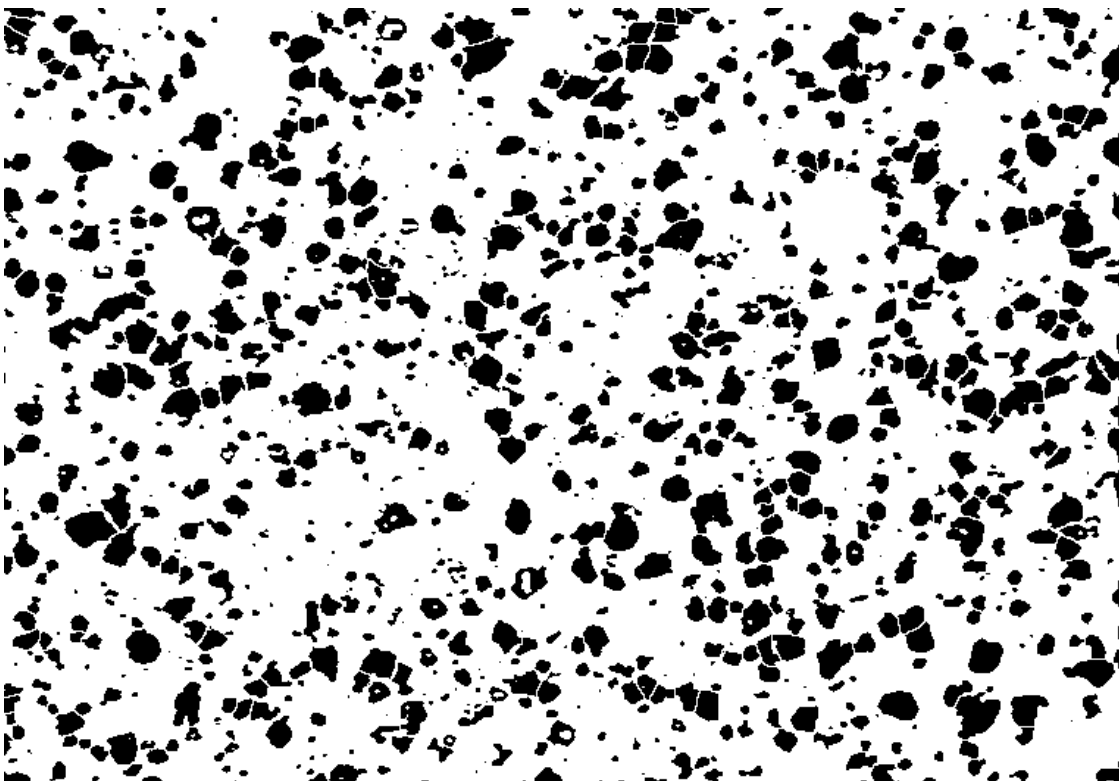
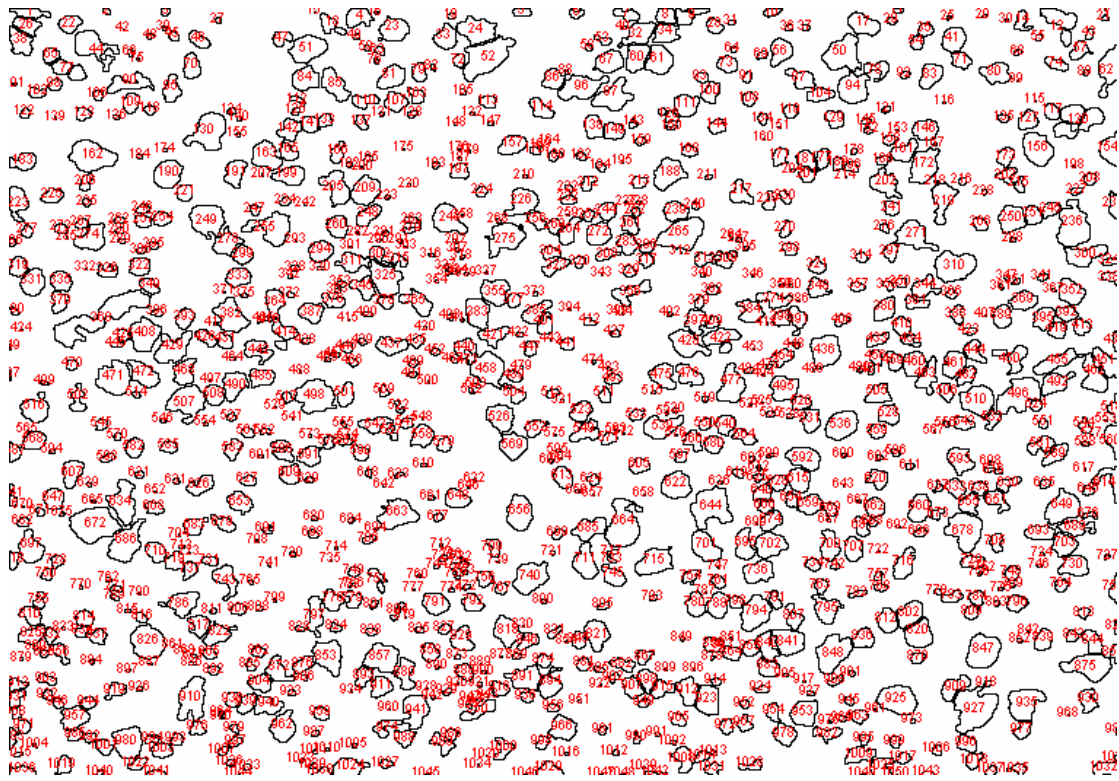
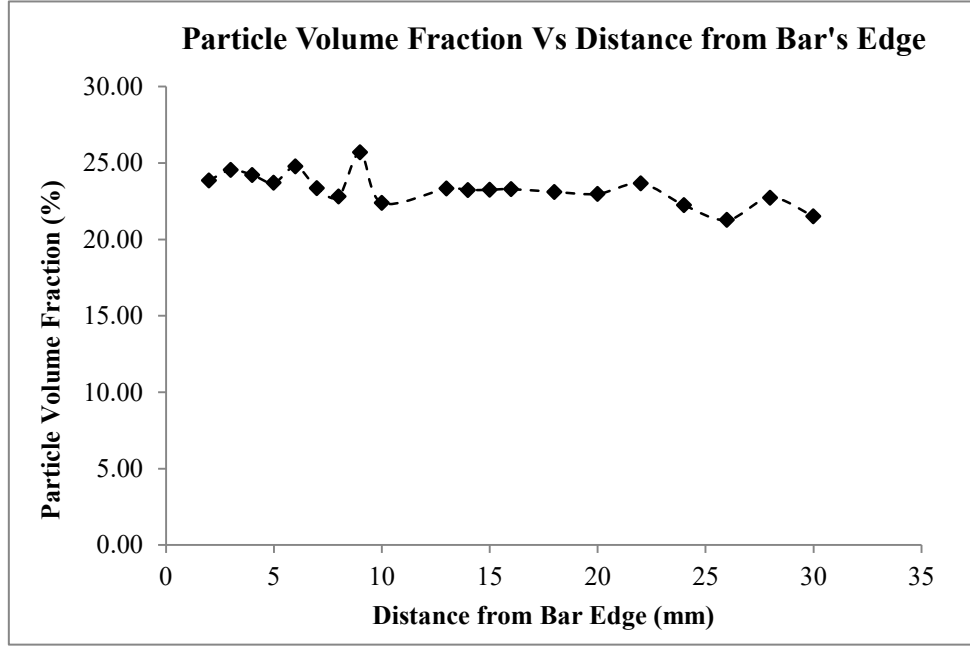


Figure 4.5. Semi-processed microstructure image of the new alloy in ImageJ.



**Figure 4.6.** Particles numbered by ImageJ.

The alloy under consideration had particle volume fraction of 22.5% according to the manufacturer (Al-13.5Mg-7Si-2Cu wt%). The same image processing procedure was carried out on all the pictures taken across the cross section of the sample and the results for particle volume fraction are given in Figure 4.7. The results indicated that the average volume fraction slightly decreased as going towards the centre of the bar, however; the variation was insignificant. The results obtained confirmed the specified volume fraction of 22.5% by the manufacturer.



**Figure 4.7.** Particle volume fraction across the sample's cross section.

The 2D particle areas obtained from image processing results were used to determine the 3D particle sizes using equations (4.1–4.3). Radii of the 2D particles were determined from the area of each particle using equation (4.1); assuming the particles as circular. The 2D particles were then converted to 3D using equations (4.2 and 4.3) (Pedrazzini *et al.*, 2016).

$$A_s = \pi r_s^2 \quad (4.1)$$

Where  $A_s$ ,  $r_s$  are area of 2D particle and radius of the 2D particle

rearranging the equation gives

$$r_s = \sqrt{\frac{A_s}{\pi}}$$

radius of the 3D particle ( $r_v$ )

$$r_v = \sqrt{\frac{3}{2}} r_s \quad (4.2)$$

$$D_{ps} = 2 r_v \quad (4.3)$$

Where  $D_{ps}$  is size of the 3D particle

Results of the average 3D particle size across the bar's cross section can be seen in Figure 4.8 along with the standard deviation. The results showed that the average particle size decreased towards the centre of the bar and so did the respective standard deviation.

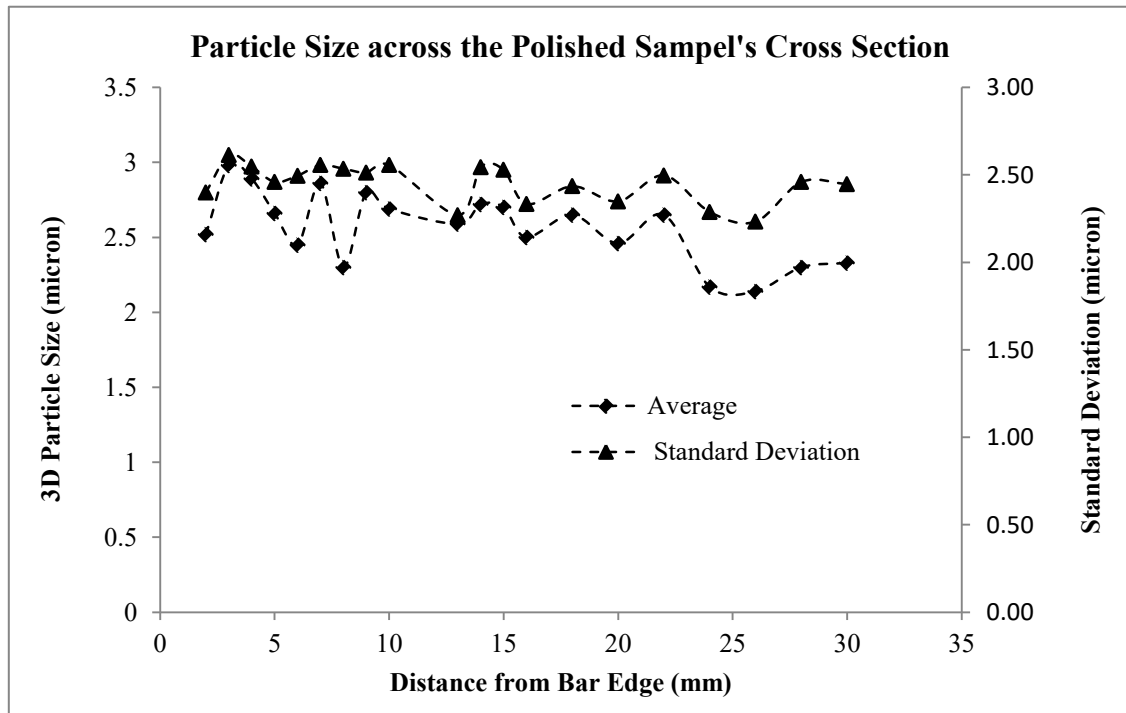


**Figure 4.8.** Average 3D particle size across the bar's cross section

Results from the image processing were also useful to determine the frequency of all 3D particles observed. The 3D particle size vs. frequency results are given as a histogram in Figure 4.9 and it can be seen that nearly 50% and 90% of the particles had sizes of about 1.7 and 2.5  $\mu\text{m}$  respectively. The actual particle sizes were likely to be smaller than measured because majority of the particles had been dislodged from the aluminium matrix during grinding and polishing of the sample. The voids left which were measured were expected to be larger than the particles. The two distinct peaks on the left may show the two intermetallics observed in the X-Ray diffraction (XRD) analysis presented later in the chapter.

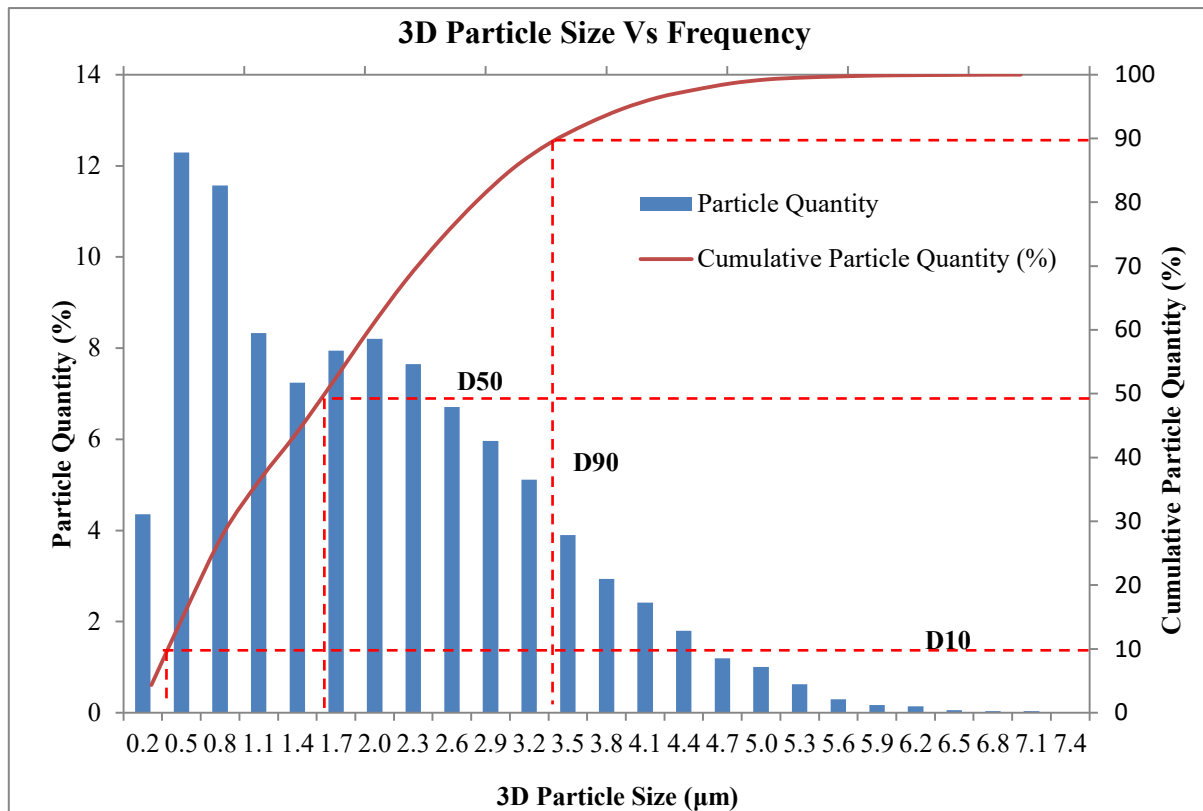


**Figure 4.9.** Particle distribution of all the observed particles

After analysing the microstructural homogeneity through optical microscopy, hardness tests (Vicker's hardness) were carried out across the sample cross section (as illustrated in Figure 4.3) to confirm the results of the particle analyses. The hardness test results of the as-received material are presented in Figure 4.10 and it can be seen that the hardness along the cross section did not fluctuate significantly. This showed that the material had homogenous hardness and was more likely to have homogenous mechanical properties across the bar. The load used for the hardness test was 10 Kilogram. There were two reasons for using Vicker's hardness; first, this involved a much smaller impression than with the Brinell ball which eliminated the effect of different depths on the hardness. Secondly, it was readily available at the laboratory.



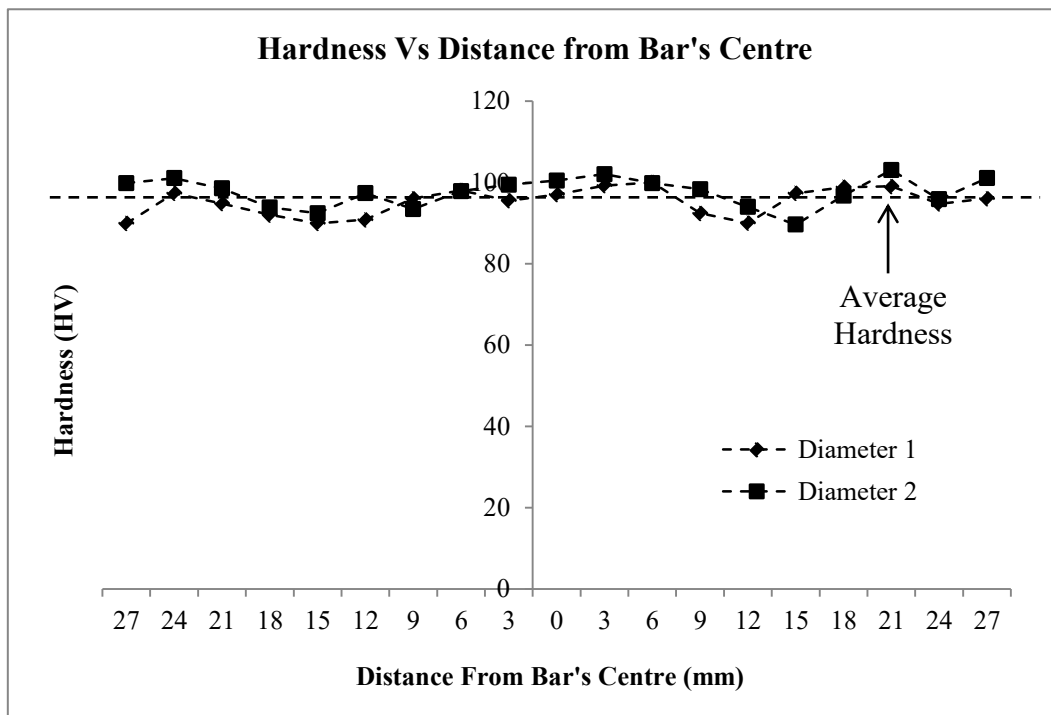


**Figure 4.10.** Hardness test results along the bar's cross section of the as-received material.

#### 4.3.2. Scanning electron microscopy

Scanning electron microscopy (SEM) is a method for high-resolution imaging of surfaces. The scanning electron microscope (SEM) uses electrons for imaging, much as a light microscope uses visible light. The advantages of SEM over light microscopy include much higher magnification and greater depth of field up to 100 times that of light microscopy. Qualitative and quantitative chemical analyses information are also obtained using an energy dispersive x-ray spectrometer (EDS) with the SEM (MEE, 2014) (Section 4.3.2.2). The scanning electron microscope was used in two modes as described below.

##### 4.3.2.1. Secondary electron (SE) and back scatter (BS) modes

The electron beam in SEM dislodges various forms of emissions from the sample's surface, amongst them secondary electrons are emitted by atoms close to the surface and offers greater surface resolution. While the backscattered electrons scatter in a way that they re-emerge from the sample's surface, but as a result the topographical characteristics suffer. On the other hand, backscatter electrons are sensitive to the atomic masses of the nuclei and



heavier elements appear brighter in a backscattered electron image. Back scatter emission is useful because it detects compositional differences (AME, 2018).

Backscattering is highly directional hence,

- If the sample is tilted, the penetration depth and scattering angles are both reduced.
- Uneven topography gives poor composition results so samples should always be well polished.

#### ***4.3.2.2. Energy dispersive spectroscopy (EDS)***

Energy-dispersive spectroscopy (EDS) or energy-dispersive X-ray spectroscopy (EDX) is a technique used for the chemical characterisation of a sample. It is normally used in conjunction with scanning electron microscopy (SEM) (MEE, 2014).

#### ***4.3.2.3. SEM results***

The sample used for SEM analyses was prepared using the method given in Section 4.2.1. The large sample prepared in Section 4.2.1 was cut into 8x8 mm samples for heat treatment. One of these 8 x 8 mm samples was used for the SEM analyses since the smaller sample was easy to mount and automatic polishing was used to achieve a sample with good surface finish. For this project, EDS was used in conjunction with SEM, and EDS analyses were planned to be performed on bulk image and large particles.

A SEM image of the alloy's microstructure can be seen in Figure 4.11 and its EDS spectrum is shown in Figure 4.12. The EDS was performed on the whole imaged area and the quantitative results of the EDS spectrum are tabulated in Table 4.1. The brighter areas are the Copper present in the alloy. In order to obtain acceptable average compositional values, EDS was performed in six different locations and the average quantitative results are given in Table 4.2.

The output of the analyses gave the ratios of the elemental compositions of the alloy, however they did not match the exact specification (Al-13.5Mg-7Si-2Cu wt%) provided by the manufacturer (RSP Technology). This was perhaps due to the fact that the particles were dislodged from the aluminium matrix during grinding and polishing of the sample.

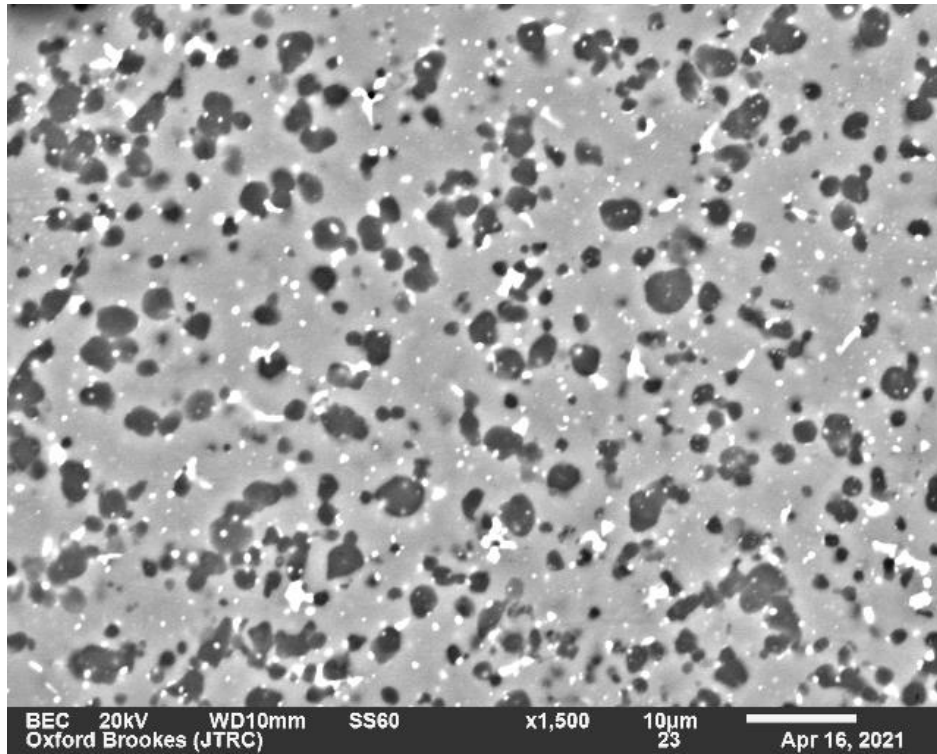


**Figure 4.11.** SEM image used for bulk EDS analysis.

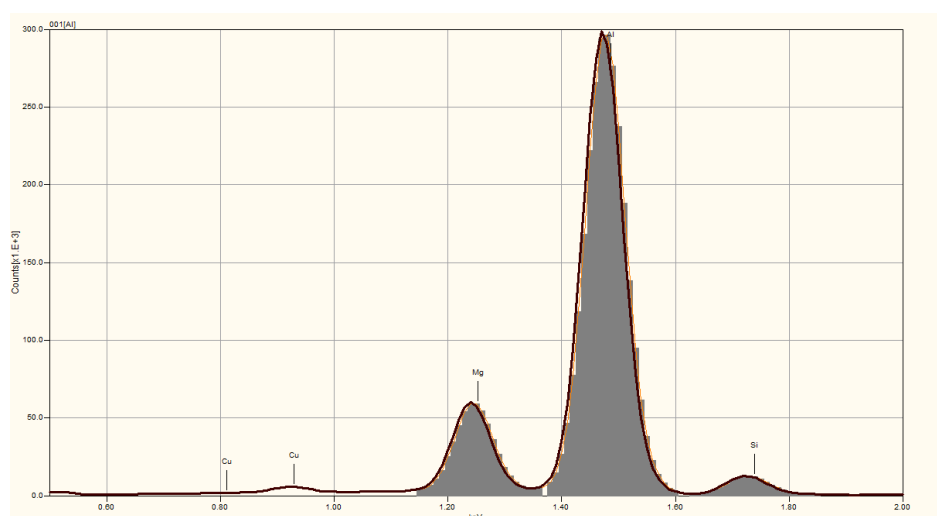


**Figure 4.12.** EDS spectrum of the bulk material in as-received state.

<b>Formula</b>	<b>Mass %</b>	<b>Atomic %</b>	<b>Sigma</b>
Mg	18.29	19.99	0.02
Al	77.63	76.46	0.04
Si	3.48	3.29	0.01
Cu	0.60	0.25	0.01
Total	100.00	100.00	-

**Table 4.1.** Bulk elemental analysis results of the alloy in as-received state.

<b>Formula</b>	<b>Mass %</b>	<b>Atomic %</b>	<b>Sigma</b>
Mg	18.73	20.44	0.02
Al	76.92	75.65	0.04
Si	3.56	3.36	0.01
Cu	0.61	0.26	0.01

**Table 4.2.** Averaged bulk elemental analyses results of the alloy in as-received state.

Images of the alloy's microstructure can also be seen in Figures 4.13 and 4.14 in secondary and backscattered modes respectively. The copper elements with the highest atomic mass appear the brightest in backscattered mode. The EDS spectrum taken on a particle in Figure 4.13 can be seen in Figure 4.15 while the results are tabulated in Table 4.3. EDS analyses were performed on many particles and their averaged results are tabulated in Table 4.4. EDS results are discussed in Section 7.2.

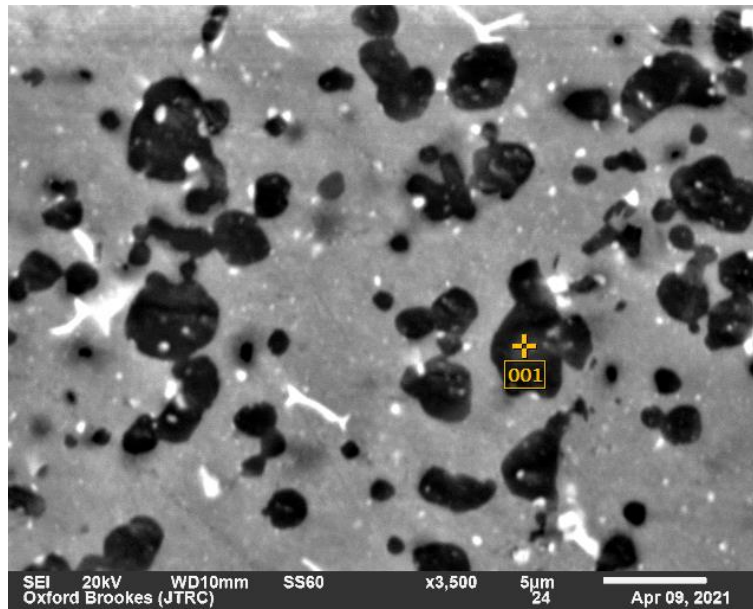


**Figure 4.13.** SEM image of the alloy's microstructure in SE mode.

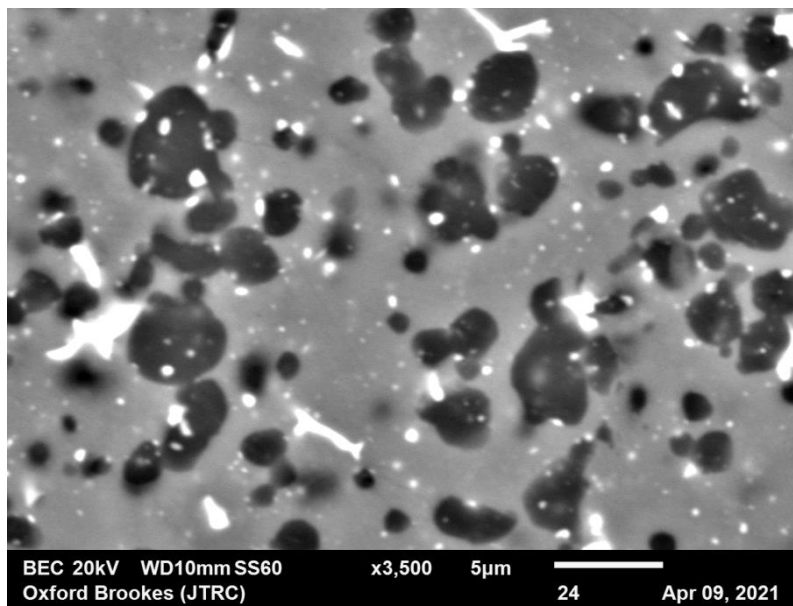


**Figure 4.14.** SEM image of the alloy's microstructure in BS mode.

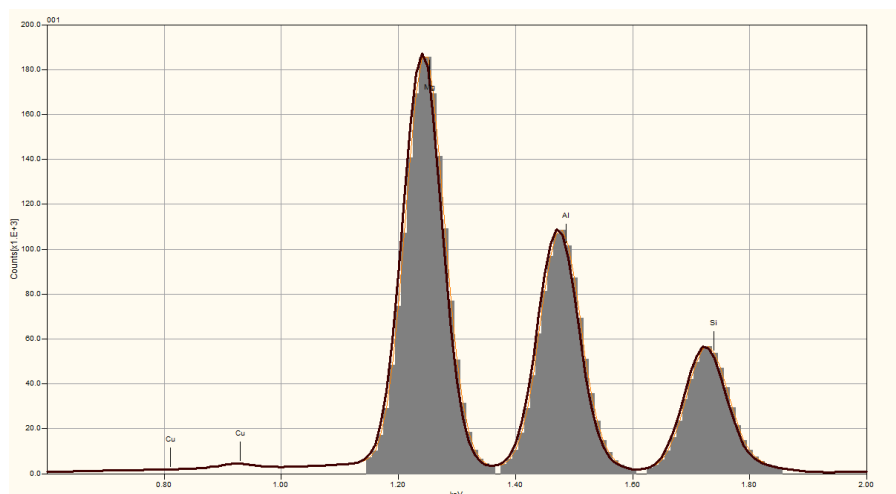


**Figure 4.15.** EDS spectrum of a large particle in as-received state.

Formula	Mass %	Atomic %	Sigma
Mg	48.76	51.69	0.03
Al	37.87	36.17	0.03
Si	13.12	12.04	0.02
Cu	0.25	0.10	0.01
Total	100	100	-

**Table 4.3.** Elemental analysis results of the large particle in as-received state.

Formula	Mass %	Atomic %	Sigma
Mg	51.18	54.00	0.03
Al	35.80	34.13	0.03
Si	12.55	11.47	0.02
Cu	0.31	0.13	0.01

**Table 4.4.** Averaged elemental analyses results of large particles in as-received state.

#### **4.4. Heat treatment for T6 determination**

##### **4.4.1. Heat treatment methodology**

The material sample in Figure 4.3 was further sectioned according to the material cutting plan in Figure 4.16. Each of the samples was numbered using engraver to avoid confusion of the heat-treated samples since different samples were heat treated (artificial aged) at different temperature and for different lengths of time.

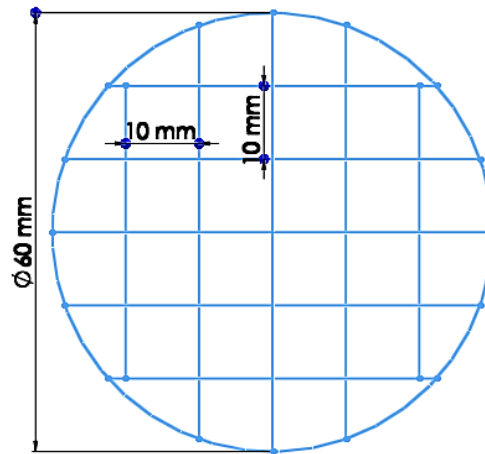


**Figure 4.16.** Material cutting plan for the heat treatment

In total, 22 different samples were used and the heat treatment was carried out on one sample at a time. The heat treatment methodology used to determine the T6 condition is illustrated in Figure 4.17. The temperature selected for the solid solution was 530 °C and the soak time was one hour. The average quench delay achieved was 1.89 second and quenching was carried out using water at room temperature and the sample was agitated to avoid any increase in the local temperature that could affect the treatment.

The artificial aging of the sample was started within 35–40 minutes of the quenching to stop any precipitation formation because the alloy contained copper and some precipitation could take place at room temperature after the solid solution quenching. To achieve this time window, the furnace was forced cooled using a fan to lower down the temperature to aging temperature. The furnace used for the heat treatment was an air furnace.

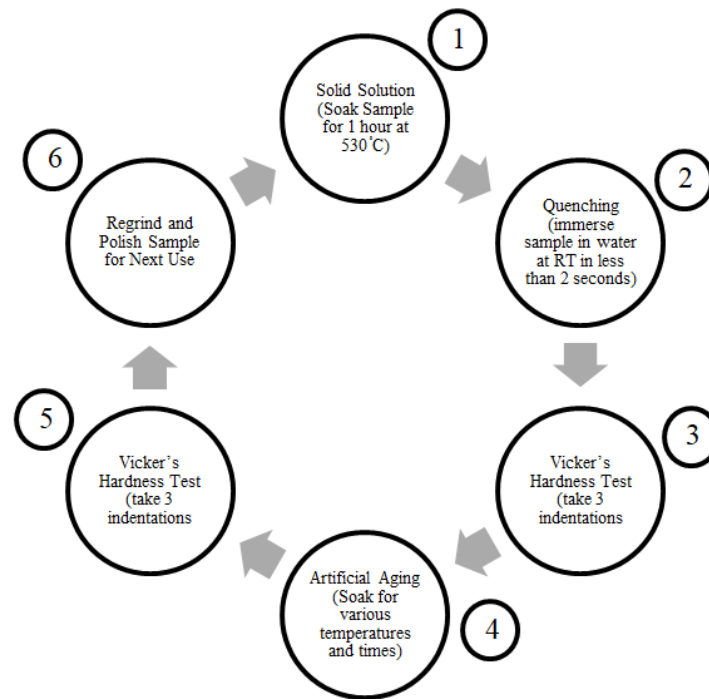


**Figure 4.17.** Heat treatment methodology diagram to determine T6

Artificial aging was carried out at temperatures varying from 140 °C to 180 °C (140, 160, 165, 170, 175, 180 °C) and the aging time was varied from 0.5 hour to 72 hours. Vickers hardness tests were carried out on heat treated samples as a means of measuring the effects of different heat treatment conditions on the alloy. A minimum of three indentations were taken on each sample to get an average. Furthermore, the hardness on each sample was measured twice. Once as the sample was removed from the furnace and quenched, and the other time, on the same sample after leaving it at room temperature (RT) for a week. This was to see if any major changes occurred in the hardness of the alloy with time after completion of the heat treatment.

#### **4.4.2. Heat treatment results for T6 condition**

The artificial aging results to determine the T6 condition are given in Figures 4.18 and 4.19. The T6 was not really clear, but it could be seen that the aging results for 160 °C followed the theoretical curve pattern for T6 condition. Furthermore, the hardness of the sample heat treated at 160 °C for 30 hours did not change significantly after removing it from the furnace

and leaving it at RT for a week. This seemed to correspond to the T6 condition. The hardness of the new alloy increased from an average of 97 HV in as-received state (Figure 4.10) to 175.5 HV in T6 (Figure 4.19). The hardness of the new alloy was 35% higher than of corresponding to Al-2618 (130 HV in T6). The heat treatment results with the scatter and for other temperatures are presented in Appendix A.1-A.2.

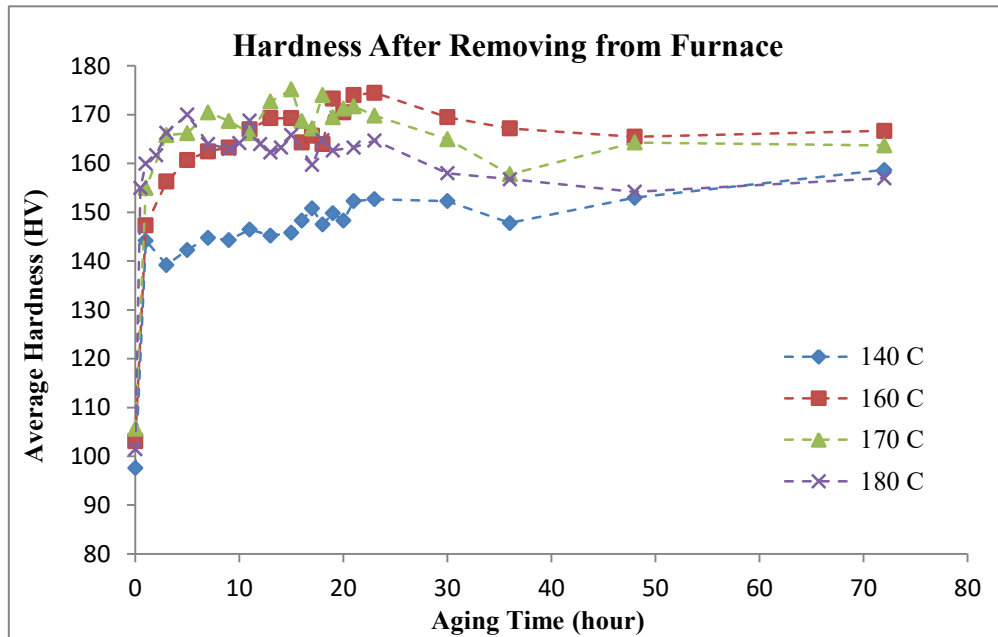


**Figure 4.18.** T6 heat treatment results after removing the samples from furnace.

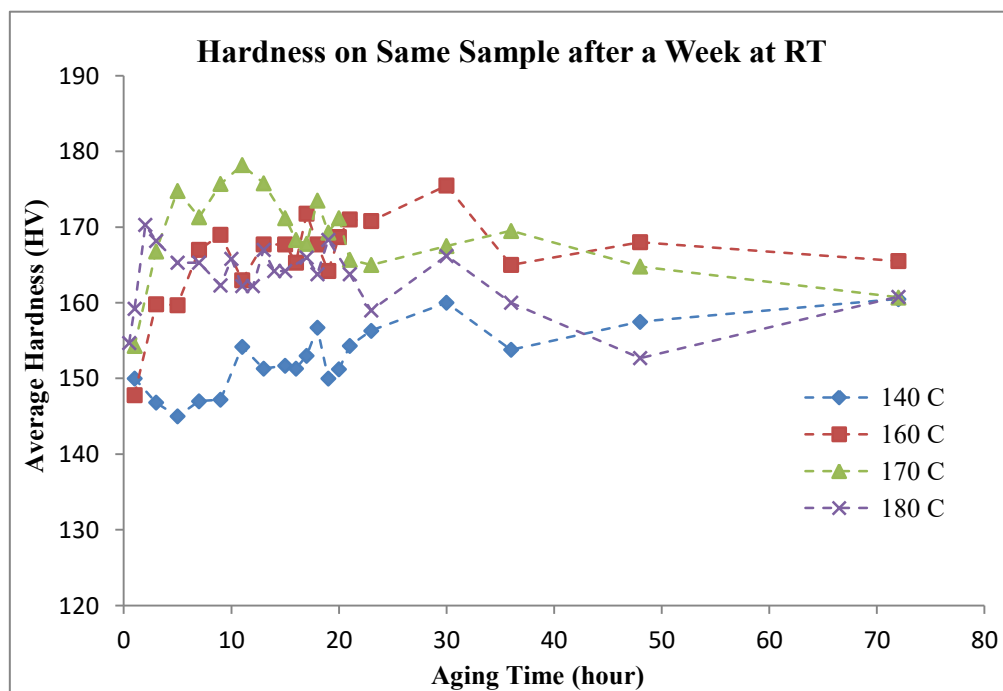


**Figure 4.19.** T6 heat treatment results a week after removing the samples from furnace



Since the heat treatment samples were reused and to ensure that the samples had returned back to their original solid solution state hardness value (average = 101.9 HV), hardness tests were taken on random samples at solid solution states and the results are presented in Figure 4.20. The results did not show any significant variation in hardness values, therefore it was confirmed that the samples returned to their original solid solution state.

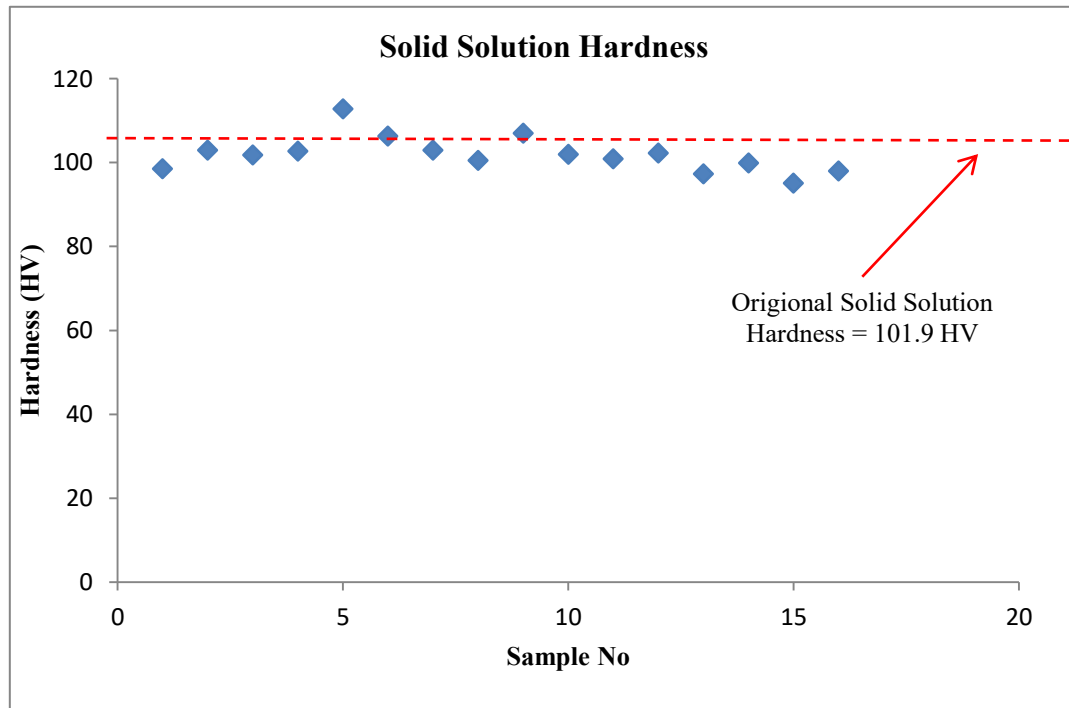


**Figure 4.20.** Solid solution results for the reused heat treated samples.

#### 4.5. Microstructural stability heat treatments

Microstructure of a heat treatable alloy is time and temperature dependent. This can cause inconsistencies in high temperature tensile test results since the microstructure undergoes changes during the tensile tests. To avoid this, the microstructure needed to be in a stable state which was achieved through isothermal studies. This involved soaking of the alloy at relevant temperatures at which the tensile tests would be carried out for long enough time until the microstructure did not change anymore. Hardness tests were used as a means to establish stability; the microstructural stability was achieved once the hardness of the alloy

stabilised. The methodology followed to carry out stabilisation heat treatments is illustrated in Figure 4.21.

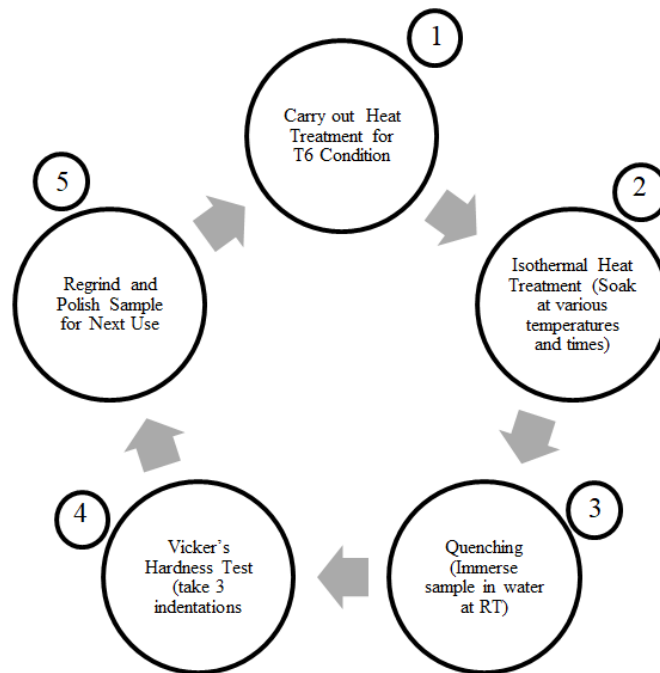


**Figure 4.21.** Microstructural stabilisation heat treatment methodology diagram.

#### 4.5.1. Microstructural stability results

The microstructural stability results are presented in Figures 4.22-4.23 and the hardness was measured twice on each sample similar to the T6 heat treatment. The result showed that the material's hardness did not change for samples after removing from furnace and the same samples being left at room temperature for a week after the isothermal treatment. The samples heat treated at different temperatures reached stability at different lengths of times; however the samples at 200 °C took the longest (100 h) to reach stability. While the samples treated at 150 °C did not have any impact on the hardness at all. All the tensile test specimens were stabilised for 100 hours in their respective temperatures at which the tensile and compression tests were carried out.

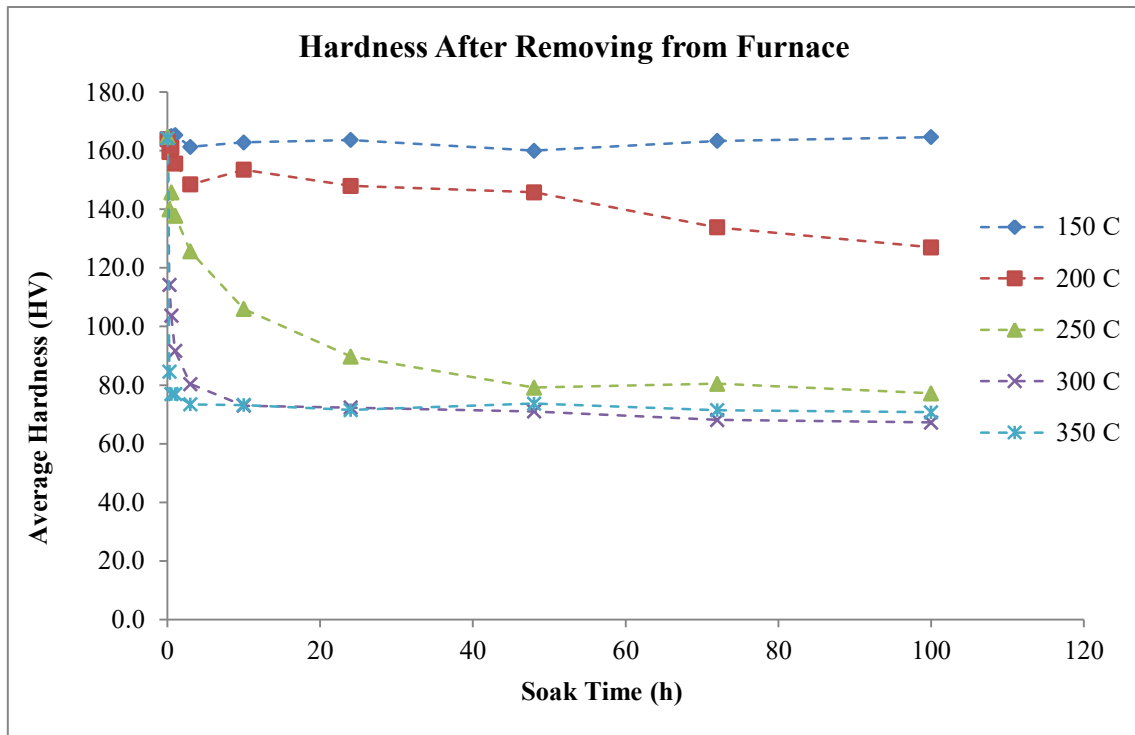


**Figure 4.22.** Microstructural stability results after removing the samples from furnace.

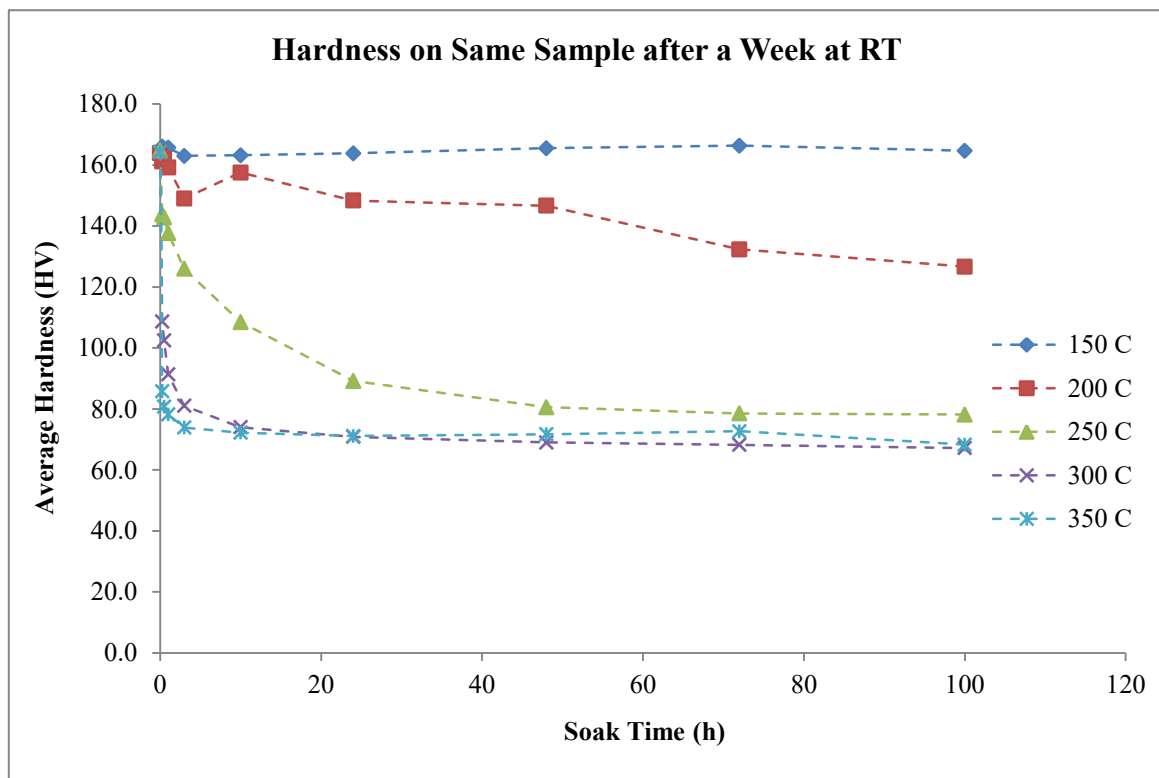


**Figure 4.23.** Microstructural stability results a week after removing the samples from furnace

#### 4.6. Tensile tests results and fracture surface analysis

In order to obtain the tensile strength values of the new alloy at piston operating temperatures, high temperature tensile tests were carried out at piston operating temperature range. Extruded aluminium alloys have anisotropic mechanical properties, and tests are therefore normally carried out in three directions with respect to the extrusion direction (ED) (0, 45 and 90 degrees) (Chen *et al.*, 2009). However, due to the lack of material in this project it was not possible to test all three directions; it was therefore decided to cut the samples only in 90° to ED because it is generally the weakest direction in extruded aluminium alloy bars. The material was the hardest/strongest in extrusion direction due to the alignment of the grains. This was true in the case of this alloy too as can be seen in compression test results in Section 4.7.

The specimens used for tensile tests were flat dogbone shaped as illustrated in Figure 4.24 and the tensile tests were carried out by me in the Faculty of Engineering at the University of Buenos Aires (UBA). The test facility used for the tensile tests can be seen in Figure 4.25a and the machine used was Interactive Instruments Model 1K Universal Materials Tester. When setting up the sample in the machine, it was ensured that the top and bottom of the specimen were aligned in the slot (Figure 4.25b) to avoid any bending of the sample during the tests. All the tests were carried out at strain rate of  $1 \times 10^{-4}$  per second which is the standard strain rate used for aluminium alloys (American Society for Testing and Materials, 1984; Audebert *et al.*, 2002). All the specimens were stabilised for 100 hours prior to testing according to the microstructural stability results in Section 4.5. The 2D engineering drawing of the dogbone specimen is given in Appendix A.3.



**Figure 4.24.** A picture of the flat dogbone specimen used for the tensile tests.

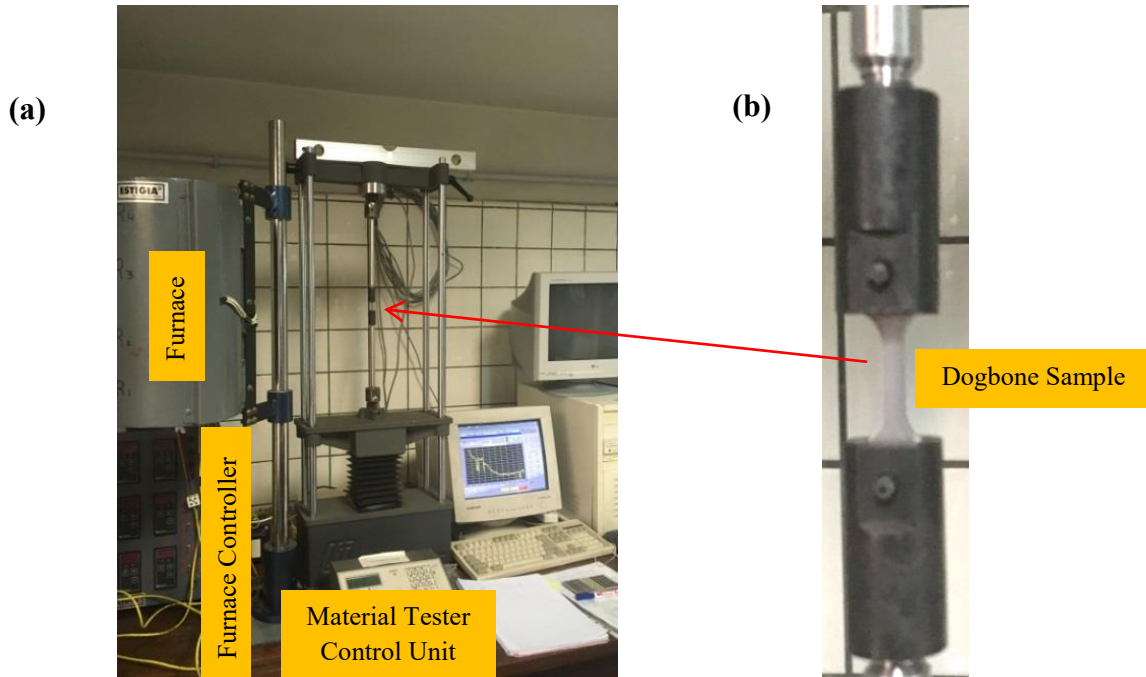


**Figure 4.25.** a) Test setup for the high temperature tensile tests. b) Alignment of the sample in the slot.

#### 4.6.1. Tests at elevated temperatures

The high temperature tensile tests were carried out at 25, 100, 150, 200, 250, 300 and 350 °C. The results are presented in Figure 4.26 and it can be seen that the samples in room temperature or T6 condition had the highest yield strengths with an average value of approximately 409 MPa, but showed no appreciable deformations. On the other hand, the samples at 350 °C had the lowest strengths with an average value of approximately 26 MPa, but had the highest deformations (Figure 4.27). The results also indicated that the alloy did not show any significant reduction in strength till about 150 °C. Furthermore, there was no significant variation/scatter in the test results for different samples under the same testing

conditions because the test specimens were stabilised. All the tested samples were preserved for fracture surface analyses. The horizontal axis of the graph is offset by 0.05 for each temperature from the previous temperature to better visualise the results at each temperature else the lines falls on top of each other especially at temperatures 200 °C and lower. All strain curves should actually pass through the origin. The data past yield points or plastic region has been cut off and not shown as it was not of an interest in this work.

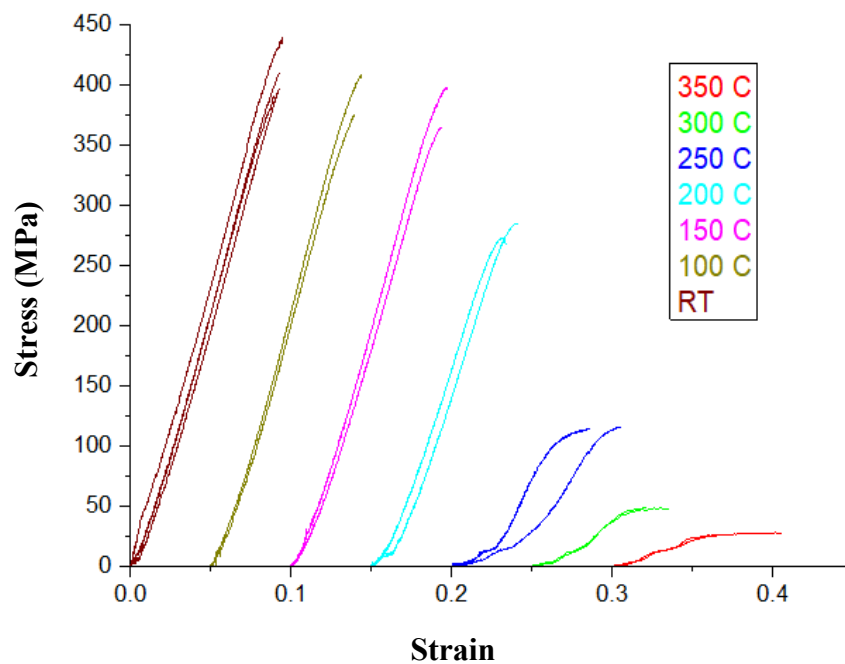


**Figure 4.26.** Tensile test results at various temperatures.

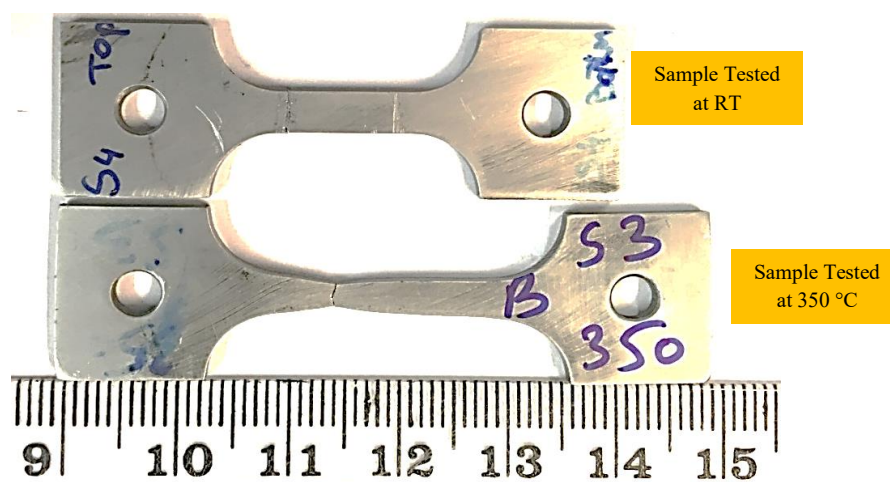


**Figure 4.27.** Deformed flat dogbone specimens.

The plots in Figure 4.28 show the yield strength comparison of the alloy Al-2618 and the new alloy under consideration in this project. The yield strength values for Al-2618 were obtained from these sources (American Society for Metals. Handbook, 1979; Kaufman, 1999) while the yield strength values for the new alloy were obtained from stress-strain graphs using 0.2% offset yield strength method. The new alloy had approximately 1.09–1.82 times higher yield strength than Al-2618 depending on the temperature. The comparison of the new alloy with other high strength aluminium alloys used in piston applications is given in Section 4.9.

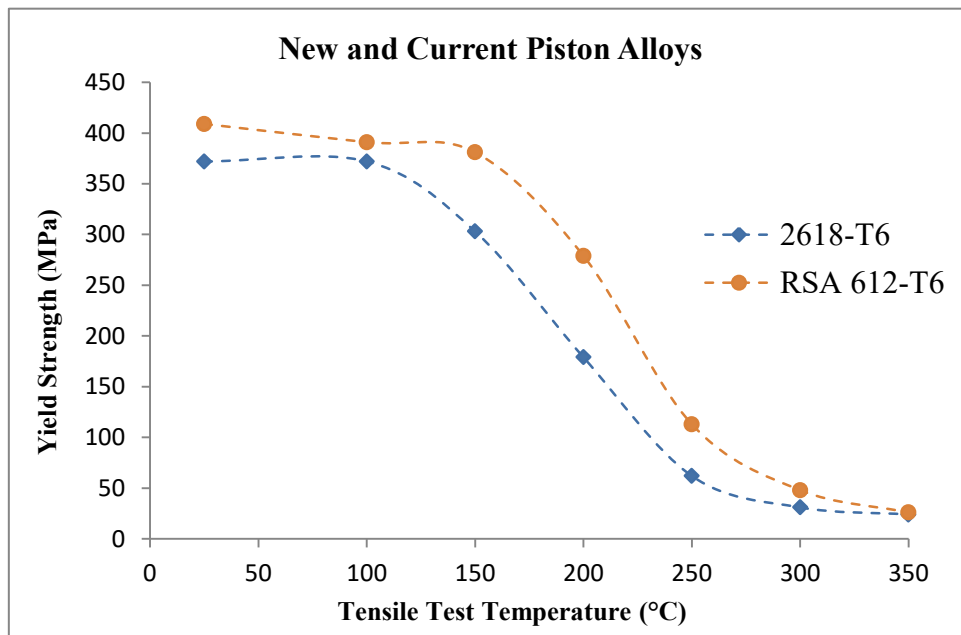


**Figure 4.28.** Yield strength comparison of Al-2618 and the new alloy at a range of tensile test temperatures.

#### 4.6.2. Tests at room temperature after 100 hours of use

The stabilised samples were also tested at room temperature to assess if the alloy's strength recovers after 100 hours of exposure to the relevant temperatures. The test results are shown in Figure 4.29 while the comparison plot of yield strengths during high temperature testing and room temperature is shown in Figure 4.30. The results showed that there was no significant difference in yield strengths till about 150 °C and some of the alloy's strength recovered after 100 hours of exposure at various temperatures. Similar to Figure 4.26 the

horizontal axis of the graph is offset by 0.05 for each temperature from the previous temperature to better visualise the results at each temperature. All strain curves should actually pass through the origin.

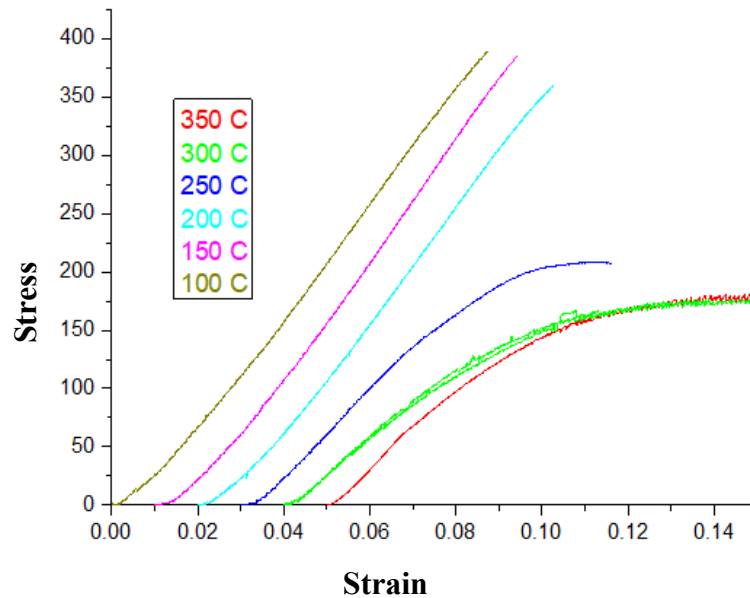


**Figure 4.29.** Tensile test results after 100 hours of use at the relevant temperatures.

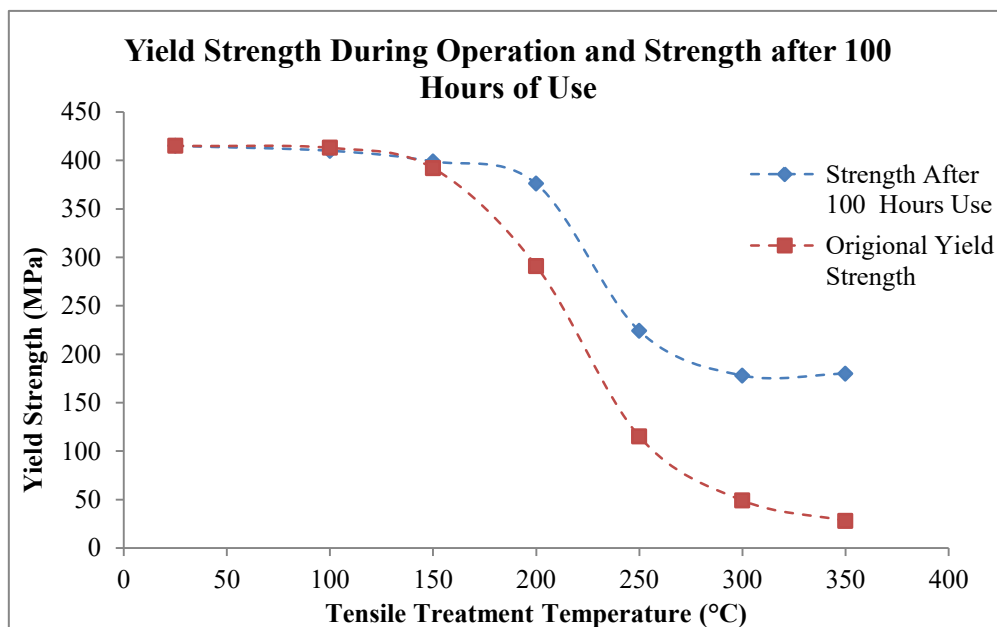


**Figure 4.30.** Yield strength comparisons of the new alloy during operation and after 100 hour of use.



#### 4.6.3. Fracture surface analyses of tensile specimen

Fractography was carried out to determine the cause/mode of failures in the tested tensile specimens. The SEM images in Figures 4.31a and 4.31b show the fractured tensile test samples at different heat treatment conditions. It can be seen that the sample tested at RT had failed in brittle manner and no necking could be observed. While the sample tested at 350 °C had appreciable necking and failed in ductile manner (reduction in cross section).

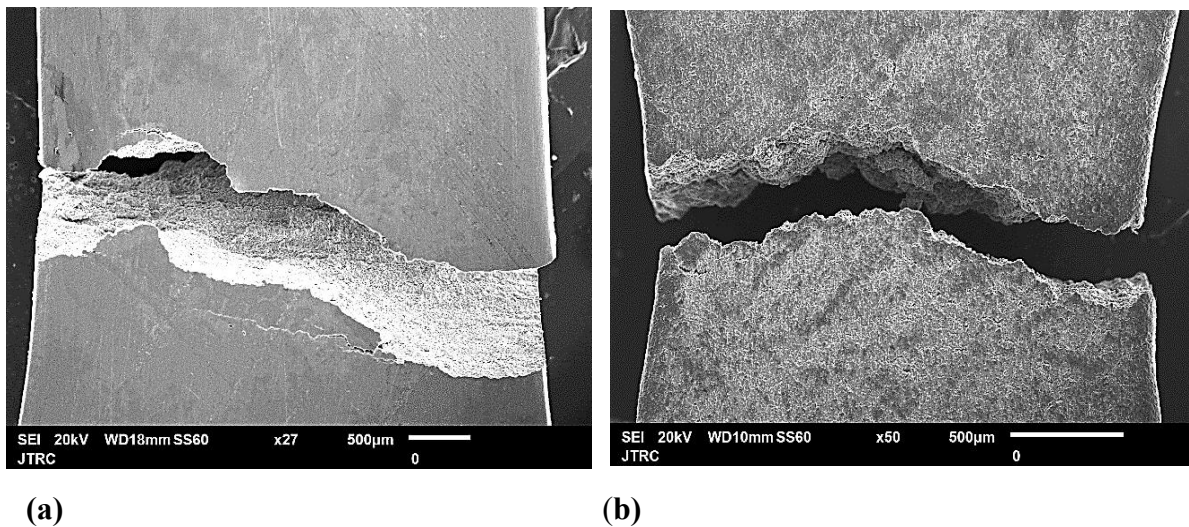


**Figure 4.31.** SEM images of the fractured samples tested at a room temperature T<sub>6</sub> and b 350 °C

The images in Figure 4.32 show the regions next to the fractures in samples tested at different conditions. The red arrows on the images show the direction of the applied force and it can be seen that the test sample at RT fractured approximately 45° to the applied load (Figures 4.31a and 4.32a). While the sample tested at 350 °C fractured 90° to the applied load, showing that the fracture was caused by shear stress (Figures 4.31b and 4.32b).

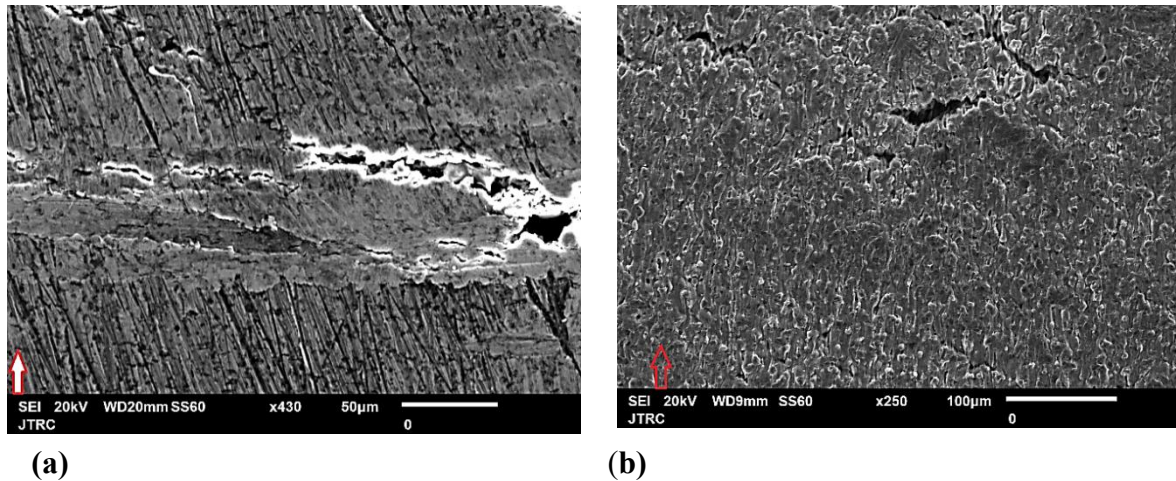


**Figure 4.32.** Zoomed in SEM images of the fractured samples tested at a room temperature T6 and b 350 C

The SEM images of the fractured faces of the samples at two different heat treatment conditions are shown in Figures 4.33 and 4.35. The surface of fracture in the T6 state (Figure 4.33) did not show any appreciable microplasticity compared to the sample tested at 350 C (Figure 4.35). Furthermore, there were more micro-cracks in the T6 sample than at 350 C sample due to the lack of microplasticity, indicating that the aluminium matrix had been sheared.

Large particles, made of Al, Mg and Si were observed in the fractured faces which formed pits around them. The EDS spectrums of these large particles for the test samples at RT and 350 °C are presented in Figures 4.34 and 4.36 respectively. These could have been the likely cause of the fracture initiation.

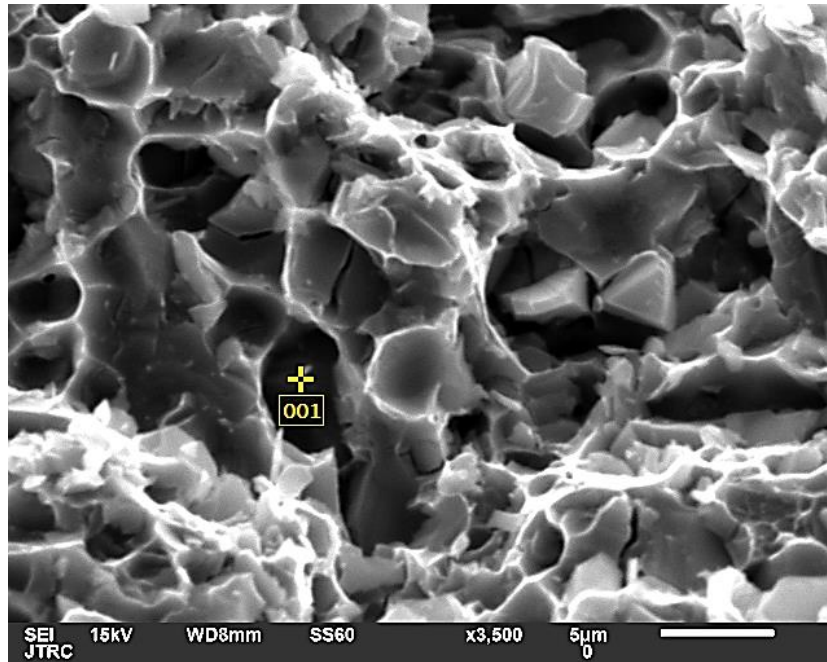


**Figure 4.33.** SEM image of the fractured face of the specimen tested in room temperature  
(T6)

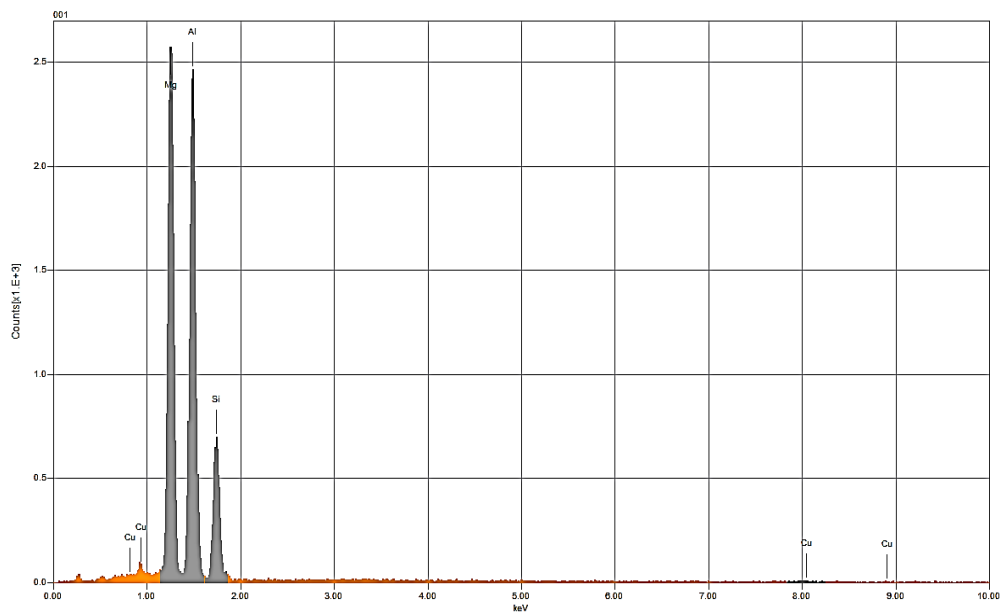


**Figure 4.34.** EDS spectrum of the large particle in the fractured face of the sample tested in  
room temperature.

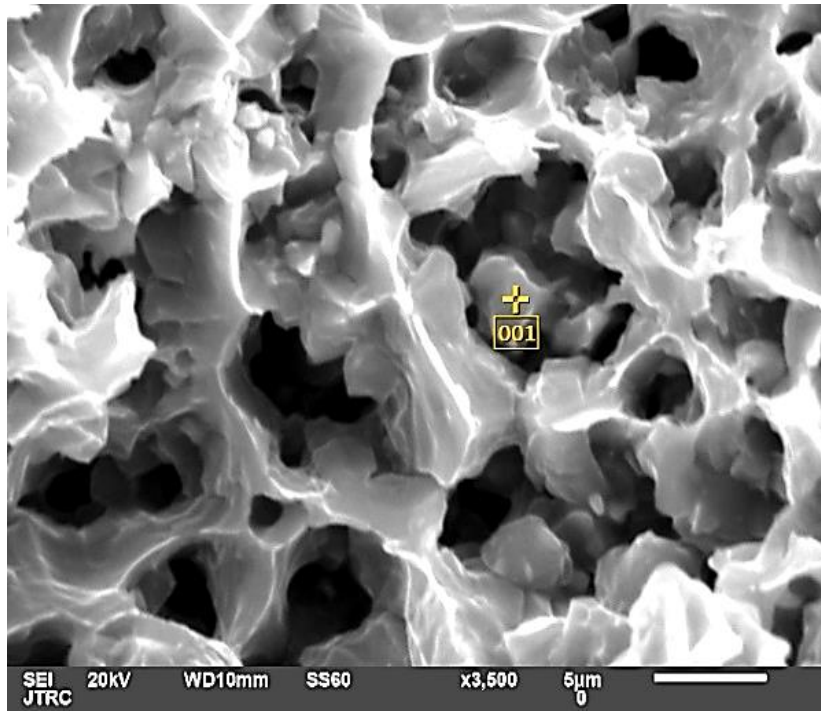


**Figure 4.35.** SEM image of the fractured face of the sample tested at 350 C.

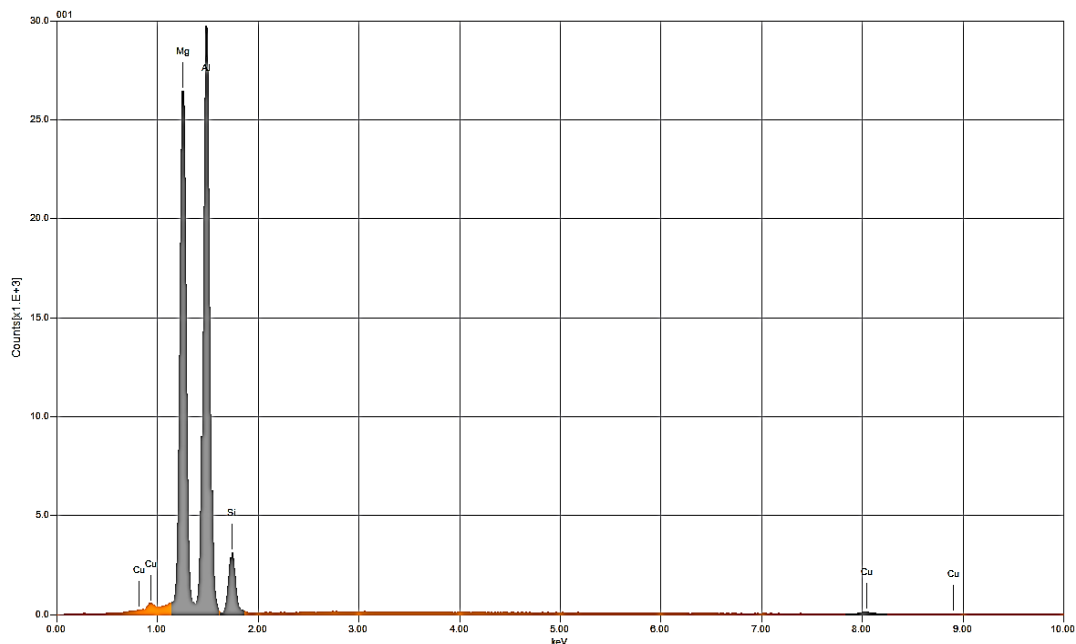


**Figure 4.36.** EDS spectrum of the large particle in the fractured face of the sample tested at 350 C

#### **4.7. Compression test results and fracture surface analyses**

As the combustion pressure of an engine generates compressive stresses in a piston, it is therefore essential to test the material in compression. Most metallic materials have nearly

15–20 % higher yield strengths when tested in compression than in tension. The compression tests were performed on cylindrical samples with length to diameter (L/D) ratio of 2:1. The ratio was used to avoid buckling; longer samples with smaller diameter are likely to buckle (American Society for Testing and Materials, 1984). Furthermore, to avoid bending/buckling during the test, the two ends of the cylinder were set parallel. A drawing of the sample dimension used in this project can be seen in Appendix A.3.

The tests were performed using the fixture/test set up shown in Figure 4.37. The fixture was designed in a way that allowed the machine to operate in tensile mode while the test sample was being compressed. The reason for using this fixture was that tensile test machines are known to be more accurate in tensile mode compared to compression. Vaseline was applied to the test sample ends and the plates on the fixture to help reduce friction.

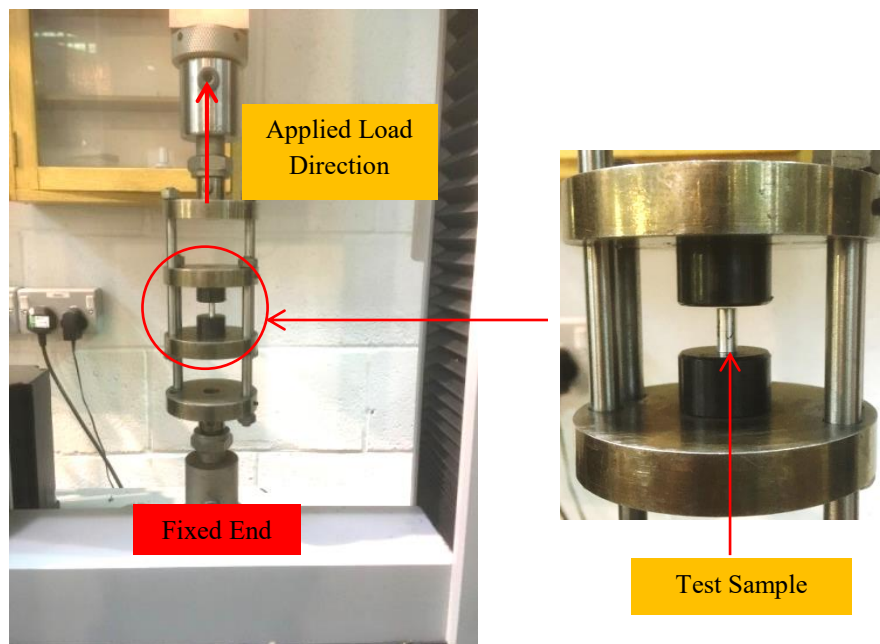


**Figure 4.37.** Test fixture used for the compression tests.

The compression tests were carried out on samples cut from the bar in the extrusion direction and 90 degree to the ED called as transverse direction . Three samples were tested for each orientation and all the samples were heat treated to T6 and stabilised at RT, similar to the

tensile test specimen. The compression test results are shown in Figure 4.38 and it can be seen that the samples in the ED had higher yield strengths compared to the transverse direction. Furthermore, the average yield strength of the transverse sample was approximately 550 MPa which was 34.5% more compared to 409 MPa in tension. Similar to Figures 4.26 and 4.29 the horizontal axis of the graph is offset by 0.1 for samples with different cut/grain directions.

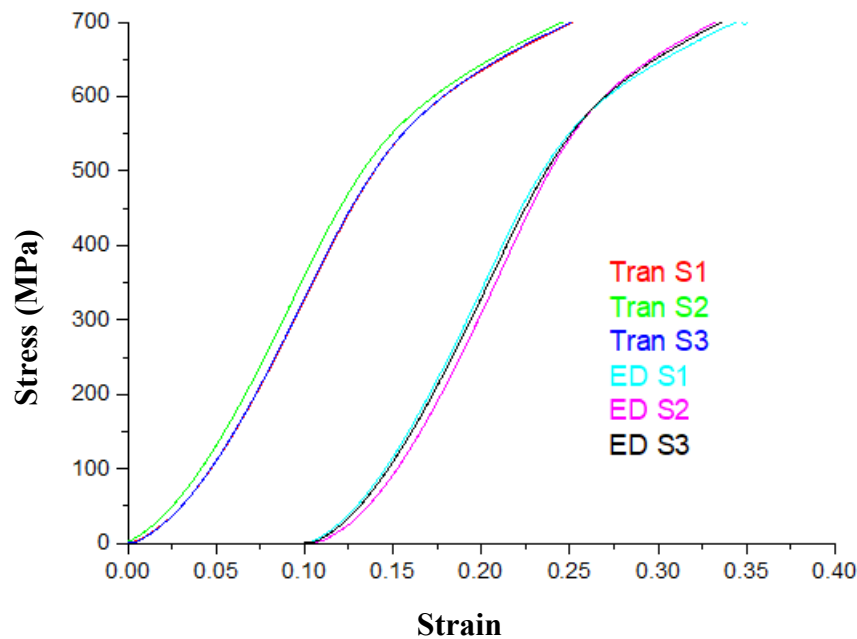


**Figure 4.38.** Compression test results of the new alloy for samples cut from the extruded bar in two different directions.

#### 4.7.1. Fracture surface analyses of compression specimen

Fractography of the compression test specimens showed that pitting was caused by large particles (Figures 4.39 and 4.41) which could have led to the initiation of cracks. The large particles mainly consisted of Al, Mg and Si as can be seen in Figures 4.40 and 4.42.



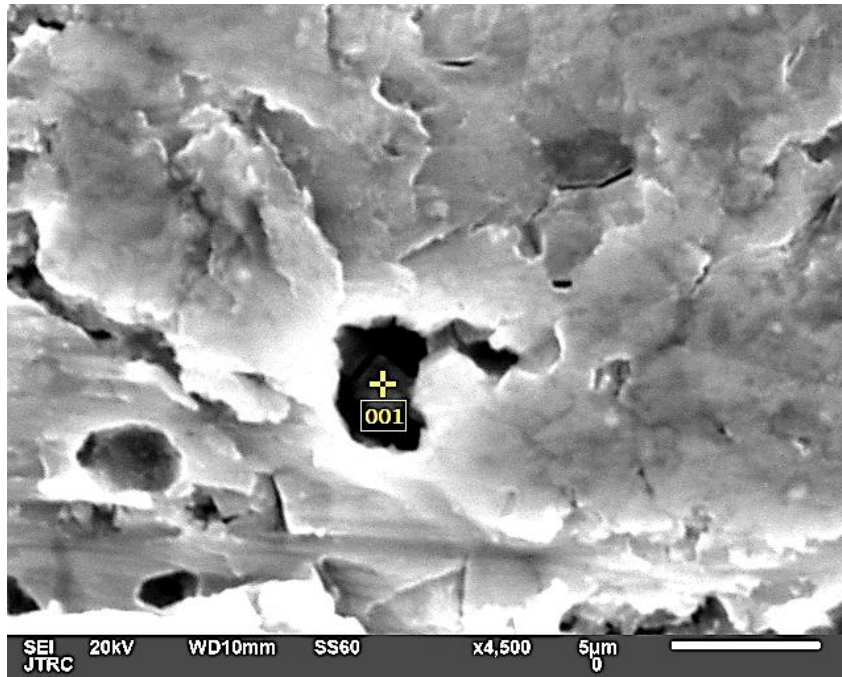


**Figure 4.39.** SEM image of the fractured face of the sample in extrusion direction.

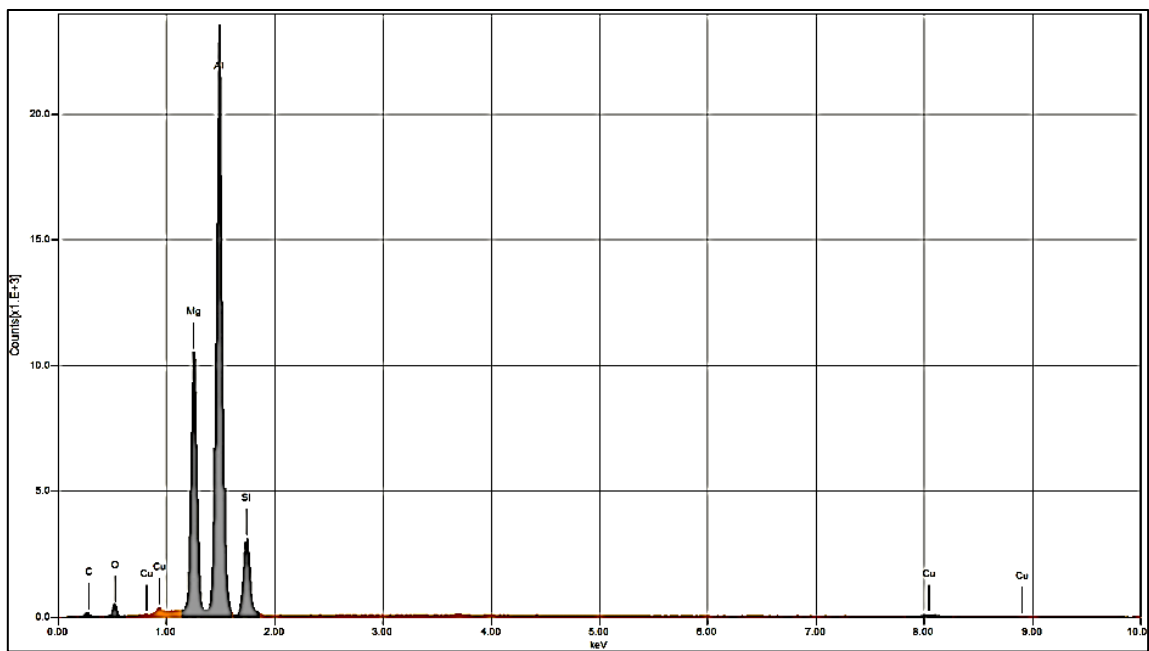


**Figure 4.40.** EDS spectrum of the large particle in the sample tested in extrusion direction.

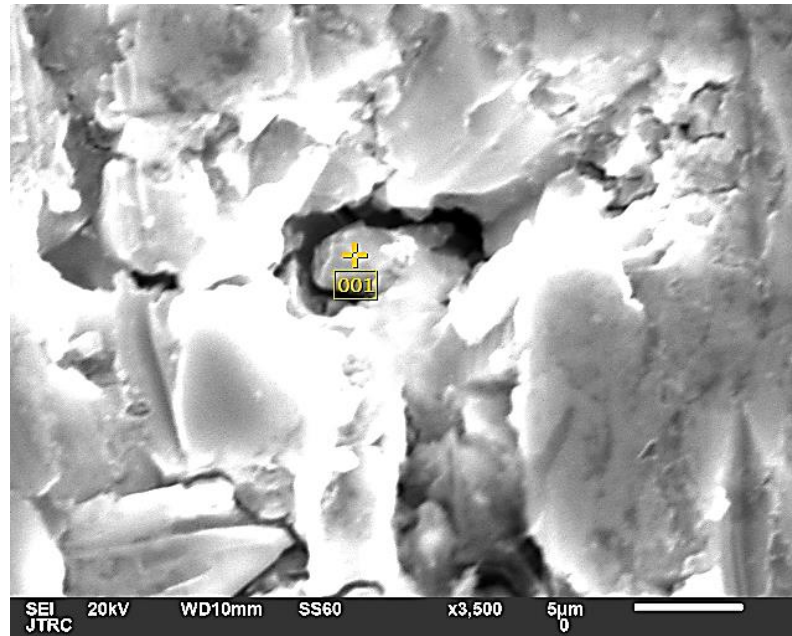


**Figure 4.41.** SEM image of the fractured face of the sample tested in transverse direction

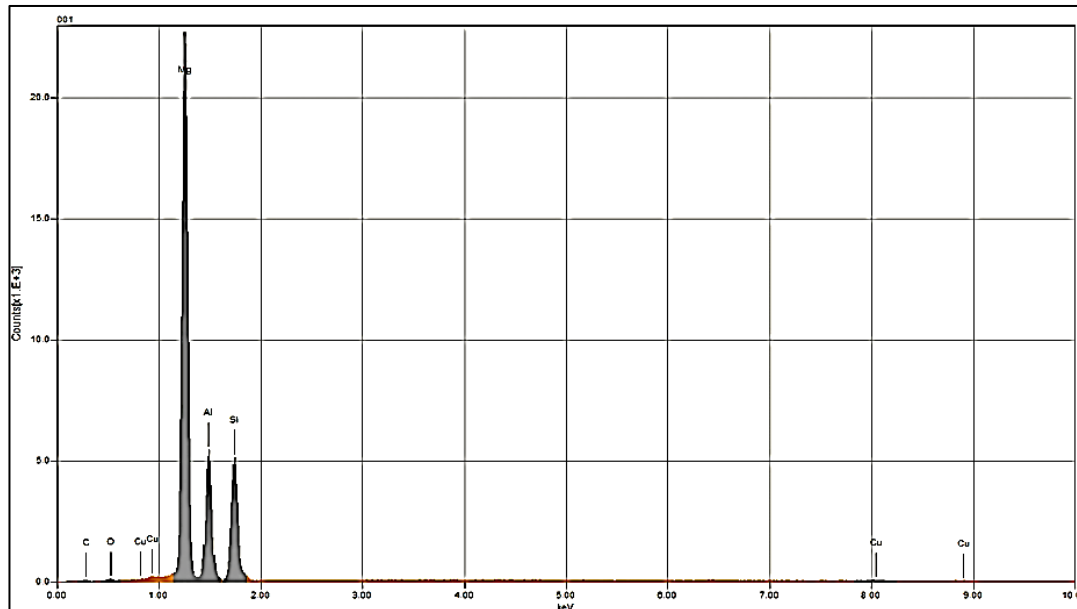


**Figure 4.42.** EDS spectrum of the large particle in the sample tested in transverse direction.

#### 4.8. X-Ray diffraction (XRD) analysis

X-ray diffraction (XRD) analysis is a material characterisation technique; primarily used for the phase identification of a crystalline material and can provide information on unit cell dimensions. It is also used for reverse engineering and competitive analysis and other applications (Callister and Rethwisch, 2011; Dutrow and Clarke, 2017). In this project it was used for phase identification.



The reference XRD cards used to identify the phases are attached in Appendix A.4. The XRD results presented in this thesis (Figure 4.43) utilised the facility in the Department of Materials at the University of Oxford. The results indicated that three different phases were present in the samples, the most dominant being the Al ( $\alpha$ ) with the widest peak. The other two intermetallics were  $\text{Mg}_2\text{Si}$  and  $\text{Mg}_{17}\text{Al}_{12}$  which corresponded to the two peaks observed in the particle distribution analysis in Figure 4.9.

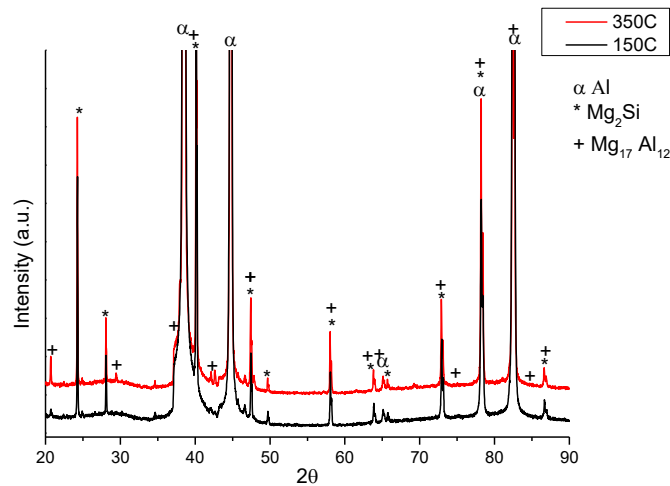


**Figure 4.43.** Diffractograms of the samples in two different heat treatment conditions.

#### 4.9. Suitability of the new alloy for piston application and comparison with existing aluminium alloys

The tensile test results obtained in Section 4.6.1 for the new alloy showed an improvement over the alloy Al-2618 which was used in the test engine piston for this project, however Al-2618 is not the only aluminium alloy used in piston applications. Figures 4.44 and 4.45 show the yield and ultimate tensile strengths of some of the aluminium alloys used for different piston applications, but the two most commonly used aluminium alloys for pistons are Al-2618 and Al-4032. The Al-2618 is dominant in racing while the Al-4032 is used for racing, but more commonly used in production pistons.

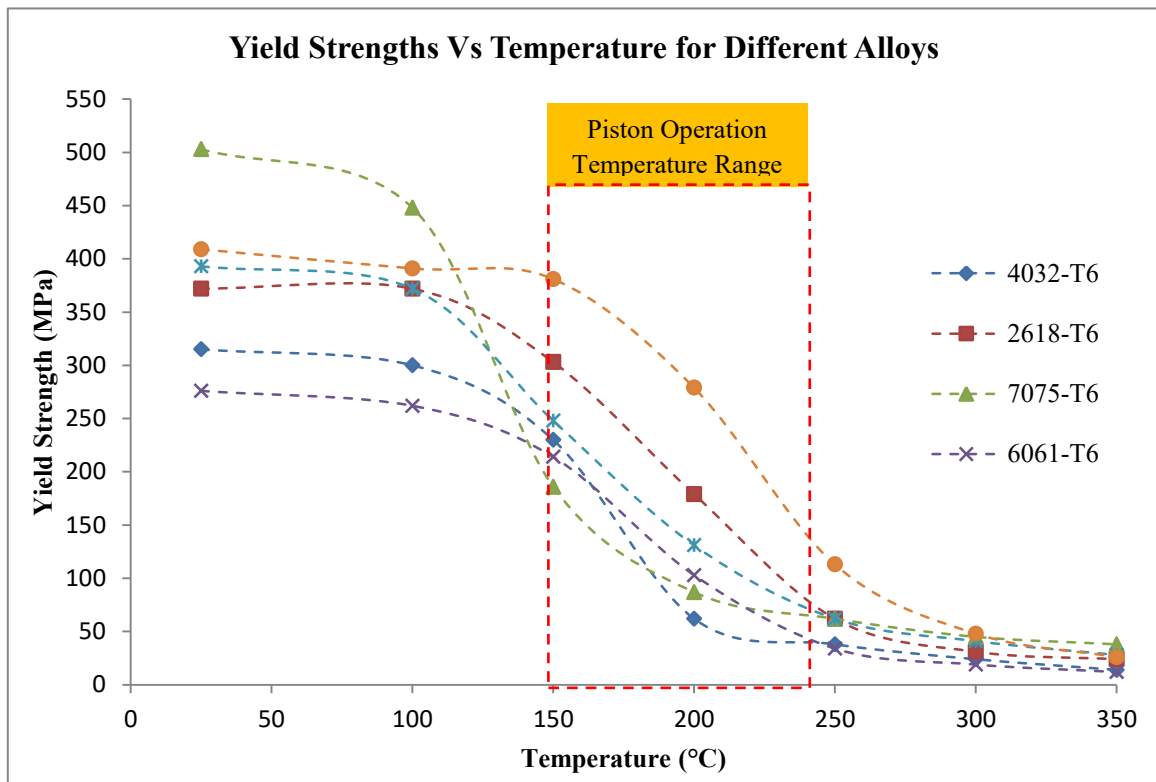


**Figure 4.44.** Yield strength comparison of different aluminium alloys.

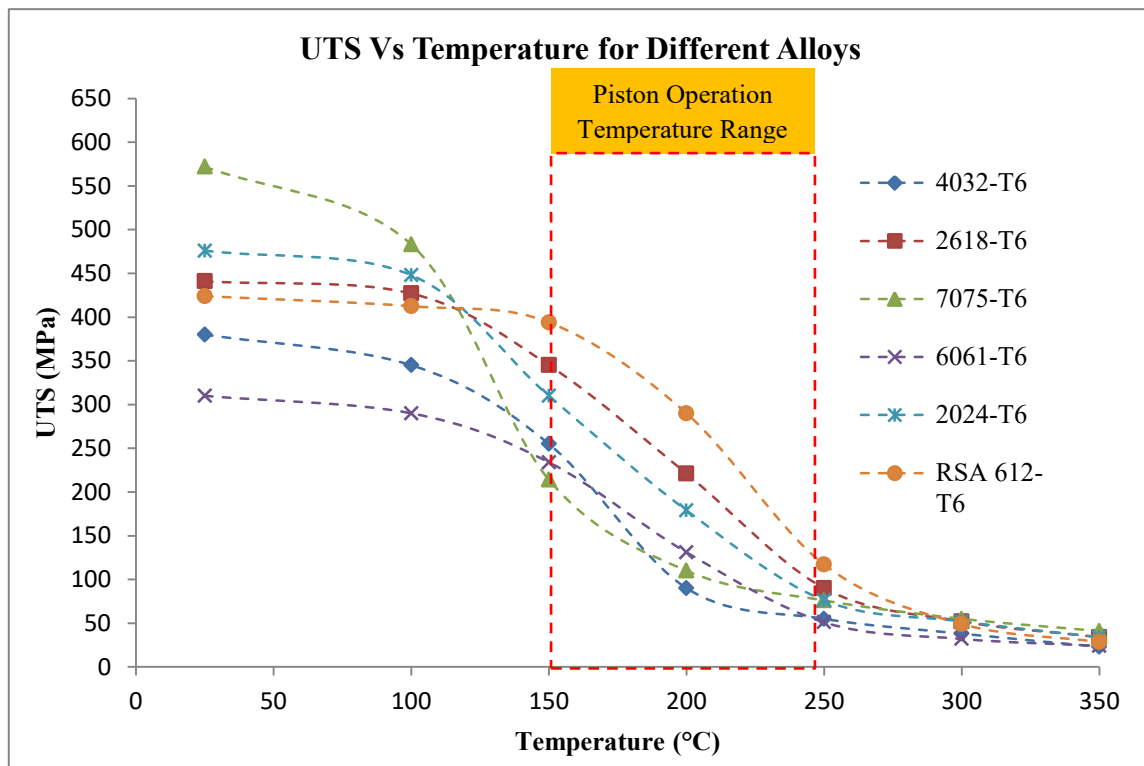


**Figure 4.45.** Ultimate tensile strength comparison of different aluminium alloys.

It can be seen from Figures 4.44-4.45 that the yield and ultimate tensile strengths of the new alloy were consistently higher than the other alloys except 7075-T6. The 7075 only maintains higher strength than the new alloy up to 110 °C, which is not very helpful in piston application in terms of reducing mass. Figure 4.46 shows the distribution of piston mass and temperature for the test engine and it can be seen that nearly 82% (Schwaderlapp *et al.*, 2000) of the piston mass lied above the pin hole centre where the temperature ranged from 120–265 °C. The higher strengths of the new alloy at higher temperatures therefore enables to reduce piston mass.

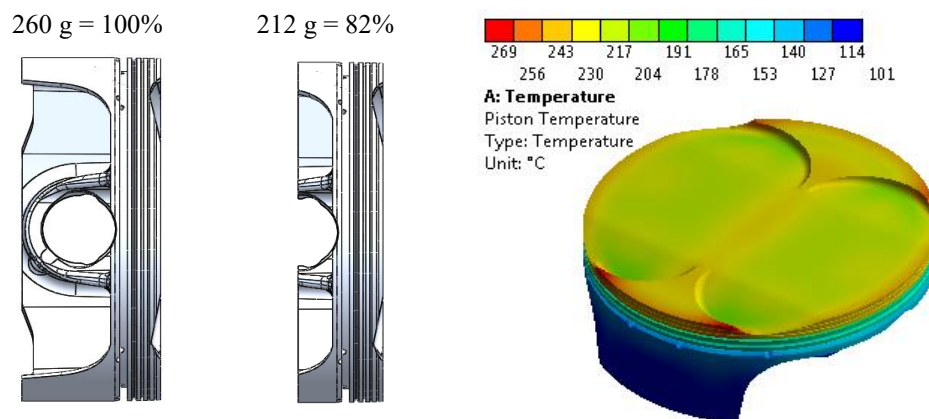


**Figure 4.46.** Temperature and mass distributions of KTM 450 XCF.

#### 4.10. Summary

The microstructural examination showed that the material was homogenous along the bar's cross-section. This was also confirmed through Vickers hardness. The T6 condition was determined and the alloy's hardness increased from 97 HV on average in as received state to 175.5 HV in T6. The T6 conditions were 30 hours at 160 °C obtained using the results from aging heat treatments. The high temperature tensile tests demonstrated that the new alloy had higher strengths at piston operating temperatures compared to Al-2618 alloy. This is the widely used alloy for piston applications in racing. Furthermore, the new alloy had significantly higher strengths than the existing aluminium alloys used in different piston applications, promising significant piston mass reduction.

## **Chapter 5: Piston design, finite element analysis and manufacturing**

### **5.1. Introduction**

Pistons are critical components in the power conversion systems of internal combustion engines as they transfer energy from the combustion of the air-fuel mixture to the motion of crankshafts with the aid of the connecting rod. Pistons are also one of the most stressed moving components in the engine. They must be designed to withstand thermal and dynamic loads and avoid structural failure, noise and skirt scuffing. They should also be light to minimise inertial loads, reduce friction and transmit the unconverted heat generated in the combustion chamber. The finite element analysis (FEA) has become a well-accepted method in the industry to make predictions before expensive manufacturing and testing are carried out. This Chapter explains how FEA was carried out for the current and design of a new lightweight piston using the new aluminium alloy introduced in Chapter 4. The chapter also explains manufacturing of the new pistons and the challenges encountered with piston design and manufacturing.

### **5.2. Piston finite element methodology**

The methodology used for the FEA work is highlighted in sections 5.3 and 5.4 and it is illustrated as a flowchart in Figure 5.1.

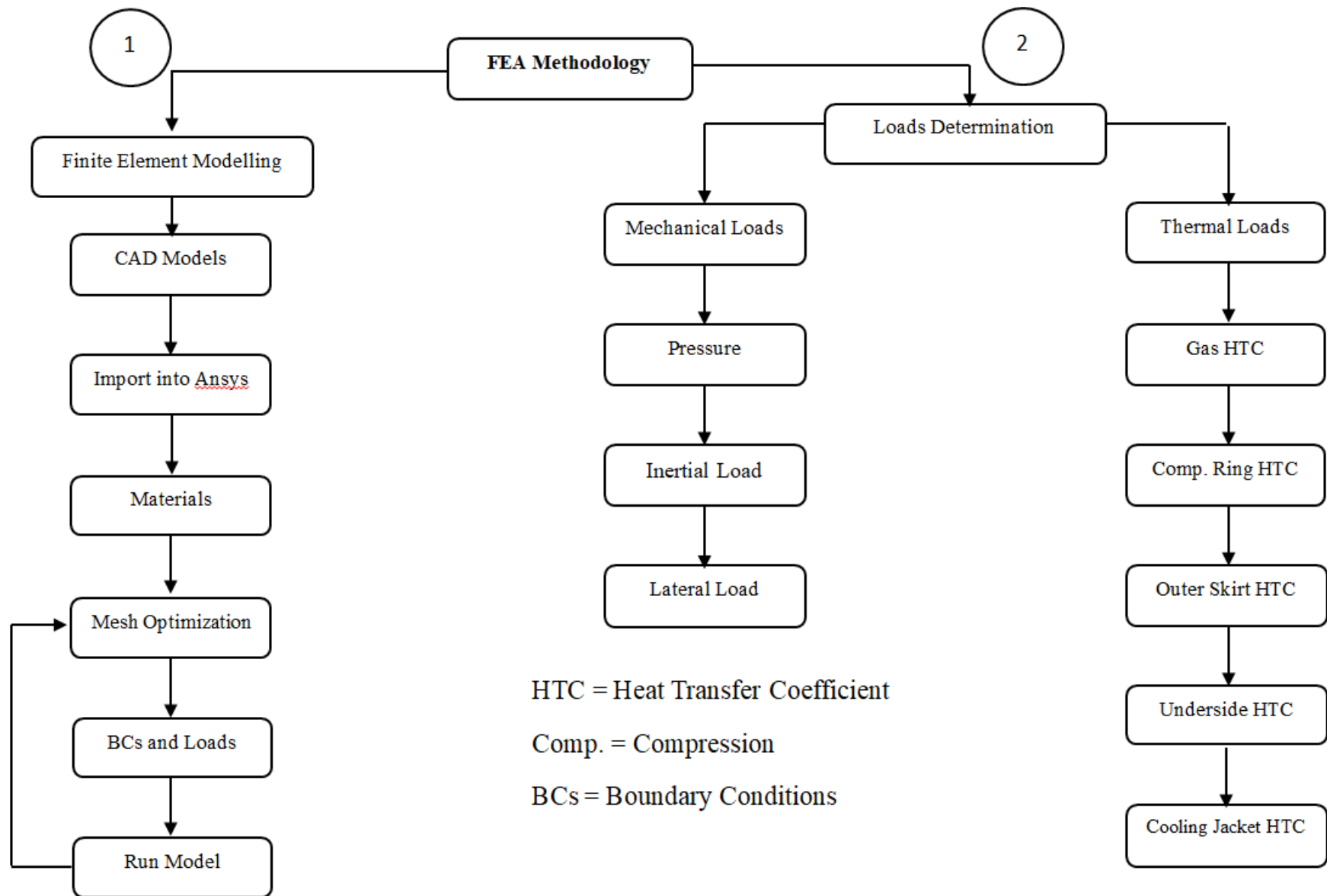


**Figure 5.1.** Methodology flowchart for the piston finite element analysis.

### 5.3. Piston finite element modelling

The development of the finite element model of the piston requires the use of computer aided design to construct the geometry. Idealisation of the geometry is a common practice in formulating finite element models to enable rapid meshing, reduced processing time and reduced resource requirements. Eliminating certain parts and features of the geometry may remove the interdependencies and could lead to flawed results.

Two different approaches are repeated in the literature for idealisation of piston loading model; of which the most widely used simplification is based on the use of piston and gudgeon pin geometry only (referred to as Model 1 in Figure 5.2) (Okamoto, Anno and Itoh, 1992; Carvalheira and Gonçalves, 2006; Singh *et al.*, 2015). Mahle (2016) though suggests that the geometry used for a piston should include some portion of the connecting rod's small end and the cylinder in addition to the piston and gudgeon pin (referred to as Model 2 in Figure 5.3). Mahle (2016) however, did not explain why model 2 was better than model 1. Furthermore, Mahle (2016) stated that there are three types of mechanical loads acting on a piston; combustion pressure, inertial and lateral forces (Section 3.6.1), but most of the published papers did not account for the lateral force.

In this work, equations were derived from the crank slider mechanism (Norton, 2008) to calculate the lateral force for inclusion in the FEA in order to evaluate its effect on piston. No clear comparative analyses have been carried out in the literature about the relative effectiveness of the two approaches in terms of realistic model representation. In this research, both models were analysed to study the predictions from each and the effect of the lateral force has been investigated.

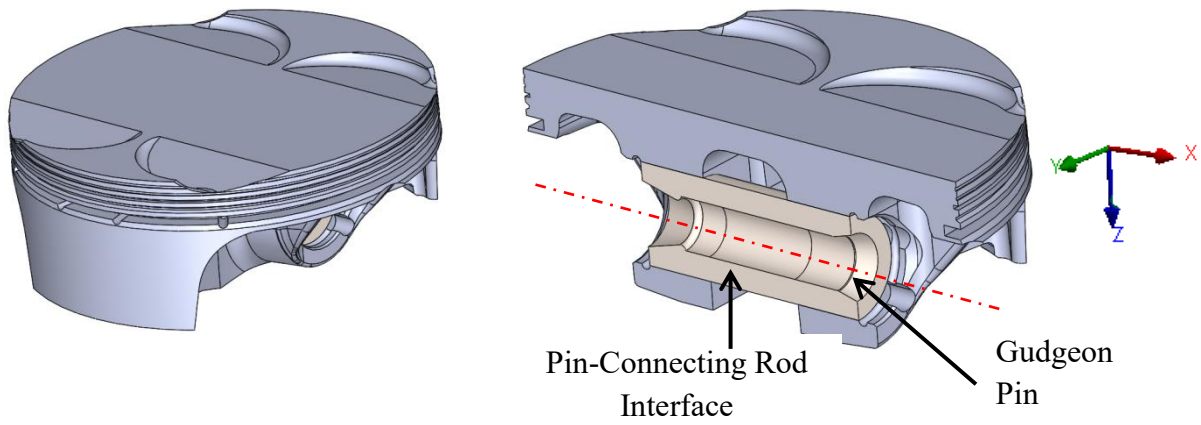


**Figure 5.2.** Model 1 assembly for the piston finite element analysis.

The model suggested by Mahle (2016) proved difficult to be constrained in a manner that represents realistic conditions, hence the whole cylinder, its casing, cylinder mounts and washer were also included in the CAD geometry (Figure 5.3).

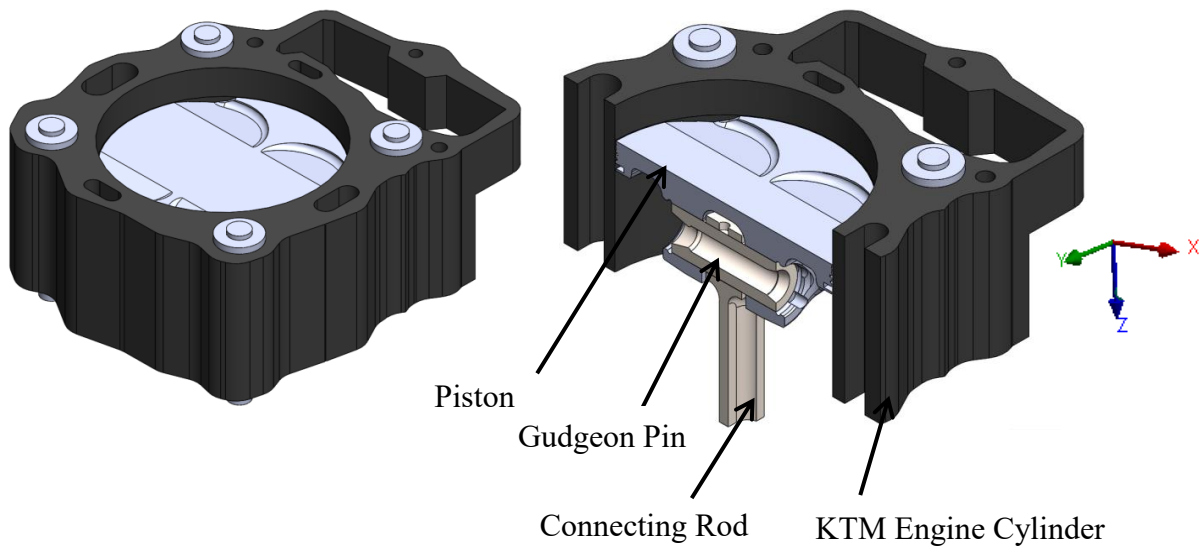


**Figure 5.3.** Model 2 assembly for the piston finite element analysis.

### 5.3.1. Geometric constraints and contacts in the FE models

To simulate the support that the connecting rod provides to the pin in model 1, most publications used cylindrical support that was applied at the pin and connecting rod interface as illustrated in Figure 5.4a (Carvalho and Gonçalves, 2006). The cylindrical support surfaces were allowed to deform/move freely in the radial and axial directions while fixed in the tangential direction as suggested by (Carvalho and Gonçalves, 2006). The definition of

a cylindrical support according to the Ansys Workbench<sup>TM</sup> manual is illustrated in Figure 5.4b.

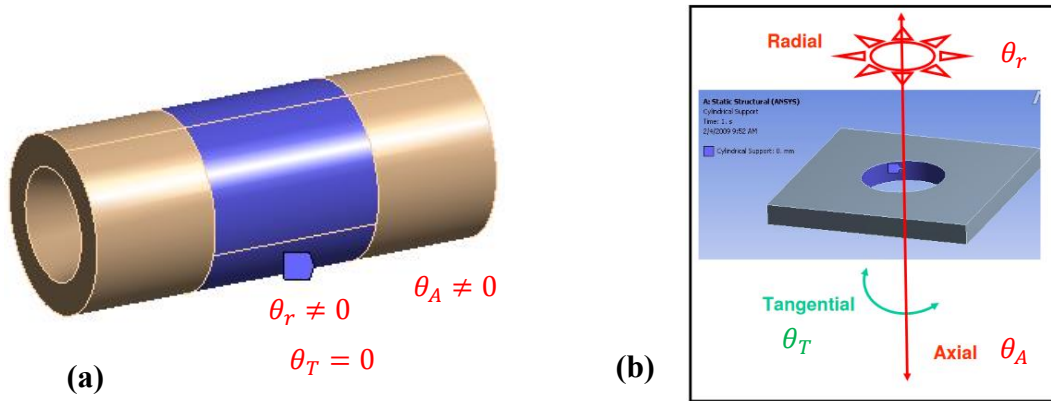


**Figure 5.4. a)** Application of the cylindrical support on pin-connecting rod interface.

**b)** Definition of the cylindrical support according to the Ansys Workbench<sup>TM</sup> manual.

To constrain Model 2; a node was fixed in the middle of the connecting rod's bottom face (Figure 5.5a) and fixed supports were used on the bottom cylinder washers and studs to represent the cylinder being attached to the engine body (Figure 5.5b). Furthermore, a pressure of 5.22 MPa was applied to the top washers (Figure 5.5c) to represent the clamping force of 30 N (engine tightening torques in Appendix B.1) that was applied to the studs/nuts on the cylinder. Equation 5.1 was used to convert the torque into force (F) which was then converted into pressure using the surface area of the washers (Edge, 2018b). The calculations are given in Appendix B.2.

$$T = cDF \quad (5.1)$$

Where T, c, D and F are torque, coefficient of friction constant, nominal bolt diameter and F is the bolt tension (axial load).



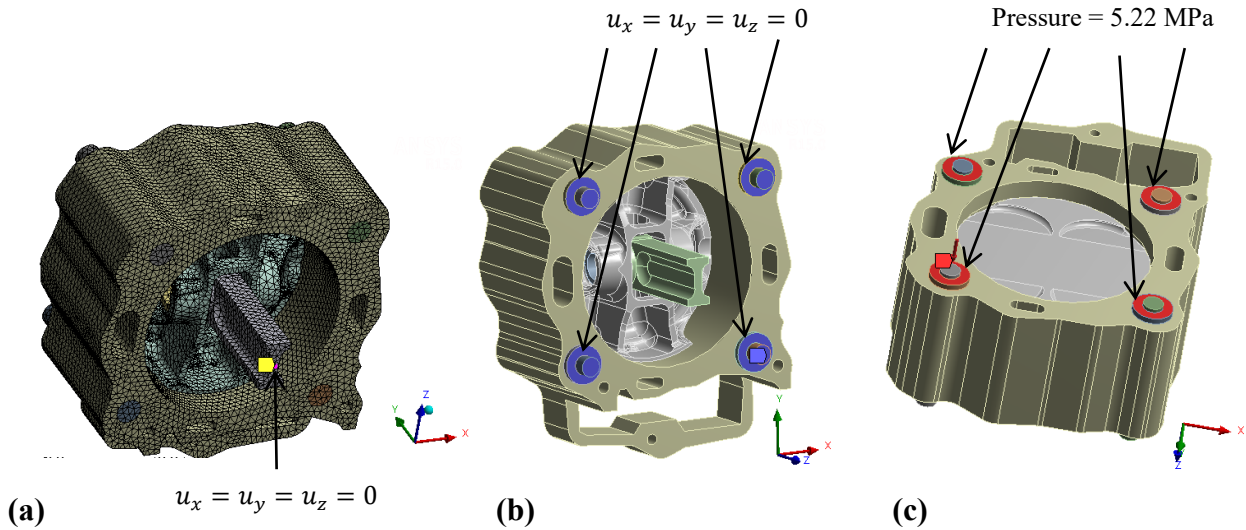


**Figure 5.5.** Application of the boundary conditions to FE model 2.

The contacts between piston-pin, pin-connecting-rod and piston-cylinder were specified as frictional contacts which required the friction coefficient values to be specified. Determining the real friction coefficient values between these contacts was practically difficult. Other researchers such as (Schneider, Halbhuber and Wachtmeister, 2016) had tried to determine these coefficients, giving values that change with the engine speed. A constant value of 0.01 is used in this work which is also used in literature (Carvalho and Gonçalves, 2006).

Contact solutions were very complicated and it was recommended by (AnsysWorkbench, 2018) to employ programme controlled settings whenever possible. As physical contacting bodies do not interpenetrate and to prevent them from passing through each other in the analysis, Ansys provided several contact formulations when frictional contact was selected. The default contact formulation was **Pure Penalty** which was used in this work too. However, (TrainingManual, 2005) also suggested to use **Augmented** or **Normal Lagrange** with frictional contact modelling. The suggested contact formulations were implemented to see the impact on the FEA results (Table 5.13). Furthermore, there were gaps present between the different contacting components which were due to the manufacturing and

operational requirements of these components. The components might indicate rigid body motion during the analysis when loaded and to prevent this from happening, Ansys Workbench<sup>TM</sup> offered 3 contact interface treatment options (AnsysWorkbench, 2018), but the ones applicable to this work were **Add offset Ramped Effects** and **Add offset No Ramping**. These required the offset values/gaps between the piston-pin (0.01 mm), pin-con-rod (0.01 mm) and piston-cylinder (0.04 mm). Both options were modelled in this work, but the latter was selected because it produced higher stress and it is also the default option (Table 5.10).

The contacts between the cylinder-mounting studs, mounting studs-washers and washer-cylinder were assumed to be bonded (Figure 5.6), since there was no movement and bonded contacts reduced the simulation solving time.

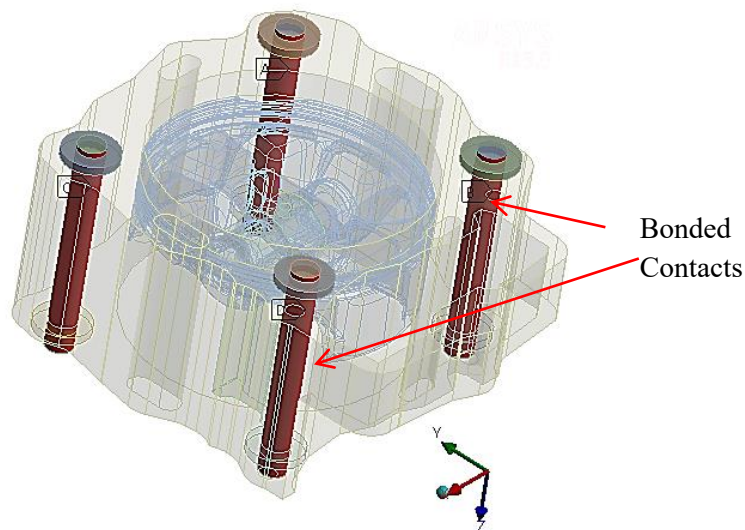


**Figure 5.6.** Contacts between the cylinder-mounting studs, cylinder and washers.

### 5.3.2. Scope of the piston FEA and assumptions

The aim of the FEA in this research was to select a realistic FE model to enable piston redesign for mass reduction using the newly developed aluminium alloy. The piston operational environment is very complex; hence some assumptions were made during the FEA modelling. The following assumptions can be made:

1. The pressure from the combustion was uniform on the entire piston crown and the cylinder.
2. The heat transfer from the combustion to the piston and the cylinder was uniform.
3. The effect of piston motion on the heat transfer was neglected.
4. The compression ring did not twist due the combustion pressure and motion of the piston; hence there was no need to include them in the analysis.
5. The rings and the skirt surfaces were fully covered by oil and there was no cavitation.
6. The cyclic thermal fluctuations on the very top of the piston crown due to combustion in each engine cycle were ignored.
7. The coolant oil and water temperatures were uniform.
8. The densities of the materials did not change with temperature.
9. The values of the frictional contact coefficients were considered constant and did not change with engine speeds.

### 5.3.3. Reverse engineering of the current piston

A geometrical 3D model (Figure 5.7) of the piston was reversed engineered based on the actual KTM piston which was scanned using a three dimensional (3D) laser scanner.

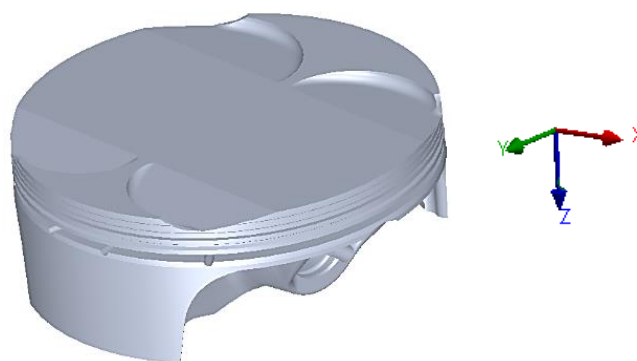


**Figure 5.7.** A reverse engineered CAD model of the test engine's piston.

The other components such as pin, cylinder and connecting rod were reversed engineered by measuring the actual components and some dimensions were obtained from the engine

manual. The engineering drawings of the different components used in the FE models are given in Appendix B.3.

#### 5.3.4. Required material properties for piston FEA

The different parts included in the piston FEA were made from different materials. The KTM piston for the test engine was made of Al-2618 which is widely used alloy for high performance engines such as in motorbikes. The properties used in the FEA are given in Table 5.1. The material properties of the new alloy RSA-612-T6 used for Piston FEA are also given in the same table. Some of these values were obtained from testing while others were provided by the manufacturer (RSP Technology).

Property		Al-2618-T6	RSA-612-T6
Density, $\rho$ ( $\frac{Kg}{m^3}$ )		2760	2550
Poisson Ratio, $\nu$		0.33	0.33
Thermal Conductivity, $k$ (W/m°C)		146	130
	Temperature (°C)		
Young's Modulus, $E$ (GPa)	25	74	85
	100	72	82.5
	150	70	81
	200	68	79
	250	65	77.5
	300	61	75
	350	51	72.5
Ultimate Tensile Strength, $\sigma_u$ (MPa)	25	441	424
	100	427	412.5
	150	345	394
	200	221	290
	250	90	117
	300	52	49
	350	34	28.5
Yield Strength, $\sigma_y$ (MPa)	25	372	409
	100	372	391
	150	303	381
	200	179	279
	250	62	113
	300	31	48
	350	24	26
Coefficient of Thermal Expansion, CTE ( $\mu m/m.K$ )	25	20.6	18
	100	22.3	19.5
	200	23.2	20.2
	300	24.1	21

**Table 5.1.** Mechanical properties of the two piston alloys.

The mechanical properties and some further information about the different material used for the various components in the piston FEA are given in Appendix B.4.

#### 5.4. Determination and application of engine loads on piston

The test engine used was a motorbike engine (KTM 450 XCF 2008) and the load calculations required some engine parameters, which are given in Table 5.2 below.

Engine Type	Single cylinder, 4-stroke
Total Displacement/Volume ( $V_t$ , cc)	449.30
Bore (B, mm)	97
Stroke (S, mm)	60.8
Compression Ratio ( $r_c$ )	12.5:1
Connecting Rod Length (l, mm)	107.40

**Table 5.2.** The test engine specification (KTM 450 XCF 2008).

The different engine loads on piston and their application in the FEA are given in the following sections.

##### 5.4.1. Consideration of mechanical loads

The engine was tested on a dynamometer in its original configuration to obtain the baseline engine performance parameters such as the in-cylinder pressure, fuel consumption, air fuel ratio etc. The in-cylinder pressure sensor used was a spark plug integrated sensor from Optrand which measured the combustion pressure (Section 6.4.9 and Figure 6.11). The different mechanical loads acting on the piston are depicted in the following Figure 5.8.

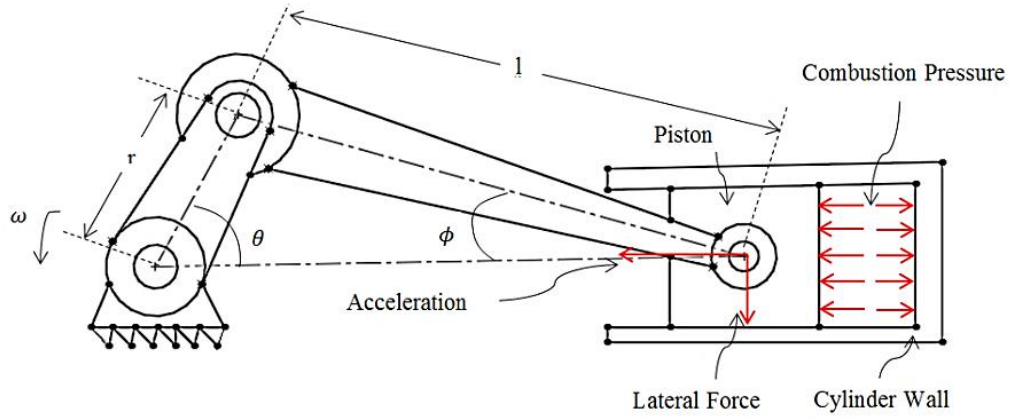


**Figure 5.8.** A representation of the crank slider mechanism and the piston mechanical loads.

where  $r$ ,  $\omega$ ,  $\theta$ ,  $\phi$  and  $l$  are crank offset or crank radius (m), crank angular velocity (rad/sec), crank angle (rad), angle that the connecting rod makes with the cylinder axis and the connecting rod length (m) respectively.

#### 5.4.1.1. Combustion pressure

The in-cylinder pressure traces obtained from the engine testing in Section 6.7 and their application to the FE models are illustrated in Figures 5.9 and 5.10 respectively. The pressure values were measured directly from the cylinder using spark mounted in-cylinder pressure sensor (Section 6.4.9) and the crank angle was determined using encoder (Section 6.4.7).

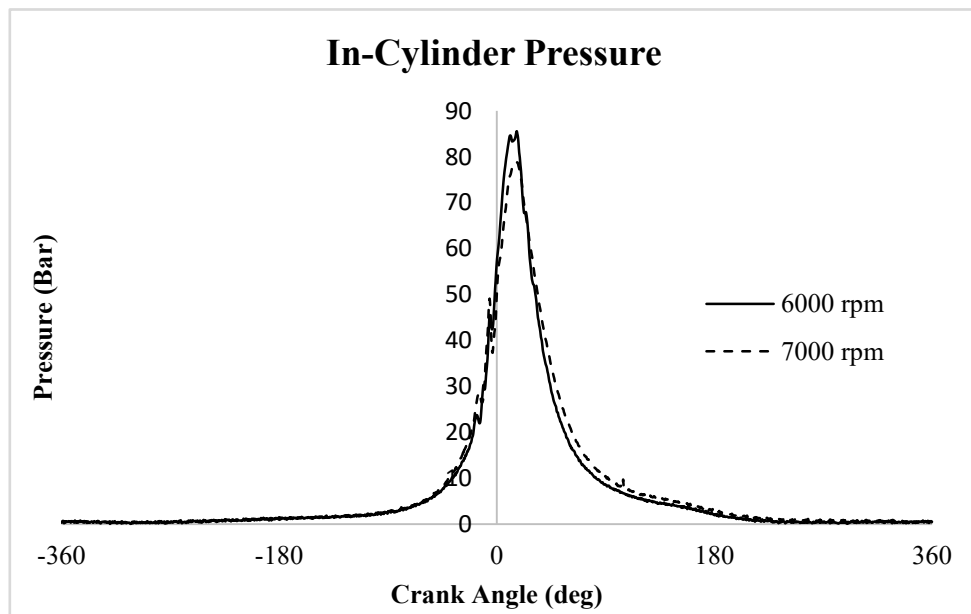


**Figure 5.9.** The in-cylinder pressure traces of the test engine at different engine speeds.

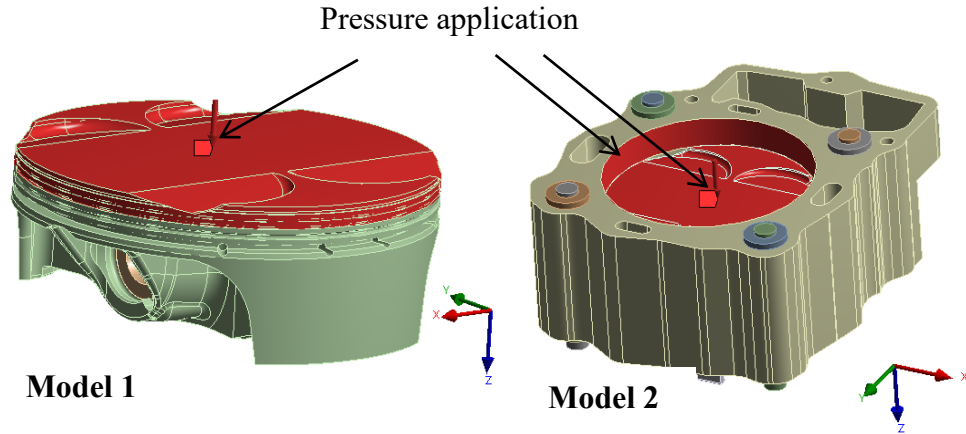


**Figure 5.10.** Application of in-cylinder pressure to the FE models 1 and 2.

#### 5.4.1.2. Inertial force/acceleration

Using the equations provided in Section 2.9.1.2, the piston accelerations were calculated for the different engine speeds and the results are shown in the plots in Figure 5.11. The application of the acceleration to the FE models is illustrated in Figure 5.12.

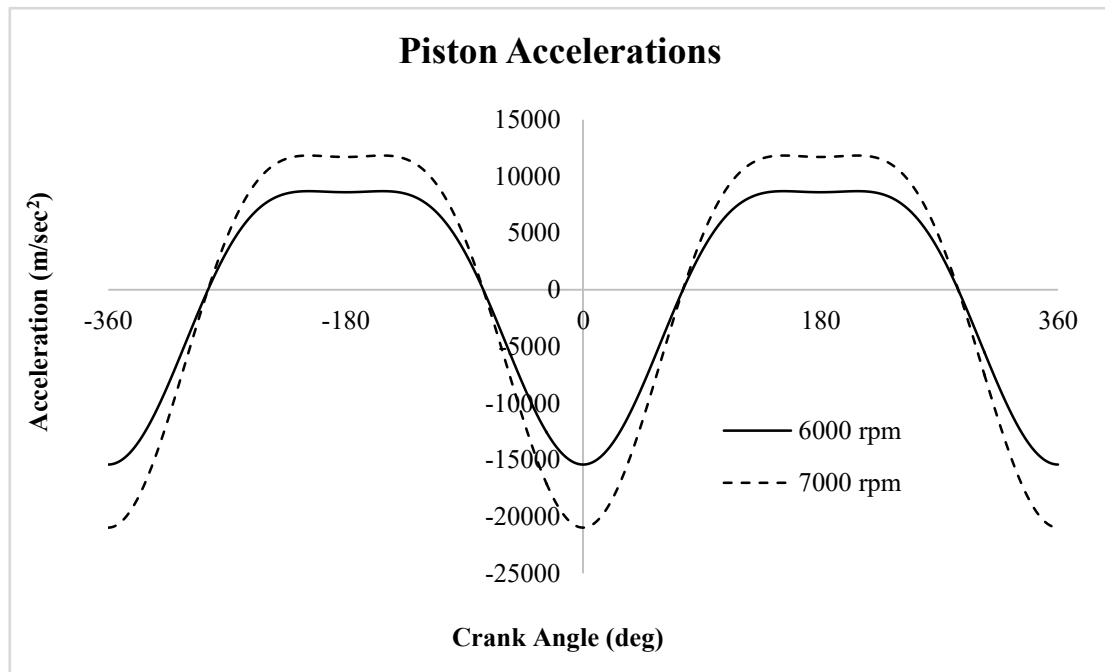


**Figure 5.11.** Piston accelerations of the test engine at different engine speeds.

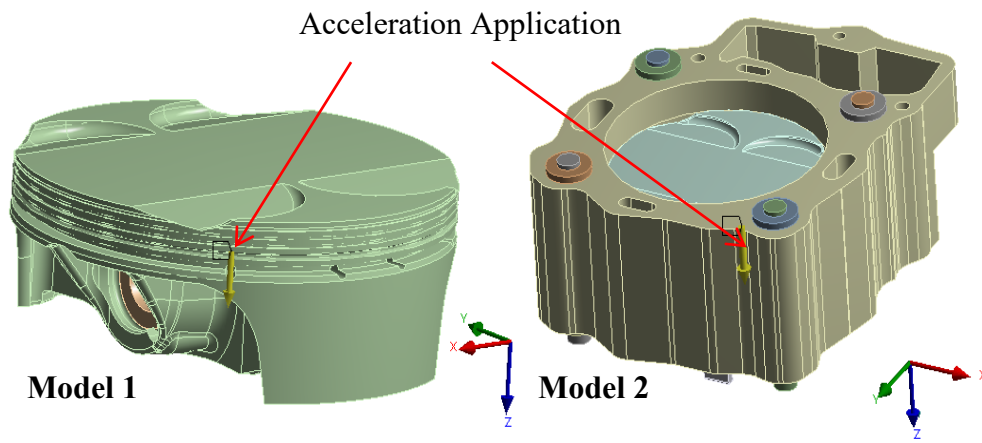


**Figure 5.12.** Application of the acceleration to FE models 1 and 2.

#### 5.4.1.3. *Lateral force*

The lateral forces for the different engine speeds were calculated using equation (2.3) in Section 2.9.1.3; the results and their application to the FE models are illustrated in Figures 5.13 and 5.14 respectively. The calculation required the masses of the reciprocating components which are given in the following Table 5.3.

Component Name	Mass (g)
Piston	268.59
Pin	68.98
<u>Circlip</u>	0.84
Compression Ring	4.74
Oil Ring	6.44
Connecting Rod Small End	105.73
<b>Total</b>	<b>455.32</b>

**Table 5.3.** Reciprocating components masses.



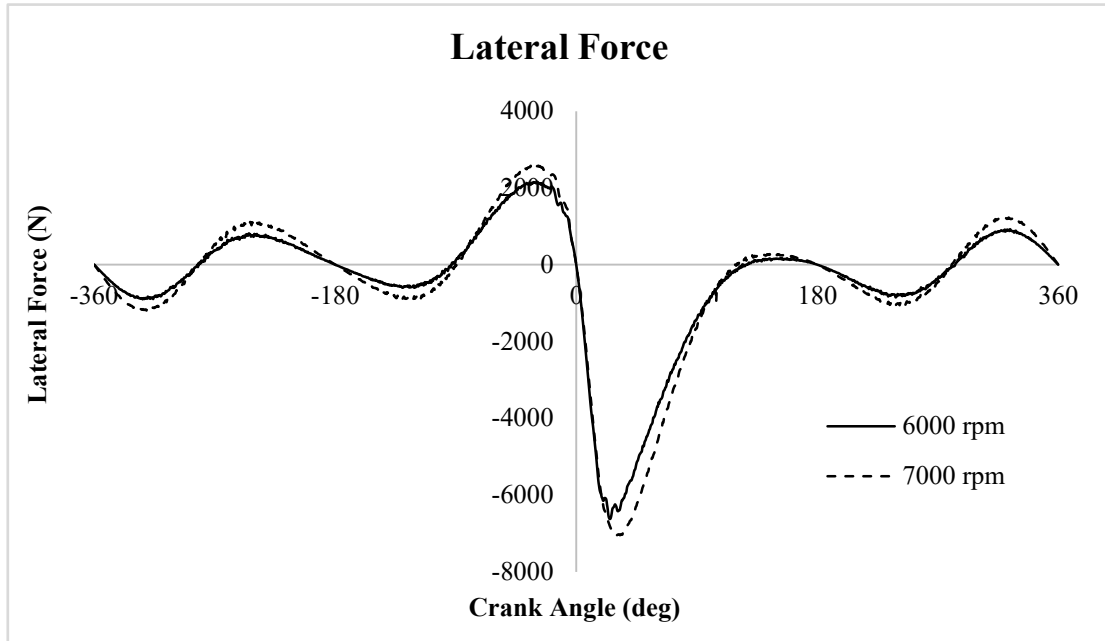


**Figure 5.13.** Lateral forces of the test engine at different engine speeds.

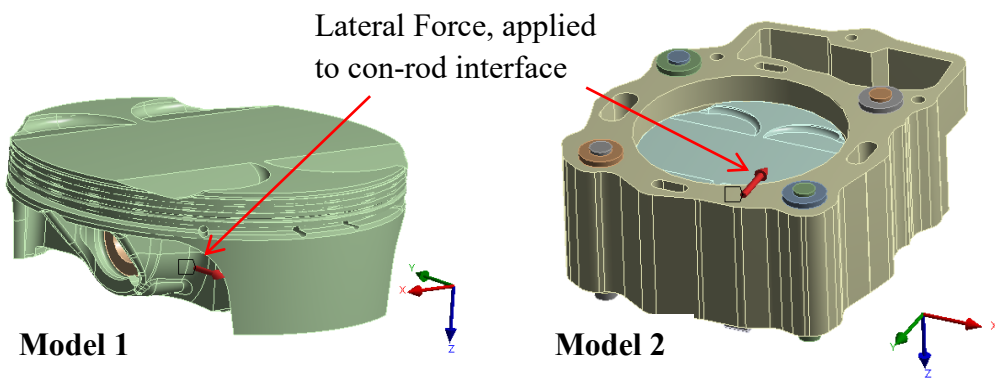


**Figure 5.14.** Application of the lateral forces to FE models 1 and 2.

#### 5.4.2. Consideration of thermal loads

Having used equations (2.6–2.10) to determine the combustion gas temperature the heat transfer between the piston and its surroundings was evaluated. The theoretical instantaneous gas temperature results over the whole engine cycle for the two different engines speeds are given in Appendix B.5. Sections 5.4.2.1 to 5.4.2.5 explore the different areas of the piston where the heat transfer takes place. The engine cooling oil properties and other relevant data, which were needed to determine the heat transfer coefficients at different piston regions, are given in Table 5.4.

Property	Value
Density ( $\frac{Kg}{m^3}$ )	848
Dynamic Viscosity (kg/ m sec)	0.025
Thermal Conductivity (W/m.K)	0.137
Specific Heat Capacity kJ/(Kg.K)	2160
Engine Lubrication	10W50
Engine Oil Temperature (°C)	100
Lubricating Oil Film (Piston-cylinder gap) ( $\mu m$ )	61

**Table 5.4.** Engine cooling oil properties and other relevant data (Thermal-FluidsCentral, 2011)

The heat transfer coefficient evaluations at different piston regions are given in the following sections.

#### **5.4.2.1. Heat transfer between the combustion gas and piston crown**

The instantaneous heat transfer coefficient between the combustion gas temperature and the piston crown was determined using equation (2.11) and the results are given in Appendix B.5. The quasi-static temperature analysis carried out in this work needed the mean heat transfer coefficient ( $h_m$ ) and the mean gas temperature ( $T_m$ ) which were obtained using equations 2.13 and 2.14 (Table 5.5). The application of the gas heat transfer coefficient to the piston and the cylinder for the two FE models is illustrated in Figure 5.15.

Property	Engine Speed (rpm)	
	6000	7000
Mean Gas Heat Transfer Coefficient (W/m <sup>2</sup> .K)	475	580
Mean Gas Temperature (K)	1285	1177

**Table 5.5.** Mean gas heat transfer coefficient and temperature values for two different engine speeds.

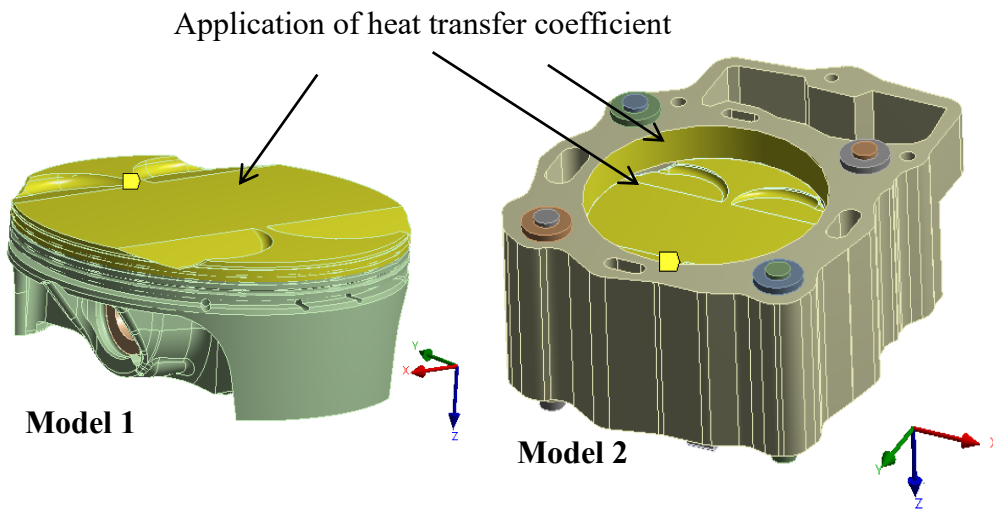


**Figure 5.15.** Application of gas heat transfer coefficient to the piston crown and cylinder in FE models 1 and 2.

#### 5.4.2.2. Compression ring heat transfer coefficient

It was stated in Section 2.9.2.2 that determining the real heat transfer coefficients for the compression ring was complicated and beyond the scope of this work. The values were therefore taken from literature (Mizuno *et al.*, 2009) and stated in Table 5.6. The heat transfer coefficients for the upper and lower faces of the compression ring were different as indicated in Table 5.6 and their application to the piston is illustrated in Figure 5.16.

Property	Compression Ring Faces	
	Upper Face	Lower Face
Heat Transfer Coefficient ( $\text{W/m}^2\cdot\text{K}$ )	885	1818
Temperature (K)	433	433

**Table 5.6.** Heat transfer coefficient values of the compressing ring (Mizuno *et al.*, 2009).

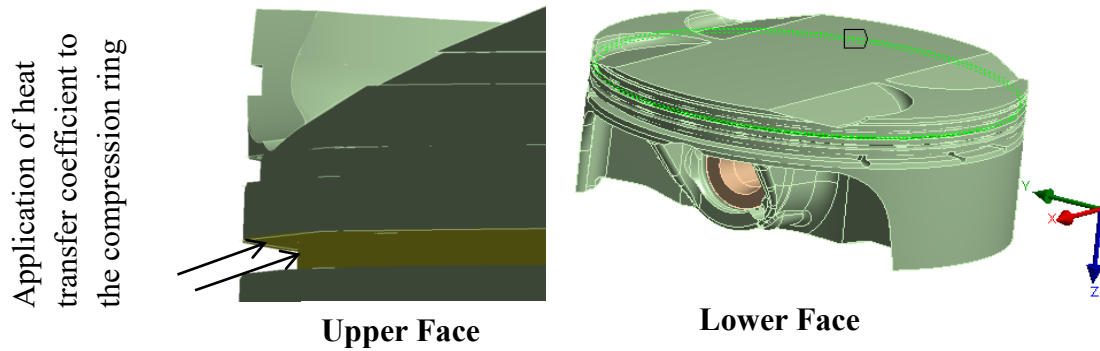


**Figure 5.16.** Application of the heat transfer coefficients to the compression ring in the FE models 1 and 2.

#### 5.4.2.3. Heat transfer between ring lands and piston outer skirt and the cooling oil

The heat transfer coefficient (HTC) between the ring lands, the piston outer skirt and the cooling oil was calculated using equations (2.16–2.17) and the results are given in Table 5.7. In both FE models, the HTC was applied to all the outer surfaces of the piston below the compression ring as indicated in Figure 5.17. Note that defining the HTC required the engine oil temperature which depended on many factors. This information is not specified by the manufacturer in the engine manual. However, it was suggested by (Turner, 2018) that the average engine oil temperature for the engine considered is 100 °C (Table 5.4).

Property	Engine Speed (rpm)
	6000 and 7000
Heat Transfer Coefficient (W/m <sup>2</sup> .K)	4624
Temperature (K)	373

**Table 5.7.** Heat transfer coefficient values of the ring lands and outer piston skirt.

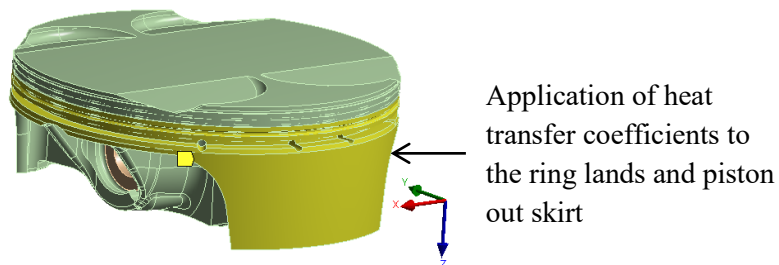


**Figure 5.17.** Application of the heat transfer coefficients to the ring lands and piston outer skirt in the FE models 1 and 2.

#### 5.4.2.4. Heat transfer between the piston under-crown and inner walls of the piston skirt and the cooling oil

The heat transfer coefficient between the piston under-crown and the inner walls of the piston skirt was calculated using equations (2.21–2.22) and the results are given in Table 5.8. The application of the heat transfer coefficients to models 1 and 2 can be seen in Figure 5.18.

Property	Engine Speed (RPM)	
	6000	7000
Heat Transfer Coefficient ( $\text{W/m}^2\cdot\text{K}$ )	1705	1929
Ambient Temperature (K)	373	373

**Table 5.8.** Heat transfer coefficient values of the piston under-crown and the inner walls of the piston skirt.

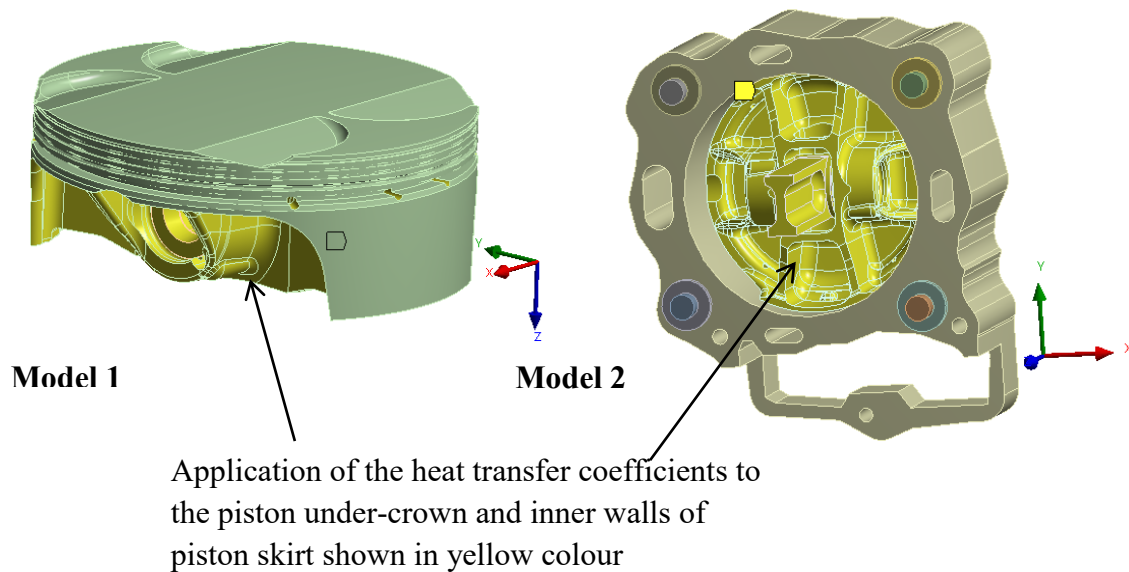


**Figure 5.18.** Application of the heat transfer coefficients to the piston under-crown and inner walls of piston skirt in the FE models 1 and 2.

#### 5.4.2.5. Cooling jacket heat transfer coefficient

It was stated in Section 2.2.2.5 that the heat transfer coefficient of the combustion engine cooling jacket was determined experimentally and it was beyond the scope of this work. The

value used in this work was therefore taken from literature (Esfahanian, Javaheri and Ghaffarpour, 2006) as  $1480 \text{ (W/m}^2\text{K)}$  for spark ignition engines similar to the engine considered in this project. The average water temperature was taken to be  $373 \text{ K}$  or  $100 \text{ }^\circ\text{C}$  (Turner, 2018). The application of the heat transfer coefficient to the cooling jacket can be seen in Figure 5.19.

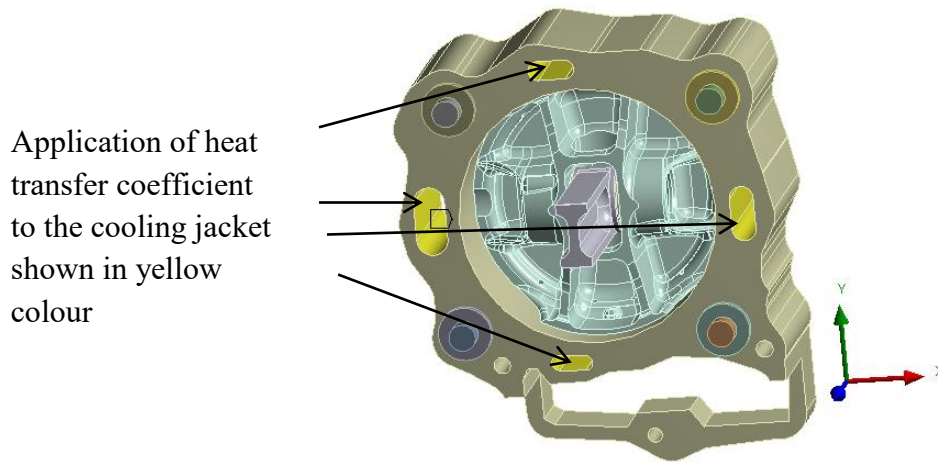


**Figure 5.19.** Application of the heat transfer coefficient to the cooling jacket in FE model 2.

## 5.5. FEA results of the baseline piston

The results presented in this section were based on the critical load condition highlighted in Section 5.5.1. Results are presented for piston temperature distribution (Section 5.5.2.2), maximum principal stress (Section 5.5.2.3), plastic strain (Section 5.5.2.4) and deformation (Section 5.5.2.5). These values were significant factors in piston design analysis. A mesh convergence analysis was carried out which indicated that convergence occurred at an element size of  $3.5 \text{ mm}$  (Figures 5.20–5.21). The directional Cartesian axes used for the analyses aligned with the pin longitudinal direction (X), radial to the pin longitudinal direction (Y) and the notional direction of the piston motion (Z), as shown in Figures 5.2 and 5.3 (page 70).

### 5.5.1. Critical load cases

It can be deduced from Figures 5.9, 5.11 and 5.13 that the maximum values for different mechanical loads occurred at different angular positions of the crankshaft. In order to avoid neglecting any combination of these forces that might be critical, a number of appropriately selected points in time were analysed as suggested by Mahle (2016). These included the points at which the individual mechanical loads reached a maximum. This gave three load cases in a given engine speed and engine cycle which were the points of maximum combustion pressure, maximum inertial and maximum lateral forces. The maximum combustion pressure for the engine operating envelope occurred at 6000 rpm and the maximum acceleration occurred at 7000 rpm. The acceleration produced flexure against the combustion pressure at the point of maximum pressure during an engine cycle and acted along the pressure direction during the compression stroke just before the piston reached the top dead centre. So in total 4 critical loaded cases were present, these loading conditions were modelled and the results are given in Table 5.14 (page 91).

The maximum combustion pressure load case that occurs at a crank angle of  $16.5^\circ$  after the top dead centre (TDC) for the analysed engine speed of 6000 rpm, turned out to be the most critical. The results presented in this work therefore focused on this load case. The mechanical load values for the maximum combustion pressure load case at 6000 rpm are given in Table 5.9.

Load	Value
Pressure (bar)	85.5
Acceleration ( $\text{m/sec}^2$ )	14356
Lateral Force (N)	5626

**Table 5.9.** Mechanical load values in the maximum combustion load case at 6000 rpm.

### 5.5.2. Results

As indicated in Section 5.3.1 Ansys Workbench<sup>TM</sup> provided different contact formulations and interface treatments for consideration of the piston modelling. While for the contact formulation Ansys Workbench<sup>TM</sup> recommended the use of programme controlled option whenever possible, but for the contact interface it did not make any recommendations. To establish a starting point for the FEA, programmed controlled (**Pure Penalty**) contact formulation was selected with the interface treatment of **Add offset Ramped Effects** and **Add offset No Ramping**. The offset values used are given in Section 5.3.1. Furthermore, the gaps or offset values were also doubled to assess the sensitivity of the model to offset variation. The stress results for mesh size of 5 mm and the interface treatment and offset results are given in Table 5.10.

The maximum principal stresses were assessed at critical locations that caused thermo-mechanical fatigue failures in pistons as reported by (Silva, 2006; Floweday *et al.*, 2011; M, Sanjay and Mandloi, 2016). The most critical location was the crown area located on the same vertical plane that contained the pin hole (encircled in red in Figure 5.26). The thermo-mechanical fatigue crack originates on the crown and travels towards the high stress region in the pin hole (encircled in red in Figure 5.27). The stress in the pin hole was therefore also assessed.

<b>Interface Treatment and Offsets</b>	<b>Crown Stress (MPa)</b>		<b>Pin Hole Stress (MPa)</b>	
	<b>Model 1</b>	<b>Model 2</b>	<b>Model 1</b>	<b>Model 2</b>
No Ramping, Actual Offset Values	131.12	130.18	233.81	260.97
Ramping, Actual Offset Values	127.93	122.60	229.29	267.70
No Ramping, Double Offset Values	125.64	119.24	231.80	286.24
Ramping, Double Offset Values	121.82	108.15	227.01	299.45

**Table 5.10.** Stress values in both FE models with various contact interface treatments.



It can be seen from the results in Table 5.10 that doubling the offset values had an impact on the stresses therefore the correct offset values were important. Furthermore, **No ramping with added offset** option which was the default option had higher stresses in the critical area (piston crown) than **with ramping effects**. No ramping option was selected as it was the default option and produced the highest stresses in the crown area in both FE. This will lead to a conservative design in terms of factor of safety. Once the interface treatment was selected, mesh convergence analyses were carried as highlighted the following section.

#### 5.5.2.1. Mesh convergence analyses

The mesh convergence analyses were carried out at the piston crown which was the most critical location due to the thermo-mechanical fatigue failure and the pin hole. The results are plotted in Figures 5.20 and 5.21 respectively. The results indicate that the mesh converged at an element size of 3.5 mm.

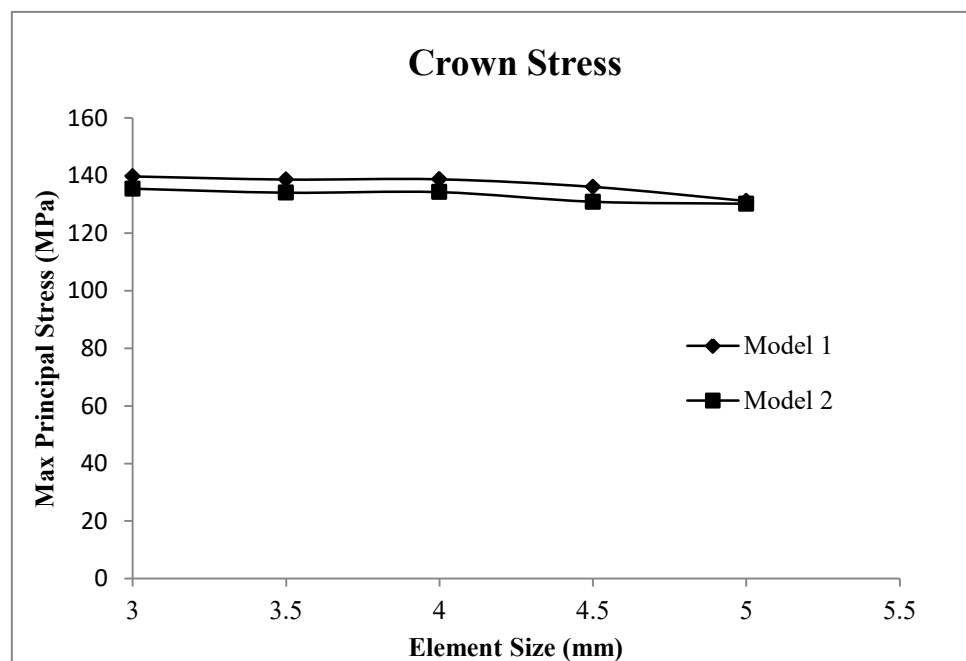


**Figure 5.20.** Mesh convergence analyses at crown for both FE models.

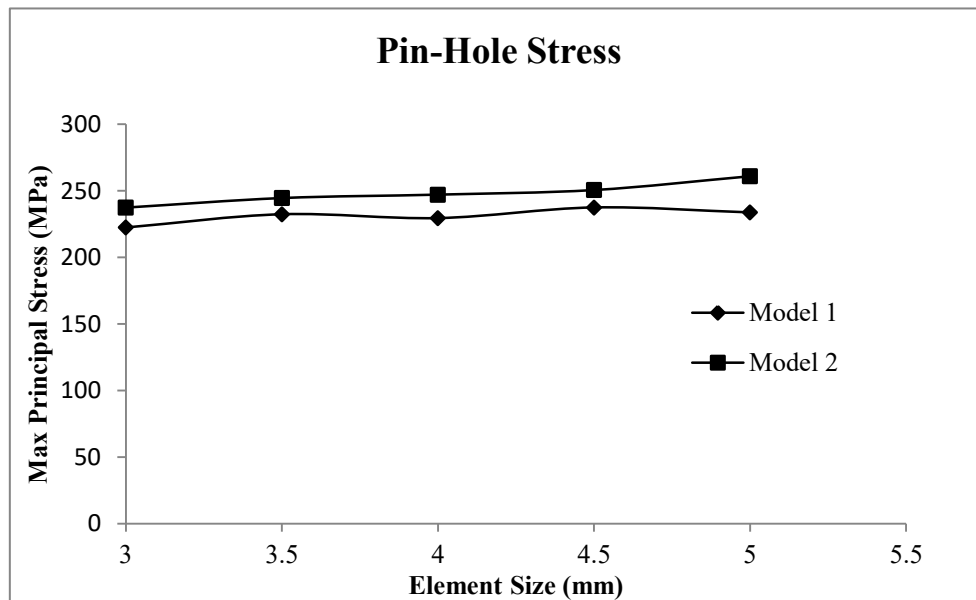


**Figure 5.21.** Mesh convergence analyses at the pin hole for both FE models.

Due to the presence of nonlinear contacts and nonlinear material properties, the simulation model took very long time to solve especially for the model 2. To reduce the solving time, the mesh size in the non-critical parts was increased. The non-critical parts were the connecting rod, the cylinder, the mounting studs and the washers. The mesh sizes used were 6 and 9 mm and the element size 6 mm gives the results closer to the originally converged element size of 3.5 mm. The results are given in Table 5.11.

Mesh Size (mm)	Crown Principal Stress (MPa)	Pin Hole Principal Stress (MPa)
3.5 (Original)	134	244.58
6	134.17	242.95
9	132.69	242.12

**Table 5.11.** Mesh convergence analyses results for the non-critical parts.

The mesh at the pin hole was further refined up to 3 times to assess its impact on stress and the results are given in Table 5.12. Refinement 2 was selected as it produced the highest stress in the piston crown which is the critical region.

Mesh Refinement	Crown Principal Stress (MPa)		Pin Hole Principal Stress (MPa)	
	Model 1	Model 2	Model 1	Model 2
1	137.54	132.52	233.03	249.48
2	136.49	131.27	249.40	258.62
3	136.62	131	252.44	262.93

**Table 5.12.** Mesh refinement at the pin hole for both FE models.

Once the mesh convergence and refinement analyses were carried out, the other two contact formulations highlighted in Section 5.3.1 were also analysed and the results are given in Table 5.13.

Contact Formulation	Crown Principal Stress (MPa)		Pin Hole Principal Stress (MPa)	
	Model 1	Model 2	Model 1	Model 2
Pure Penalty (Default)	136.49	131.27	249.40	258.62
Augmented Lagrange	136.56	131.10	249.40	258.62
Normal Lagrange	133.75	124.65	244.77	256.56

**Table 5.13.** Different contact formulations for both FE models.

**Pure Penalty** was selected as the stresses were higher than Normal Lagrange and virtually the same as Augmented Lagrange. This would lead to a more conservative design. It was also the default option suggested by Ansys Workbench<sup>TM</sup> (AnsysWorkbech, 2018). **Pure Penalty** is computationally inexpensive and less likely to over-constrain the formulation unlike Lagrange formulations. Over-constraining leads to incorrect stresses and deformation.

Once the FE model settings were established, all the four critical load cases described in Section 5.5.1 were simulated and the results are given in Table 5.14.

Critical Load Cases	Crown Principal Stress (MPa)		Pin Hole Principal Stress (MPa)	
	Model 1	Model 2	Model 1	Model 2
Maximum pressure point at 6000 rpm	136.49	131.27	249.4	258.62
Maximum acceleration point at 6000 rpm	107.17	101.18	196.13	203.28
Maximum lateral force point at 6000 rpm	104.22	101.02	189.54	204.65
Maximum acceleration point at 7000 rpm	98.95	93.73	180.49	186.84

**Table 5.14.** Piston stresses in critical areas for the critical load cases.

It can be seen from the results in Table 5.14 that the maximum combustion load case at 6000 rpm caused the highest principal stress. To ensure that the no other points caused higher stresses, other points at 6000 rpm were also analysed for Model 2 and the results are given in Figures 5.22–5.23.

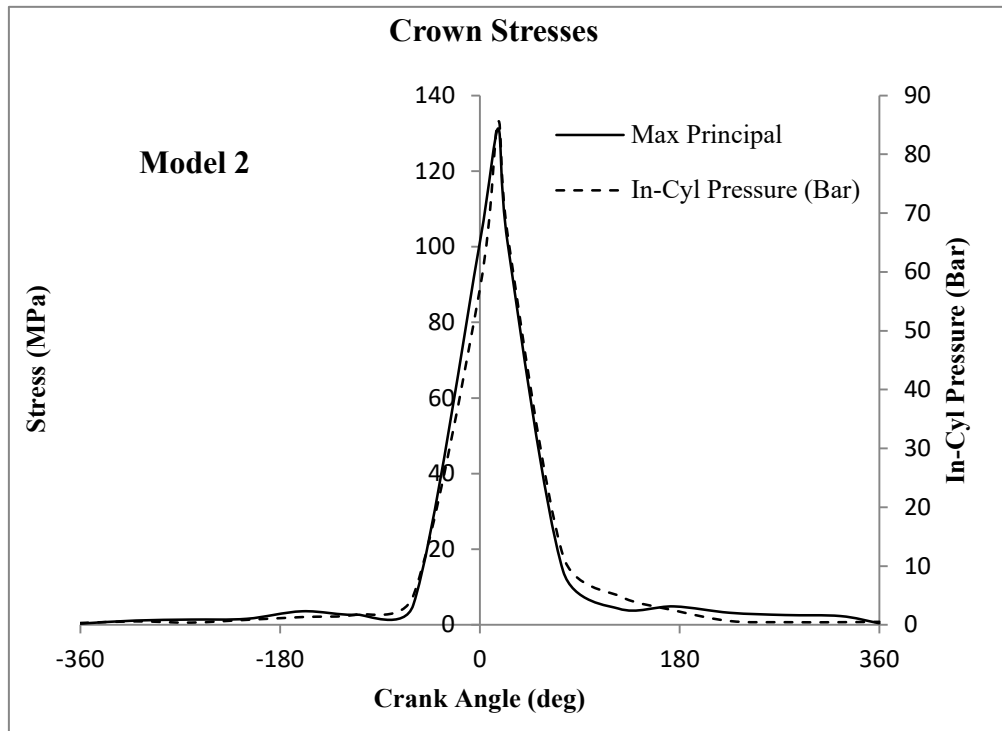


**Figure 5.22.** Maximum principal stresses in piston crown over an entire engine cycle at 6000 rpm in Model 2.

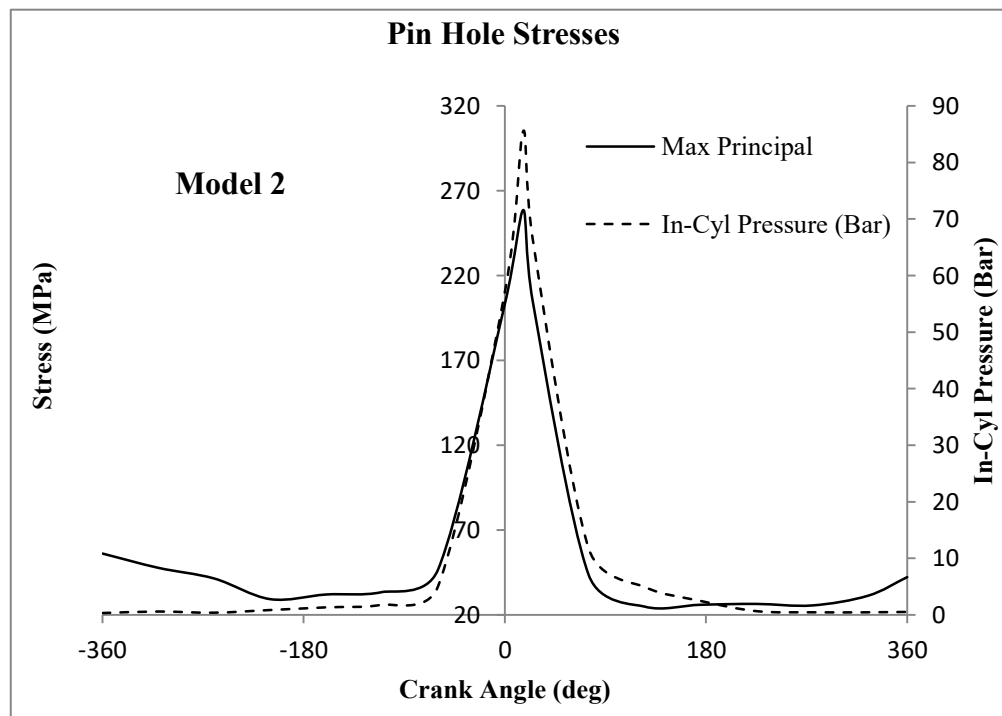


**Figure 5.23.** Maximum principal stresses in piston pin hole over an entire engine cycle at 6000 rpm in Model 2.

The detailed results for the maximum combustion pressure load case that occurred at 6000 rpm are given below.

### 5.5.2.2. Temperature distribution in Piston

Thermo-mechanical analysis was carried out on the two models using the mechanical loads and heat transfer coefficients determined in Sections 5.4.1 and 5.4.2 respectively. The quasi-static temperature distribution of the piston for both FE models can be seen in Figure 5.24 while the temperature distribution in the cylinder is given in Figure 5.25.

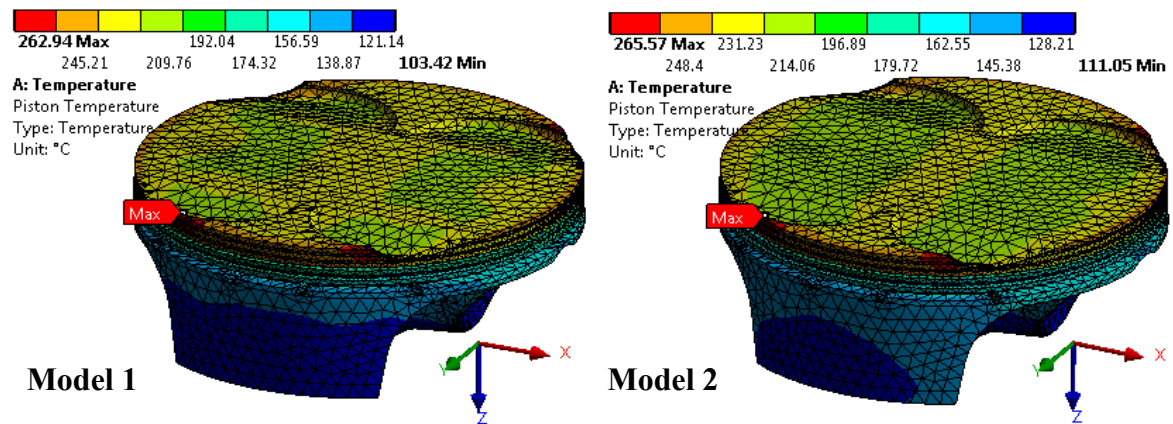
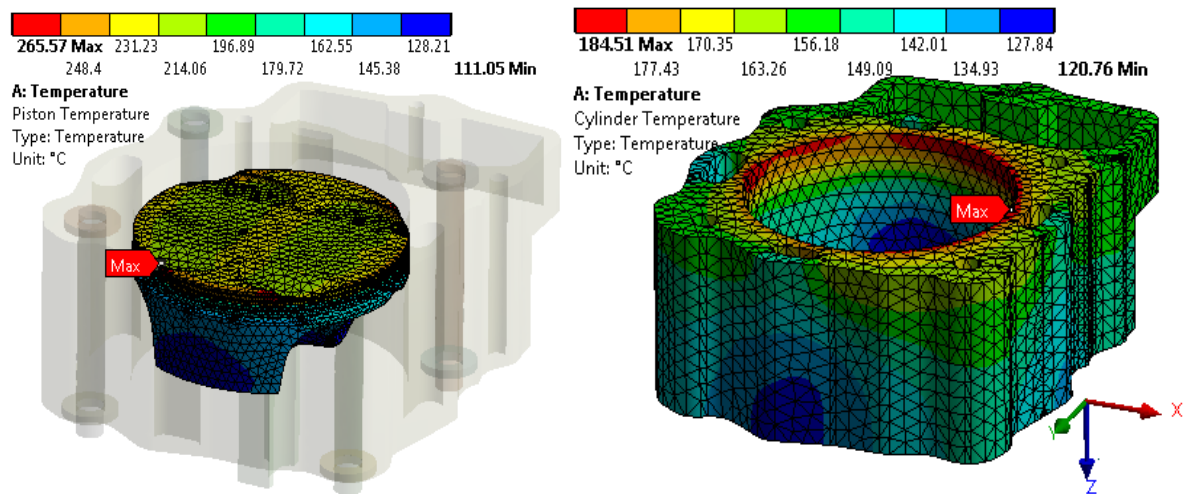


Figure 5.24. Piston temperature distributions in both FE models.



The temperature distribution results showed that the maximum temperature in model 1 was approximately 3 degrees lower than model 2 and for both models the maximum temperature

occurred at the locations (valve pocket edges) that were the furthest from any cooling surfaces.

### 5.5.2.3. Maximum principal stress distribution in piston

Majority of the pistons produced are heat treated to T6 condition which reduces the ductility from the as manufactured component. Reduced ductility combined with the stress concentrations at the pin hole and web-boss interface may cause the piston to fail in brittle manner as described by (Floweday *et al.*, 2011). Brittle failure or fracture is associated with no visual or macroscale plastic deformation of a material (Becker, 2002). It was therefore deemed important to investigate the maximum principal stresses in the pistons which were probed at the same locations as mentioned in Section 5.5.2. The results of the principal stresses are shown in Figures 5.26 and 5.27 for models 1 and 2 respectively. The stresses in model 1 were approximately 4% higher, but 3.6% lower than model 2 at the crown and the pin hole locations respectively.

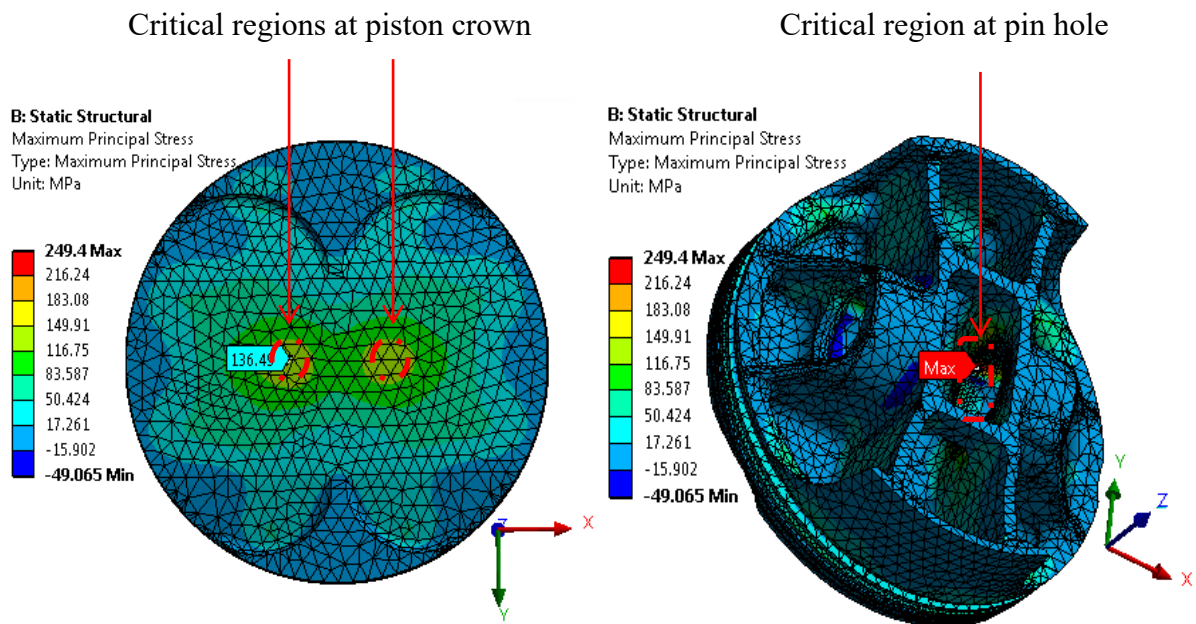


**Figure 5.26.** Maximum principal stresses in piston in model 1.

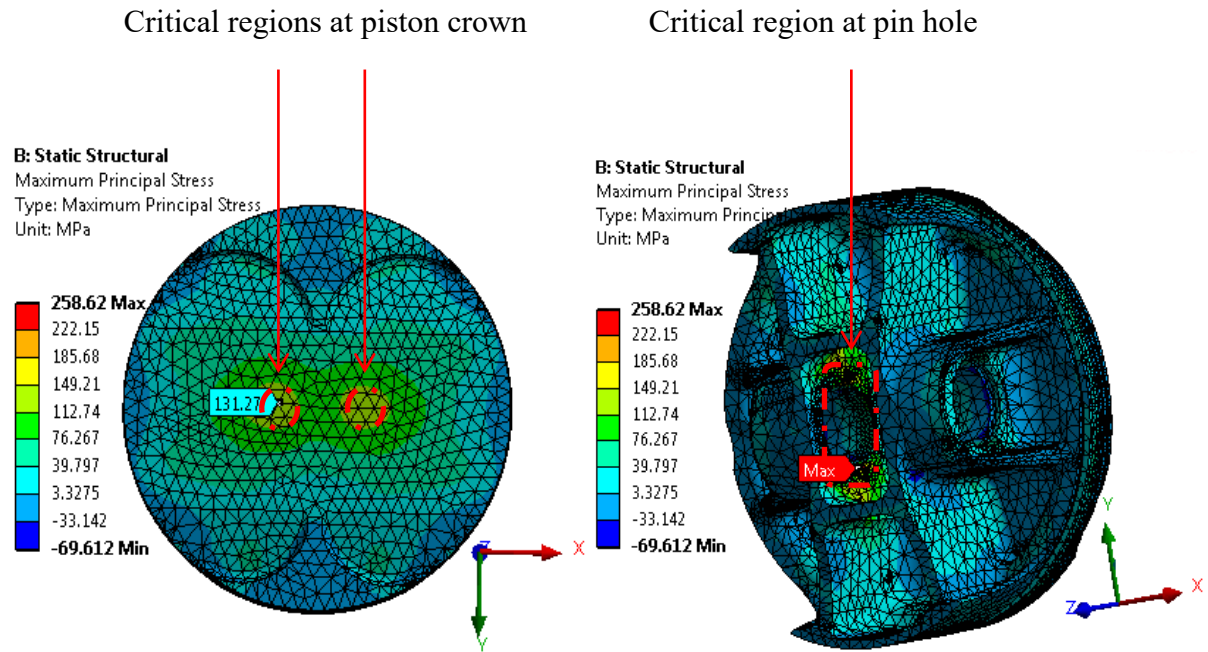


**Figure 5.27.** Maximum principal stresses in piston in model 2.

#### 5.5.2.4. Plastic strain distribution in piston

The plastic strains were also assessed to see if any plastic deformation occurred under the piston operating conditions. As indicated in Figures 5.28 and 5.29 no plastic deformations occurred at the pistons' crowns in the critical regions.

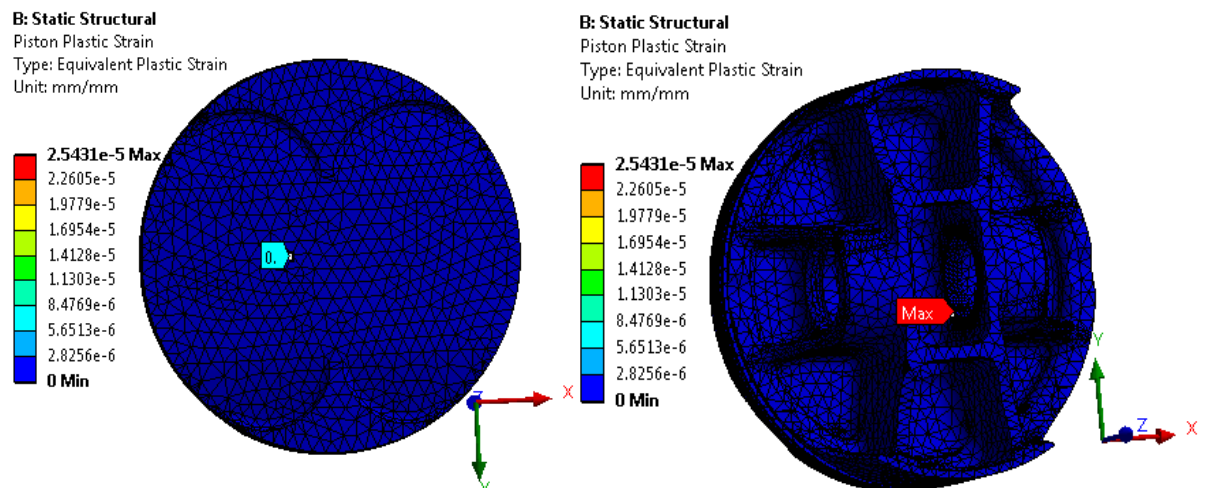


**Figure 5.28.** Plastic strain in piston in model 1.



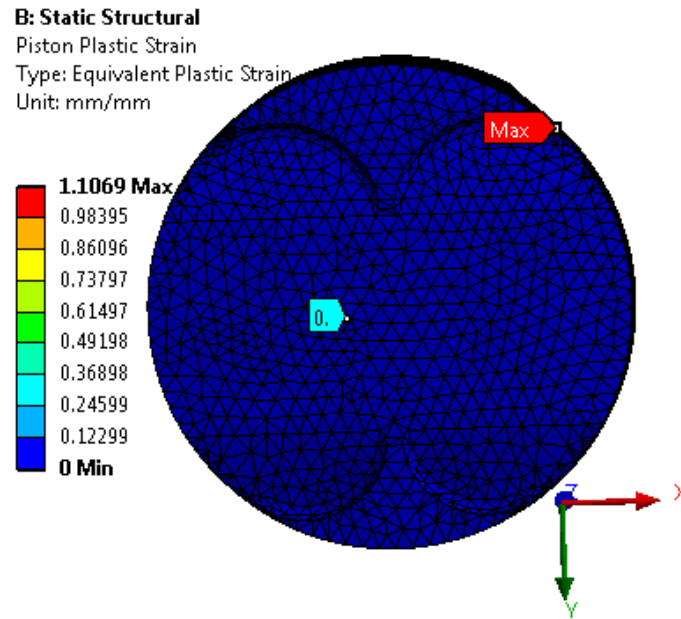


**Figure 5.29.** Plastic strain in piston in model 2.

From the results it can be seen that model 1 gave higher stresses than model 2 at the piston crown and would therefore be more conservative in terms of piston design. Depending on how critical piston mass reduction is in terms of the engine design, model 1 or 2 might be selected based on the stresses only. It is important to state that stress is not the only criterion that needs to be considered when designing pistons. The deformation that the piston undergoes during engine operation governs the piston cold mounting clearance values and must also be taken into account (Mahle, 2016). The results for the piston deformations are given in the following section.

#### **5.5.2.5. Piston directional deformations**

The directional deformations of the piston are illustrated in Figures 5.30–5.36. All the piston directional deformations were taken relative to piston crown centre on the top surface. The red dashed lines on the plots represent the positions along which measurements were made.

The piston deformations in the X directions for both models are shown in Figure 5.30, measured along the dashed line shown in Figure 5.31, with the respective piston displacement plots shown in Figure 5.31.

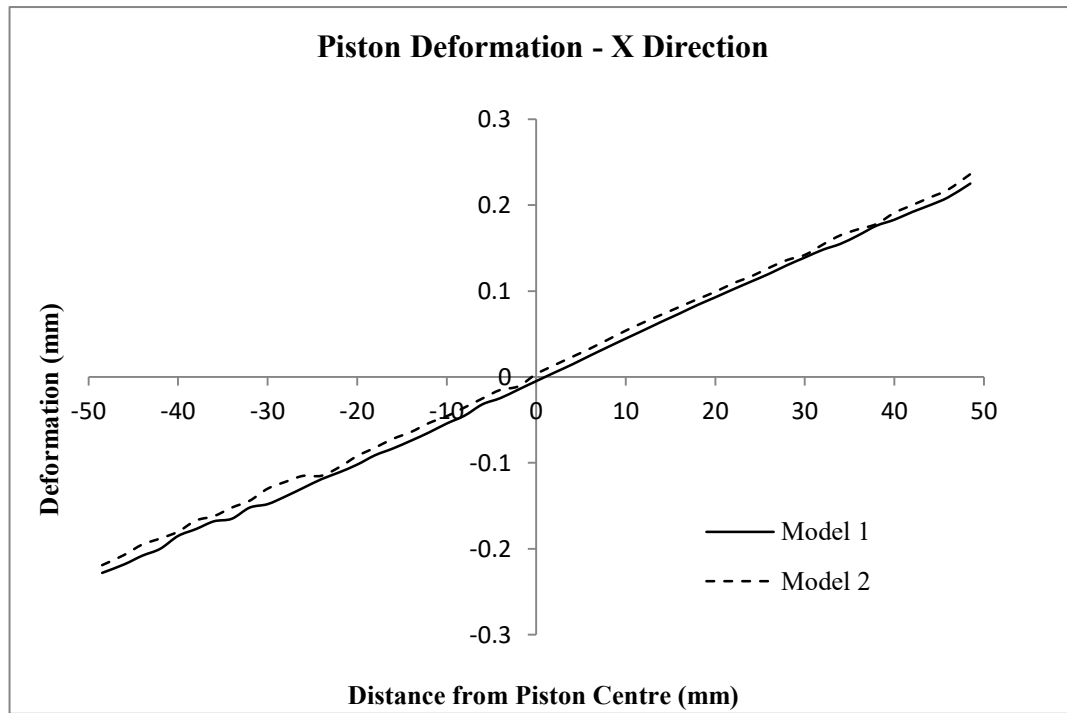


**Figure 5.30.** Piston deformation graphs in X directions for both FE models.

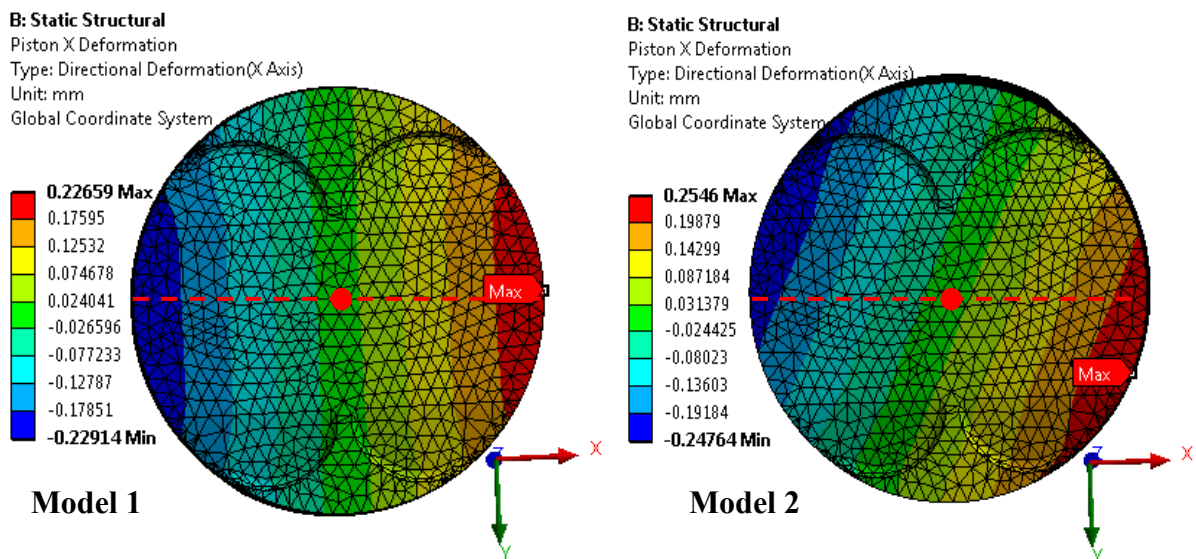


**Figure 5.31.** Piston deformation plots in X directions for both FE models.

The piston deformations in the Y directions for both models are shown in Figure 5.32, measured along the dashed line shown in Figure 5.33, with the respective piston displacement plots shown in Figure 5.33.

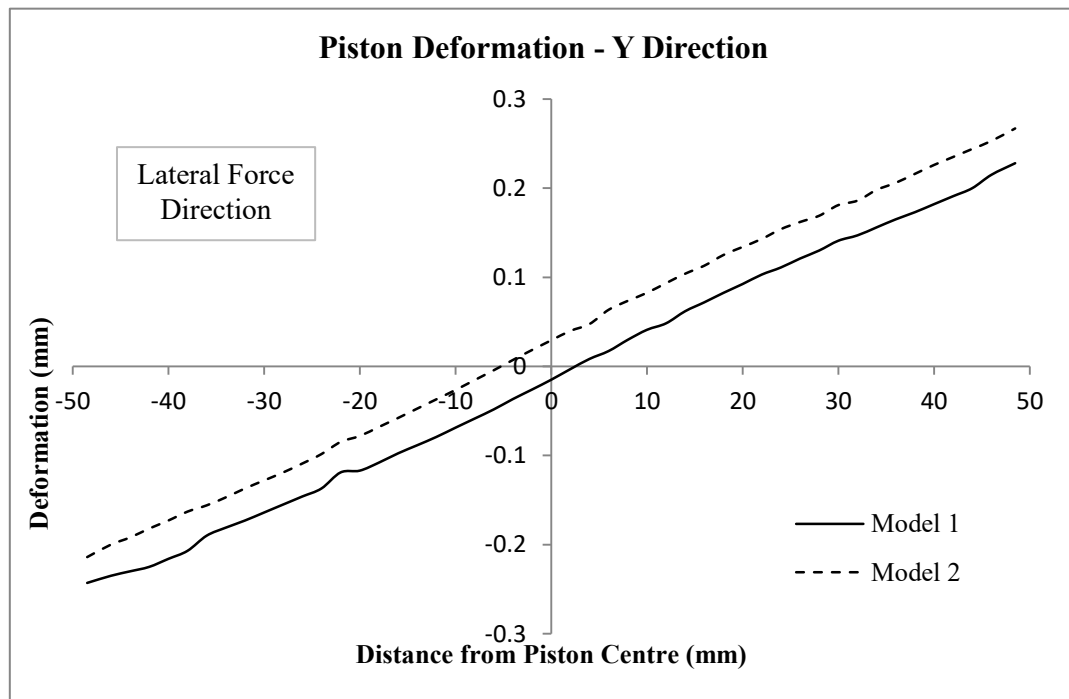


**Figure 5.32.** Piston deformation graphs in Y directions for both FE models.

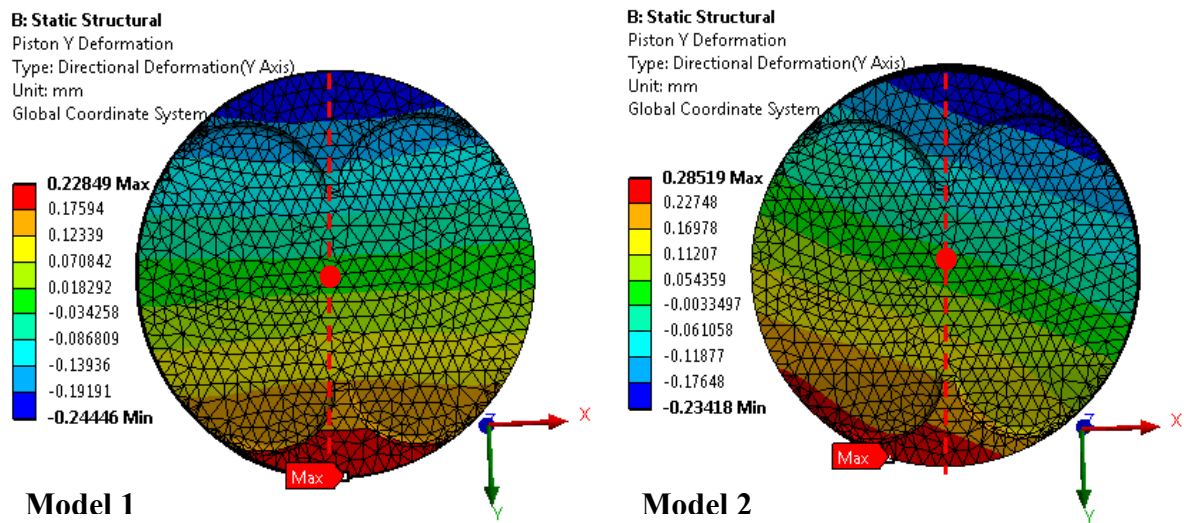


**Figure 5.33.** Piston deformation plots in Y directions for both FE models.

The piston deformations in the Z directions for both models are shown in Figure 5.34, measured along the red dashed line shown in Figure 5.35, with the respective piston displacement plots shown in Figure 5.35.

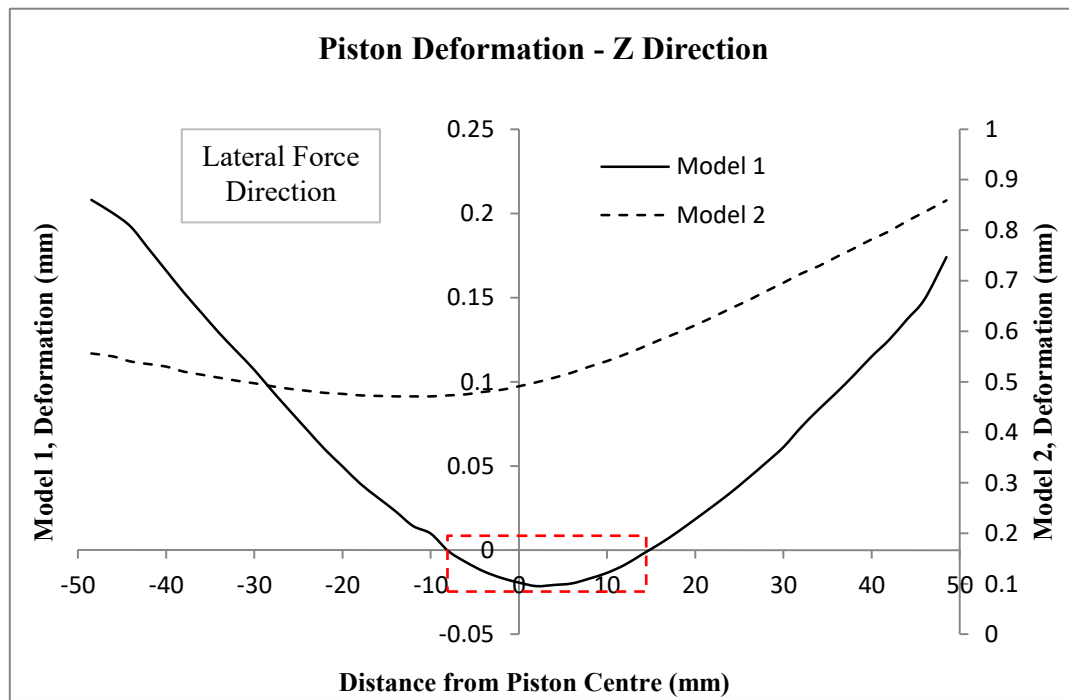


**Figure 5.34.** Piston deformation graphs in Z directions for both FE models.

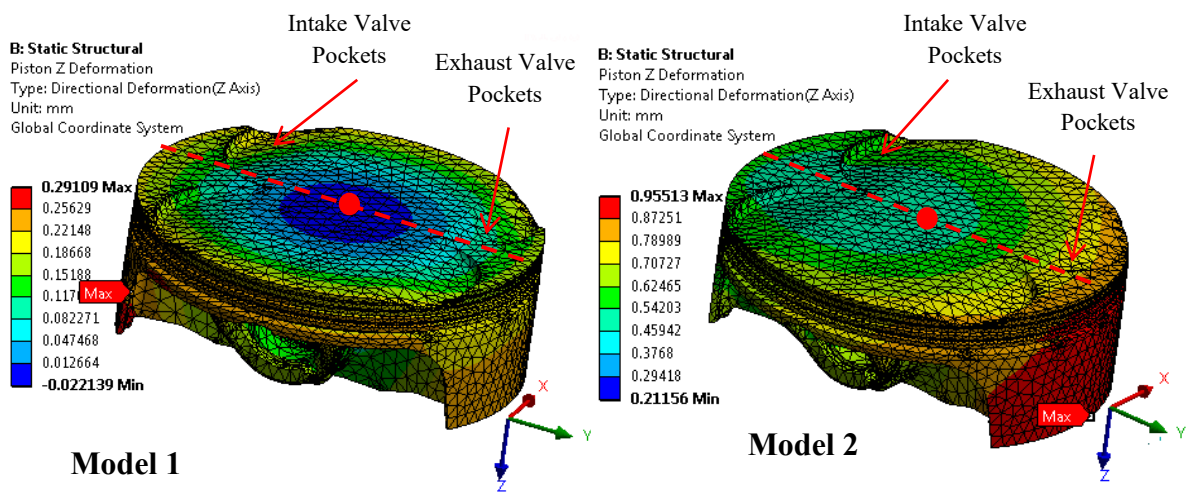


**Figure 5.35.** Piston deformation plots in Z directions for both FE models.

Figure 5.36 shows the pin deformations looking along the Z axis for the two different models. The pin in model 1 indicates a dome shaped deformation, while the pin in model 2 is compressed by the connecting rod in the middle.

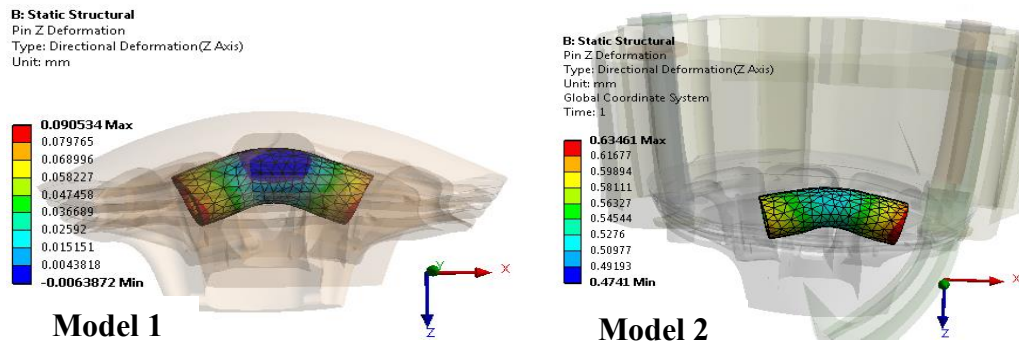


**Figure 5.36.** Pin deformation plots in Z direction in both FE models.

Based on the discussion of the original piston FEA results in Section 7.6, model 2 came out to be more representative of the load conditions that the piston is subjected to in reality. The new piston design was based on model 2 simulation conditions and the development of the new piston design is presented in Section 5.6.

#### 5.5.2.6. Fatigue life

Fatigue life curves for Al-2618 given by Lunn (Lumm, 1972) at various temperatures can be seen in Figure 5.37. Based on model 2 stress at crown (131.27 MPa), the piston should last 9-10 million cycles. According to the engine manual, the piston should last 4 – 7.2 million cycles or up to 40 service hours (Appendix B.1).

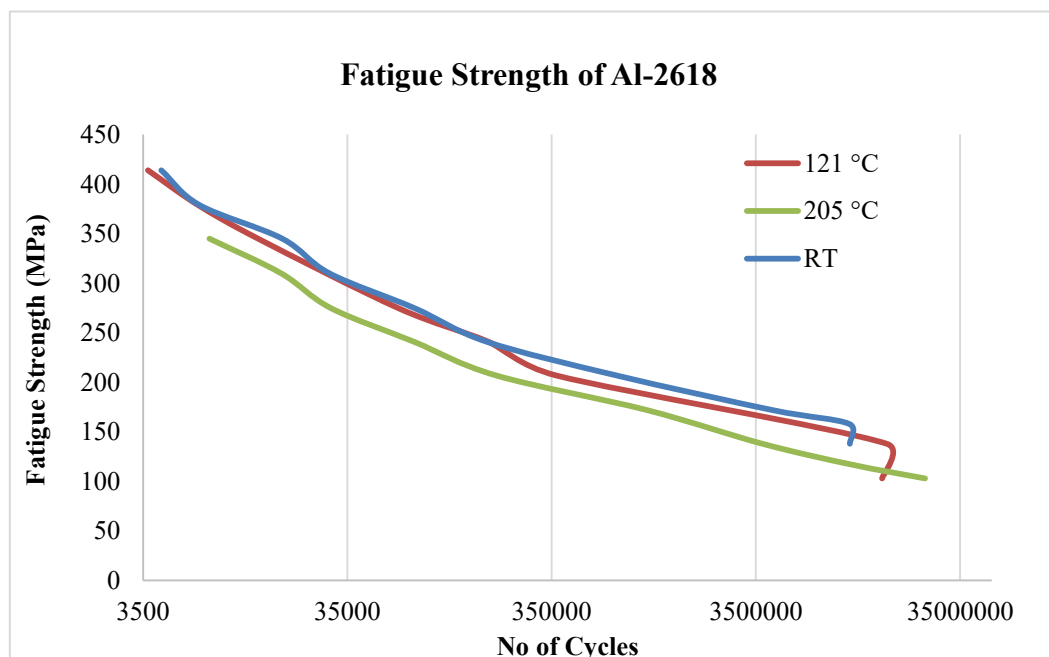


**Figure 5.37.** Fatigue strength of Al-2618 at different temperatures.

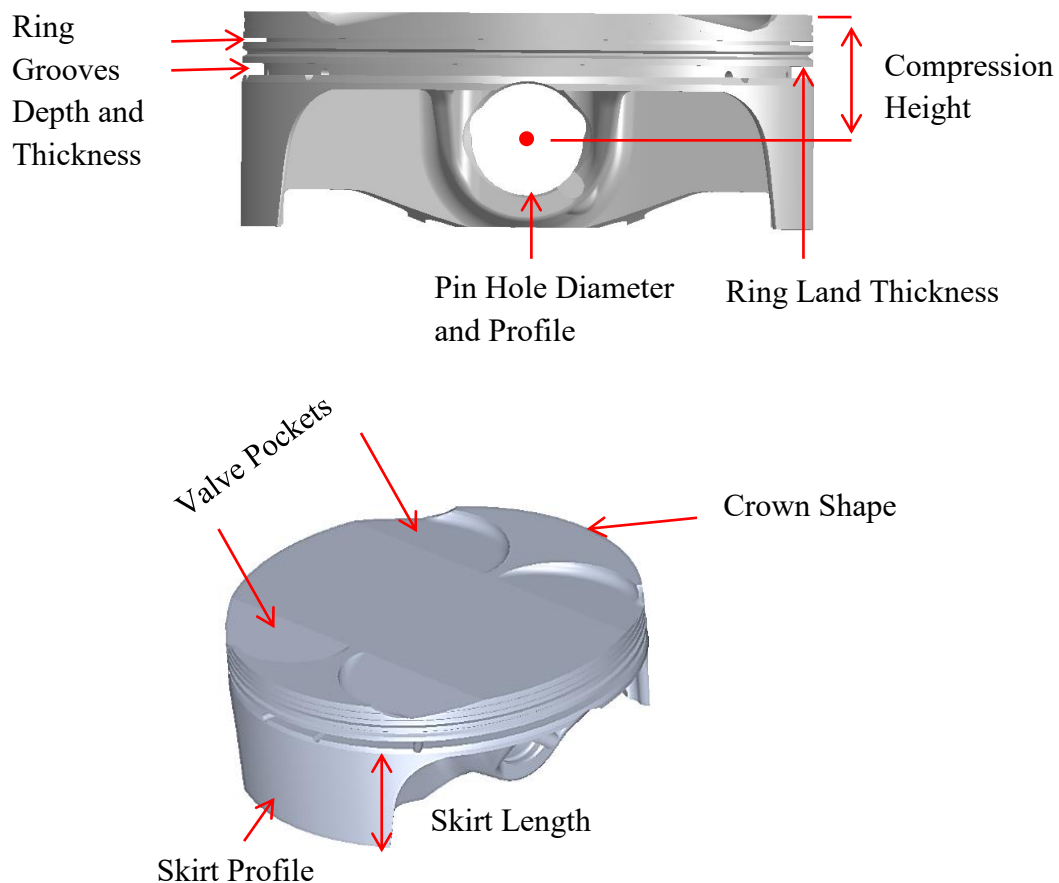
## 5.6. New lightweight piston design

The existing engine components imposed certain limitations on design of the new piston assembly compatibility. These limitations are given in Section 5.6.1 while the different design approaches and their results are given in Sections 5.6.2 and 5.6.3.

### 5.6.1. Design approach to reduce piston mass and limitations due to the existing engine components

The design approach was to reduce piston mass by thinning different sections of the piston as stated in Sections 1.1.1 and 4.9. This was feasible because the new alloy has higher strength and Young's Modulus (Table 5.1, page 75).

For the new piston to be compatible with existing engine assembly there were certain features and sections of the piston that needed to be kept the same. These are highlighted in this section (Figure 5.38). These regions were excluded from the optimisation analysis as highlighted in Figure 5.39.



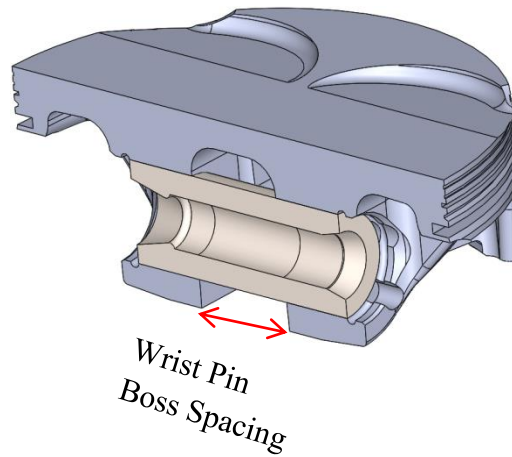


**Figure 5.38.** Features and regions of piston that we were left unmodified.

- Compression height and the ring land thickness: Reducing this could have affected the compression ratio which in turn could affect the combustion process. On the other hand, increasing the compression height could increase the likelihood of collision between the piston and the valves (Winship, 1967).
- Valve pockets cut-outs and crown shape: These could affect the combustion process and to keep the combustion mechanism unaffected, these were kept the same as the original.
- Ring grooves depth and thickness: The groove depth and thickness could affect performance of the compression and oil rings. They affect the blow-by and friction respectively; hence they were kept as the original geometry.
- Pin hole diameter and profile: The pin hole diameter and profile were kept the same since this could affect the interaction between the pin and piston and any change could affect the stresses in piston (Winship, 1967).
- Skirt profile: Pistons rely on skirts for guidance and thus proper dynamic behaviour. It was therefore left unmodified (Azevedo and Filho, 1988a).
- Skirt length: The skirt length below the centreline of the wrist pin is a must consideration in any piston design because it affects piston stability, noise and endurance.
- Wrist pin boss spacing: It has to be left unmodified else it con-rod will not fit.

The piston manufacturing considerations/limitations are given in Section 5.7.

### **5.6.2 Topology optimisation for piston mass reduction**

Topology optimisation has become a useful tool for the design of many structures and components. The topology optimisation tool in Ansys Workbench™ was first introduced in the version 18.2; in this work version 19.1 was used. The topology optimisation tool in Ansys Workbench™ was not sufficient for the piston design in this project; hence its limitations for this project are highlighted in the following section.

#### ***5.6.2.1 Limitations of topology optimisation in Ansys***

The topology optimisation tool in Ansys Workbench™ had many limitations, but the relevant ones for the piston design in this project are highlighted as follows (Scharcnet, 2018):

- Nonlinear contacts such as frictional contacts required for this study were not supported. The supported contact types included bonded or no separation. However, changing from frictional to bonded or no separation gave noticeably higher stresses in pin hole, which also affected the stresses in crown.
- Thermal effects could not be considered.
- Acceleration or inertial load could not be supported if the topology optimisation was linked with static structural analysis which was the case in this project.

To avoid aforementioned limitations and for the topology optimisation tool to function, the frictional contacts were changed to contact type bonded. The thermal and inertial loads were suppressed or excluded from the analysis.

#### ***5.6.2.2. Topology optimisation methodology and results***

The instructions on how to use the topology optimisation analysis tool is given in (Scharcnet, 2018). The objective of the topology optimisation analysis was to reduce the mass and the constraints were to keep the piston deformation the same as the original piston.



In addition to the features in Section 5.6.1 (Figures 5.38-5.39), cylinder, mounting studs, washers, pin and connecting rod were also excluded from the optimisation regions.

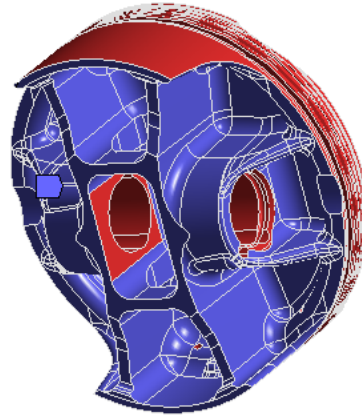


**Figure 5.39.** Exclusion regions (red) for the piston topology optimisation.

The results from the topology optimisation are given in Figure 5.40.

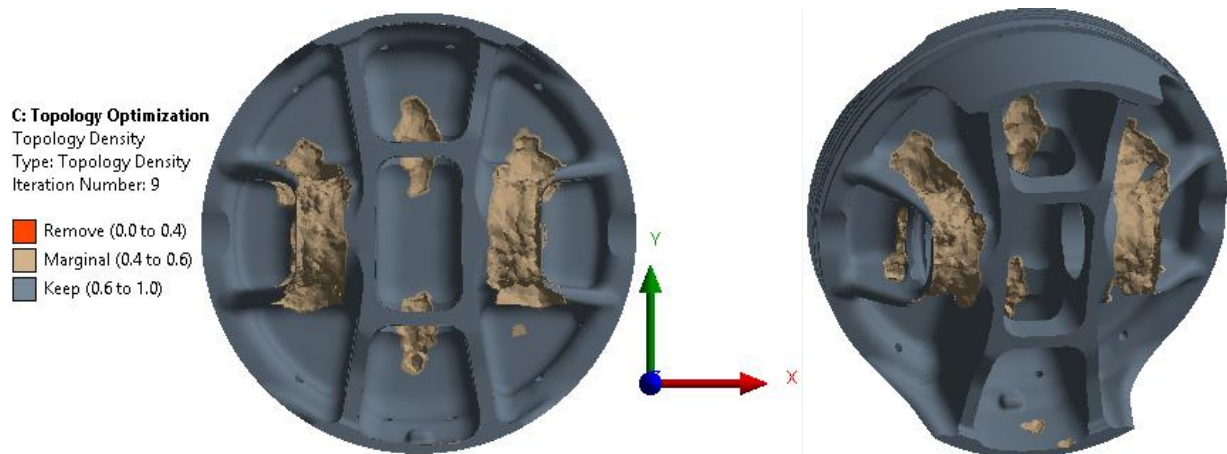


**Figure 5.40.** Optimised piston design from the topology optimisation analysis.

Although topology optimisation has produced some results (Figure 5.40), they cannot be relied upon for piston redesign because it did not consider, acceleration, thermal loads etc. as mentioned in the previous section. Furthermore, the results suggest removing material from areas where the stresses may be lower compared to other regions of the piston. However, the temperature in these regions is low (110 °C) and it is assumed that in the original design these

regions would have been designed optimally using the original alloy. The new alloy at these temperatures is slightly stronger than the original alloy (Figures 4.44 – 4.45), but not by a large margin as in the rest of the temperature range, therefore reducing too much material in these areas (pin boss) could affect the integrity of the design.

It was therefore decided to redesign/optimize the piston by inspection (Section 5.6.3) rather than by an Ansys based automatic optimisation process, due to its limitations.

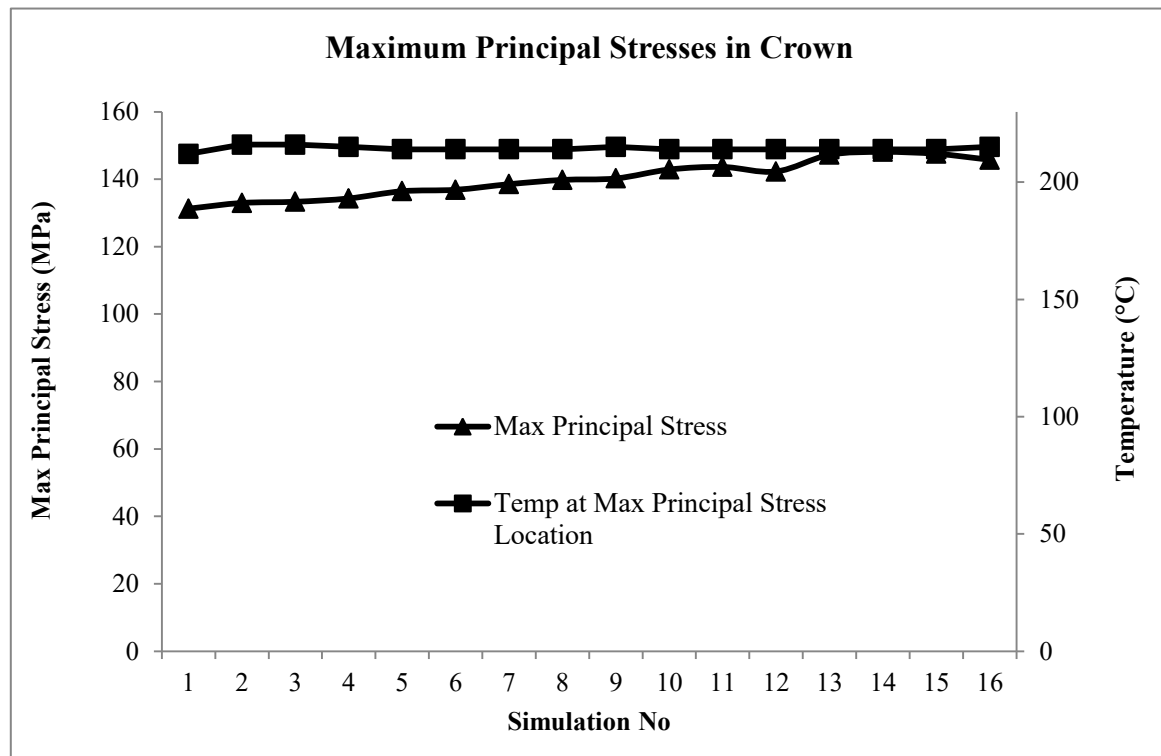
### **5.6.3. Piston design optimisation by inspection**

The inspection design optimisation was carried out by removing material from low stressed locations of the piston and re-evaluating stress and deformation response to verify acceptability. The parameters measured were the maximum principal stress, temperature and deformations and the simulated results are given in Figures 5.41–5.47. The incremental material removal steps are tabulated in Table 5.15 which shows where the geometrical changes were made; resulting in material removed.

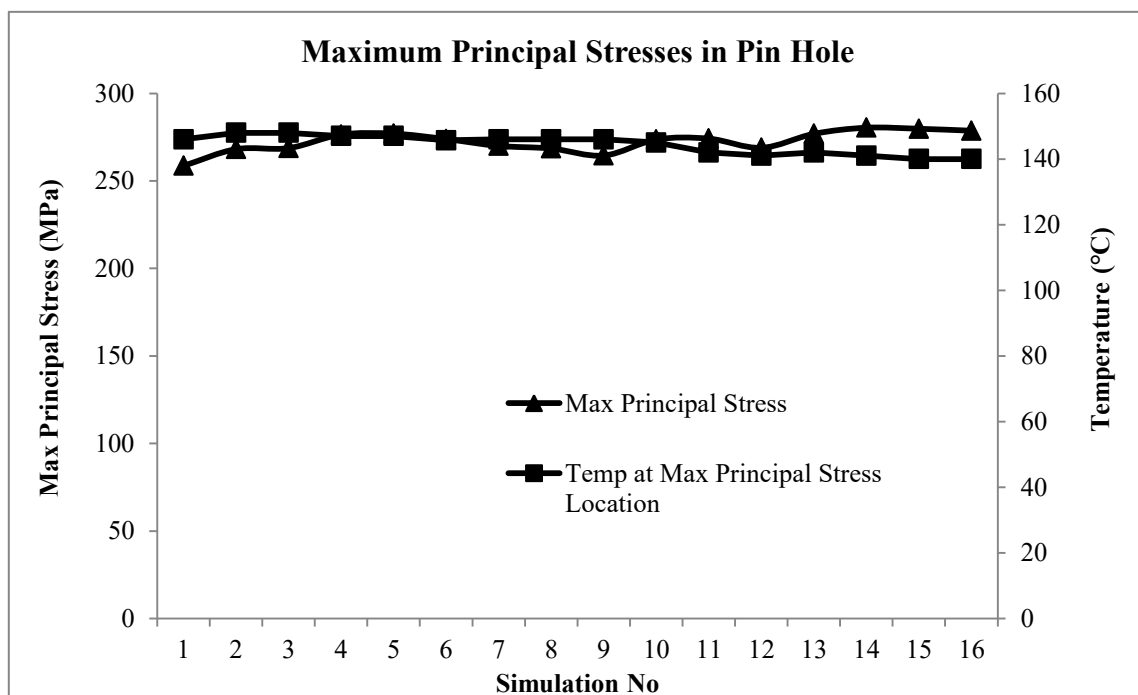
Simulation No	Piston Features	Original Dimensions (mm, Degree)	New Dimensions (mm, Degree)	Mass (g)	% Mass Reduction from Original
1	Original Piston Design with Original Material			261.13	0
2	Original Piston Design with New Material Properties Only			241.26	7.61
3	Piston Crown	5.542 mm	5 mm	239.9	8.13
4	Piston Crown		4.5 mm	238.73	8.58
5	Ring Land Area	6.893 mm	6.5 mm	233.84	10.45
6	Ring Land Area		6 mm	225.13	13.79
7	Skirt Thickness	2.505&2.255 mm	2.3&2.1 mm	224.03	14.21
8	<u>Undercrown</u> Web Thickness			219.98	15.76
9	Web Fillets	5 <u>Deg</u>	3 <u>Deg</u>	218.62	16.28
10	Web Cut	33.302 mm	30 mm	215.4	17.51
11	<u>Undercrown</u> -Boss Fillets	5.2 mm	3 mm	215.04	17.65
12	Web-Boss Fillets	3.8&3 <u>Deg</u>	3&2.7 <u>Deg</u>	214.75	17.76
13	<u>Undercrown</u> -Skirt Fillet	6&5.5 mm	4&3.5 mm	212.11	18.77
14	<u>UnderCrown</u> -Boss-Skirt Fillets	3.5-3.2-3.5 <u>Deg</u>	2.8-2.6-2.80 <u>Deg</u>	211.49	19.00
15	Web-Skirt Fillets	5.1 & 2.9 <u>Deg</u>	3.5&2 <u>Deg</u>	210.48	19.39
16	Piston Crown	6 mm	6.2 mm	218.35	16.38

**Table 5.15.** Descriptions of geometrical changes for manual piston optimisation.

The maximum principal stresses in the critical regions for the manual inspection piston design optimisation are given in Figures 5.41–5.42.

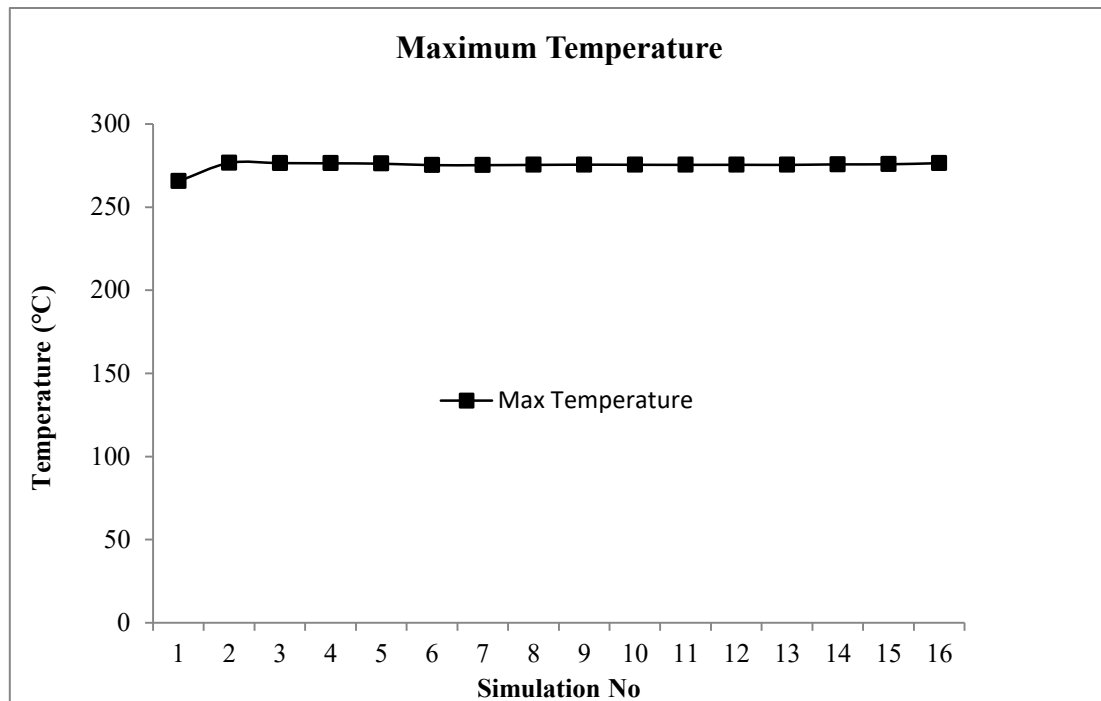


**Figure 5.41.** Maximum principal stresses in the piston crown due to incremental material removal.

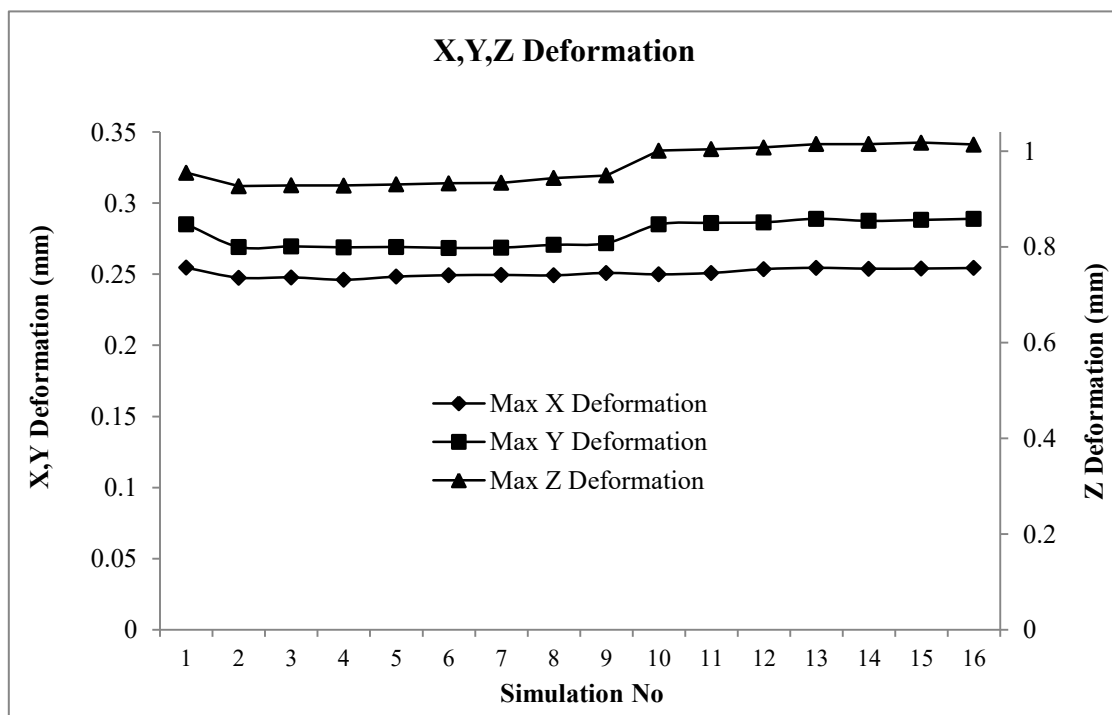


**Figure 5.42.** Maximum principal stresses in pin hole due to incremental material removal.

The maximum piston temperature and maximum deformations in X, Y and Z directions due to the incremental material removal can be seen below in Figures 5.43 and 5.44 respectively.

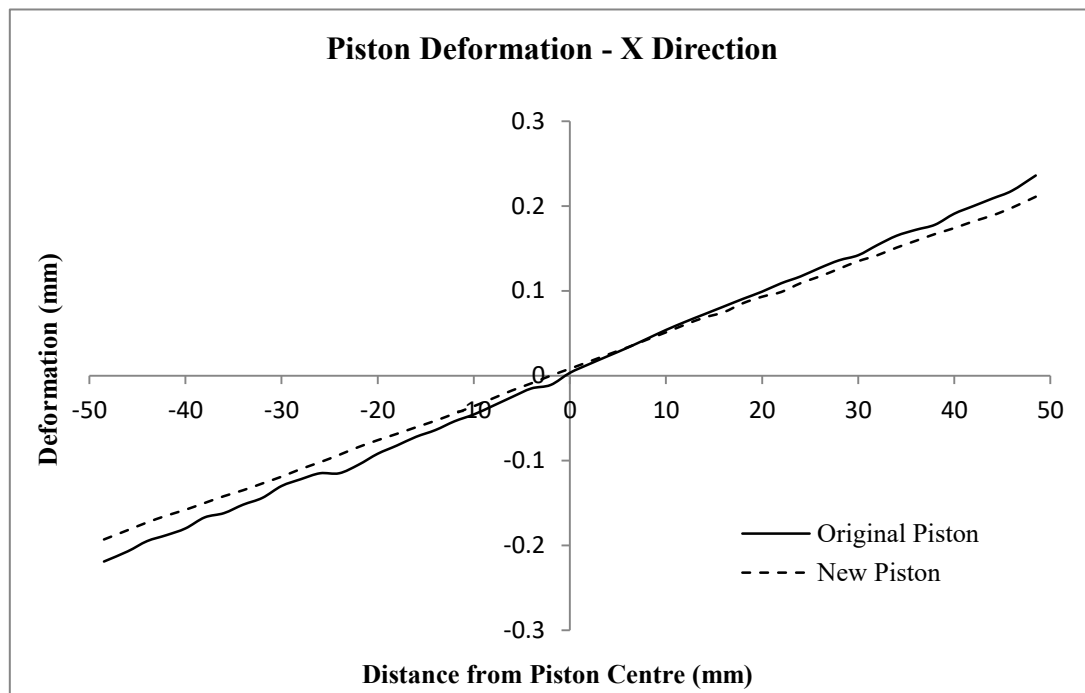


**Figure 5.43.** Maximum temperature changes in piston due to incremental material removal.

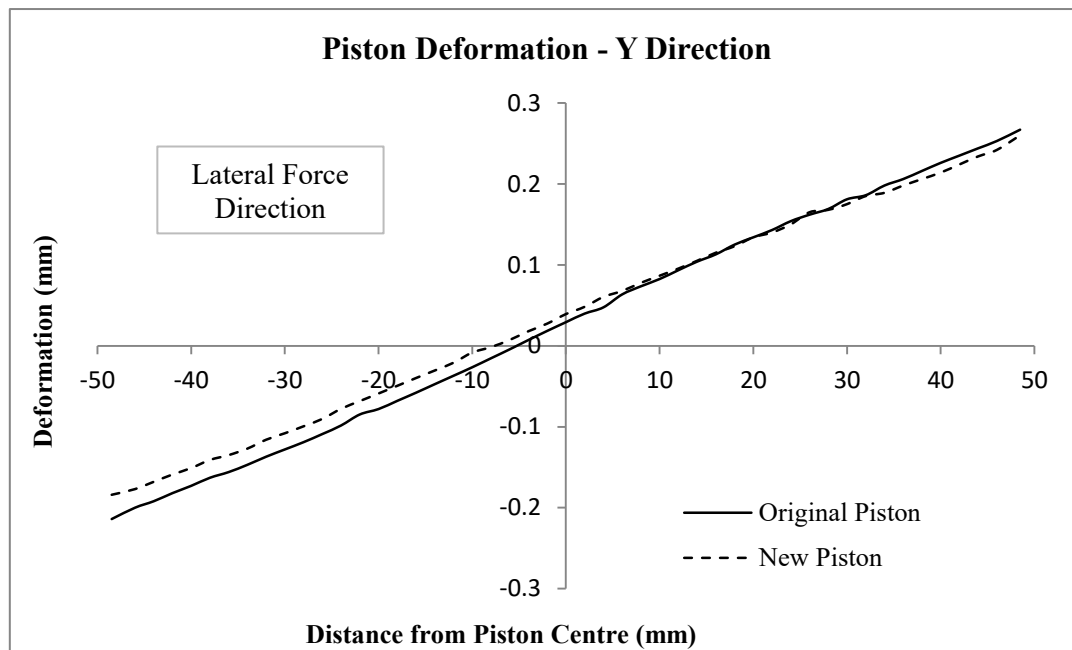


**Figure 5.44.** Deformation changes in piston due to incremental material removal.

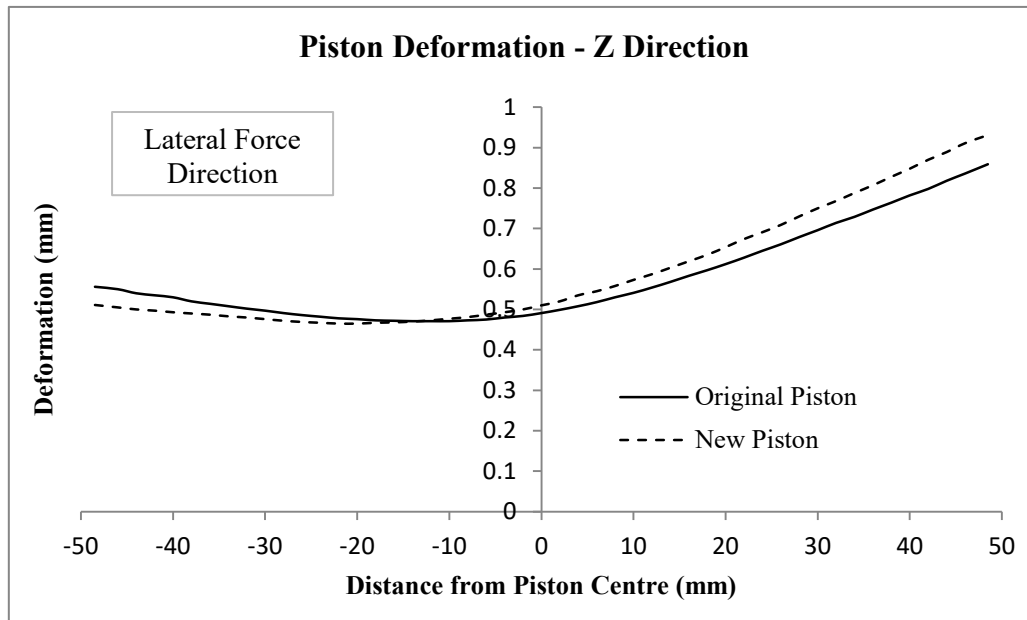
The comparison of the directional deformations of the manually optimised piston in X, Y and Z directions can be seen in Figures 5.45–5.47. The measurements were taken on the piston crown similar to what was carried out in Section 5.5.2.



**Figure 5.45.** Piston deformation graphs in X directions for original and new pistons.

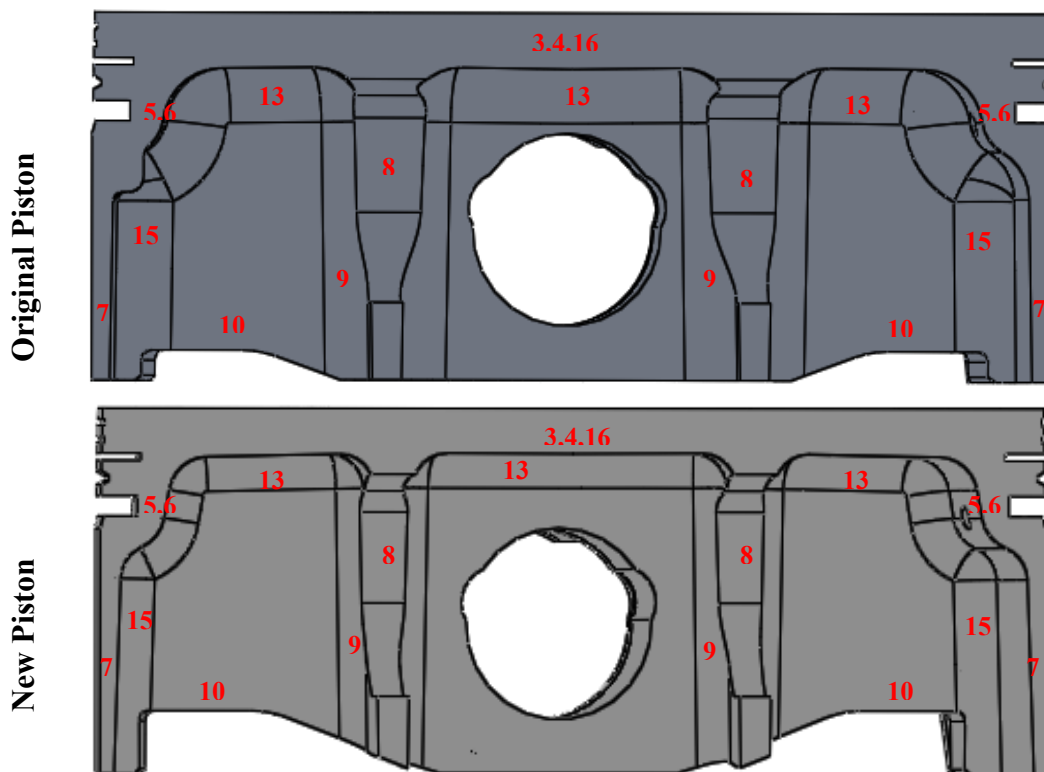


**Figure 5.46.** Piston deformation graphs in Y directions for original and new pistons.



**Figure 5.47.** Piston deformation graphs in Z directions for original and new pistons.

A dimensional and feature comparison of the original and new pistons is illustrated in in Figure 5.48. The different features are highlighted/ numbered with respect to the features outlined in Table 5.15.



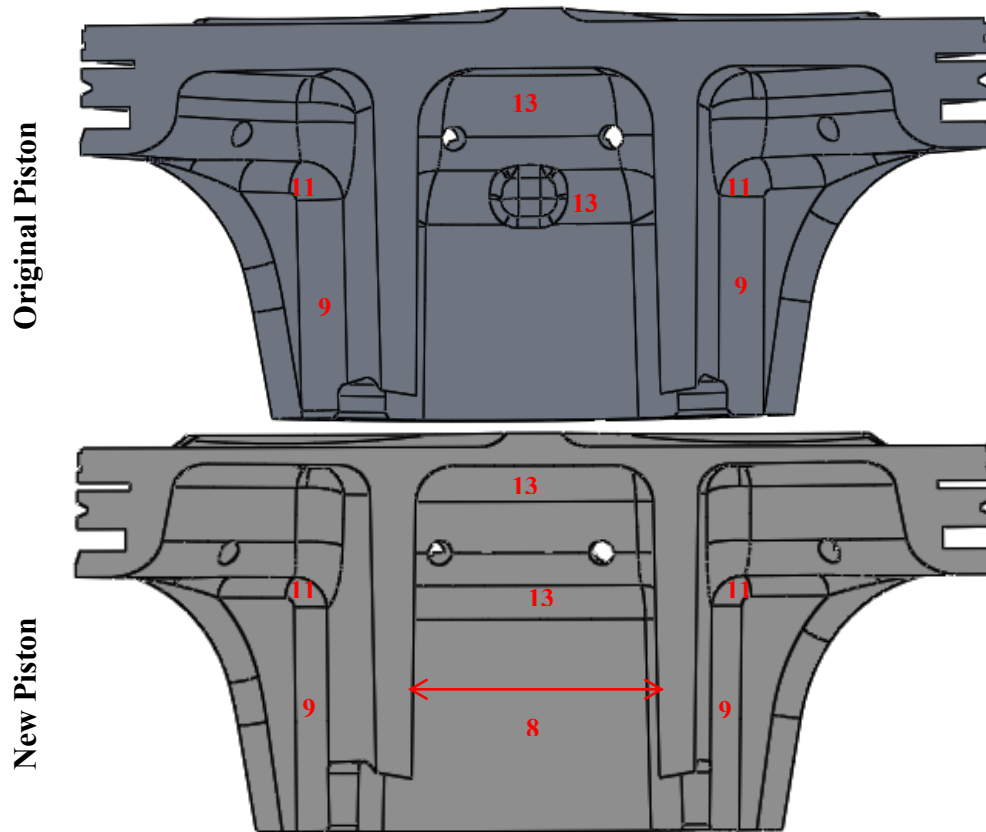


**Figure 5.48.** Comparison of original and new piston designs.

The manufacturing of the new piston and the modifications needed to accommodate the new piston in the existing engine for compatibility are presented in Chapters 5 & 6 in Sections 5.7 and 6.5 respectively.

### **5.7. Manufacturing of the new piston design**

Once the new piston design was finalised and before the manufacturing could proceed, the material had to be upset forged to a larger diameter. The material was available in a bar form of 60 mm diameter and 340 mm in length (Figure 5.49). However a billet of 103 mm in diameter and length of 50 mm was required to machine a piston with 97 mm diameter and 36.3 mm length.



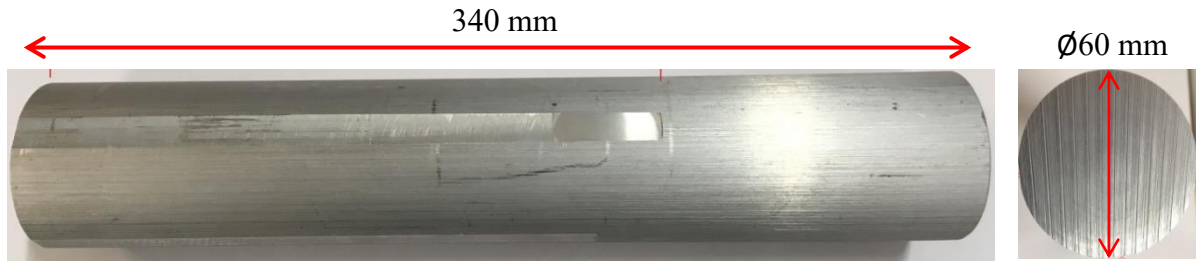


**Figure 5.49.** The available material before upset forging.

The bar was cut into pieces with lengths of 155 mm to be forged into billets of the required size, the calculations for determining the 155 mm length are given in Appendix C.4. Images of one of the forged billets can be seen in Figure 5.50. Post forging, the billets were heat treated according to the methodology given in Section 4.4.

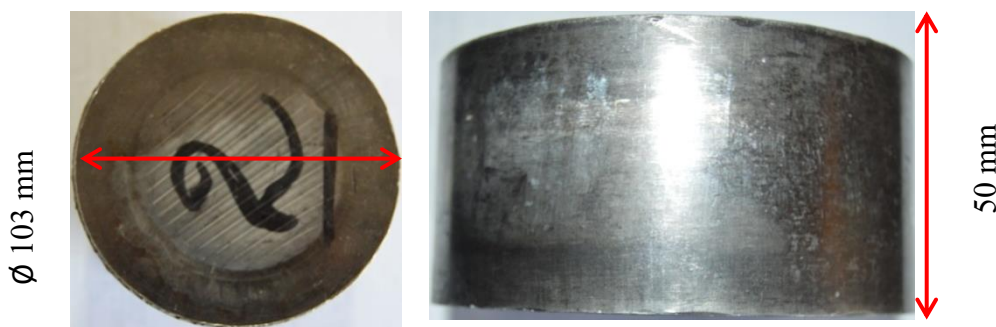


**Figure 5.50.** Pictures of the upset forged billets.

The heat treated billets were sent to GE Precision Engineering for machining. GE Precision Engineering has been manufacturing similar pistons for a long time and the engineers noticed that the original piston had not been reverse engineered correctly and therefore suggested some small changes such as ring groove profiles. The changes required were incorporated in the optimised model and the FE analysis was re-run. The small geometrical changes did not make any significant impact on the FE results (in fact the stress at the pin hole was reduced, see Table 5.16). The FE simulated maximum principal stress distribution results after changes are shown in Figure 5.51 and it is very close to the first optimised model (Figures 5.41–5.42). The comparison of the stress values at critical locations can be seen in Table 5.16.

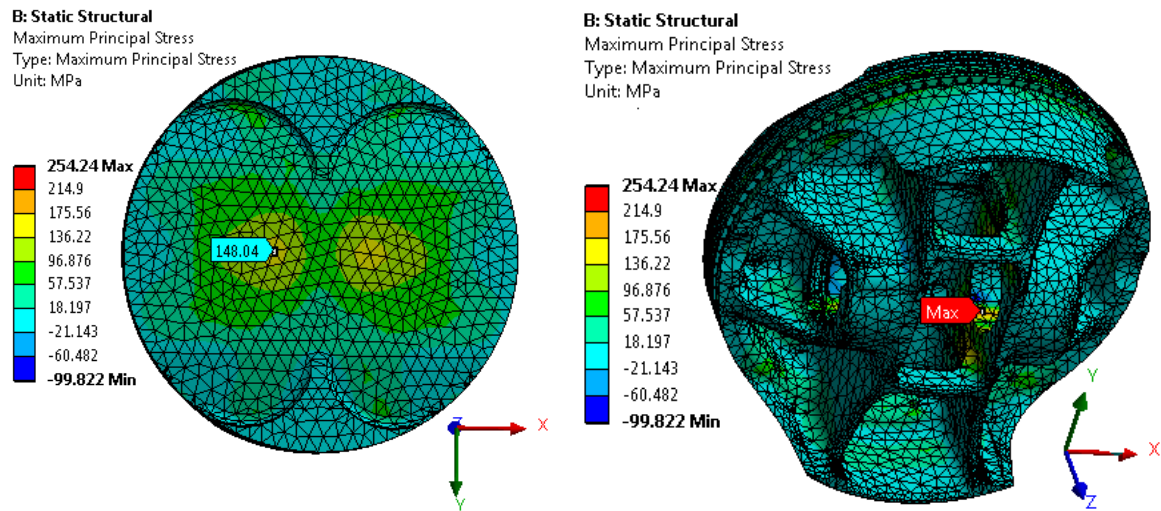


**Figure 5.51.** FE results after the suggested changes were made (optimised model).

Model	Crown Stress (MPa)	Pin Hole Stress (MPa)
First Optimised Model	145.78	278.7
After Changes	148.04	254.24
% Change	Increase of 1.55	Decrease of 8.77

**Table 5.16.** Stresses of first optimised piston and after the suggested changes for machining

Images of the machined pistons can be seen in Figure 5.52 while pictures of the coated piston can be seen in Figure 5.53. The coating used was Xylan 1010 which is also used in F1 pistons (Whitford, 2018).



**Piston Top View**



**Piston Underside View**

**Figure 5.52.** Images of the machined pistons.

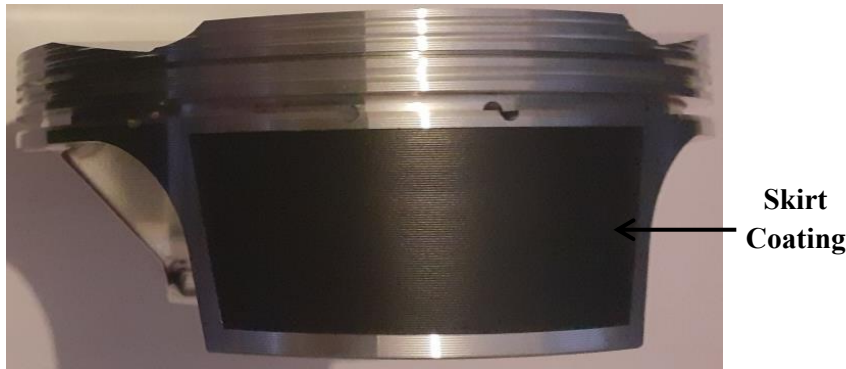


**Figure 5.53.** Images of the coated piston.

#### **5.7.1. Challenges encountered with piston design and manufacturing**

- Not all geometrical features of the original piston were adequately acquired because the scanning laser could not reach those features such as ring grooves sufficiently.
- The company which agreed to forge the material at the beginning of the project had management restructure, and the new management was not willing to forge high silicon content alloy as there was risk of breaking the die.
- Finding a forging company with correct die size was challenging. Smaller die would not produce the required billet size while there was not enough material for larger die to produce two billets.
- After forging the material in Argentina and shipping it back to UK, the HomeOffice withheld the material until they were completed their investigations which resulted in significant delays for project the manufacturing.

### **5.8. Summary**

The work undertaken in this chapter analysed two different approaches for the FE modelling of a piston as suggested in literature. It highlights the importance of accounting for the lateral forces in piston numerical simulation, which were largely ignored in most publications. The results showed that using piston, pin, some portion of the connecting rod and a cylinder (model 2) was a more realistic representation of the structural response of the piston assembly

compared to the combination of only piston and pin (model 1) that was widely used in literature. The results are discussed in Section 7.6. Based on model 2 and using the new alloy's properties, the piston was redesigned by thinning the different sections of the piston to reduce the overall piston mass. The new piston's mass was 218.35 grams which is 16.38% lighter than the original piston with mass of 261.13 grams. The stress in the critical areas of the redesigned piston increased approximately proportionally due to the thinning of the piston. This was however not a concern because of the higher strength of the new alloy.

The chapter also explained manufacturing of the new pistons and challenges encountered with piston design and manufacturing.

## Chapter 6: Engine testing and results

### 6.1. Introduction

This Chapter explains the modifications made to the engine, auxiliary components design and installation of various sensors to prepare the engine for dynamometer testing based on the objectives of the research. It also describes the test methodology and engine performance parameters required to be measured. The engine test scope, test limitations and technical challenges encountered are highlighted. Furthermore, it covers the new piston design, manufacturing challenges and the modifications needed to the engine to accommodate the new piston. The engine test results with the original and new pistons are presented and compared to assess any modifications in engine performance.

### 6.2. Engine test methodology

The methodology used for the engine testing is illustrated in the flowchart shown in Figure 6.1.

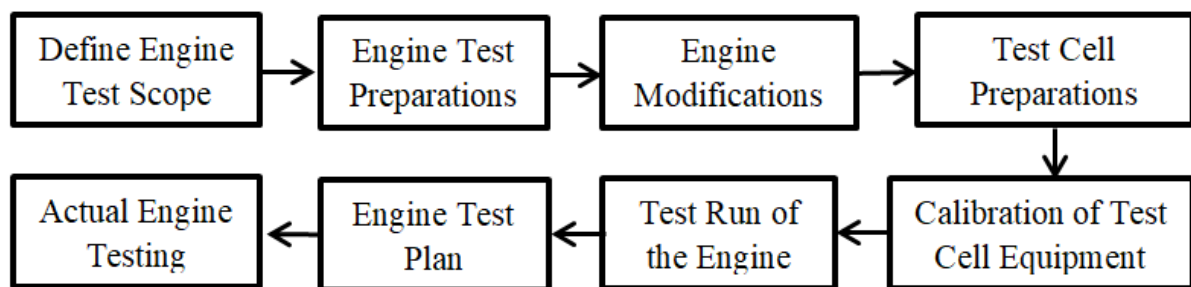


**Figure 6.1.** Flow chart of the engine test methodology.

### 6.3. Engine test scope and limitations

The engine used in this project was a high performance motorbike engine, KTM 450 XCF 2008 (Table 5.2). The scope of the initial engine testing was to obtain performance parameters that were required as baseline for the new piston design. The parameters measured and/or calculated included engine speed, in-cylinder pressure, coolant temperature,

air-fuel ratios, torque and fuel consumption. Other parameters such as air intake temperature and pressure that could affect the engine performance were also measured.

Engine operation can be affected by numerous factors. In this project, every effort was made to control these factors, however some assumptions were made during the engine testing which are given below:

1. The engine rotational speed was assumed to be constant.
2. The slight temperature variation (1-2 °C) in the engine tests cell was assumed not to have significant impact on the intake air temperature which could affect the engine performance.
3. The small variation in engine coolant temperature did not have any impact on the thermal stability of the engine hence no impact on the engine performance.
4. The small insignificant variations in air-fuel ratios were ignored.
5. Humidity of the test cell was not controlled and it was assumed to be stable and not have any significant effect on the engine performance.

#### **6.4. Engine test preparation**

The test engine used in this project was a production engine which was modified to allow for the installation of the sensors required for the data acquisition.

##### **6.4.1. Choice/selection of dynamometer**

The dynamometer or dyno for short, used in this project was a Schenck, type W130 (Eddy-Current Dynamometer) (Schenck, 2001). To ensure that the dyno was suitable for the project, the expected maximum torque and power-speed curves of the engine were superimposed on the dynamometer performance envelope (Martyr and Plint, 2007). This showed that the test requirements were within the dyno capability. The specifications of the dyno are given in Table C.1 and Figure C.1 in Appendix C.1

#### 6.4.2. Mount design

The correct mounting of an engine is one of the extremely important aspects of engine testing and neglecting it can lead to misleading results and increases the likelihood of accidents. The test engine used in this project was a single cylinder, and therefore prone to vibrations. The mount was designed to keep the vibrations to a manageable level by utilising the same mounting locations as in the motorbike in which the engine is normally installed.

A schematic of the engine mount with the engine can be seen in Figure 6.2. The 2D engineering drawings of the individual components and exploded view of the assembly are given in Appendix C.2.

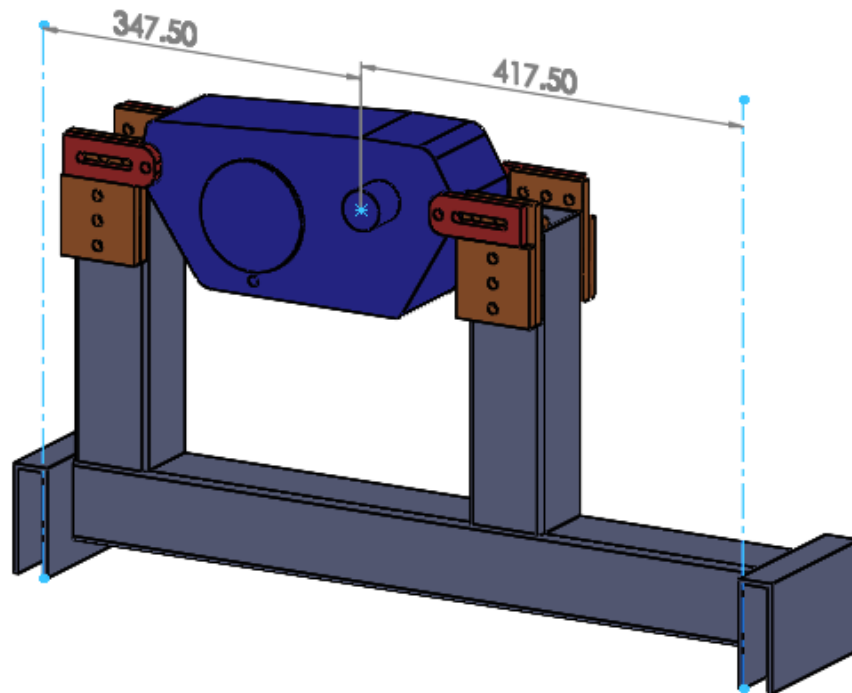


**Figure 6.2.** CAD model of engine mount assembly (units in mm).

#### 6.4.3. Coupling with dynamometer

Selecting the appropriate couplings and shaft for connecting to the engine is another key aspect of engine testing. Choosing an inappropriate couplings can lead to various problems such as torsional oscillations, whirling of coupling shaft, catastrophic failure and others (Jayabalan, 2004; Martyr and Plint, 2007; Mohd Hasnun Ariff, 2012). The design and

fabrication of the shaft is a complicated and specialist task that was beyond the scope of this project. To find the correct shaft for the application in this project, a specialist company (Voith Turbo HighFlex GmbH & Co.KG) was contacted to recommend a suitable solution. Upon investigation, it was discovered that they had designed two shafts for Oxford Brookes University in the past for such applications. Pictures of the coupling shaft used in this project can be seen in Figure 6.3.

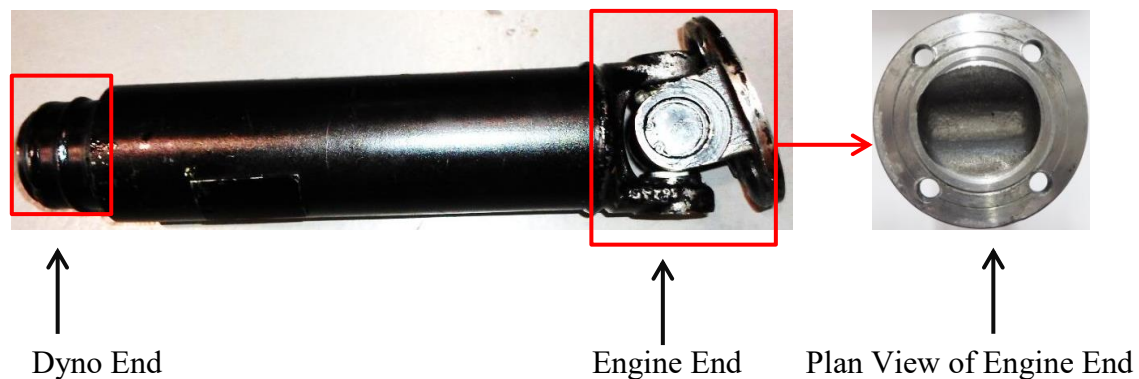


**Figure 6.3.** Pictures of the coupling shaft with universal joint used in this project.

The test engine came with a standard sprocket (Figure 6.4a) at the drive end, but had to be modified to be coupled with the coupling shaft end (Figure 6.3 Plan View). The external teeth of the sprocket were machined and the rest of the sprocket was welded to a flange with holes as can be seen in Figure 6.4b.

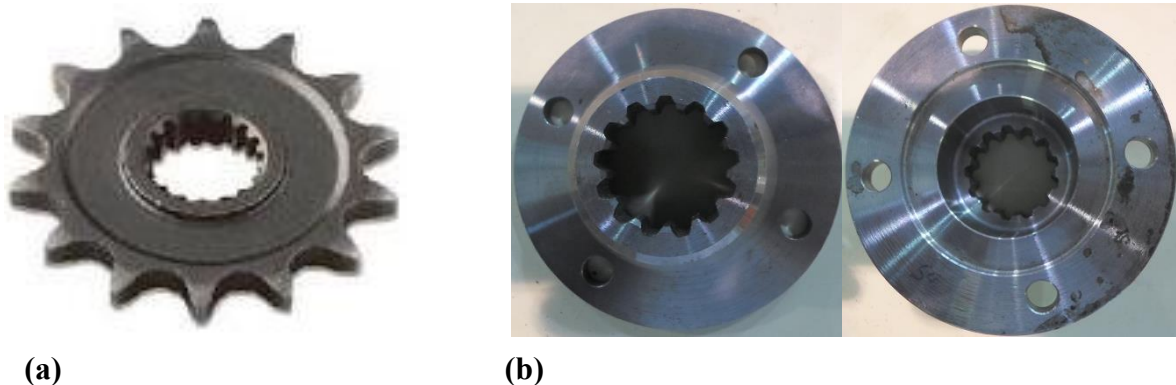


**Figure 6.4.** a) Pictures of the standard sprocket for the test engine. b) Modified sprocket.



#### **6.4.4. Electrical wiring harness and cranking**

The wiring system of an engine plays a central role in connecting a number of important components such as electronic control unit (ECU), spark plug, starter motor, lighting etc. The approach used for this project was to take the existing harness system of the engine and disconnect the wires not needed.

A standard starter motor for the test engine was used to crank the engine and it was powered by a standard 12 V battery that was available in the test cell.

#### **6.4.5. Exhaust system and lambda sensor**

The space limitation, layout and congested nature of the test cell heavily affected the design of the exhaust system. The exhaust system was designed to avoid compromising the safety of the cell operators by keeping proximity with hot metal exhaust piping to a minimum as specified by (Martyr and Plint, 2007). The exhaust system was designed to accommodate an O<sub>2</sub> sensor as the project needed one (Figure 6.5).

The exhaust system was designed (Figure 6.6) to be similar to the original system especially the length of the primary pipe because any changes in the length of the primary pipe could lead to changes in the exhaust and induction process as a result of changes in the pattern of exhaust pulses in the system. This could affect the volumetric efficiency and power output of the engine.



**Figure 6.5.** Installation of the boss on exhaust pipe for lambda sensor.

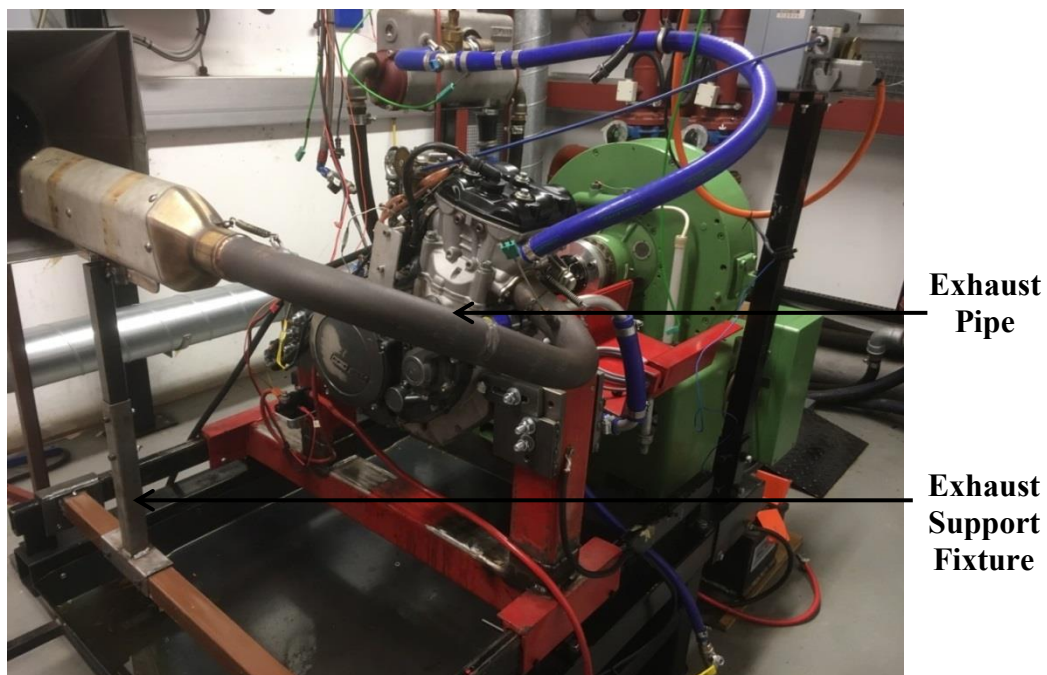


**Figure 6.6.** A picture of the exhaust system and support fixture used for the test engine.

#### 6.4.6. Cooling system

The cooling system of the test cell was capable of providing water of suitable quality, temperature and pressure to allow sufficient volume to pass through the engine for sufficient cooling. The coolant medium used for the test engine was a mixture of water and antifreeze

(ethylene glycol). The recommended coolant flow rate for the test engine was 1.2 l/min which was within the test cell capacity.

#### 6.4.7. Crank position location system

The purpose of the crank position system was to locate the piston (top dead centre) and use it as a trigger point for measuring the in-cylinder pressure readings. The location of the piston/crank was needed to superimpose the pressure with other forces acting on the piston. The encoder mounting assembly is shown in Figures 6.7-6.8.

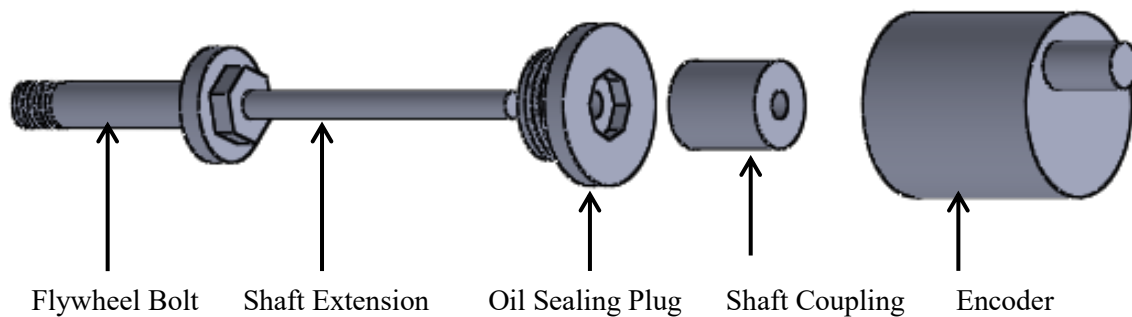


**Figure 6.7.** Representation of the crankshaft extension for the encoder installation.

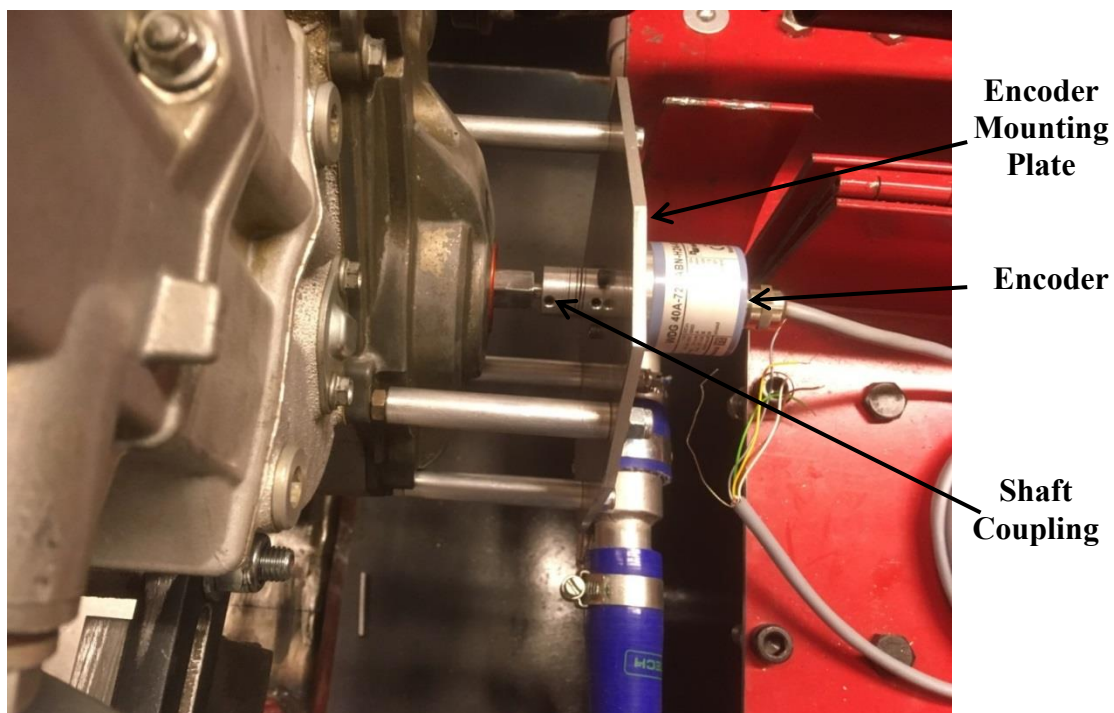


**Figure 6.8.** Encoder assembly mounted on the engine.

#### 6.4.8. Torque, speed and fuel measuring systems

The torque and engine speed were determined using a dynamometer control and data logging software CADET. To ensure the accuracy of torque and speed measurements, the dynamometer was calibrated before the testing by the manufacturer of the engine control and data acquisition system, Sierra-CP. The CADET system was also implemented by Sierra-CP.

The fuel consumption of the engine during testing was measured using an FMS-1000 fuel system, which was a gravimetric fuel measuring system from Sierra-CP (Figure 6.9). The FMS-1000 system was controlled and monitored by CADET, which recorded and displayed the data obtained (Engineering, 2003; Barbour *et al.*, 2008). A screen shot of the control system can be seen in Figure 6.10. The new fuel measuring system installed for this project was commissioned and calibrated by Sierra-CP.

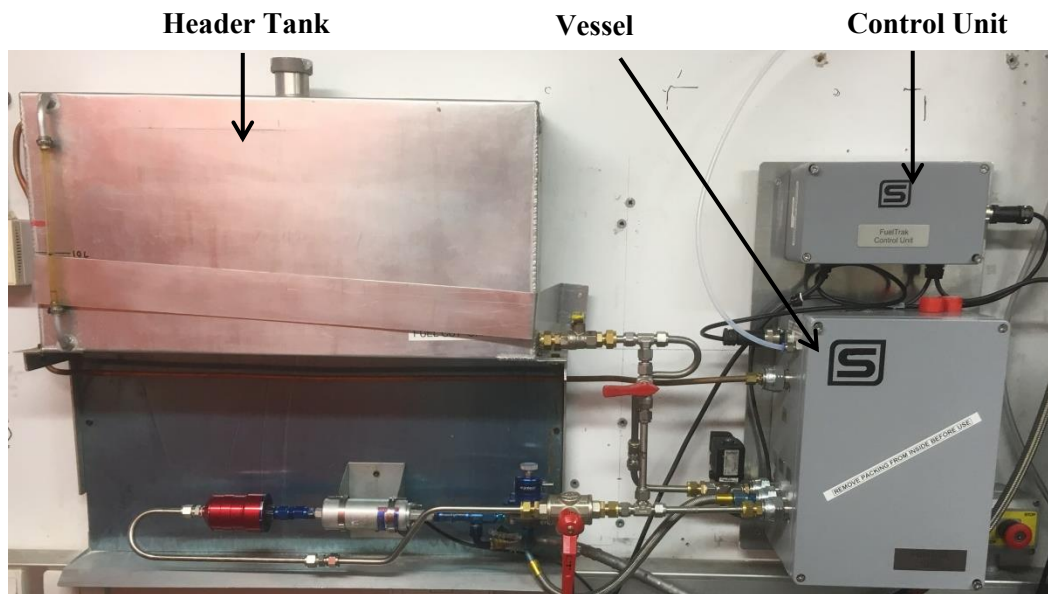


**Figure 6.9.** FMS-1000 fuel weigher system used in this project.



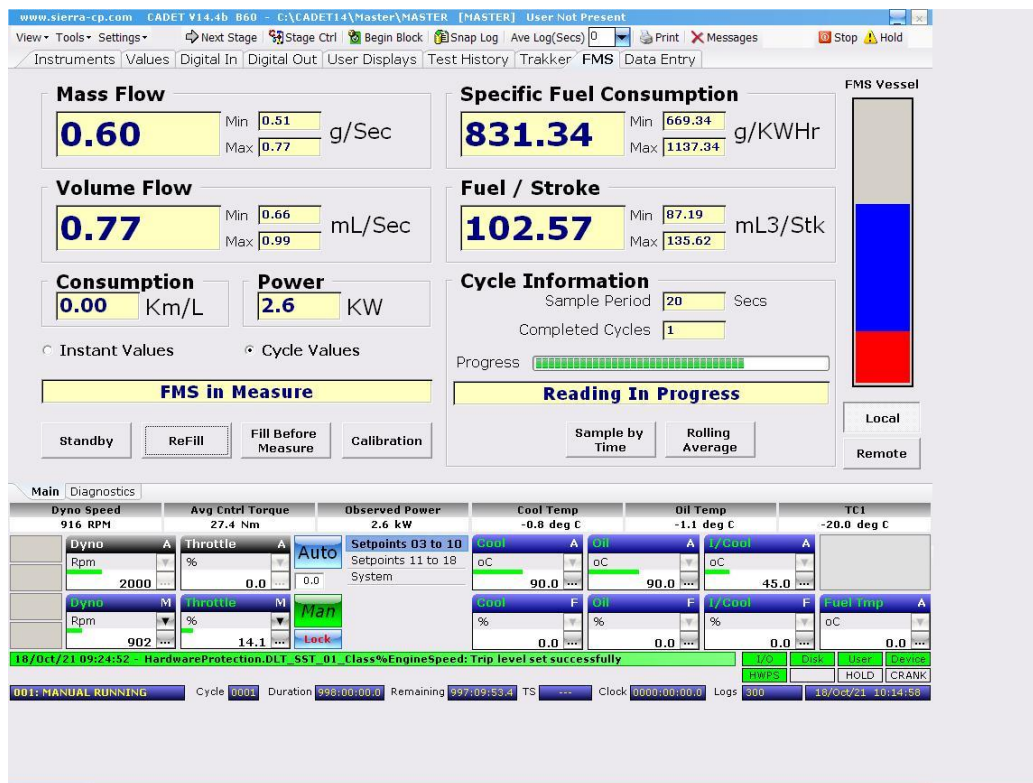
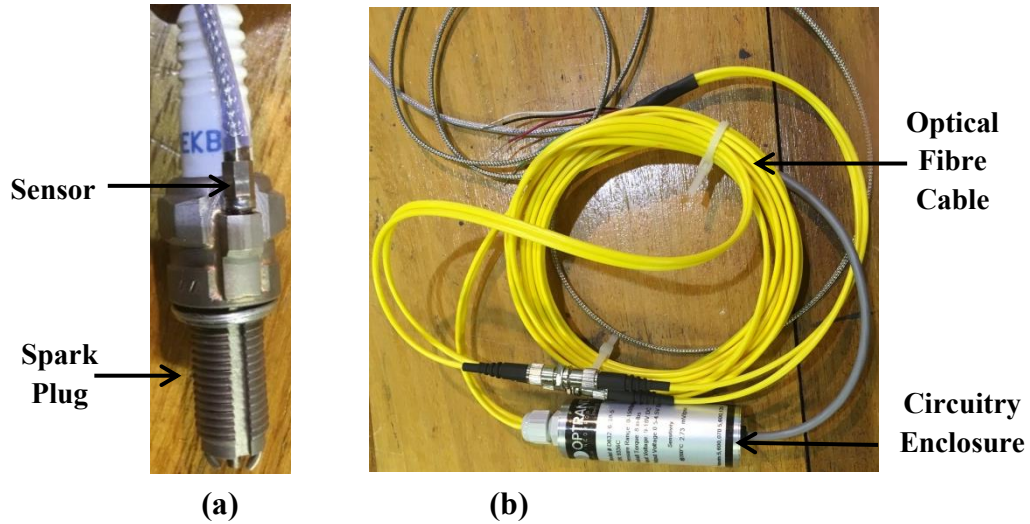


Figure 6.10. Screenshot of the FMS 1000 control.

#### 6.4.9. Installation and Calibration of in-cylinder pressure sensor

The in-cylinder pressure measurements can be used for various analyses (Trimby *et al.*, 2017), but in this project it was measured to determine the maximum combustion pressure and hence determine the worst case loading for the piston. The pressure measurements were also used to derive thermal loading on the piston (Section 2.9.2). The pressure sensor used for this project was a spark plug integrated sensor from Optrand which is fibre optic sensor (1/4-20 UNC Flange) (Figure 6.11a).

A picture of the modified spark plug with sensor can be seen in Figure 6.11a. The sensing element needed to be connected to an enclosure that housed all the electronic circuitry via an optical fibre cable (Figure 6.11b).



**Figure 6.11.** a) Sensor mounted modified spark plug. b) Pressure sensor electronic circuitry

Further information about the sensor can be found in the sensor specification (Appendix C.3) and (Optrand, 2001; Optron, 2013).

To calculate the pressure from the pressure sensor's output voltage, the following formula (6.1) was used (Optron, 2013).

$$P = (V - V_{\min})/s \quad 6.1$$

where  $P$ ,  $V$ ,  $V_{\min}$  and  $s$  are pressure (PSI), output voltage (V), minimum output voltage (V) and sensitivity (V/PSI). The sensitivity factor value was indicated on the circuitry enclosure (2.73 mV/PSI at 200 °C) in unit of mV/PSI.

#### **6.4.10. Installation and calibration of air intake pressure sensor, temperature and carburettor**

Engine performance could be affected by the condition of incoming air and needed to be accounted for. These parameters stayed fairly stable during for specific test conditions. In this project some of these parameters were monitored to check that no significant deviation occurred. According to the European and American Standards for testing internal combustion engines, the values for the three parameters are as follows:

- Pressure (atmospheric pressure or 1 bar)
- Temperature (25 C or 298 K)
- Relative humidity (30%) (Martyr and Plint, 2007)

Since the test engine was naturally aspirated, the inlet temperature remained nearly the same as the room temperature. On the other hand, the inlet pressure was measured using another Optrand sensor (Figure 6.12).

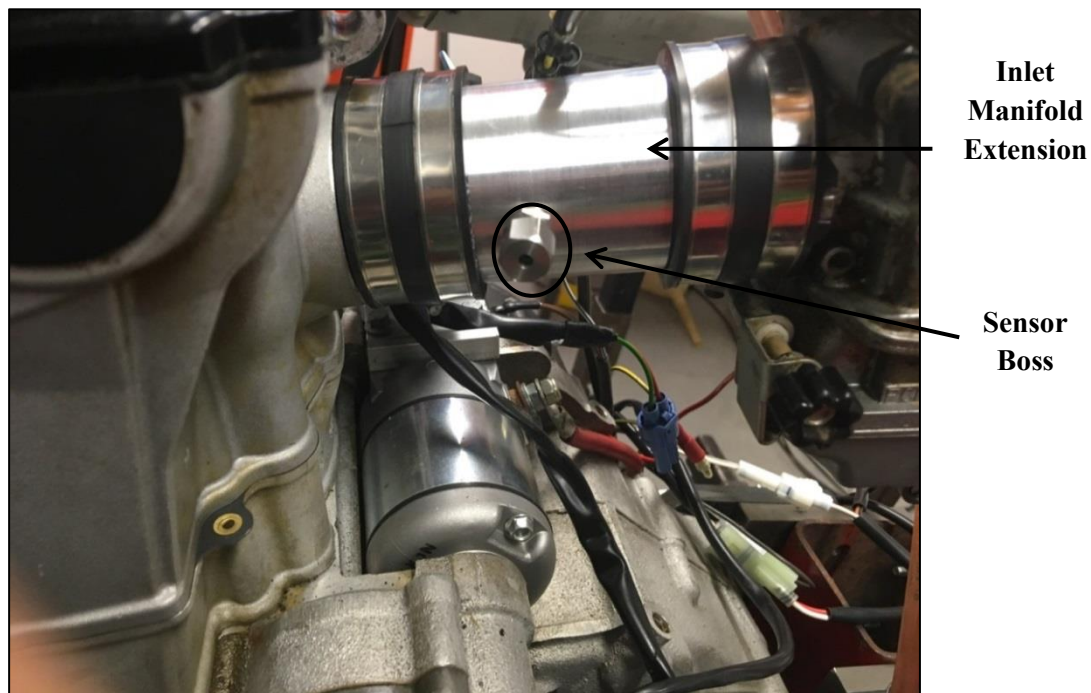


**Figure 6.12.** Air inlet modification to allow for the sensor installation.

#### **6.4.11. Other engine test considerations**

Other considerations included throttle position control, gear changing mechanism, data acquisition system.

### **6.5. Modifications required for the accommodation of new piston in the test engine**

Balancing the rotating assembly is critical to maximise the engine performance and longevity. Any mass changes made to any component in the rotating assembly require

rebalancing of the whole assembly; more information can be found in these sources (Builder; Builder, 2009; Massingill, 2016). Pictures of the modified crankshaft can be seen in Figure 6.13.

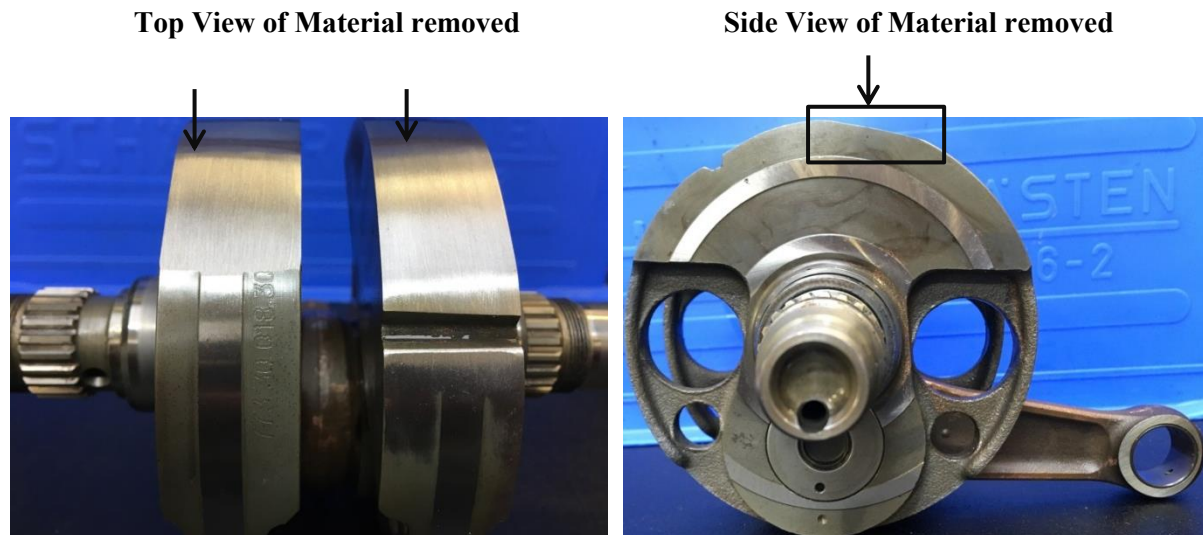


**Figure 6.13.** Pictures of modified crankshaft assembly.

## **6.6. Comparison of the original and new engine configurations**

Engine developers use various performance indicators for comparing different engine configurations. Some of these indicators can be measured experimentally while others can be calculated from experimental data using various equations. The various performance indicators that were measured experimentally for both test configurations were fuel consumption (g/sec), torque (Nm), intake pressure (bar), test cell temperature (°C), coolant temperature (°C), air fuel ratio (AFR) and in-cylinder peak pressure (bar). Other fundamental performance indicators include mass flow rate of air (MFR<sub>air</sub>), which can be used as an indication of load instead of torque; and brake specific fuel consumption (BSFC), which can be used instead of fuel consumption. MFR<sub>air</sub> can be calculated from air fuel ratio or lambda ( $\lambda$ ) using equation (6.2)



$$\text{Lambda (AFR)} = \frac{1}{\phi} \quad (6.2)$$

$\phi$  is equivalence ratio which is the inverse of air fuel ratio and can be calculated using equation (6.3)

$$\phi = \frac{AFR_{st}}{AFR_{act}} = \frac{(\frac{m_a}{m_f})_{st}}{(\frac{m_a}{m_f})_{act}} \quad (6.3)$$

Substituting (6.3) into (6.2) and rearranging for  $(m_a)_{act}$  gives

$$(m_a)_{act} = (\frac{m_a}{m_f})_{st} \times AFR \times (m_f)_{act} \quad (6.4)$$

Where  $m_a$ ,  $m_f$ ,  $(m_a)_{act}$ ,  $(m_f)_{act}$ , AFR and  $(\frac{m_a}{m_f})_{st}$  are mass of air (g), mass of fuel (g), mass of air actual (g), mass of fuel actual (g), air fuel ratio and air fuel ratio standard/stoichiometric.  $(\frac{m_a}{m_f})_{st}$  is 14.7 (standard commercial gasoline), AFR and  $(m_f)_{act}$  are measured experimentally.  $(m_f)_{act}$  is actual fuel consumption and measured as g/sec.

Brake specific fuel consumption (BSFC, g/kW.hr) can be calculated using equation (6.5)

$$BSFC = \frac{m_f}{P_b} \quad (6.5)$$

Where  $P_b$  is brake power (kW) and can be determined from equation (6.6)

$$P_b = 2\pi T_b \frac{N}{n_r} \quad (6.6)$$

Where  $T_b$ ,  $N$  and  $n_r$  are torque (Nm), engine speed (rpm) and the number of revolution per cycle.  $n_r$  is 1 and 2 for two and four stroke engine respectively.  $\frac{N}{n_r}$  is the rate at which the

engine functions (i.e. at which it produces work output). Note to convert N from revolution per minute to revolution per second.

Volumetric efficiency, when comparing the two different pistons, is critical to explain the difference in performance. Engine torque and hence power are directly related to the amount of air the engine can ingest in each cycle and volumetric efficiency measures the actual amount of air ingested by a 4 stroke engine during the open or breathing part of the cycle.

Volumetric efficiency can be calculated using equation (6.7)

$$\eta_v = (m_a)_{act} \times \frac{1 \times n_r}{\rho_a \times V_d \times N} \quad (6.7)$$

Where  $\eta_v$ ,  $\rho_a$ ,  $V_d$  are volumetric efficiency, air density (Kg/m<sup>3</sup>) and displacement volume of the engine (m<sup>3</sup>).

Various performance indicators such as brake specific fuel consumption, mass flow rate of air and volumetric efficiency were calculated using equations (6.2-6.7) and the experimental data from engine tests. These performance indicators were plotted in graphical forms, as reported in Section 6.7. The engine test results in Figures 6.14-16 in two different configurations could not clearly show if the engine performance improved with the new piston compared to the original piston. The results however did show that the new piston was more fuel efficient at lower speed (3000 rpm) and lower torques (Figure 6.14a-b) which could be due to the new piston running leaner; the data showed the engine had higher volumetric efficiency with new piston (Figure 6.14c-d). An engine with higher volumetric efficiency is generally more fuel efficient and therefore uses less fuel to produce the same output.

For the other two engine speeds of 4500 rpm and 6000 rpm, the results showed that the new piston was more fuel efficient than the original piston at lower torque and MFR<sub>air</sub> values. For engine speed of 4500 rpm, these torque and MFR<sub>air</sub> values were less than 10 Nm and 145

g/sec respectively (Figure 6.15a-b). For engine speed of 6000 rpm, these torque and MFR<sub>air</sub> values were 13 Nm and 235 g/sec respectively (Figure 6.16a-b). Overall, the new piston showed benefits at 3000 and 6000 rpm.

Even though testing of the new piston has demonstrated application of the new alloy in higher temperature applications such as pistons for internal combustion engine. However, the engine testing facility available for this research was not able to control certain parameters that could affect the engine performance such as air-intake temperature, humidity etc. The test cell temperature was measured during testing, but it could not be controlled. On average the test cell temperature was 6 °C higher for new piston than the original piston and this would have negatively impacted the engine performance.

Many researchers (Birtok-Băneasă, Rațiu and Hepuț; Pan *et al.*, 2015; Treeamnuk, Treeamnuk and Papakae, 2018; Khaifullizan *et al.*, 2021) have investigated the impact of intake air temperature on engine performance specifically fuel consumption and all reported that decreasing air intake temperature decreases fuel consumption due to the increasing amount of Oxygen in air. Colder air has higher Oxygen density compared to hotter air. In addition; lower air intake temperature reduces ignition delay and the combustion starts at the end of the compression stroke and early expansion stroke therefore converts larger portion of the fuel energy to useful work.

Furthermore, the research by (Birtok-Băneasă, Rațiu and Hepuț; Treeamnuk, Treeamnuk and Papakae, 2018) showed that the impact of air intake temperature on engine performance is more dominant at higher engine speeds. This is due to the higher injected fuel at higher engine speed which requires more Oxygen to complete the combustion. (Birtok-Băneasă, Rațiu and Hepuț, 2017 demonstrated that a 10 degrees increase in air intake temperature

from 20 °C to 30 °C resulted in 4% more fuel consumption at 1500 rpm while this value increased to 22 % at engine speed of 3000 rpm.

Also, the test engine in this project was using carburettor not fuel injector which most modern engine use and therefore the air fuel mixture could not be controlled.

### **6.7. Tests results with original and new pistons**

The engine tests were carried out with the original and new pistons. The original piston was tested twice, where the purpose of the first tests was to obtain the worst case loading on the piston for designing the new piston. The engine was therefore tested at speeds of 3500, 4000, 5000, 6000 and 7000 rpm in half and full throttle positions. The critical load case occurred at 6000 rpm at full throttle (see Section 5.5.1).

The second set of tests with the original piston was carried out at 3000, 4500 and 6000 rpm at different fixed torques ranging from 6-24 Nm at increment of 3 Nm. In the second case with the new piston, tests were carried out at the same conditions as for the second set of the tests with the original piston. Measurements were taken under the same operating conditions in order to determine any gains or losses in the engine performance.

At each operating condition, the engine was allowed to run for about 5-6 minutes until it reached thermal stability in the new state before any measurements were taken. Thermal stability was established by monitoring the coolant temperature and the amount of exhaust oxygen (from lambda sensor readings) until they stopped fluctuating.

The engine was tested in third gear only for all the engine speeds. The engine had a gear ratio of 3.32 between the gear box and output sprocket for third gear and the torque values obtained from the dyno were therefore divided by 3.32 to get the actual torque. The engine performance results for both configurations in a graphical form are given in Figures 6.14–

6.16 while some of the experimental results are tabulated in Appendix C.5. Descriptions of the KPIs are given as the following along with why they are important to measure.

BSFC stands for brake specific fuel consumption and it describes the amount of fuel used per unit energy output. In other words, it indicates how well the fuel is utilised and it is inversely proportional to thermal efficiency. It is one of the most important criterion for comparing different engine configuration. Given everything else being the same, the engine with lower BSFC is better.

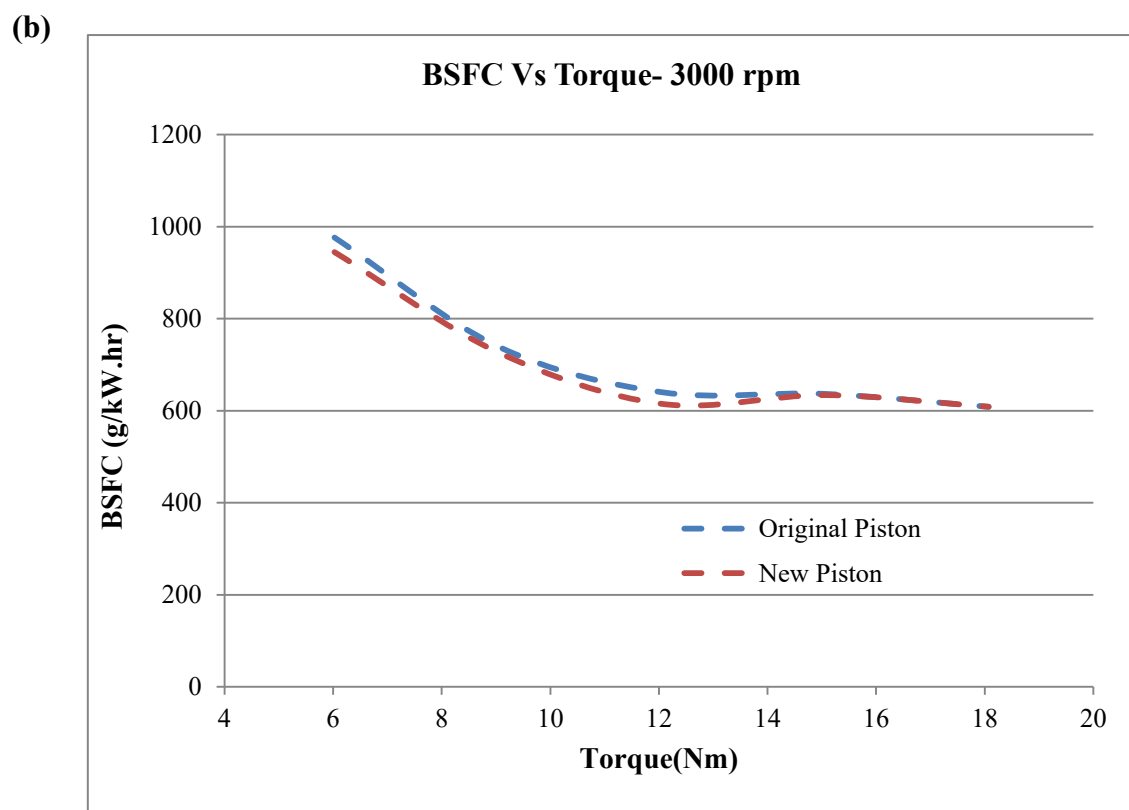
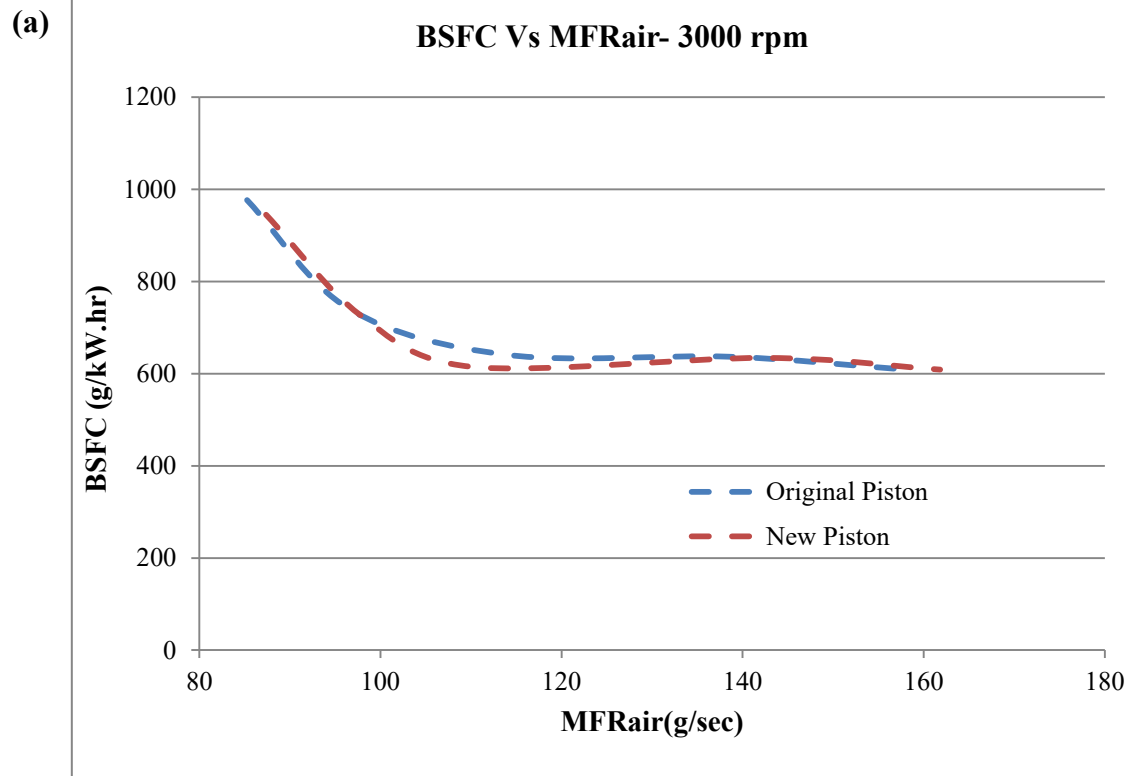
Torque is the ability of an engine to turn the crankshaft overcoming the resistance applied to the wheels and used in conjunction with BSFC. When other engine operational parameters are similar or the same, the engine with the same BSFC, but higher torque is a better performance engine, hence is a critical criterion to measures. It is measured directly from the dynamometer.

Volumetric efficiency measures the actual amount of air ingested by an engine during the open or breathing part of the engine cycle. Engine torque and hence power is directly related to the amount of air the engine ingests in each cycle. It is critical to compare the volumetric efficiencies of engine when comparing their torques as lower volumetric efficiency leads to lower torques hence the comparison will not be fair.

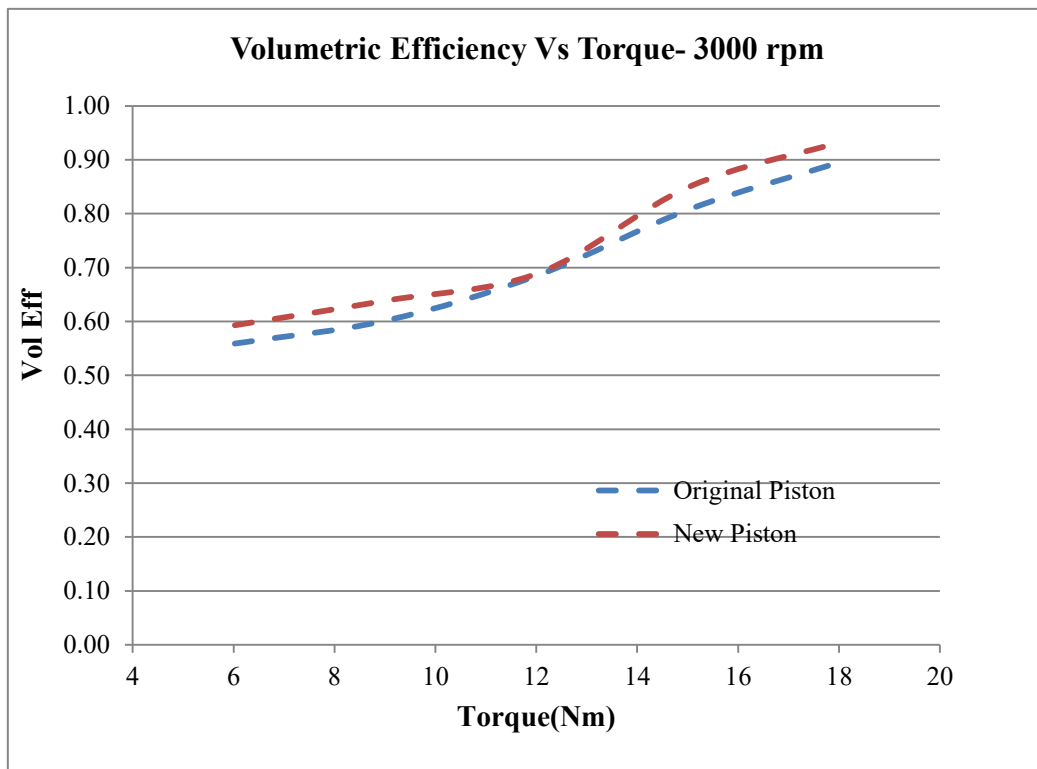
In-cylinder peak pressure has direct effect on torque and it is therefore an important indicator to consider for fair comparison when comparing different engine configurations.

#### **6.7.1. Test results at 3000 rpm**

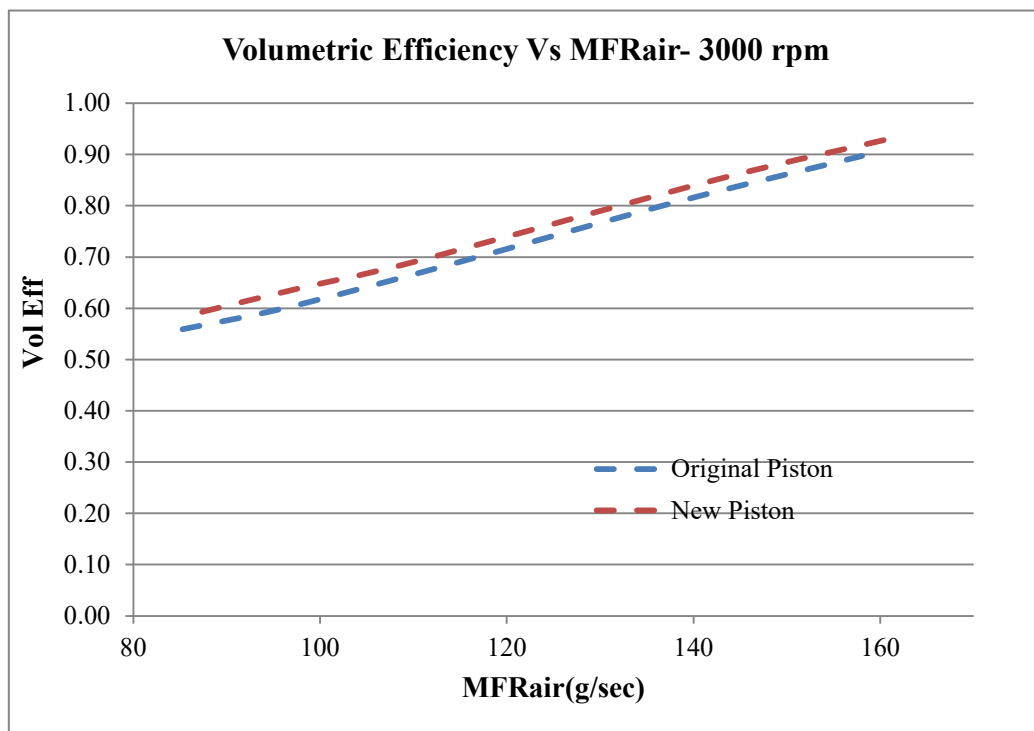
The various engine performance results for both piston configurations at 3000 rpm are plotted in Figure 6.14.



(c)



(d)



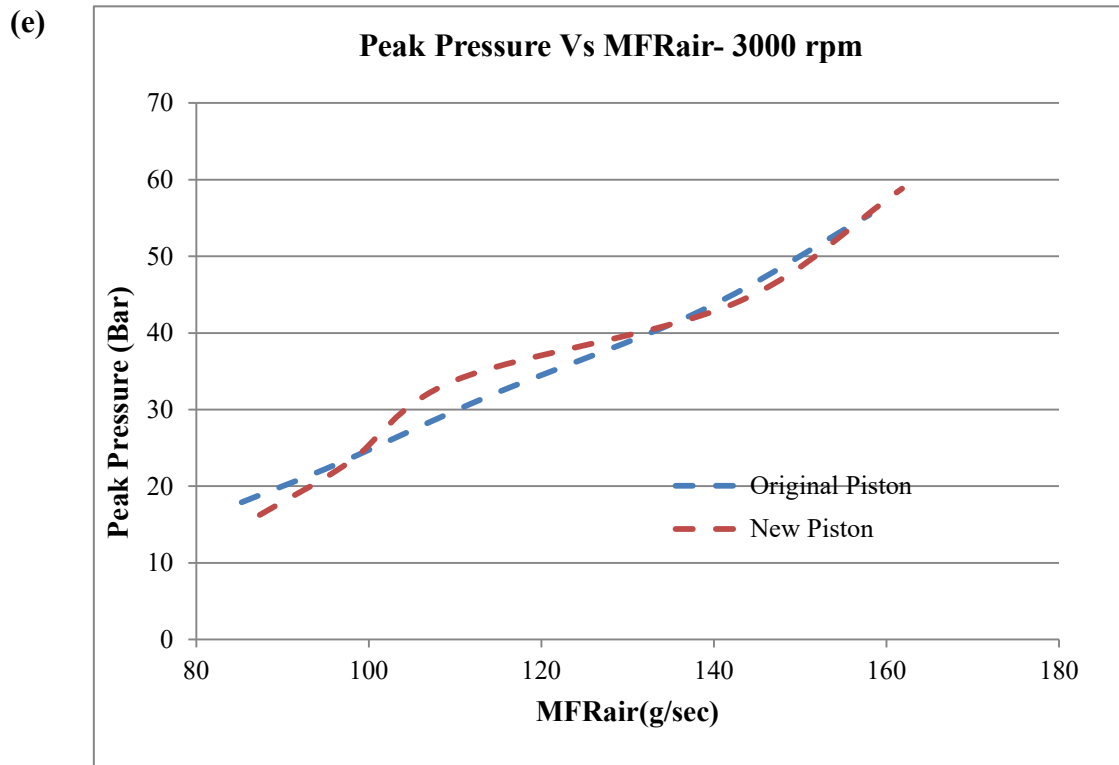


**Figure 6.14.** Comparisons of various performance indicators for original and new pistons at 3000 rpm **a)** BSFC vs. MFRair **b)** BSFC vs. torque **c)** volumetric efficiency vs. torque **d)** volumetric efficiency vs. MFRair **e)** peak pressure vs. MFRair

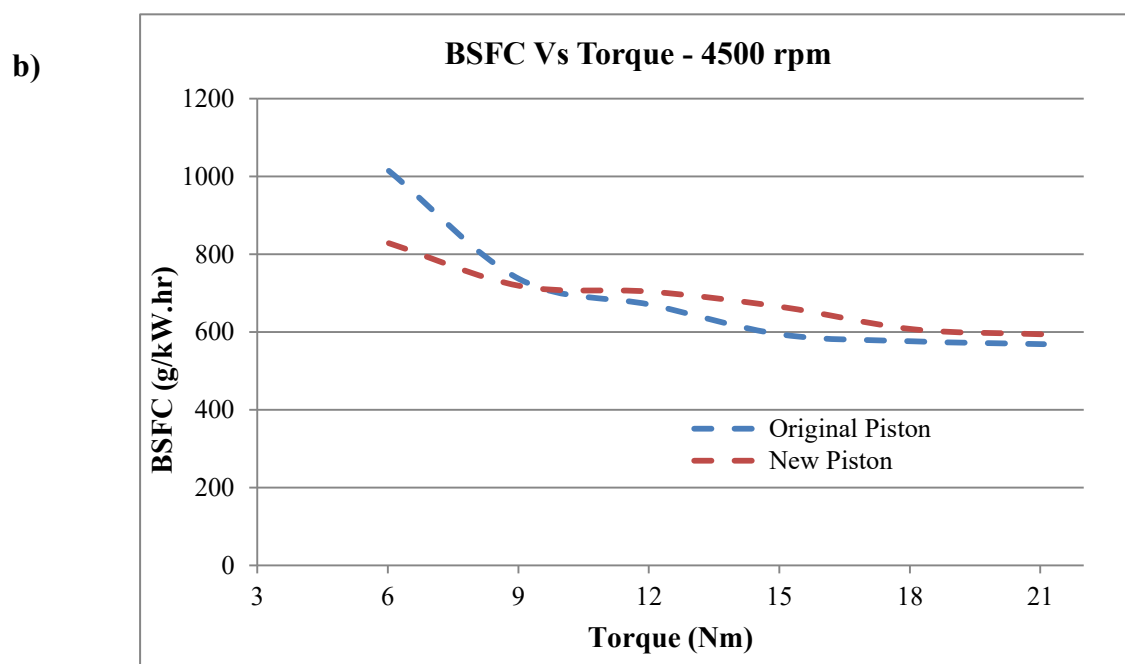
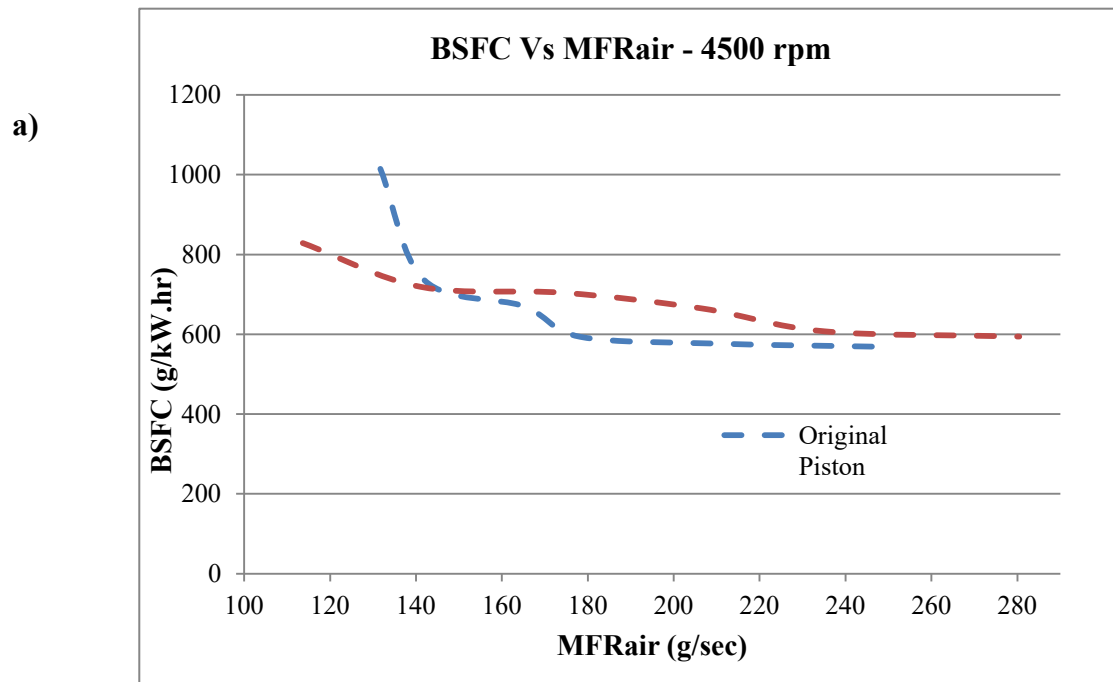
The results for 3000 rpm in Figure 6.14 indicated that the new piston was more fuel efficient compared to the original piston especially at lower torque (Figures 6.14a-b). This may be attributed to the higher volumetric efficiency of the engine which leads to leaner operation of the engine with the new piston (Figures 6.14c-d). The AFR values measured were higher / leaner for the new piston compared to the original piston (Table C.3). For the same torque, the engine with higher volumetric efficiency will consume less fuel due to the availability of more Oxygen which reduces ignition delay hence converts more of the fuel energy to useful work (Birtok-Băneasă, Rațiu and Hepuț, 2017). Furthermore, higher volumetric efficiency reduces pumping work/losses (the work in exhaust and intake strokes) which improves specific fuel consumption (Sher, 1998).



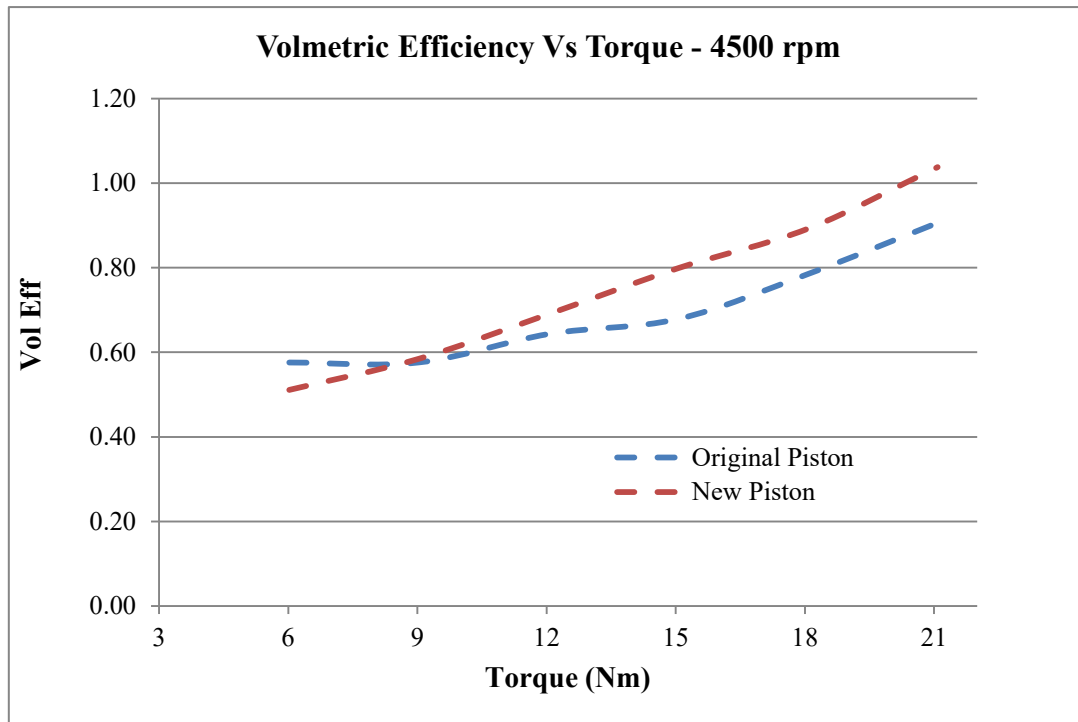
The in-cylinder peak pressure for original piston increases more linearly with MFRair compared to the new piston; the original piston follows the peak pressure as expected.

### 6.7.2. Test results at 4500 rpm

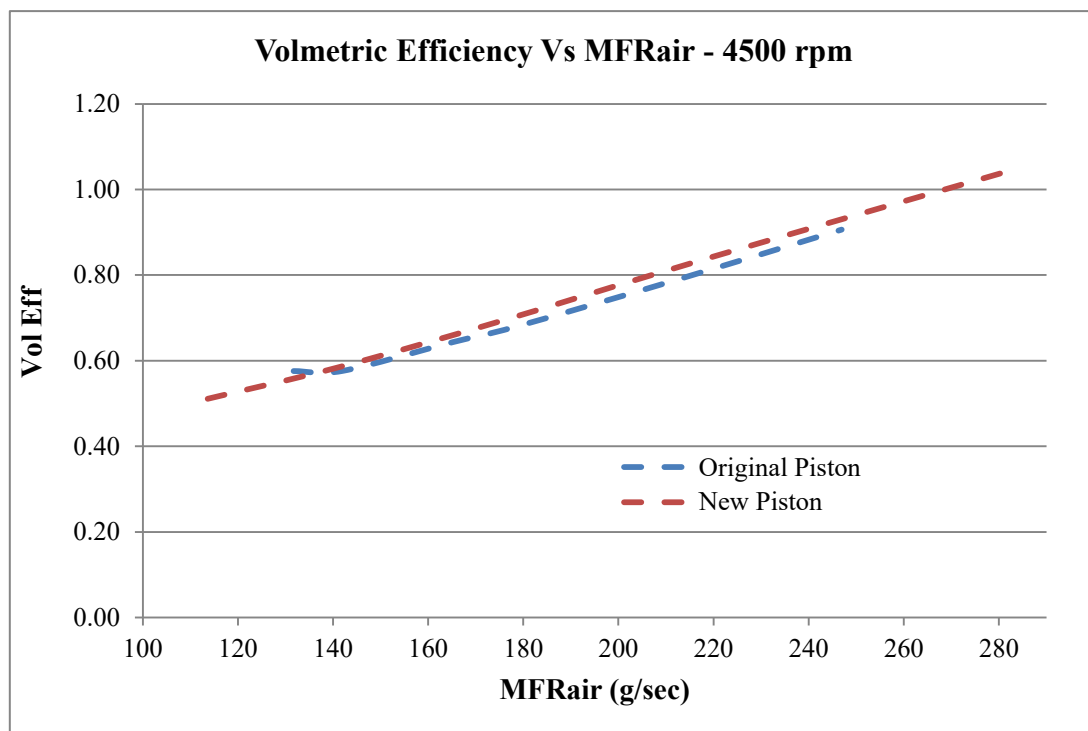
The various engine performance results for both configurations at 4500 rpm are plotted in Figure 6.15.



c)



d)



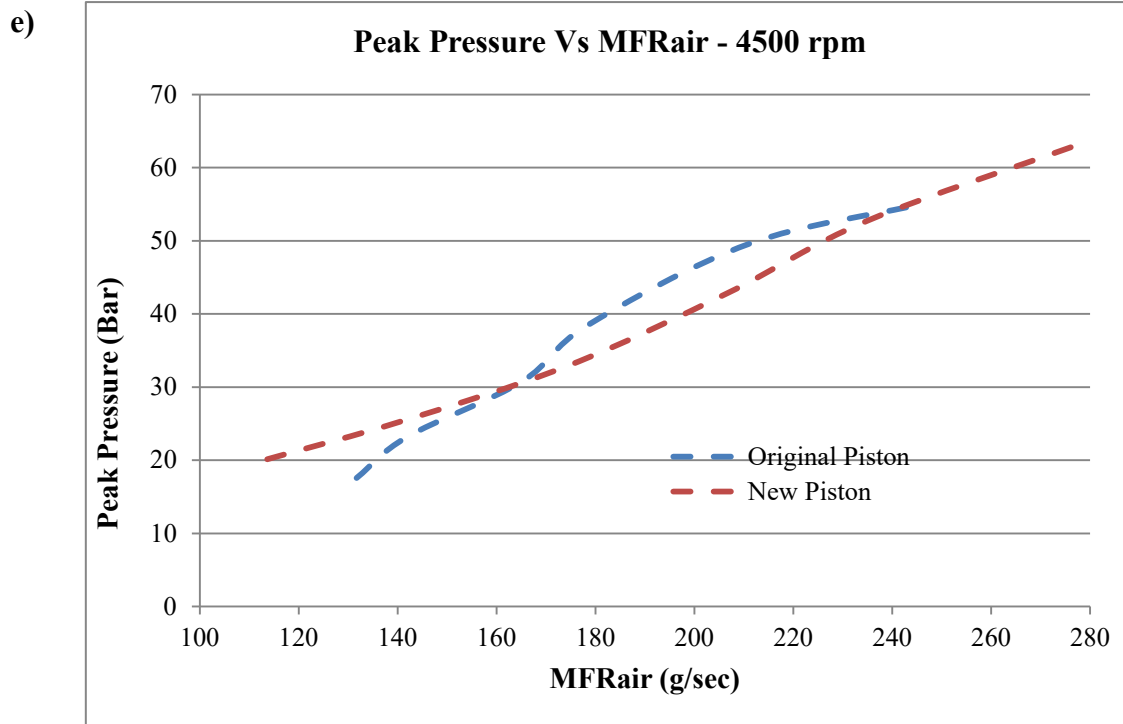


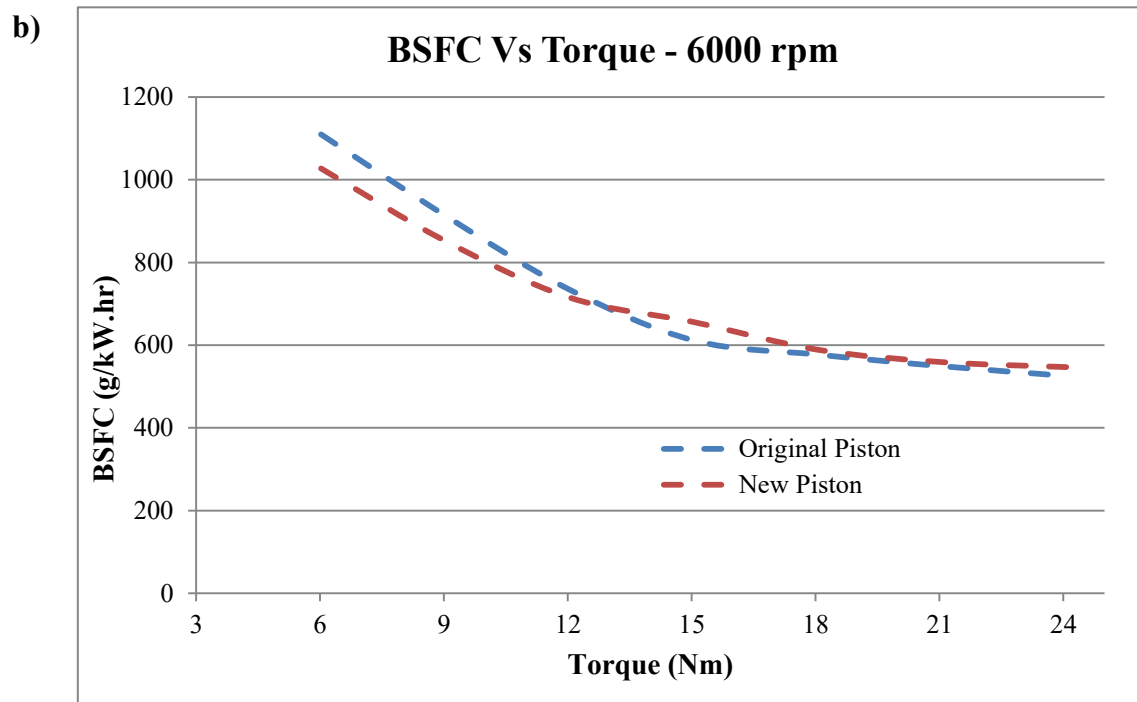
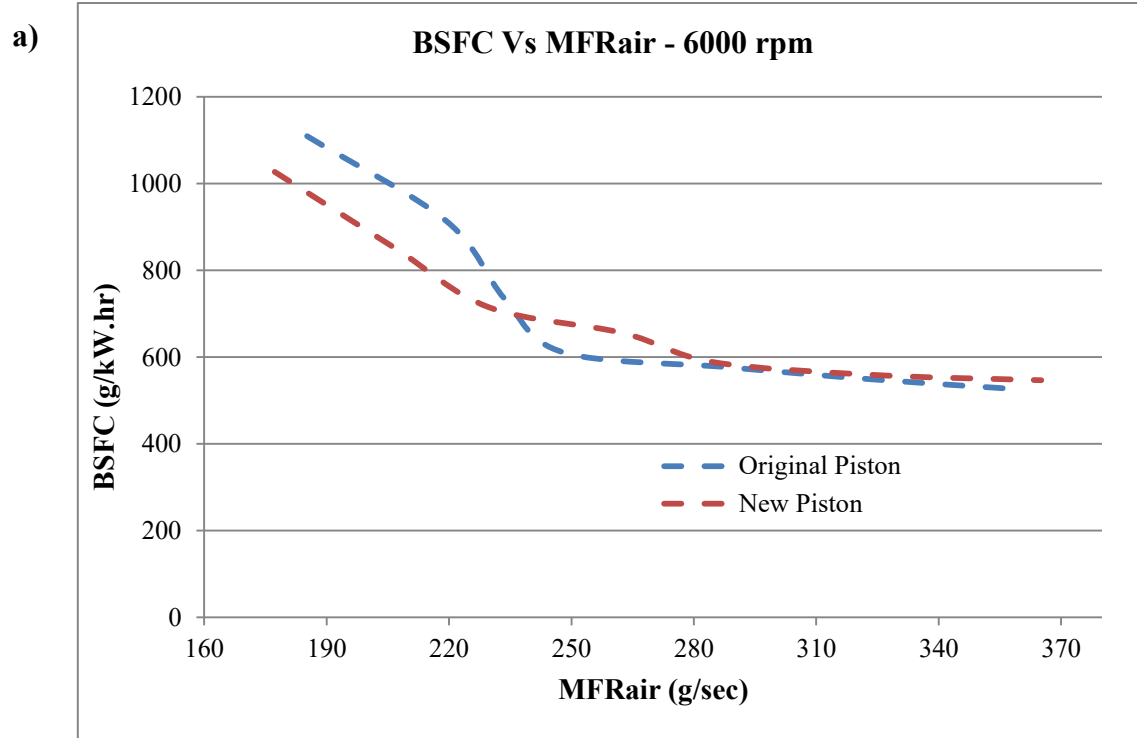
**Figure 6.15.** Comparisons of various performance indicators for original and new pistons at 4500 rpm **a)** BSFC vs. MFRair **b)** BSFC vs. torque **c)** volumetric efficiency vs. torque **d)** volumetric efficiency vs. MFRair **e)** peak pressure vs. MFRair

The results for engine speed of 4500 rpm showed that the new piston was more fuel efficient than the original piston at lower torque and MFRair values of less than 10 Nm or 145 g/sec respectively (Figures 6.15a-b). This was despite that the engine with new piston had smaller volumetric efficiency in the aforementioned MFRair range (Figures 6.15c-d). The lower fuel efficiency of new piston at certain torque values despite higher or similar volumetric efficiency especially at higher torque values may be due to the higher intake air temperature which adversely affect engine performance due to decrease in Oxygen as mentioned earlier.

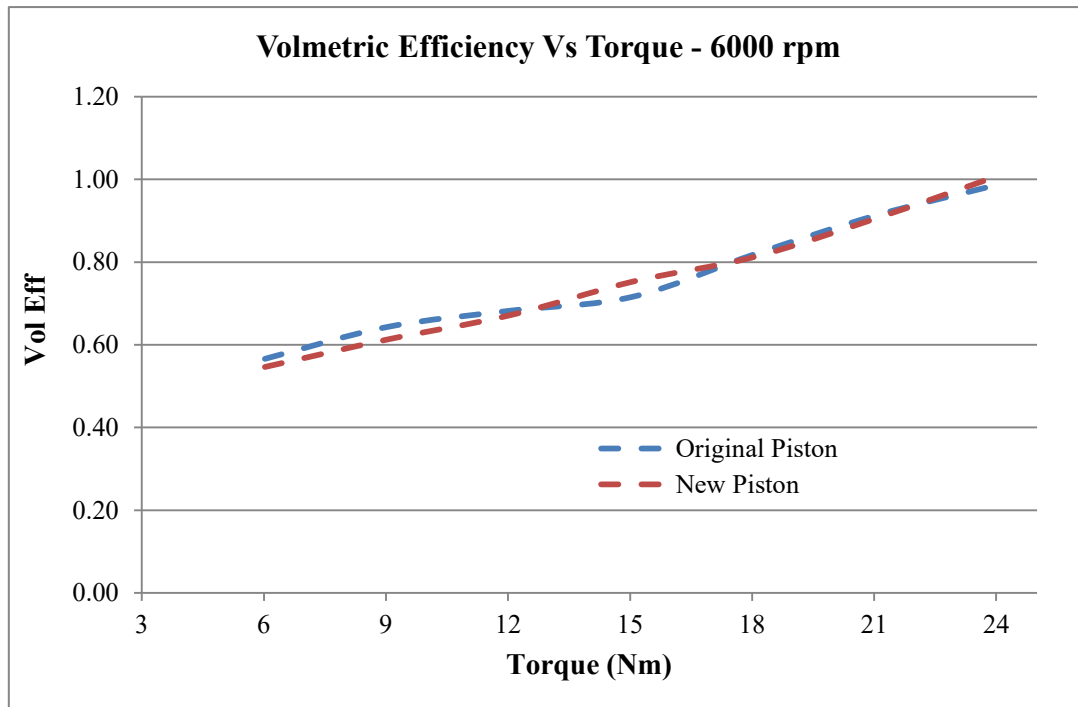
The engine with original piston showed abnormal behaviour at lower torque and MFRair values (Figures 6.15a-b) as the BSFC values drop sharply (Figures 6.15a).

### 6.7.3. Test results at 6000 rpm

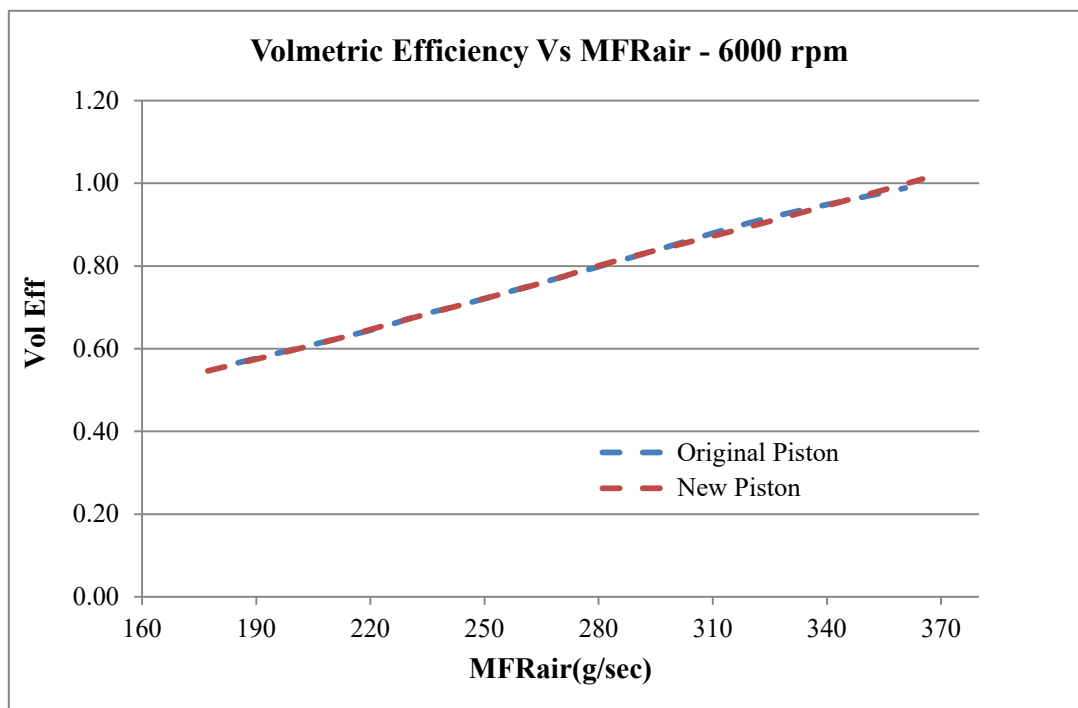
The various engine performance results for both configurations at 6000 rpm are plotted in Figure 6.16.



c)



d)



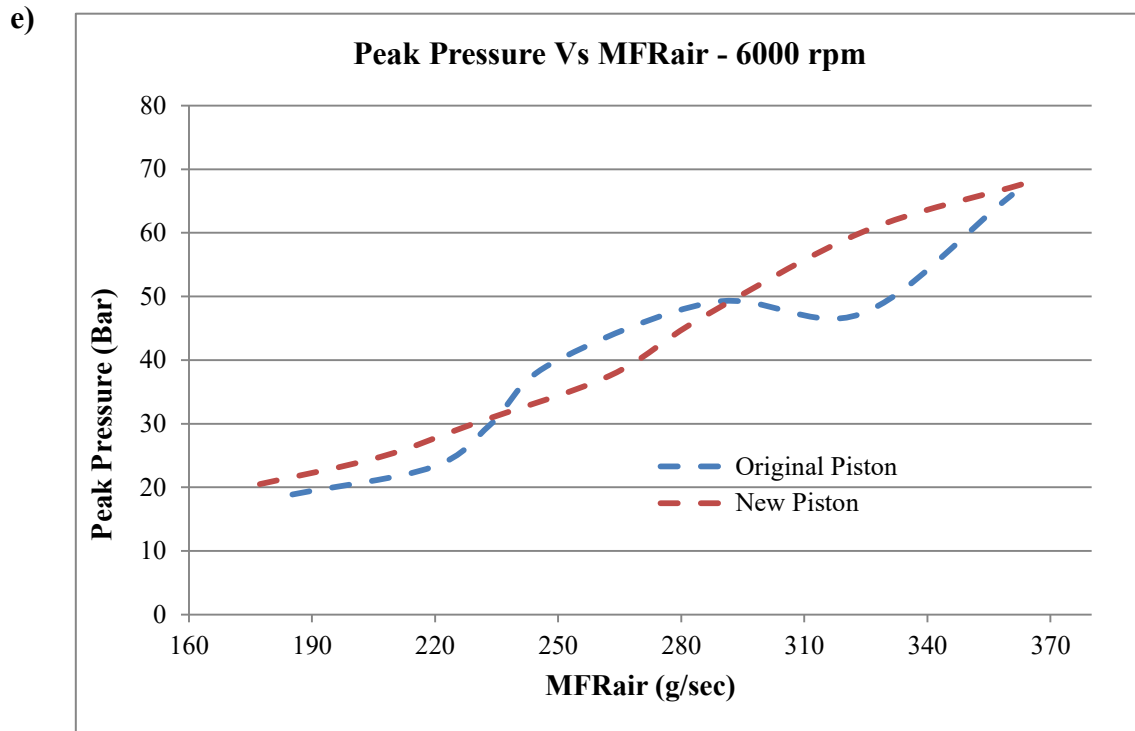


**Figure 6.16.** Comparisons of various performance indicators for original and new pistons at 6000 rpm **a)** BSFC vs. MFRair **b)** BSFC vs. torque **c)** volumetric efficiency vs. torque **d)** volumetric efficiency vs. MFRair **e)** peak pressure vs. MFRair

The results for engine speed of 6000 rpm showed that the new piston was more fuel efficient than the original piston at lower torque and MFRair values of less than 13 Nm or 235 g/sec respectively (Figures 6.16a-b). The engine with both pistons had nearly the same volumetric efficiencies (Figures 6.16c-d), but higher in-cylinder peak pressure with new piston in the aforementioned MFRair range (Figures 6.16e). The engine with original piston showed abnormal behaviour at lower MFRair values as the BSFC values drop sharply (Figures 6.16a). The lower fuel efficiency of new piston at certain torque values despite similar volumetric efficiency especially at higher torque values may be due to the higher intake air temperature which adversely affect engine performance due to decrease in Oxygen as mentioned earlier.

The limited engine testing results presented in this work have shown that the new piston produces enhanced performance in certain operating conditions, whilst performing similarly or slightly worse in others. To ultimately determine whether the new lightweight piston would generate any sizeable difference in engine performance and/or efficiency across the wider engine running envelope, further work is needed.

## **6.8. Summary**

The chapter started by laying out the engine test methodology and defining the test scope and limitations. The engine test preparations were explained in details along with the modifications required to balance the crankshaft due to the lightweight piston. The work undertaken in this chapter consisted in testing the engine with the old and new lightweight pistons installed. The engine results for the two cases were presented in graphical forms in this chapter.

## **Chapter 7: Discussion**

### **7.1. Introduction**

The literature review showed that racing engineers and engine designers knew from the very early stage of engine development that engine performance could be improved by increasing the mean piston speed (MPS). Reducing piston mass was one of the approaches identified to increase MPS hence the engine designers experimented with stronger and lighter materials and switched from cast iron to steel. That trend has continued ever since with the application of different alloys and composites in pistons as described in Chapter 2 and the investigation of the new nanostructured aluminium alloy for piston application in this project is one more event in the evolution of piston materials.

In order to assess the suitability of the new alloy for piston application and to obtain the mechanical properties required for piston design, the alloy's microstructure was characterised and a series of mechanical tests were carried out as detailed in Chapter 4. Furthermore, to understand the piston operating environment, a number of engine tests were carried out with the unmodified original piston. To develop a new lighter piston with nearly the same structural integrity, a finite element analysis approach was used as described in Chapter 5.

The discussion summarises findings of the results from the testing and simulation work described in the preceding chapters. Through the work undertaken, it will be shown that the overall aim of the project, and the objectives identified in Chapter 1 have been achieved.

### **7.2. Microstructure of the alloy**

From investigating the results obtained in Chapter 4, it was concluded that accurate results had been achieved. The microstructural homogeneity of the as-received alloy observed and determined through optical microscopy and particle analyses corresponded to the hardness



tests taken across the sample surface. The approximately same averaged particle size and little varying hardness across the sample's surface was indicative of the alloy having isotropic properties throughout the bar's cross section.

The particle volume fraction results confirmed the specified volume fraction of 22.5% by the manufacturer (Figure 4.7) and it can be seen in Figure 4.4 in Chapter 4 that the particles were uniformly dispersed which can be attributed to rapid solidification as suggested by (Rafiei, Varahram and Davami, 2012; Abed, 2014). The results of all observed particles in Figure 4.9 determined that nearly 50% and 90% of the particles had 3D sizes of about up to 1.7 and 3.2  $\mu\text{m}$  respectively. The particles sizes were many folds smaller compared to the aluminium alloys produced using industrial metallurgy (IM) methods where the particle sizes vary 10 – 100  $\mu\text{m}$  (Lobry *et al.*, 2011). The smaller size of particles can be ascribed to the rapid solidification (RS) method melting spinning used to produce the alloy investigated in this work (Rafiei, Varahram and Davami, 2012).

In addition, the results in Figure 4.9 showed that there was significant variation in particle sizes of all the observed particles across the bar's cross section. The actual particle sizes were likely to be smaller than measured because a significant number of the particles had been dislodged from the aluminium matrix during grinding and polishing of the sample and left voids which were expected to be larger than the particles. The two distinct peaks seen on the left side of the graph in Figure 4.9 showed the two intermetallics observed in the XRD analysis in Figure 4.43.

The X-ray diffraction (XRD) analyses (Figure 4.43) determined the presence of three different phases with the most dominant being Al  $\alpha$ , while the other two were  $\text{Mg}_2\text{Si}$  and  $\text{Mg}_{17}\text{Al}_{12}$ . The latter two are known to improve not only strength of the alloy, but other

properties such as wear, corrosion and ductility (Yan, 2014; Asghar *et al.*, 2020; Moharami *et al.*, 2020; Wang *et al.*, 2021)

Furthermore, the energy dispersive X-rays (EDS) analyses for the bulk alloy (Figure 4.12 and Tables 4.1-2) showed the respective compositional ratio of the elements specified by the manufacturer, however in some instances the EDS results did not exactly match the manufacturer specification. It was due to the dislodging of the particles. The EDS analyses carried out on large particles showed that they were mainly composed of Al, Mg and Si respectively (Figure 4.15 and Tables 4.3-4) which also correlated to the intermetallic particles identified in XRD results shown in Figure 4.43.

### **7.3. Heat treatments**

A soaking temperature and time of 530 °C and 1 hour respectively were used for solid solution heat treatment and there were some bases from literature for selecting these values; however no specific tests were carried out to determine the effects of them on the aging process or T6 condition.

As the alloy contained large amount of copper and previous knowledge of the similar alloys have shown that the artificial aging should start within 45 minutes of quenching to avoid precipitation that could compromise the hardness of the alloy in T6 condition. This was achieved through force cooling the furnace from solid solution temperature (530 °C) to aging temperature (140–180 °C) using a fan. However the time varied from 35–45 minutes as it depended on the ambient temperature at the laboratory. This little time variation between quenching and aging did not seem to have any effect on the T6 condition.

As the material contained combination of alloying elements hence exhibited a multistage precipitation which made it difficult to select clearly defined T6 condition. It was not straight forward to determine the T6 condition from the artificial aging heat treatment results in

Figures 4.18–4.19 as the results overlapped and fluctuated. However, the aging results at 160 °C followed the theoretical curve pattern for T6 condition which increases incrementally reaching a maximum and then slowly decreases. Furthermore, the hardness of the sample heat treated at 160 °C for 30 hours did not change significantly after removing from the furnace and leaving it at RT for a week (Figure 4.19). This seemed to correspond to a T6 condition. The hardness of the new alloy increased from an average of 97 HV (Figure 4.10) in as-received state to 175.5 HV in T6 (Figure 4.19). Furthermore, the scatter in the hardness results was less than 4% (Figures A3 – A14).

The samples soaked at different temperatures reached stability at different amount of times; however the samples at 200 °C took the longest (100 h) to reach stability (Figures 4.22–4.23). While the samples treated at 150 °C did not have any impact on the hardness at all, indicating that no significant microstructural changes occur in the alloy up to 150 °C. The alloy reached thermal stability in approximately 100 hours for all temperatures.

#### **7.4. Mechanical properties, deformation and fracture behaviour**

It can be seen from the tensile tests results in Figure 4.26 that the specimens in room temperature or T6 condition had the highest yield strengths with an average value of approximately 409 MPa, but showed no appreciable deformations/strains (Figure 4.27). On the other hand, the specimens at 350 °C had the lowest strengths with an average value of approximately 26 MPa (Figure 4.26), but had the highest deformations (Figure 4.27). The results also indicated that the alloy did not show any significant reduction in strength up to 150 °C similar to stability results in Figures 4.22-23 which could be due the lack of coarsening of the strengthening particles (Lobry *et al.*, 2011). Furthermore, there was not any significant scatter in test results for different specimens for the same testing conditions because the test specimens were stabilised prior to testing.

Fracture analyses of a tensile test specimen tested at room temperature showed that the specimen had failed in brittle manner as no necking could be observed (Figure 4.31a). While a specimen tested at 350 °C had appreciable necking and failed in ductile manner (Figure 4.31b). Furthermore, the specimen tested at RT fractured approximately 45° to the applied load while the specimen tested at 350 °C fractured 90 to the applied load, showing the fracture was caused by shear stress.

Fractographic analyses of the fractured faces (Figures 4.33 and 4.35) showed that the large particles made of Al, Mg and Si formed pits around them and could have been the likely cause of fracture/crack initiation. The average dimple sizes were 3.8 and 5.4 micron for samples tested at RT and 350 °C respectively. In addition, the fracture surface of the specimen tested in T6 state (Figure 4.33) did not show any appreciable microplasticity compared to the specimen tested at 350 °C Figure 4.35. The microplasticity at 350 °C could be due to the aluminium matrix becoming overly ductile and flows. Furthermore, there were more micro-cracks in the specimen tested in T6 state than the specimen tested at 350 °C; this could have been due to the lack of microplasticity indicating that the aluminium matrix had been sheared.

The compression test results in Figure 4.38 demonstrated that the specimens in extrusion direction (ED) had higher yield strengths compared to the transverse direction. This was because of the grains alignment along the extrusion direction due to the nature of the extrusion process (Chen *et al.*, 2009; Wang *et al.*, 2016). Furthermore, the average yield strength in transverse direction was approximately 510 MPa which was 25% higher compared to 409 MPa in tension. Fractographic analyses of the specimens tested in compression also revealed that pitting occurred around large particles (Figures 4.39 and 4.41) that were made of Al, Mg and Si (Figures 4.40 and 4.42).

The tensile test results obtained in Section 4.6.1 for the new alloy showed an improvement over other conventional aluminium alloys at the test temperatures. Figure 7.1 compares the yield strengths of the new alloy and two conventional aluminium alloys used in high temperature applications such as internal combustion engine pistons. The yield strength values for the conventional alloys were obtained from (American Society for Metals. Handbook, 1979; Kaufman, 1999).

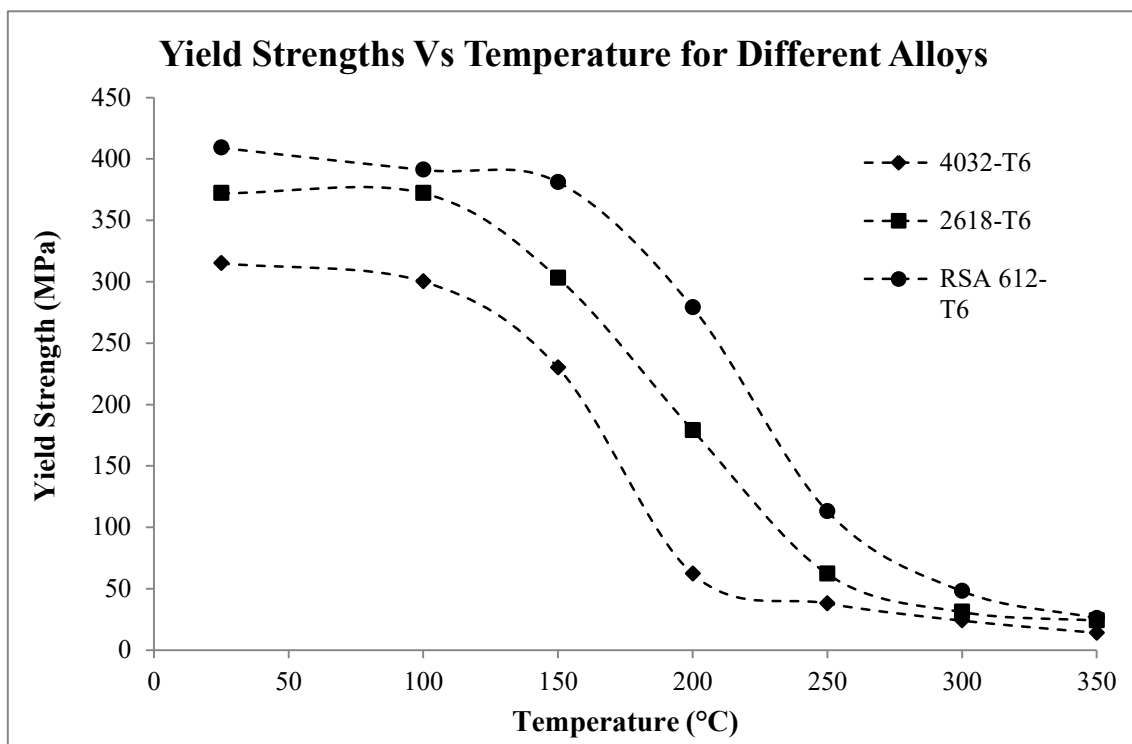


**Figure 7.1.** Yield strength comparison of two different piston aluminium alloys vs. the new alloy (American Society for Metals. Handbook, 1979; Kaufman, 1999).

The yield strength comparison graph of the new alloy and two conventional aluminium alloys in Figure 7.1 shows that the new alloy has better yield strengths at varying test temperatures than the conventional aluminium alloys. This opens doors for wide types of high temperature applications such as internal combustion engine components. On the basis of microstructural analyses carried out in this work and results of similar materials from literature (Tellkamp,

Lavernia and Melmed, 2001; Han *et al.*, 2003; Shanmugasundaram *et al.*, 2010), it appears that the higher yield strengths of the new alloy can be attributed to strengthening mechanisms such as grain size refinement (Hall-Petch effect) and precipitation hardening (Orowan mechanism) made possible by rapid solidification (Shanmugasundaram *et al.*, 2010). It has been shown by (Liu *et al.*, 2010) that increase of Mg content in aluminium decreases average grain size and improves grain distribution. Again, addition of high Mg content to aluminium has been facilitated by rapid solidification.

## 7.5. Strength contribution of different strengthening mechanisms

In order to estimate the contribution of each strengthening mechanism to the yield strength of an alloy, an in-depth characterisation of the microstructure is needed. There are few publications such as (Pedrazzini *et al.*, 2016) that have carried out such characterisation on aluminium based nanostructured aluminium alloys. The strength contributions of different strengthening mechanisms to the investigated alloy have been estimated as the following.

### 7.5.1. Particle strengthening

The effect of particles on dislocation movement depends on their location in the microstructure, type of interface, strength and size. Dislocations either shear through particles or bow around particles which leave a dislocation loop around the particles and the latter is known as Orowan mechanism. Orowan mechanism is the more common strengthening mechanism in alloys such as the one investigated in this work. Its contribution to the yield strength can be estimated by equation (7.1) (Galano and Audebert, 2022)

$$\Delta\sigma_p = M \frac{G \cdot b \cdot v}{L_{ps}} \quad (7.1)$$

Where  $\Delta\sigma_p$  is the strengthening contribution to yield stress (MPa) due to the hard particles, M is the Taylor factor that accounts for the homogeneous deformation of the individual grains in

a polycrystal,  $G$  is the shear modulus (27 GPa for aluminium),  $b$  is the Burgers vector (0.286 nm) (Shanmugasundaram *et al.*, 2010) and  $L_{ps}$  is the edge to edge planar inter-particle spacing (nm) for the spherical particles that can be estimated using equation (7.2) (Galano and Audebert, 2022)

$$L = \frac{2.D_s}{3.f_v} (1 - f_v) \quad (7.2)$$

Where  $f_v$  is particle volume fraction (22.5%) and  $D_s$  is the mean planar particle diameter (nm), which is related to the particle diameter in volume (7.3),  $D_p$  as (Galano and Audebert, 2022)

$$D_s = D_p \sqrt{\frac{2}{3}} \quad (7.3)$$

For an aluminium based nanostructured alloy (Al-Cu), (Galano and Audebert, 2022) estimated the precipitate diameter ( $D_p$ ) to be 110 nm and it is the value assumed for this alloy.

$M$  in equation (7.1) is dependent on the matrix texture and therefore different values are reported in literature, but for an aluminium based hot extruded nanostructured alloy ( $Al_{93}Fe_3Cr_2Ti_2$ ), it has been adopted to be 3.5 (Pedrazzini *et al.*, 2016; Galano and Audebert, 2022) and the same value is used here.

Substituting equation (7.3) into (7.2) and then (7.2) into (7.1) gives equation (7.4).

$$\Delta\sigma_p = M \frac{G.b}{\frac{2.D_p\sqrt{\frac{2}{3}}}{3.f_v} (1-f_v)} \quad (7.4)$$

Substituting the above values into equation (7.4) estimates that nearly 131 MPa or 32% of the alloy's strength is contributed by particles strengthening which aligns with values reported in literature (Pedrazzini *et al.*, 2016).

### 7.5.2. Grain boundary strengthening

Grain boundary strengthening can be estimated by the so-called Hall-Petch (H-P) relation, as shown in equation (7.5), which has been found to match quantitatively the grain size effect on the yield strength of polycrystalline materials (Eshelby, Frank and Nabarro, 1951; Galano and Audebert, 2022). They found that the development of intra-granular dislocation pile-ups has a slip length proportional to the inverse square root of the mean grain size:

$$\Delta\sigma_{gb} = \sigma_0 + \frac{k}{\sqrt{d}} \quad (7.5)$$

Where  $\Delta\sigma_{gb}$  is the strengthening contribution to yield stress (MPa) due to the grain boundaries,  $\sigma_0$  is the lattice frictional stress (for Al, it is commonly taken  $\sigma_0 = 16$  MPa),  $d$  is the average grain size (nm), and  $k$  is known as the “locking parameter” ( $\text{MPa}\sqrt{m}$ ), which measures the relative hardening contribution of the grain boundaries.

Deviations of the inverse square root of the average grain size have been theoretically proposed and experimentally found in the literature. The H-P relation was proposed to be re-written as equation (7.6):

$$\Delta\sigma_{gb} = \sigma_0 + k \cdot d^{HP} \quad (7.6)$$

Where HP is known as the Hall-Petch exponent (originally proposed as  $HP = -0.5$ ) which is influenced by the microstructural state of the alloy. The value of  $k$  can be obtained as the slope of the straight line when the yield strength values are plotted against  $d^{HP}$  or using theoretical models (Conrad, 1963).



Theoretical estimations for the grain size exponent (HP) have suggested different values (Kocks, 1970; Hirth, 1972; Dunstan and Bushby, 2014), but (Christman, 1993) fitted experimental grain-size strengthening data for the FCC metals and found it to be -0.33 and this value is used here too.

For an aluminium based nanostructured alloy (Al-Cu), (Shanmugasundaram *et al.*, 2010) estimated the average grain size (d) and locking parameter (k) to be 30 nm and 0.13 MPa  $\sqrt{m}$  respectively.

Substituting the above values into equation (7.6) estimates that nearly 55.5 MPa or 13.6% of alloy's strength is contributed by grain size strengthening.

### 7.5.3. Dislocation-dislocation interaction strengthening

Dislocation-dislocation interaction is an important strengthening mechanism to be considered here and it can be estimated using equation (7.7) (Galano and Audebert, 2022)

$$\Delta\sigma_d = M \cdot \alpha \cdot G \cdot b \sqrt{\rho_d} \quad (7.7)$$

Where  $\Delta\sigma_d$ , M,  $\alpha$ , G, b and  $\rho_d$  are strengthening contribution to yield stress (MPa) due to the dislocation-dislocation interaction, Taylor factor, dislocation strengthening efficiency, shear modulus (GPa), Burger vector (nm) and dislocation density ( $m^{-2}$ ).

Dislocation strengthening efficiency is a function of the strain rate and temperature, and at strain rate of  $10^{-4} \text{ s}^{-1}$  and room temperature, it is reported to be 0.3. According to (Galano and Audebert, 2022), a reasonable dislocation density value for hot extruded nanostructured alloy is in the order of  $10^{14} \text{ m}^{-2}$ .

Substituting the values into 7.7 estimates that nearly 81 MPa or 19.8% of alloy's strength is contributed by dislocation-dislocation interaction which aligns with values reported in literature.

#### 7.5.4. Solid solution strengthening

Considering the high solubility of the alloying elements in this alloy facilitated by rapid solidification method melt spinning, the remaining strength 141 MPa or 34.6% is assumed to be contributed by the solid solution strengthening.

Table 7.1 summarises the contributions of different strengthening mechanism determined above.

Strengthening Mechanisms	Strength Contribution (MPa)	Strength Contribution (%)
Particle Strengthening	131	32
Grain Boundary Strengthening	55.5	13.6
Dislocation-Dislocation Interaction Strengthening	81	19.8
Solid Solution Strengthening	141	34.6

**Table 7.1.** Summary of various strengthening mechanisms contributions.

#### 7.6. Finite element analysis of the original piston

The quasi-static temperature distribution in the pistons shown in Figure 5.24 indicated that the maximum temperature was nearly 3 degrees higher in model 2 than model 1. This could be due to the presence of the cylinder that restricts the heat flow from the piston to the environment as the top portion of the cylinder is also exposed to the combustion gases (Figures 5.15 and 5.25).

From the stress results in Figures 5.26 and 5.27, it was clear that the different approaches were significant in terms of the difference in stresses produced. The stresses in model 1 were approximately 4% higher, but 3.6% lower than model 2 at the crown and the pin hole locations (critical regions) respectively. The lower stress in piston crown in model 2 was

associated with the larger inertial force, generated by the higher mass of the moving components due to addition of the connecting rod and the fact that the inertial force generates opposing flexure to that of the combustion pressure effect (Wang, Liu and Shi, 2010). The plastic strain results given in Figures 5.28 and 5.29 indicated that no plastic deformation was occurring in both the FE models.

Piston deformations in the X and Y directions affect the piston to cylinder running clearances which in turn might affect the engine performance. Larger piston-cylinder clearances lead to compression loss while smaller piston-cylinder clearances increase friction between piston and cylinder. Both of these conditions are likely to reduce engine performance. Improper piston-cylinder clearances also reduce piston fatigue life and can cause engine seizure (Bonelli *et al.*, 2014).

The piston deformations in the X directions for both models were nearly the same as can be seen in Figure 5.30 and their respective deformation plots shown in Figure 5.31. The equal deformations in the X directions were due to the same loading conditions on both side of the piston crown centre in the X directions.

The piston deformations in the Y directions in Figures 5.32 and 5.33 indicate that the piston in model 2 deformed more in the positive Y direction compared to negative Y direction due to the lateral force. The movement in the negative Y direction will generate compressive stresses due to the piston being pressed against the cylinder wall. On the other hand, the piston deformations in the Y directions were approximately symmetrical in model 1 (Figures 5.32–5.33), it indicated that the lateral force was not fully transferred to the piston due to the pin-connecting rod interface constraint.

The piston deformations in the Z directions in Figures 5.34–5.35 suggested that the piston in model 2 deformed approximately 5 times more on one side (opposite to the lateral force)

compared to model 1. This was because the lateral force pressed the piston against the cylinder resulting in increased friction between the piston and cylinder, hindering the piston deformation in the Z direction, caused by the combustion pressure. On the other side of the piston there was reduced friction allowing more of the effect of the combustion pressure to be realised which increased the Z direction deformation.

The piston deformations in the Z directions suggested that the piston crown in model 1 deformed in the negative Z direction (shown in red box dashed lines in Figure 5.34). Piston deformation in the Z direction affects the clearances between piston crown, intake and exhaust valves. The deformation in negative Z direction in model 1 may cause the piston designer to allow larger piston-valve clearances than necessary which will impact the compression ratio leading to reduced engine performance.

The piston-valve clearances have tight tolerances and in the case of the engine used in this work the cold piston-valve clearance ranges were 0.07–0.13 mm for intake and 0.12–0.18 mm for exhaust valves respectively. The larger clearances required on the exhaust valves are due to the exhaust valves expanding more than the intake valves. The incoming air and fuel keep the intake valve pockets cooler. The deformations of the intake and exhaust valve pockets in both models were probed to determine the valve pocket deformations that will suggest the least piston to valve clearances (more likely to make contact with the valves). The higher deformation of the valve pockets in the negative Z direction or lower deformation in positive Z direction will dictate piston to valve clearances. The deformations of the intake valve pockets were 0.04 and 0.47 mm, while for the exhaust valve pockets the values were 0.05 and 0.65 mm for models 1 and 2 respectively.

The results indicated that the exhaust valve pockets deformed more than the intake valve pockets in both FE models, which is realistic. However, the smaller deformations of intake

and exhaust valve pockets in the positive Z direction in model 1 indicate that model 1 will predict smaller piston to valve clearances than model 2. Based on the valve pockets deformations, model 1 was indicating 12 and 13 times lower piston to valve clearances than model 2 for the intake and exhaust valve pockets respectively. This could lead to allowing larger piston-valve clearances than needed (affecting piston compression height), to avoid piston hitting the valves, which will affect the compression ratio and may reduce engine performance.

The anti-thrust side (opposite to the lateral force direction side or the exhaust valve pocket side) of the piston skirt is made thicker in designs to resist the larger deformation as described above (model 2 in Figure 5.34). These deformation differences cannot be seen in model 1 and would therefore lead to flawed skirt design. The skirt thicknesses in thrust and anti-thrust sides for the piston investigated in this work were 2.255 mm and 2.505 mm respectively. The strength of the skirt maintains the piston axis parallel to the cylinder axis and is the major controlling factor at operating temperatures affecting ring land size and outside diameter, and the ring attitude normal to the cylinder face (Azevedo and Filho, 1988b).

The unrealistic piston deformations in the Z direction in model 1 may have been caused by the unrealistic pin deformation. As the ends of the pin bend in the positive Z direction (bowed down) due to the combustion load, the middle of the pin bends in the negative Z direction (see deformation plots in Figure 5.36) due to the pin-connecting rod constraint. Since the piston was supported by the pin; the piston followed the same deformation pattern which may have led to improper piston deformations in the Z direction at the middle of the crown. The pin deformation plots in Figure 5.36 showed that the pin in model 2 was compressed in the middle by the connecting rod, which seems more realistic.

Based on the discussion of the results for the two different FE models, it can be concluded that model 2 was more representative of the load conditions that the piston was subjected to in reality. Model 2 was used as a foundation to design the new piston using the new alloys properties and the discussion of the new piston design is given in the following section.

### **7.7. Finite element analysis of the new lightweight piston and implementation of the new piston in the engine with existing components**

In order for the new piston to be compatible with the existing engine components, the new piston had to be designed with a number of constraints (See Section 5.6.1). These constraints made it more challenging to reduce the mass as many sections of the piston could not be modified (Figures 5.38-39). One of the two approaches used to reduce the piston mass was topology optimisation (Section 5.6.2), but it was too limited for application in this project. However, some adjustments were made to see if it will work. Despite, these adjustments the results were not of any practical use (Figure 5.40) hence it was decided to use an iterative/inspection approach to reduce the piston mass using the FEA methodology developed in Section 5.5.

The different iterations carried out are tabulated in Table 5.15 and it can be seen that the piston mass was reduced by 16.38% without increasing the stresses significantly as indicated in Figures 5.41–5.42. The small increase in stress is not of any concern since the new alloy has higher strengths at elevated temperatures than the original alloy (Al-2618). Furthermore, the directional deformations of the new piston design stayed nearly the same as the original piston (Figures 5.45–5.47).

The final machined piston turned out to be slightly heavier than the final optimised piston, it was due the coating and also some modifications needed to make the design machinable. However, the final machined piston was still 13.5% lighter than the original piston.

## **Chapter 8: Conclusions and further work**

### **8.1. Conclusions**

#### **8.1.1. Overall research findings**

The most fundamental conclusion arising from this study is that it is feasible to use the new nanostructured aluminium alloy in piston applications that enable to design a lightweight piston. Furthermore, it was determined that the new alloy has better mechanical properties than the existing piston material at piston operating temperature range. All the objectives set out in Chapter 1 were met.

#### **8.1.2. Critical review of piston material evolution**

Due to the ever growing concerns over the emissions, global warming and to reduce fuel consumption, the automotive industry is under immense pressure to improve the efficiency of internal combustion engines. Reducing frictional losses, more specifically the frictional losses caused by the piston and rings assembly, is one of the primary approaches by the engine designers to achieve this. Reducing piston mass is known to have significant impact on the piston and ring assembly frictional losses, a high demand for the development of lightweight pistons was identified. This trend in the automotive industry further motivated to assess the feasibility of the newly developed nanostructured aluminium alloy in lightweight piston applications. The literature research critically reviewed the recent innovations in the development of nanostructured aluminium alloys for high temperature applications such as pistons.

It was found that nanostructured aluminium alloys have attracted significant attention during the last two-three decades due to their superior mechanical properties at higher temperatures compared to conventional aluminium alloys. Furthermore, through the literature research it

was discovered that efforts have been made to assess the feasibility of certain nanostructured aluminium alloys in piston applications. However, the introduction of even better nanostructured aluminium alloys made possible by improved manufacturing processes led to the programme of work for this project. In addition, the government plans to leap back to petrol engines in smaller engine vehicles will further catapult the effort to develop better nanostructured aluminium alloys for piston application as the aluminium alloys are the preferred choice of material for pistons in petrol engines.

### **8.1.3. Characterisation of the new alloy for piston applications and its comparison with existing piston alloys**

The as-received alloy was characterised using numerous intrusive and non-intrusive techniques. It was established that the alloy had homogenous microstructure and therefore had homogenous hardness across the bar's cross section. Furthermore, the EDS analysis confirmed the composition of the alloy specified by the manufacturer and it was shown that the large particles were mainly consisted of Al, Mg and Si respectively.

The heat treatment results indicated that T6 condition was achieved at 160 °C for 30 hours and the hardness of the alloy increased from an average of 97 HV in as-received state to 175.5 HV in T6. The hardness of the new alloy at T6 was 35% higher than corresponding to Al-2168 (130 HV in T6) that is used in the test engine piston in this project.

The high temperature tensile tests carried out at piston operating temperature showed that the new alloy had 1.09–1.82 times higher strengths than Al-2618 depending on the test temperature. In addition, the new alloy also had higher strengths than other aluminium alloys used in piston applications. The only exception was 7075 which had slightly higher strength up to 120 °C, but that was not much of an importance for piston mass reduction since majority of the piston mass lies above the pin whole where the temperature varies from 120–



265 °C. The significantly less fluctuation in tensile test results was attributed to the stabilisation of the dog-bone specimen prior to testing.

The different strengthening mechanisms that contributed to the strength of the new alloy were estimated to be 34.6% 32%, 19.8%, 13.6%, solid solution strengthening, particle strengthening, dislocation-dislocation interaction and grain size strengthening.

#### **8.1.4. Finite element modelling of the original & new piston and manufactured pistons**

Through the completion of this project a contribution to knowledge has been made in understanding the geometry idealisation for finite element analysis of piston design. Two different approaches were used in the literature for idealisation of piston loading model; of which the most widely used simplification is based on the use of piston and gudgeon pin geometry only. Mahle (2016) though suggests that the geometry used for a piston should include some portion of the connecting rod's small end and the cylinder in addition to the piston and gudgeon pin. Furthermore, Mahle (2016) stated that there are three types of mechanical loads acting on a piston (combustion pressure, inertial and lateral forces), but most of the published papers did not account for the lateral force. According to dynamic and free body diagram analysis of the crank slider mechanism, nearly one-third of the connecting rod's mass acts on the piston side of the crank slider mechanism Norton, 2008 . The inertial force acts in the opposing direction to the effect of the combustion pressure.

The work undertaken in this research analysed two different approaches as suggested in literature for the FEA modelling of a piston. The results showed that using piston, pin, some portion of the connecting rod and a cylinder (model 2) is a more realistic representation of the structural response of the piston assembly compared to the combination of only piston and pin (model 1) that is widely used in literature. The work highlights that, model 1 may overestimate the stresses and produce unrealistic deformations in the piston which may lead

to an improper design. Model 2 leads to more realistic pin deformation and allows the action of the lateral force on the piston to be incorporated. The deformations obtained have significant effect on possible piston clearances and skirt design choices. The results demonstrate the significance of making appropriate model choices in order to obtain realistic results for piston design.

Based on the discussion of the original piston FEA results in Section 7.6, model 2 came out to be more representative of the load conditions that the piston is subjected to in reality. Therefore the new piston design was based on model 2.

One of the two approaches used to reduce the piston mass was topology optimisation, but it was too limited for application in this project. Hence it was decided to use an iterative/inspection approach to reduce the piston mass using the FEA methodology. The design approach was to reduce piston mass by thinning the different sections of the piston. The new piston's mass was 218.35 grams which was 16.38% lighter than the original piston with mass of 261.13 grams. The final machined piston turned out to be slightly heavier than the final optimised piston, it was due to the coating and also some modifications needed to make the design machinable. However, the final machined piston was still 13.5% lighter than the original piston.

#### **8.1.5. Engine performance with new configuration**

It could not be conclusively said from the results if the new piston was more fuel efficient overall in all test conditions, but the new piston was more fuel efficient than the original piston at higher speeds and lower torques. At lower speed of 3000 rpm, the new piston was more fuel efficient in all torque values. Overall, the new piston has higher volumetric efficiency compared to the original piston, but at higher engine speed of 6000 rpm and higher torque the new piston had lower volumetric efficiency.

The research also highlighted the limitations such as controlling test cell temperature, humidity etc. in the engine test facility available for the research, which would have negatively affected the engine performance. The test cell temperature, which was also the temperature of the intake air, was 6 °C higher on average for the new piston which would have adversely impacted engine performance with the new piston.

Further work is advised to ultimately determine if the new alloy gives any significant performance gains.

#### **8.1.6. Novel contribution of the research**

The novelty of this research can be attributed to the following contributions:

- A critical review of the developments in piston materials and designs for internal combustion engine applications;
- The microstructural investigations and determination of mechanical properties at piston operating temperature range.
- Better understanding of piston design using finite element analysis and proposing a more realistic finite model for piston design.
- Development of lightweight piston design with reduced mass.
- Demonstration and application of the new alloy in internal combustion engine piston.

### **8.2. Further work**

#### **8.2.1. Application of the new alloy in diesel engine piston and other high temperature applications**

It was stated earlier that the investigated alloy could be used in both diesel and petrol engine, but the focus of this research was to assess it for petrol engine. However, it may yield good results in diesel engine too and it would be desirable to test this alloy in diesel engine. Due to

the higher pressures in diesel engine, a thicker piston may need to be designed compared to steel piston that are currently used, but the lower density and higher strength of this alloy compared to other aluminium alloys may still enable lighter piston overall than steel counterpart. However, the fatigue life of the piston may be lower compared to steel, but before the piston can be tested for fatigue life, the alloy's fatigue properties need to be determined in different temperatures.

It would be desirable to carry out these tests in facility where most of the parameters that can affect the engine performance can be controlled. Once, all the development studies are done, pistons can be tested in a vehicle in real life environment to iron out further issues.

Other applications can include using nanostructured aluminium alloys in compressor blades in jet engine etc.

#### **8.2.2. Tensile tests at higher strain rates and determination of other mechanical properties at various temperatures**

It is well known that the strain rate at which the tensile tests are carried out affects the tensile strength of the material and therefore the tensile tests are normally carried out at strain rate  $1 \times 10^{-4}$  per second. Since the piston mostly work in high strain environment caused by the combustion pressures, it will be useful to see how the new alloy strength is impacted when tested at high strain rates.

Pistons have to last certain million cycles or hours, in the case of this piston; it has to last for about 10 million cycles or 40 hours. It will be beneficial to carry out the fatigue test on the material at piston operating temperature range and then carry out durability tests on the new piston to see how long it will last. If the fatigue life of the new piston is much longer than the original piston, then it will open door for further mass reduction.

## References

- Abed, E. J. (2014) 'Rapidly Solidified of Hyper Eutectic Aluminum-Silicon Alloys Ribbons by Using Melt-Spinning Techniques', *International Journal of Current Engineering and Technology*, 4, pp. 1394-1398.
- Ahmed, D. and Basim, D. (2009) 'Thermal effects on diesel engine piston and piston compression ring', *Engineering and technology Journal*, 27(8).
- Amann, C. A. and Siegl, D. C. (1981) 'Diesel Particulates—What They are and Why', *Aerosol Science and Technology*, 1(1), pp. 73-101.
- AME (2018) *SEM Illustrative Example: Secondary Electron and Backscatter Electron Images*. Columbia: Anderson Material Evaluation Inc. Available at: <http://www.andersonmaterials.com/sem/sem-secondary-backscatter-images.html> (Accessed: 27/05/2018).
- American Society for Metals. Handbook, C. (1979) *Metals handbook. Vol.2, Properties and selection: nonferrous alloys and pure metals, 9th ed.* Metals Park: American Society for Metals.
- American Society for Metals. Handbook, C. and Mills, K. (1985) *Metals handbook. Vol.9, Metallography and microstructures, 9th ed.* Metals Park, Ohio: American Society for Metals.
- American Society for Metals. Heat Treating, D. and American Society for Metals. Handbook, C. (1981) *Metals handbook. Vol.4, Heat treating, 9th ed.* Metals Park: American Society for Metals.
- American Society for Testing and Materials (1984) *Annual book of ASTM standards*. Philadelphia, Pa.: ASTM. Annual book of American Society for Testing and Materials standards.
- AnsysWorkbench (2018) *Contact Formulation Theory*. Canada: Sharcnet Available at: [https://www.sharcnet.ca/Software/Ansys/16.2.3/en-us/help/wb\\_sim/ds\\_contact\\_theory.html](https://www.sharcnet.ca/Software/Ansys/16.2.3/en-us/help/wb_sim/ds_contact_theory.html) (Accessed: 15/11/2018).
- AnsysWorkbench (2018) *Geometric Modification*. Canada: Sharcnet Available at: [https://www.sharcnet.ca/Software/Ansys/17.2/en-us/help/wb\\_sim/ds\\_geometric\\_correction.html](https://www.sharcnet.ca/Software/Ansys/17.2/en-us/help/wb_sim/ds_geometric_correction.html) (Accessed: 15/11/2018).
- Arabab, S. 2015. RESEARCH IN CARBON-CARBON COMPOSITES. Sudan: Southern Illinois University Carbondale.
- Arcoumanis, C. (1988) *Internal combustion engines*. London: Academic.
- Asghar, G. et al. (2020) 'Role of Mg<sub>2</sub>Si precipitates size in determining the ductility of A357 cast alloy', *Materials & Design*, 186, pp. 108280.
- Asgharzadeh, H., Simchi, A. and Kim, H. S. (2011) 'A plastic-yield compaction model for nanostructured Al6063 alloy and Al6063/Al<sub>2</sub>O<sub>3</sub> nanocomposite powder', *Powder Technology*, 211(2–3), pp. 215-220. Available at: <https://doi.org/http://dx.doi.org/10.1016/j.powtec.2011.04.020>.
- Audebert, F., Mendive, C. and Vidal, A. (2004) 'Structure and mechanical behaviour of Al–Fe–X and Al–Ni–X rapidly solidified alloys', *Materials Science and Engineering: A*, 375–377, pp. 1196-1200. Available at: <https://doi.org/http://dx.doi.org/10.1016/j.msea.2003.10.035>.
- Audebert, F. et al. (2002) 'Structural Characterisation and Mechanical Properties of Nanocomposite Al-based Alloys', *Materials transactions*, 43(8), pp. 2017-2025.
- Azevedo, M. N. D. and Filho, S. C. (1988a) 'Lightweight Pistons': SAE International, pp.
- Azevedo, M. N. D. and Filho, S. C. (1988b) 'Lightweight Pistons', *International Congress and Exposition*. Detroit Michigan. USA: SAE International, pp. 12.
- Barbour, C. et al. (2008) 'Fuel Flow Metering for Fishing Vessels'. Cornwall, UK: University of Exeter. Available at: [http://www.seafish.org/media/publications/fuel\\_flow\\_metering\\_phase\\_iii.pdf](http://www.seafish.org/media/publications/fuel_flow_metering_phase_iii.pdf) (Accessed: 30/07/2018).
- Bata, V. and Pereloma, E. V. (2004) 'An alternative physical explanation of the Hall–Petch relation', *Acta Materialia*, 52(3), pp. 657-665. Available at: <https://doi.org/http://dx.doi.org/10.1016/j.actamat.2003.10.002>.

- Becker, W. T. 2002. *Principals of Failure Analysis: Ductile and Brittle Fracture*. USA: ASM International.
- Birtok-Băneasă, C., Rațiu, S. and Hepuț, T. 'Influence of intake air temperature on internal combustion engine operation'. 2017: IOP Publishing, 012039.
- Birtok-Băneasă, C., Rațiu, S. and Hepuț, T. 'Influence of intake air temperature on internal combustion engine operation'. *International Conference on Applied Sciences*, 2017: IOP Publishing, 012039.
- Blackmore, D. R. and Thomas, A. (1977) *Fuel economy of the gasoline engine: fuel, lubricant and other effects*. London (etc.): Macmillan.
- Bloggers (2014) 'Engine Block Manufacturing Process'. Available at: <http://newengineeringpractice.blogspot.com/2011/08/engine-block-manufacturing-process.html> (Accessed 05/07/2018 2018).
- Bonelli, M. *et al.* (2014) 'EVALUACIÓN DE LA PERFORMANCE DE PISTONES DE COMPETICIÓN ELABORADOS CON NUEVAS ALEACIONES DE ALUMINIO'. Argentina: University of Buenos Aires.
- Builder, E. *Crankshaft Balancing*. USA: Engine Builder Available at: <https://www.enginebuildermag.com/2009/05/understanding-crankshaft-balancing/> (Accessed: 01/04/2020).
- Builder, E. (2009) *Crankshaft Balancing*. USA: Engine Builder Available at: <https://www.enginebuildermag.com/2009/05/understanding-crankshaft-balancing/> (Accessed: 01/04/2020).
- Callister, W. D. and Rethwisch, D. G. (2011) *Materials science and engineering, 8th ed., SI version*. Hoboken, N.J: Wiley.
- Carvalho, P. and Gonçalves, P. 'FEA of Two Engine Pistons Made of Aluminium Cast Alloy A390 and Ductile Iron 65-45-12 Under Service Conditions'. *5th International Conference on Mechanics and Materials in Design Porto-Portugal*, 24-26.
- Cerri, E. and Evangelista, E. 1999. *Metallography of Aluminum Alloys*. Italy: Training in Aluminium Application Technologies.
- Cha, S.-W. *et al.* (2009) 'Development of Fatigue Durability Analysis Techniques for Engine Piston using CAE', *SAE Int. J. Mater. Manf.*, 2(1), pp. 403-408. Available at: <https://doi.org/10.4271/2009-01-0820>.
- Chandrasekaran, D. (2003) 'Grain Size and Solid Solution Strengthening in Metals'.
- CheggStudy (2018) *Textbook Solutions*. USA: CheggStudy Available at: <http://www.chegg.com/homework-help/questions-and-answers/using-al-cu-phase-diagram-shown-please-answer-following-questions-temperature-composition-q19612314> (Accessed: 30/05/2018).
- Chen, Y. *et al.* (2009) 'Stress-strain behaviour of aluminium alloys at a wide range of strain rates', *International Journal of Solids and Structures*, 46(21), pp. 3825-3835. Available at: <https://doi.org/http://doi.org/10.1016/j.ijsolstr.2009.07.013>.
- Christman, T. (1993) 'Grain boundary strengthening exponent in conventional and ultrafine microstructure', *Scripta Metallurgica et Materialia;(United States)*, 28(12).
- Conrad, H. (1963) 'Effect of grain size on the lower yield and flow stress of iron and steel', *Acta metallurgica*, 11(1), pp. 75-77.
- Djurdjevic, M. *et al.* (2013) *Calculation of Liquidus Temperature for Aluminum and Magnesium Alloys Applying Method of Equivalency*.
- Donomoto, T. *et al.* (1983) 'Ceramic Fiber Reinforced Piston for High Performance Diesel Engines': SAE International, pp.
- Dunstan, D. J. and Bushby, A. J. (2014) 'Grain size dependence of the strength of metals: The Hall-Petch effect does not scale as the inverse square root of grain size', *International Journal of Plasticity*, 53, pp. 56-65.

- Dutrow, B. L. and Clarke, C. M. (2017) *X-Ray Powder Diffraction*. USA: Geochemical Instrumentation and Analysis Available at: [https://serc.carleton.edu/research\\_education/geochemsheets/techniques/XRD.html](https://serc.carleton.edu/research_education/geochemsheets/techniques/XRD.html) (Accessed: 25/01/2018).
- Edge, E. (2018a) *Coefficient of Friction Equation and Table Chart*. Georgia: Engineers Edge Available at: [https://www.engineersedge.com/coefficients\\_of\\_friction.htm](https://www.engineersedge.com/coefficients_of_friction.htm) (Accessed: 05/06/2018).
- Edge, E. (2018b) *Fastener and Screw Torque Design and Equation and Calculator*. Georgia: Engineers Edge Available at: <https://www.engineersedge.com/torque.htm> (Accessed: 05/06/2018).
- Engineering, C. (2003) *FMS-1000 Fuel Weigher*. Ltd, C.E.S.
- Esfahanian, V., Javaheri, A. and Ghaffarpour, M. (2006) 'Thermal analysis of an SI engine piston using different combustion boundary condition treatments', *Applied Thermal Engineering*, 26(2), pp. 277-287.
- Eshelby, J. D., Frank, F. C. and Nabarro, F. R. N. (1951) 'XLI. The equilibrium of linear arrays of dislocations', *The London, Edinburgh, and Dublin Philosophical Magazine and Journal of Science*, 42(327), pp. 351-364.
- Floweday, G. et al. (2011) 'Thermo-mechanical fatigue damage and failure of modern high performance diesel pistons', *Engineering Failure Analysis*, 18(7), pp. 1664-1674. Available at: <https://doi.org/http://dx.doi.org/10.1016/j.engfailanal.2011.02.002>.
- FullThrottleTahoe (2017) *Precision Crafted, High Performance Connecting Rod Kits*. USA Available at: <http://www.fullthrottletahoe.com/fullthro/publicstore/images/catalog-specs/09DirtPages/09%20Offroad%20Pages%20573-722.pdf> (Accessed: 09/05/2017).
- Gabriel, D. and Hettich, T. (2015) 'TopWeld® Steel Piston for High Speed Diesel Engines': SAE International, pp.
- Galano, M. and Audebert, F. (2022) 'Novel Al based nanoquasicrystalline alloys', *Progress in Materials Science*, 123, pp. 100831.
- Galano, M. et al. (2010) 'Nanoquasicrystalline Al-Fe-Cr-based alloys with high strength at elevated temperature', *Journal of Alloys and Compounds*, 495(2), pp. 372-376. Available at: <https://doi.org/http://dx.doi.org/10.1016/j.jallcom.2009.10.208>.
- Ganesan, V. (2012) *Internal combustion engines*. McGraw Hill Education (India) Pvt Ltd.
- Gedeon, M. (2010) 'Solid Solution Hardening & Strength', (16), pp. 2, Available at: <http://materion.com/~media/Files/PDFs/Alloy/Newsletters/Technical%20Tidbits/Issue%20No%2016%20Solid%20Solution%20Hardening%20%20Strength.pdf> (Accessed 30/03/2016).
- GmbH, M. (2016) *Pistons and engine testing, Second edition*. Heidelberg: Springer Vieweg. ATZ/MTZ-Fachbuch.
- Gorton, M. P. (1994) 'Carbon-Carbon Piston Development'. USA: Lockheed Engineering and Sciences Company23681-0001). Available at: [ntrs.nasa.gov/archive/nasa/casi.ntrs.nasa.gov/19940031440.pdf](https://ntrs.nasa.gov/archive/nasa/casi.ntrs.nasa.gov/19940031440.pdf) (Accessed: 03/03/2016).
- Govindaraju, H. K. 2015. *Theory and Design of Automotive Engines*. India: SJM Institute of Technology.
- Han, B., Mohamed, F. and Lavernia, E. (2003) 'Tensile behavior of bulk nanostructured and ultrafine grained aluminum alloys', *Journal of materials science*, 38(15), pp. 3319-3324.
- Han, B. et al. (2003) 'Mechanical properties of an ultrafine-grained Al-7.5 Pct Mg alloy', *Metallurgical and Materials Transactions A*, 34(3), pp. 603-613.
- Heuer, J. (1991) 'Development and Testing of Carbon Pistons'. Germany: Research Department of Daimler-Benz. Available at: [https://web.anl.gov/PCS/acsfuel/preprint%20archive/Files/36\\_3\\_NEW%20YORK\\_08-91\\_1088.pdf](https://web.anl.gov/PCS/acsfuel/preprint%20archive/Files/36_3_NEW%20YORK_08-91_1088.pdf) (Accessed: 06/03/2016).
- Hirth, J. P. 1972. *The influence of grain boundaries on mechanical properties*. Springer.
- Hohenberg, G. F. (1979) 'Advanced Approaches for Heat Transfer Calculations': SAE International, pp.

- ImageJ (2023) *Image Processing and Analysis in Java*. ImageJ Available at: <https://imagej.net/ij/> (Accessed: 05/03/2023).
- Inoue, A., Kimura, H. and Amiya, K. (2002) 'Developments of Aluminum-and Magnesium-Based Nanophase High-Strength Alloys by Use of Melt Quenching-Induced Metastable Phase (Overview)', *Materials transactions*, 43(8), pp. 2006-2016.
- Interlloy (2011) *8620 Case Hardening Steel*. Engineering Steels+Alloys. Australia: Interlloy Available at: <http://www.interlloy.com.au/our-products/case-hardening-steels/8620-case-hardening-steel/> (Accessed: 02/07/2018).
- J, A. P. and Agarwal, V. K. (2014) 'Effect of Design and Operational Parameters of Piston Skirt on the Performance and Efficiency of a Small Gasoline Engine': SAE International, pp.
- Jayabalan, S. (2004) 'Study and Design of Coupling Shafts Between Engine and Dynamometer': The Automotive Research Association of India, pp.
- Karpe, B., Kosec, B. and Bizjak, M. (2012) 'Analyses of the Melt Cooling Rate in the Melt-Spinning Process', *Journal of Achievements in Materials and Manufacturing Engineering*, 51(2), pp. 8.
- Karpe, B. et al. (2009) 'Effect of the Chill Wheel Cooling During Continuous Free Jet Melt-Spinning', *Materials and Geoenvironment*, 56(4), pp. 14.
- Kaufman, J. G. (1999) *Properties of aluminum alloys: tensile, creep, and fatigue data at high and low temperatures*. ASM international.
- Khaifullizan, M. N. N. et al. (2021) 'Effect of Intake Air Temperature on Engine Performance and Fuel Consumption of Passenger Car', *Fuel, Mixture Formation and Combustion Process*, 3(2).
- Knapman, C. (2014) 'Should I keep my diesel car?', *The Telegraph*, 29/07/2014. Available at: <http://www.telegraph.co.uk/motoring/green-motoring/10997571/Should-I-keep-my-diesel-car.html> (Accessed: 16/02/2016).
- Knowles, A. J. et al. (2014) 'Microstructure and mechanical properties of 6061 Al alloy based composites with SiC nanoparticles', *Journal of Alloys and Compounds*, 615, Supplement 1, pp. S401-S405. Available at: <https://doi.org/http://dx.doi.org/10.1016/j.jallcom.2014.01.134>.
- Kocks, U. F. (1970) 'The relation between polycrystal deformation and single-crystal deformation', *Metallurgical and Materials Transactions B*, 1(5), pp. 1121-1143.
- Kohashi, K.-i. et al. (2013) 'Analysis of Piston Friction in Internal Combustion Engine', *SAE Int. J. Fuels Lubr.*, 6(3), pp. 589-593. Available at: <https://doi.org/10.4271/2013-01-2515>.
- Lee, J. A. (2003) 'CAST ALUMINUM ALLOY FOR HIGH TEMPERATURE APPLICATIONS', *The Minerals, Metals & Materials Society*.
- Lewis, R. E. et al. (1984) 'A Novel Approach for Rapid Solidification Processing of High Strength PM Aluminum Alloys': SAE International, pp.
- Leyland (2016) *Leyland Engine Parts of 411/420 Piston*. Alibaba Available at: [http://www.alibaba.com/product-detail/Leyland-engine-parts-of-411-420\\_60189360502.html](http://www.alibaba.com/product-detail/Leyland-engine-parts-of-411-420_60189360502.html) (Accessed: 16/03/2016).
- Liu, M. et al. (2010) 'Grain refinement in nanostructured Al-Mg alloys subjected to high pressure torsion', *Journal of materials science*, 45(17), pp. 4659-4664.
- Lobry, P. et al. (2011) 'Effect of rapid solidification on structure and mechanical properties of Al-6Mn-3Mg alloy', *International Scientific Journal*, 49(2), pp. 6.
- Lumm, J. A. (1972) 'Mechanical Properties of 2618 Aluminum Alloy'. USA: North American Aviation, Inc. (801499, 801499). Available at: <https://apps.dtic.mil/dtic/tr/fulltext/u2/801499.pdf> (Accessed: 08/12/2019).
- M, D., Sanjay, P. S. and Mandloi, R. K. (2016) 'Analytical Study of Fatigue Failure of Aluminium Alloy Piston in IC Engines', *International Research Journal of Engineering and Technology (IRJET)*, 03(04), pp. 5.
- Ma, E. (2006) 'Eight routes to improve the tensile ductility of bulk nanostructured metals and alloys', *Jom*, 58(4), pp. 49-53.



- Ma, K. *et al.* (2014) 'Mechanical behavior and strengthening mechanisms in ultrafine grain precipitation-strengthened aluminum alloy', *Acta Materialia*, 62, pp. 141-155. Available at: <https://doi.org/http://dx.doi.org/10.1016/j.actamat.2013.09.042>.
- Mahle, G. (2016) *Pistons and engine testing, Second edition*. Heidelberg: Springer Vieweg. ATZ/MTZ-Fachbuch.
- Martin, J. W. (2012) *Precipitation hardening: theory and applications*. Butterworth-Heinemann.
- Martyr, A. and Plint, M. A. (2007) *Engine testing: theory and practice, 3rd ed.* Oxford: Butterworth-Heinemann.
- Mason, R. (2017) 'Diesel Car Owners May be Paid to Trade in Under New UK Air Quality Plans', *The Guardian*, 16/04/2017. Available at: <https://www.theguardian.com/business/2017/apr/16/scrap-diesel-cars-for-cash-says-influential-committee-chairman> (Accessed: 02/05/2017).
- Massingill, J. (2016) *Finding Balance (Part 1): The Basics of Crankshaft Balancing*. USA: On All Cylinders Available at: <https://www.onallcylinders.com/2016/03/17/the-basics-of-crankshaft-balancing/> (Accessed: 01/04/2020).
- Mavrigian, M. (2011) 'Engine Studs: Understanding the Advantages of Using Studs Vs. Bolts, and Tips on Achieving Proper Clamping Loads', Available at: <https://www.autoserviceprofessional.com/article/92024/engine-studs-understanding-the-advantages-of-using-studs-vs-bolts-and-tips-on-achieving-proper-cl> (Accessed 08/07/2018).
- McCann, K. (2017) 'Officials 'Drawing up Plans' for Diesel Scrappage Scheme to Cut Emissions', *The Telegraph*, 02/02/2017. Available at: <http://www.telegraph.co.uk/news/2017/02/02/officials-drawing-plans-diesel-scrappage-scheme-cut-emissions/> (Accessed: 02/05/2017).
- McClellan, R. O. (1987) 'Health effects of exposure to diesel exhaust particles', *Annual review of Pharmacology and Toxicology*, 27(1), pp. 279-300.
- MEE 2014. *Handbook of Analytical Methods for Materials*. USA: Materials Evaluation and Engineering Inc.
- Merkle, A., Kunkel, S. and Wachtmeister, G. (2012) 'Analysis of the Mixed Friction in the Piston Assembly of a SI Engine', *SAE Int. J. Engines*, 5(3), pp. 1487-1497. Available at: <https://doi.org/10.4271/2012-01-1333>.
- Metoki, S. and Negishi, H. (2002) 'Why are NCI Pistons Not Used in Heavy Duty Diesel Engines?': SAE International, pp.
- Mishra, A. (2018) *Friction Stir Welding Of Dissimilar Metal: A Review*.
- Mizuno, H. *et al.* (2009) 'Transient Analysis of the Piston Temperature with Consideration of In-cylinder Phenomena Using Engine Measurement and Heat Transfer Simulation Coupled with Three-dimensional Combustion Simulation', *SAE Int. J. Engines*, 2(1), pp. 83-90. Available at: <https://doi.org/10.4271/2009-01-0187>.
- Moffat, A. J. *et al.* (2005) 'The effect of silicon content on long crack fatigue behaviour of aluminium-silicon piston alloys at elevated temperature', *International Journal of Fatigue*, 27(10-12), pp. 1564-1570. Available at: <https://doi.org/http://dx.doi.org/10.1016/j.ijfatigue.2005.06.023>.
- Moharami, A. *et al.* (2020) 'Role of Mg<sub>2</sub>Si particles on mechanical, wear, and corrosion behaviors of friction stir welding of AA6061-T6 and Al-Mg<sub>2</sub>Si composite', *Journal of Composite Materials*, 54(26), pp. 4035-4057.
- Mohd Hasnun Ariff, H. (2012) *Design of a dynamometer engine coupling shaft*. Universiti Malaya.
- Munyao, E. M. *et al.* (2014) 'Simulation of Thermal-Mechanical Strength for Marine Engine Piston Using FEA', *Journal of Engineering Research and Applications*, 4(3), pp. 5.
- Nagar, P. and Miers, S. (2011) 'Friction between Piston and Cylinder of an IC Engine: a Review': SAE International, pp.
- Norton, R. L. (2008) *Design of machinery: an introduction to the synthesis and analysis of mechanisms and machines, 4th ed.* Dubuque, IA: McGraw-Hill.

- Norton, R. L. (2012) *Design of machinery: an introduction to the synthesis and analysis of mechanisms and machines, Fifth edition*. New York: McGraw-Hill Higher Education.
- Okamoto, H., Anno, N. and Itoh, T. (1992) 'New Computational and Experimental Stress Analysis Method for the Design Decision on Optimum Piston Configuration of Production Engine': SAE International, pp.
- Optrand (2001) *Fibre Optic Sensors for Extreme Environments*.
- Optron (2013) *AutoPSI Pressure Sensor Operating Instructions*. Michigan USA: Optron Incorporated.
- Pan, W. et al. (2015) 'The impact of intake air temperature on performance and exhaust emissions of a diesel methanol dual fuel engine', *Fuel*, 162, pp. 101-110.
- Patel, P., Shah, P. and Mourelatos, Z. P. (2010) 'Piston Design Using Multi-Objective Reliability-Based Design Optimization', *SAE Int. J. Mater. Manuf.*, 3(1), pp. 493-511. Available at: <https://doi.org/10.4271/2010-01-0907>.
- Pedrazzini, S. et al. (2016) 'Strengthening mechanisms in an Al-Fe-Cr-Ti nano-quasicrystalline alloy and composites', *Materials Science and Engineering: A*, 672, pp. 175-183.
- Polmear, I. (1996) 'Recent developments in light alloys', *Materials transactions, JIM*, 37(1), pp. 12-31.
- Pulkrabek, W. W. (2014) *Engineering fundamentals of the internal combustion engine, Second edition, Pearson new international edition*. Harlow, Essex: Pearson. Pearson custom library.
- Racing, S. (2017) *Connecting Rod Kits for KTM, Husaberg, Husqvarna by Hot Rods*. USA Available at: <https://slavensracing.com/shop/connecting-rod-kits-for-ktm-husaberg-by-hot-rods/> (Accessed: 24/06/2018).
- Rafiei, A., Varahram, N. and Davami, P. (2012) 'MICROSTRUCTURAL STUDY OF AL-20SI-5FE ALLOYS PRODUCED BY MELT-SPINNING PROCESS', *Association of Metallurgical Engineers of Serbia (AMES)*, 19(1), pp. 10.
- Riccio, G. (1987) 'The History of components', *Metallurgical Science and Technology*, 5(1), pp. 8.
- Robinson, J. (1964) 'The design and development of pistons for automobile engines', *Proceedings of the Institution of Mechanical Engineers: Automobile Division*, 179(1), pp. 181-211.
- Rudnik, D. et al. (2003) 'NEW MATERIAL SOLUTIONS IN COMBUSTION ENGINES', *Journal of KONES Internal Combustion Engines*, 10(3-4), pp. 11.
- Ryen, Ø. (2003) 'Work hardening and mechanical anisotropy of aluminium sheets and profiles'.
- Saarinen, M. (2017) 'Diesel Ban? New 'Toxins Tax' Could Charge Diesel Cars £20 to Enter UK Cities', *Daily*, Available at: <http://www.autoexpress.co.uk/car-news/consumer-news/98747/diesel-ban-new-toxins-tax-could-charge-diesel-cars-20-to-enter-uk> (Accessed 02/05/2017).
- Sales, O. N. (2018) *High Performance Connecting Rod Kits*. USA: ARI Network Services-Endeavor Available at: <https://shop.oneillsales.com/hot-rods-high-performance-connecting-rod-kits-detail.htm?productid=8866175> (Accessed: 24/06/2018).
- Sanli, A. et al. (2008) 'The influence of engine speed and load on the heat transfer between gases and in-cylinder walls at fired and motored conditions of an IDI diesel engine', *Applied thermal engineering*, 28(11), pp. 1395-1404.
- Scharcnet (2018) *Topology Optimization Limitations*. Canada: Scharcnet Available at: [https://www.sharcnet.ca/Software/Ansys/18.2.2/en-us/help/wb\\_sim/ds\\_topo\\_opt\\_limitations.html](https://www.sharcnet.ca/Software/Ansys/18.2.2/en-us/help/wb_sim/ds_topo_opt_limitations.html) (Accessed: 09/12/2018).
- Scharcnet (2018) *Topology Optimization Analysis*. Canada Available at: [https://www.sharcnet.ca/Software/Ansys/18.2.2/en-us/help/wb\\_sim/ds\\_topology\\_optimization.html](https://www.sharcnet.ca/Software/Ansys/18.2.2/en-us/help/wb_sim/ds_topology_optimization.html) (Accessed: 09/12/2018).
- Schenck (2001) *Technical Specification Eddy-Current Dynamometer W Series*. GmbH, S.P.
- Schneider, C., Halbhuber, J. and Wachtmeister, G. (2016) 'Measuring and Simulating Friction between Piston Pin and Connecting Rod on a Tribometer Test Bench to Define Locally Resolved Friction Coefficients': SAE International, pp.
- Schofield, A. and Wyatt, L. (1946) 'Light Alloy Piston Materials', *Proceedings of the Institution of Automobile Engineers*, 41(1), pp. 251-294.

- Schwaderlapp, M. *et al.* (2000) 'Lightweight Design and Friction Reduction-Design Potentials to Meet Fuel Consumption Targets', *FORTSCHRITT BERICHTE-VDI REIHE 12 VERKEHRSTECHNIK FAHRZEUGTECHNIK*, pp. 187-207.
- Schwaderlapp, M., Koch, F. and Dohmen, J. 'Friction reduction—the engine's mechanical contribution to saving fuel'. *FISITA World Automotive Congress*.
- Scrimshaw, P. (2014) 'Investigation into Piston Mass Reduction in an IC Engine'. Oxford UK: Oxford Brookes University.
- Shanmugasundaram, T. *et al.* (2010) 'On the Hall–Petch relationship in a nanostructured Al–Cu alloy', *Materials Science and Engineering: A*, 527(29–30), pp. 7821-7825. Available at: <https://doi.org/http://dx.doi.org/10.1016/j.msea.2010.08.070>.
- Sher, E. (1998) *Handbook of air pollution from internal combustion engines: pollutant formation and control*. Academic Press.
- Silva, F. S. (2006) 'Fatigue on engine pistons – A compendium of case studies', *Engineering Failure Analysis*, 13(3), pp. 480-492. Available at: <https://doi.org/http://dx.doi.org/10.1016/j.engfailanal.2004.12.023>.
- Singh, L. *et al.* (2015) 'FINITE ELEMENT ANALYSIS OF PISTON IN ANSYS', *International Journal of Modern Trends in Engineering and Research*, pp. 619-626.
- Singh, S. B. (2003) 'Metal Matrix Composite: A Potent Material for Futuristic Automotive': The Automotive Research Association of India, pp.
- Smith, M. T., Energy, D.o. (2012) *High Temperature Aluminium Alloys*. USA (PM044).
- Stewart, H. (2017) 'Sadiq Khan: Government Must Pay Drivers £3,500 to Scrap Diesel Cars', *The Guardian*, 12/02/2017. Available at: <https://www.theguardian.com/uk-news/2017/feb/12/london-mayor-plans-to-scrap-diesels> (Accessed: 02/05/2017).
- Taulbut, D. (2001) 'Pistons for High-Power Engines', (3), pp. 7, Available at: [http://www.grandprixengines.co.uk/Note\\_14.pdf](http://www.grandprixengines.co.uk/Note_14.pdf) (Accessed 11/03/2016).
- Taylor, C. F. (1985) *The Internal-combustion Engine in Theory and Practice: Combustion, fuels, materials, design*. MIT press.
- Tellkamp, V., Lavernia, E. and Melmed, A. (2001) 'Mechanical behavior and microstructure of a thermally stable bulk nanostructured Al alloy', *Metallurgical and Materials Transactions A*, 32(9), pp. 2335-2343.
- Thermal-FluidsCentral (2011) 'Thermo-Physical Properties: Engine Oil, Unused'. Available at: <https://www.thermalfluidscentral.org/encyclopedia/index.php/Thermophysical Properties: Engine Oil, Unused> (Accessed 07/03/2017).
- Torregrosa, A. J., Olmeda, P. C. and Romero, C. A. (2008) 'Revising engine heat transfer', *Journal of Engineering Annals of Faculty of Engineering Hunedoara*, 6(3), pp. 245-265.
- Chapter 3: Advanced Contact* (2005). Slide Player.
- Treamnuk, T., Treamnuk, K. and Papakae, S. (2018) 'Influence of Intake Air Temperature on Performance of Small Gasoline Engine', *The Asian Conference on Sustainability, Energy & the Environment 2018*. Thailand: The International Academic Forum, pp. 9.
- Trimby, S. *et al.* (2017) 'Unified approach to engine cylinder pressure reconstruction using time-delay neural networks with crank kinematics or block vibration measurements', *International Journal of Engine Research*, 18(3), pp. 256-272.
- Tsuyoshi, T. and Sasaki, K. (2010) 'Low cycle thermal fatigue of aluminum alloy cylinder head in consideration of changing metrology microstructure', *Procedia Engineering*, 2(1), pp. 767-776. Available at: <https://doi.org/https://doi.org/10.1016/j.proeng.2010.03.083>.
- Turner, M. (2018) Engine Coolant Oil Temperature.
- Uzun, O., Karaaslan, T. and Keskin, M. (2001) 'Production and Structure of Rapidly Solidified Al-Si Alloy', *Turk J Phys*, (25).
- Valdés, M. *et al.* (2001) 'Design of Carbon Pistons Using Transient Heat Transfer and Stress Analyses': SAE International, pp.

- Vartabedian, R. (2000) 'Iron's Days Are Numbered as Auto Makers Cast Their Lot With Aluminum ', *Los Angeles Times*, 18/10/2000. Available at: <http://articles.latimes.com/2000/oct/18/news/hw-37969> (Accessed: 03/03/2016).
- Vertex (2017) *Product Feature Guide*. Italy: Vertex Pistons Available at: <http://www.gb.vertexpistons.com/> (Accessed: 25/07/2017).
- Vidal, J. (2015) 'The rise of diesel in Europe: the impact on health and pollution', *theguardian*. Available at: <http://www.theguardian.com/environment/2015/sep/22/the-rise-diesel-in-europe-impact-on-health-pollution> (Accessed: 15/02/2016).
- Voort, G. V. (2016) 'Metallography and Microstructure of Aluminum and Alloys', Available at: <http://vacaero.com/information-resources/metallography-with-george-vander-voort/1217-metallography-and-microstructure-of-aluminum-and-alloys.html> (Accessed 01/05/2016).
- Wang, H. *et al.* (2016) 'In-situ analysis of the tensile deformation modes and anisotropy of extruded Mg-10Gd-3Y-0.5 Zr (wt.%) at elevated temperatures', *International Journal of Plasticity*, 84, pp. 255-276.
- Wang, J. *et al.* (2021) 'Is Mg<sub>17</sub>Al<sub>12</sub> ductile or brittle? A theoretical insight', *Journal of Magnesium and Alloys*.
- Wang, Y. X., Liu, Y. Q. and Shi, H. 'Finite Element Static and Dynamic Analysis for a Piston'. *Advanced Materials Research*: Trans Tech Publ, 3323-3326.
- Ward, W. (2014) 'Magnesium as a Piston Material', *High Power Media*.
- Whitford (2018) 'High Performance Fluoropolymer Coatings:'. USA. Available at: <https://www.whitfordww.com/wp-content/uploads/2018/06/Whitford-Engineering-Design-Guide.pdf> (Accessed: 07/08/2019).
- Winship, J. W. (1966) 'Engine Piston Design-Art or Science?': SAE Technical Paper (0148-7191).
- Winship, J. W. (1967) 'Designing an Automotive Engine Piston': SAE International, pp.
- Woschni, G. (1967) 'A Universally Applicable Equation for the Instantaneous Heat Transfer Coefficient in the Internal Combustion Engine': SAE International, pp.
- Xu, T. *et al.* (2011) 'An Advanced and Comprehensive CAE Approach of Piston Dynamics Studies for Piston Optimal and Robust Design', *SAE Int. J. Engines*, 4(1), pp. 2087-2099. Available at: <https://doi.org/10.4271/2011-01-1404>.
- Yan, F. (2014) 'Development of high strength Al-Mg<sub>2</sub>Si-Mg based alloy for high pressure diecasting process'.

## **Appendix A**

### **Appendix A.1. Averaged artificial aging results for all the test temperatures**

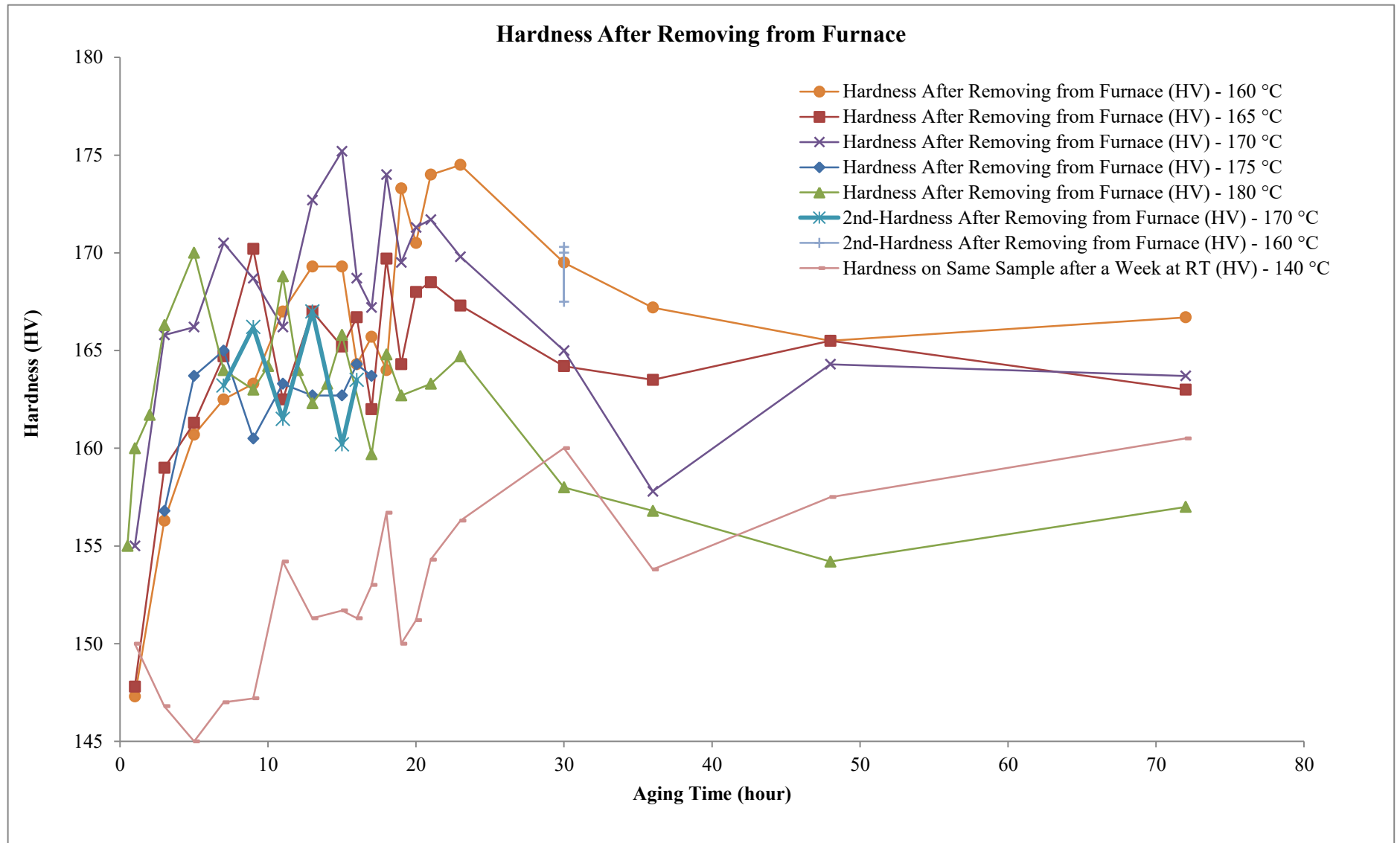


**Figure A.1.** T6 heat treatment results for all the test temperatures after removing the samples from the furnace.

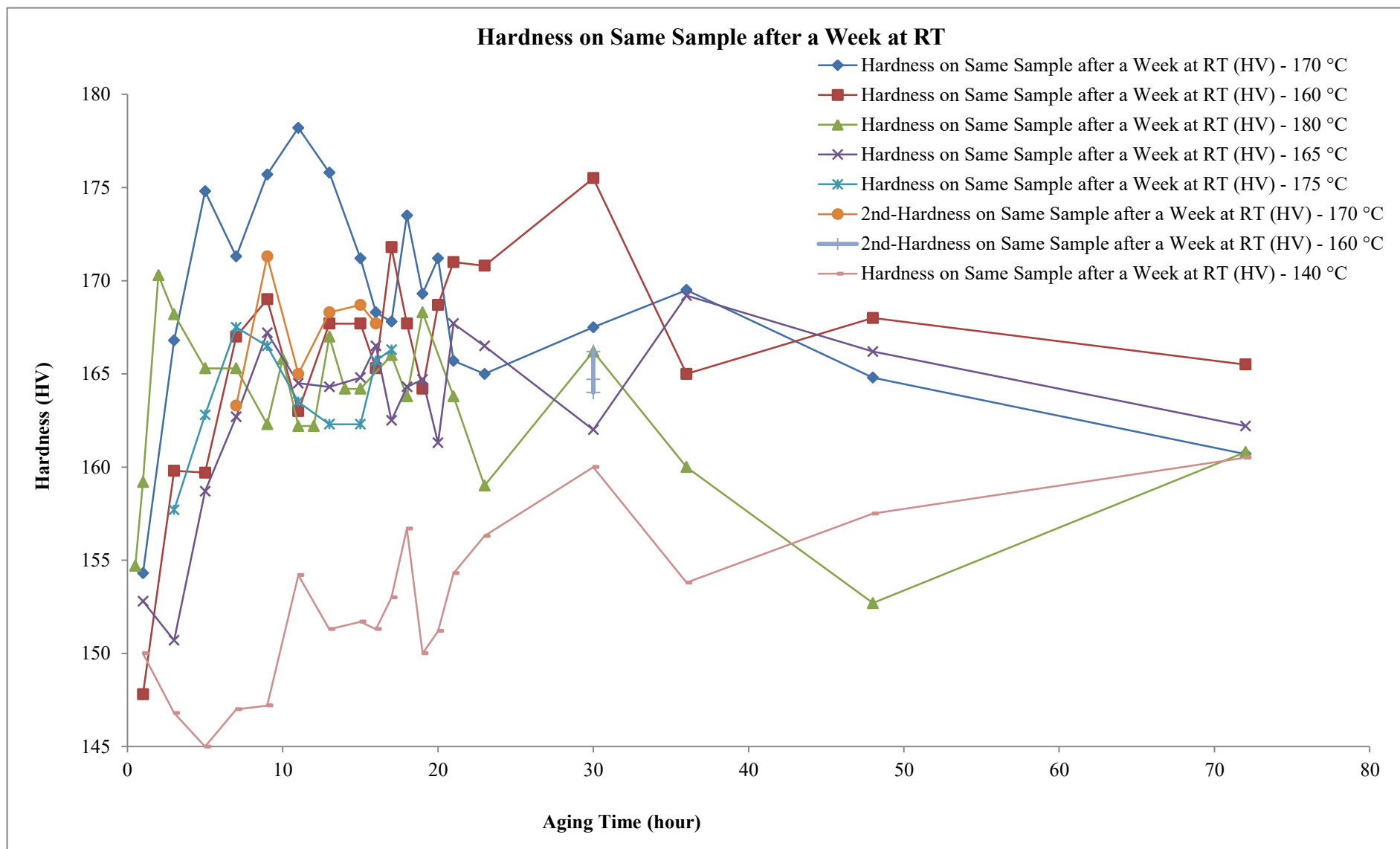


**Figure A.2.** T6 heat treatment results for all the test temperatures a week after removing the samples from the furnace

## Appendix A.2. Scatter in artificial aging results for all the test temperatures

The scatter in heat treatment results for various temperatures is given below in Figures A.3 – A.14. The error bars on the graphs are set to 3%.

### A.2.1. 140 °C

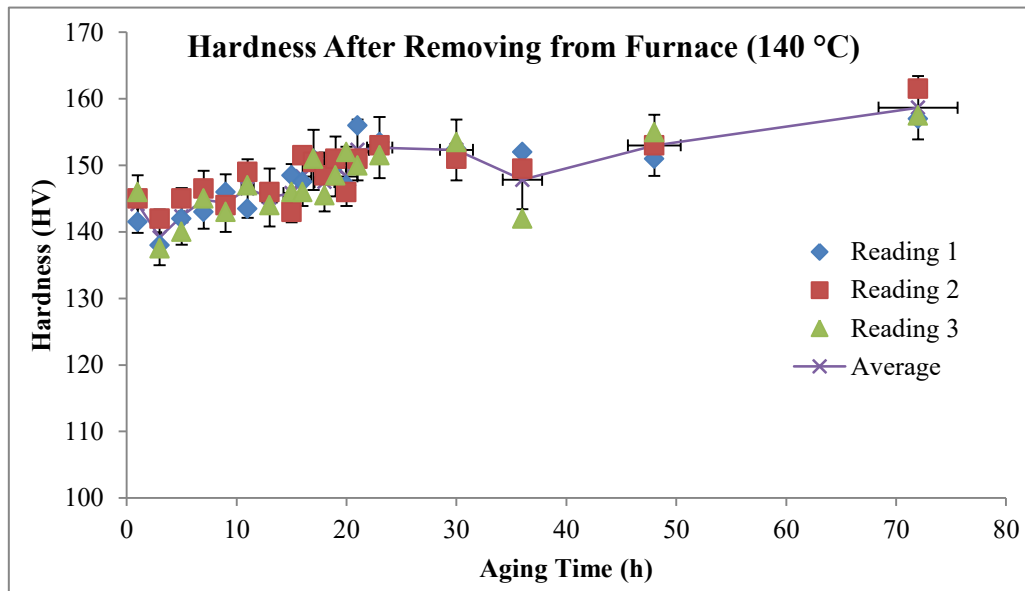


**Figure A.3.** Scatter in the 140 °C heat treatment results after removing the samples from the furnace.

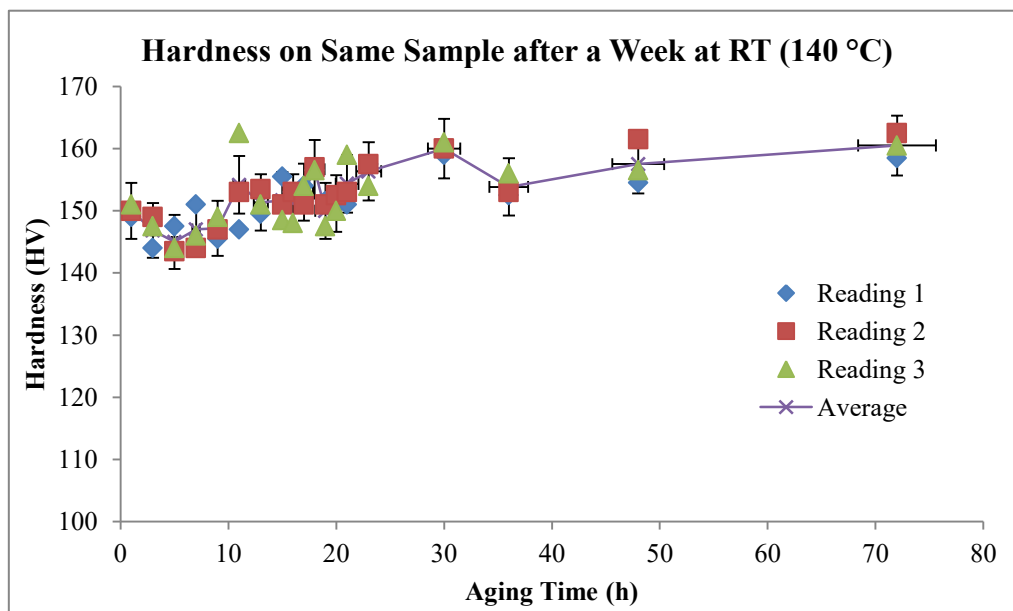


**Figure A.4.** Scatter in the 140 °C heat treatment results a week after removing the samples from the furnace.



### A.2.2. 160 °C

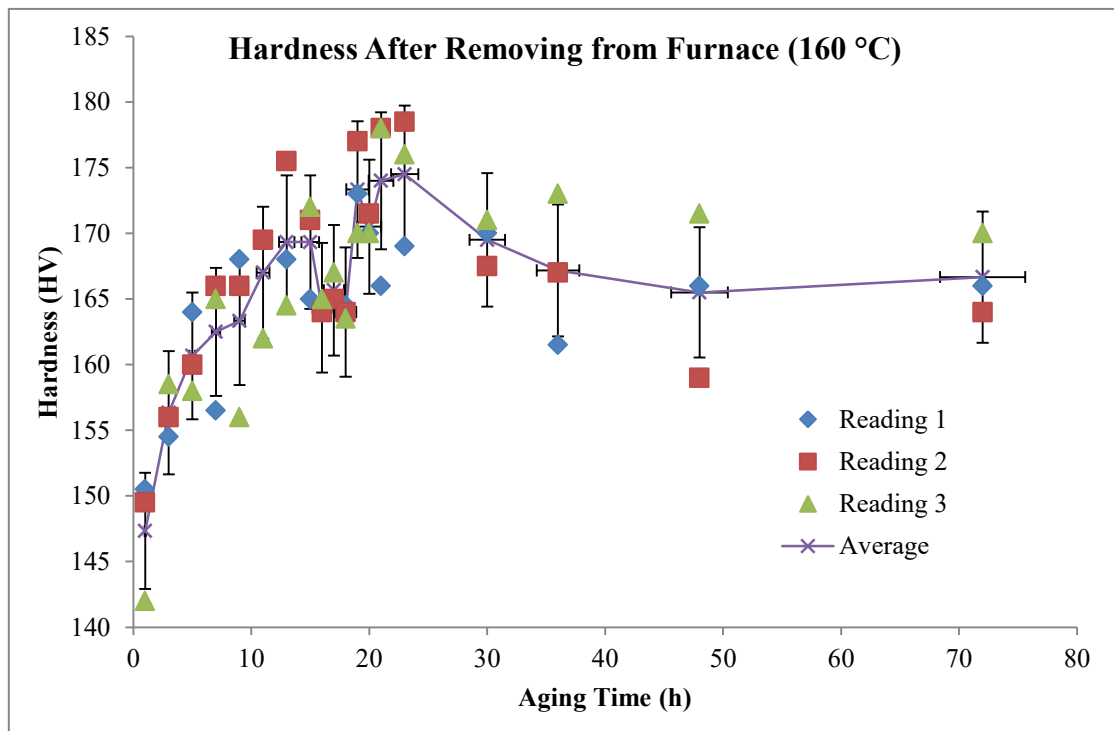


**Figure A.5.** Scatter in the 160 °C heat treatment results after removing the samples from the furnace.

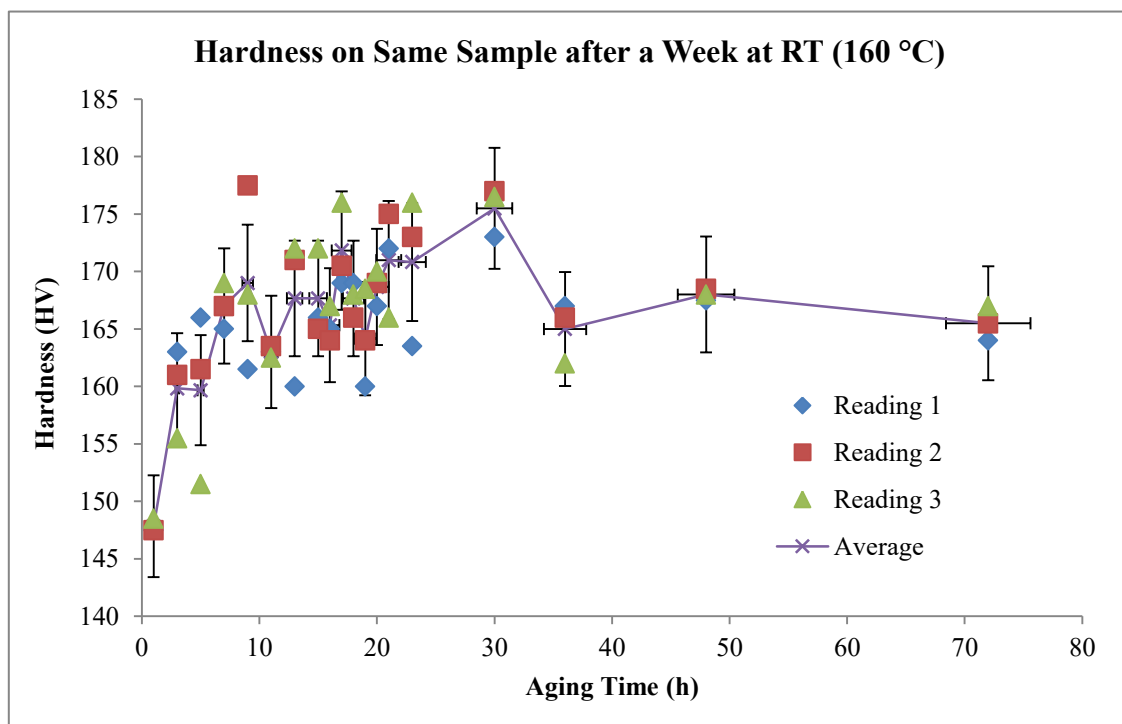


**Figure A.6.** Scatter in the 160 °C heat treatment results a week after removing the samples from the furnace.

### A.2.3. 165 °C

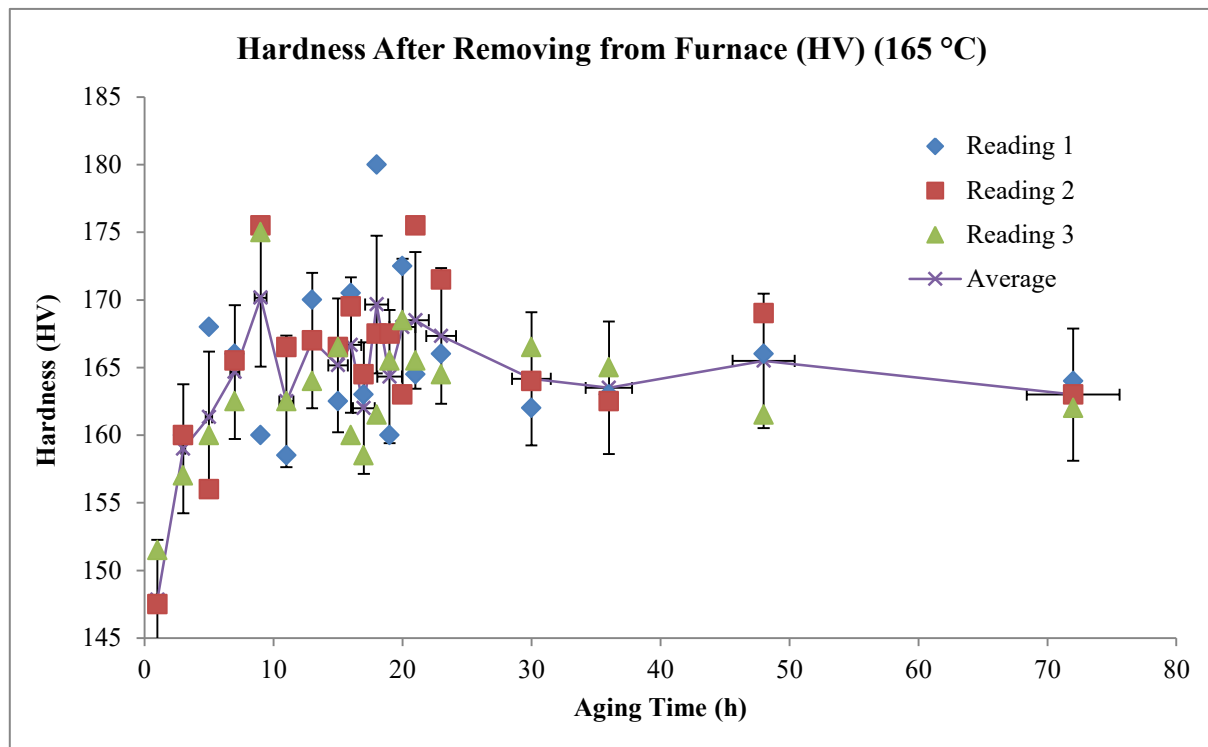


**Figure A.7.** Scatter in the 165 °C heat treatment results after removing the samples from the furnace.

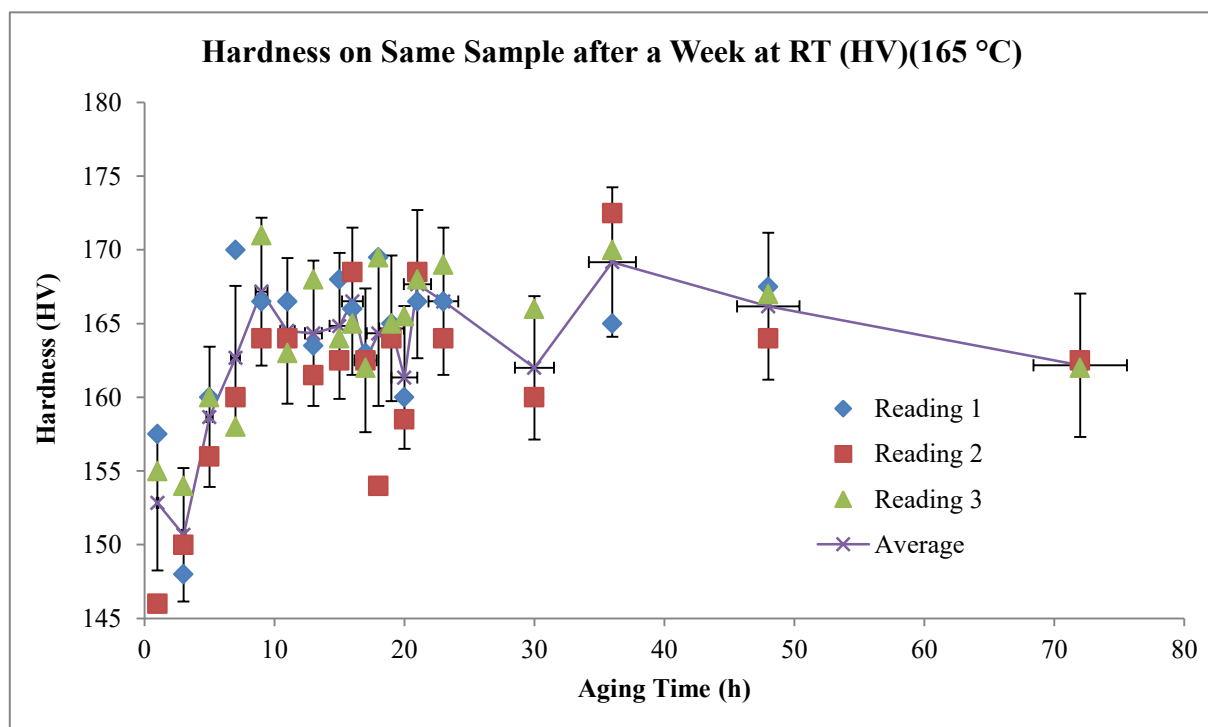


**Figure A.8.** Scatter in the 165 °C heat treatment results a week after removing the samples from the furnace.

#### A.2.4. 170 °C

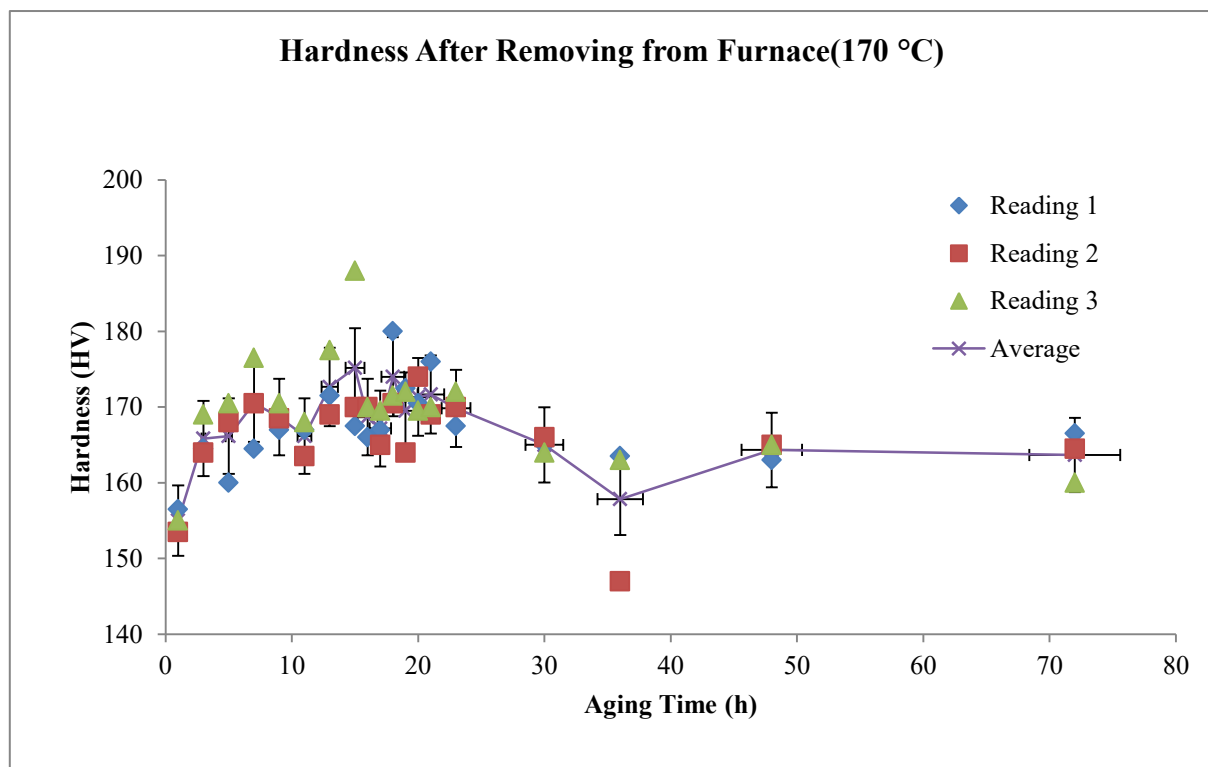


**Figure A.9.** Scatter in the 170 °C heat treatment results after removing the samples from the furnace.

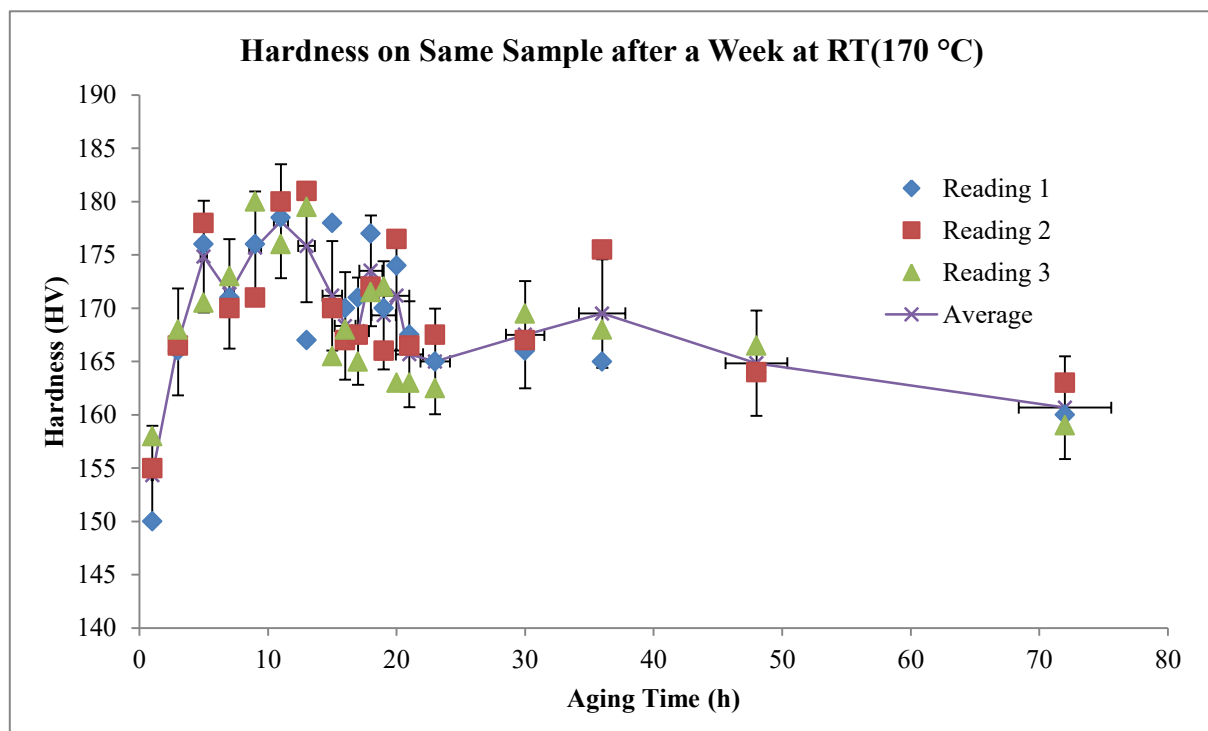


**Figure A.10.** Scatter in the 170 °C heat treatment results a week after removing the samples from the furnace.

### A.2.5. 175 °C

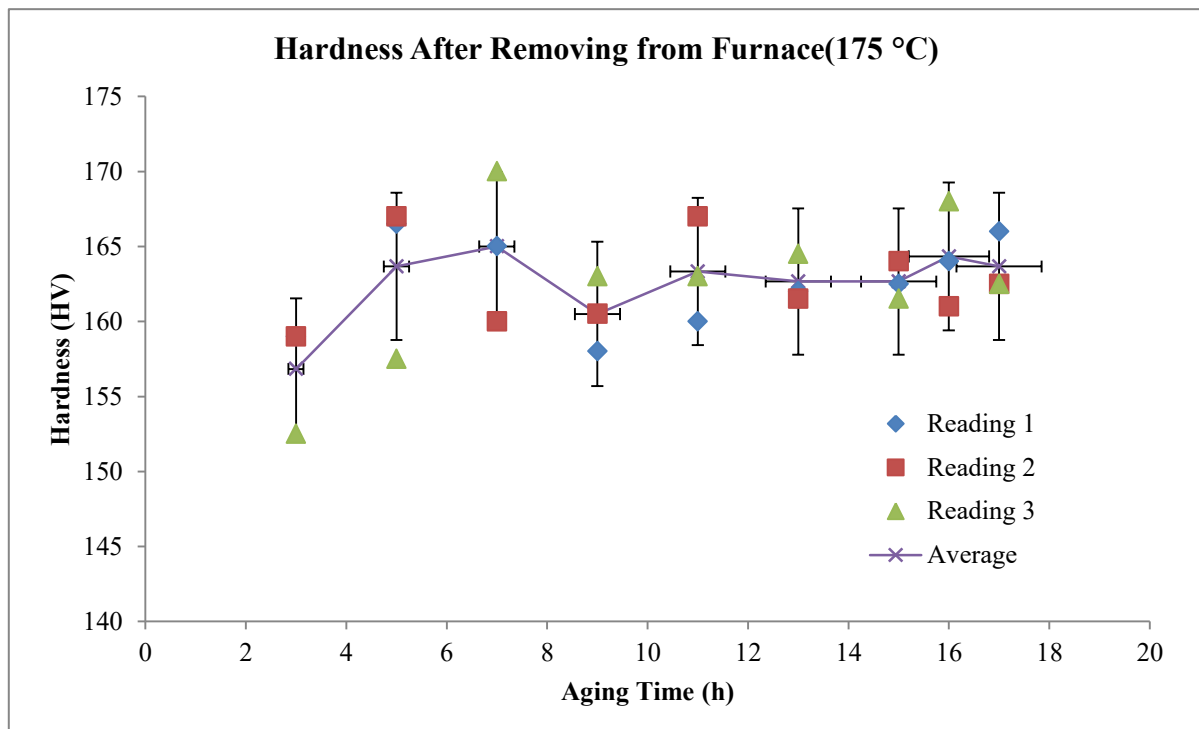


**Figure A.11.** Scatter in the 175 °C heat treatment results after removing the samples from the furnace.

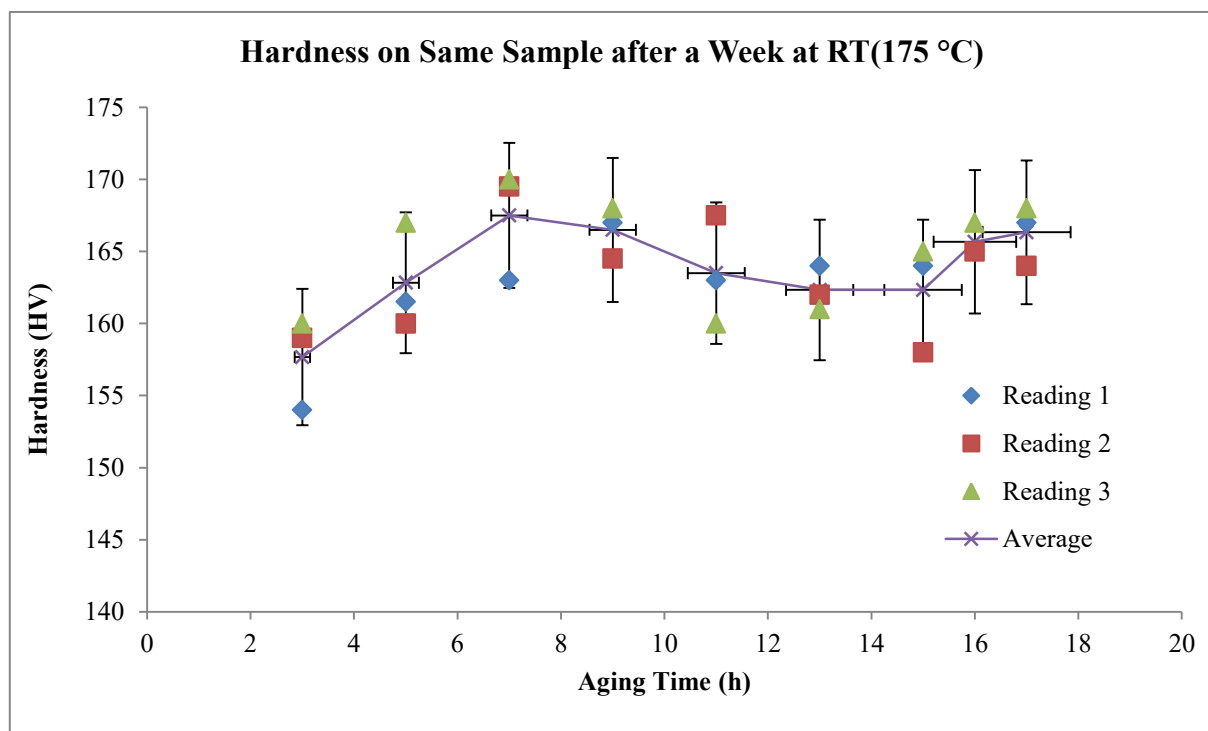


**Figure A.12.** Scatter in the 175 °C heat treatment results a week after removing the samples from the furnace.

### A.2.6. 180 °C

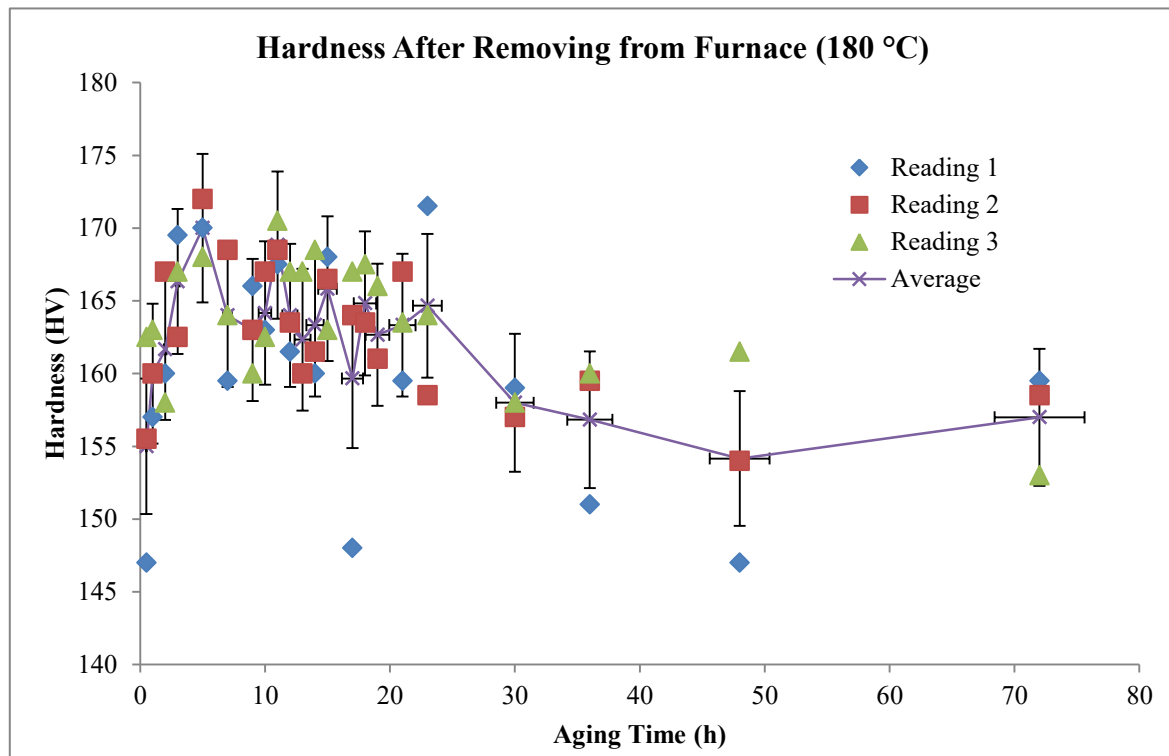


**Figure A.13.** Scatter in the 180 °C heat treatment results after removing the samples from the furnace.

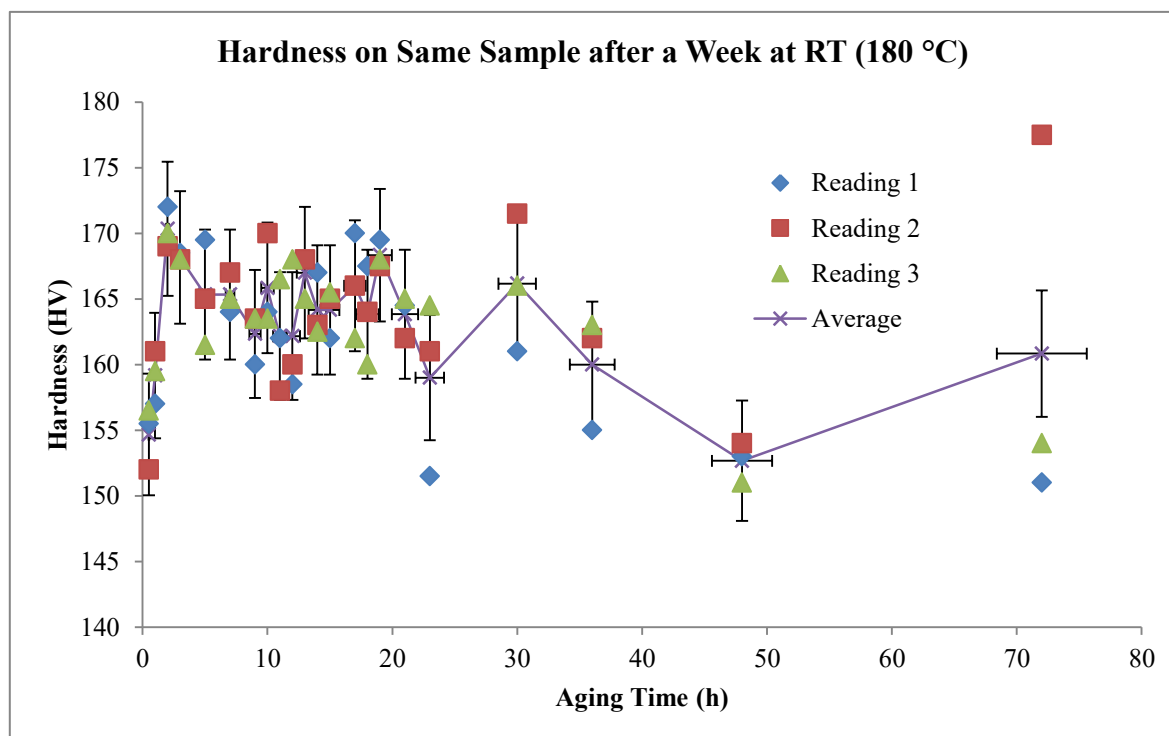


**Figure A.14.** Scatter in the 180 °C heat treatment results a week after removing the samples from the furnace.

### Appendix A.3. 2D engineering drawings of test specimen

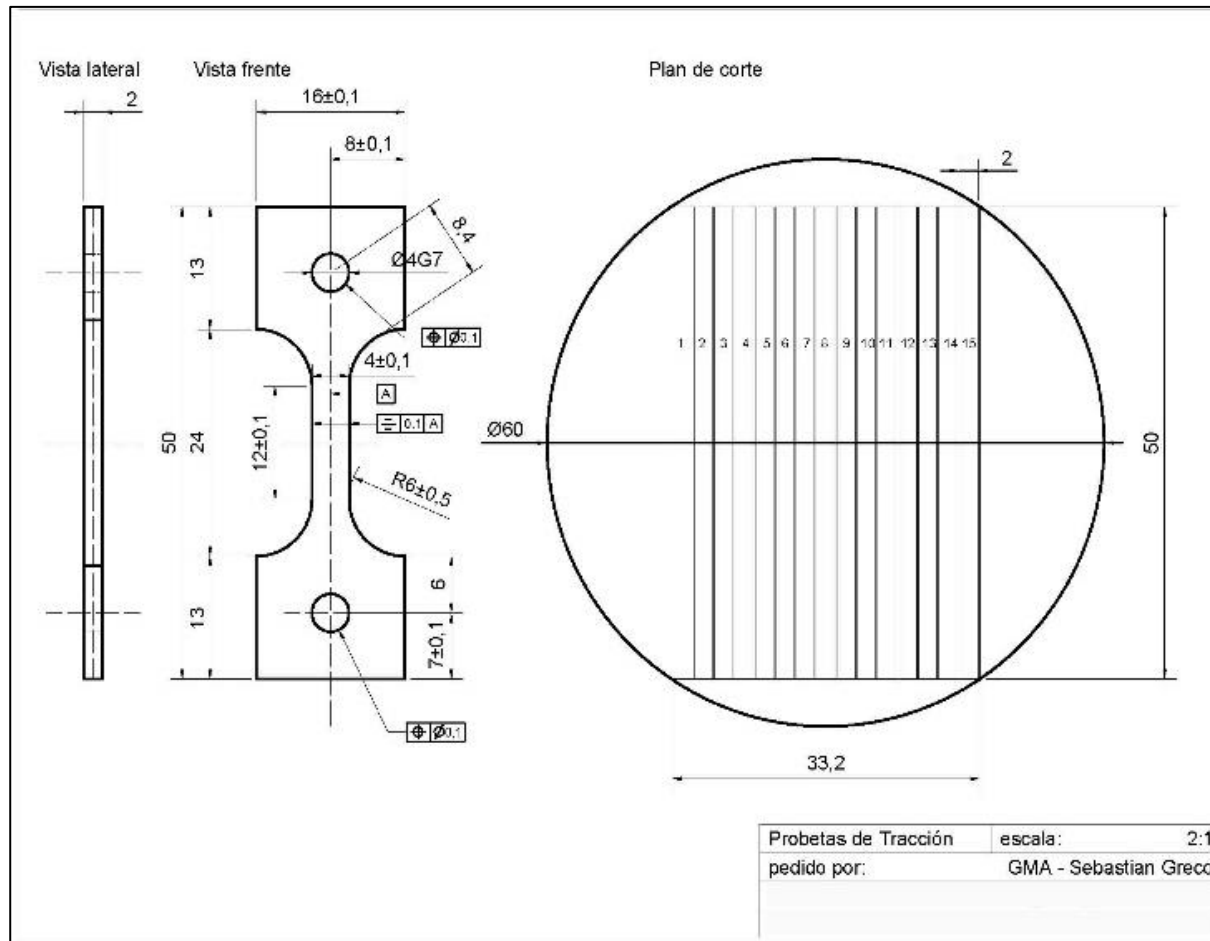


**Figure A.15.**A 2D engineering drawing of flat dogbone specimen for tensile tests.

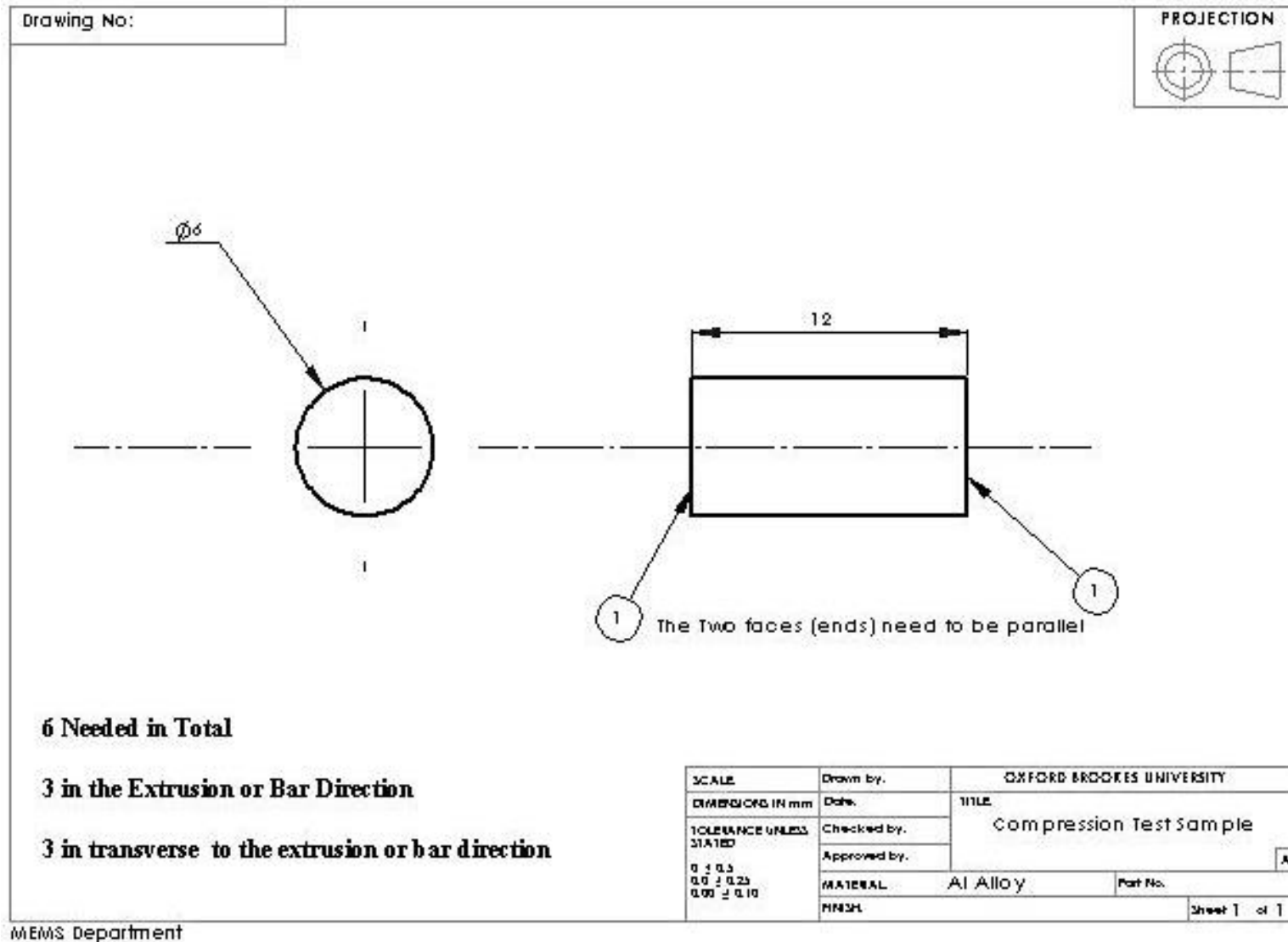


**Figure A.16.** A 2D engineering drawing of the cylindrical specimen for the compression tests

## Appendix A.4. XRD reference cards

The X-ray diffraction reference cards used in this project are given as the following.

### A.4.1. XRD card for Mg<sub>17</sub>Al<sub>12</sub> crystal structure

01-076-2702

Aug 21, 2015 12:17 PM (oums0698)

Status Primary QM: Star (5) Pressure/Temperature: Ambient Chemical Formula: Mg17 Al12

Empirical Formula: Al12 Mg17 Weight %: Al43.93 Mg56.07 Atomic %: Al41.38 Mg58.62 ANX: N12017

Compound Name: Aluminum Magnesium

Radiation: CuKα1 : 1.5406Å d-Spacing: Calculated Intensity: Calculated I/c: 2.52

SYS: Cubic SPGR: I-43m (217)

Author's Cell [ AuthCell a: 10.5492(2)Å AuthCell Vol: 1173.97Å³ AuthCell Z: 2.00 AuthCell MolVol: 586.99 ]

Dcalc: 2.085g/cm³ Dstruc: 2.08g/cm³ SS/FOM: F(30) = 999.9(0.0000, 31) R factor: 0.048

Space Group: I-43m (217) Molecular Weight: 736.96

Crystal Data [ XtiCell a: 10.549Å XtiCell b: 10.549Å XtiCell c: 10.549Å XtiCell : 90.00° XtiCell : 90.00° XtiCell : 90.00° XtiCell Vol: 1173.97Å³ XtiCell Z: 2.00 ]

Crystal Data Axial Ratio [ a/b: 1.000 c/b: 1.000 ]

Reduced Cell [ RedCell a: 9.136Å RedCell b: 9.136Å RedCell c: 9.136Å RedCell : 109.47° RedCell : 109.47° RedCell : 109.47° RedCell Vol: 586.99Å³ ]

Crystal (Symmetry Allowed): Non-centrosymmetric, Piezo (2nd Harm.)

Pearson: cI58.00 Prototype Structure: Mn Prototype Structure (Alpha Order): Mn

Subfile(s): Metals & Alloys, Forensic, Common Phase, ICSD Pattern, Inorganic, Primary Pattern Entry Date: 11/04/2008

Last Modification Date: 01/19/2011

References:

Type Reference

Primary Reference Structure Calculated from ICSD using POWD-12+  
"Limits of the Mg-Al gamma-phase range by ball-milling", Crivello, J.-C., Nobuki, T., Kaji, T. Intermetallics 15, 1432 (2007).

Database Comments: ANX: N12017. Analysis: Al12 Mg17. Formula from original source: Mg17 Al12. ICSD Collection Code: 158247. Wyckoff Sequence: g2 c a (I4-3M). Unit Cell Data Source: Powder Diffraction.

d-Spacings (θ) - 01-076-2702 (Fixed Slt Intensity) - Cu K1 1.54056Å

2	d(Å)	I	h	k	l	*	2	d(Å)	I	h	k	l	*	2	d(Å)	I	h	k	l	*
11.8542	7.459410	6	1	1	0		67.5712	1.385180	27	7	3	0		106.2355	0.963006	15	10	4	2	
16.7945	5.274000	1	2	0	0		70.1913	1.339750	31	6	5	2		107.5124	0.955080	20	11	1	0	
20.6063	4.306690	14	2	1	1		72.7686	1.298520	11	8	1	1		110.0943	0.939797	20	10	5	1	
23.8376	3.729710	17	2	2	0		74.0438	1.279280	11	8	2	0		111.4010	0.932426	1	8	8	0	
26.7006	3.335950	1	3	1	0		75.3109	1.260870	9	6	5	3		112.7194	0.925226	2	11	3	0	
29.3033	3.045290	5	2	2	2		76.5702	1.243240	58	8	2	2		114.0507	0.918190	1	8	8	2	
31.7105	2.819390	9	3	2	1		77.8236	1.226320	14	7	4	3		115.3959	0.911312	14	11	3	2	
33.9640	2.637300	58	4	0	0		79.0705	1.210090	3	6	6	2		116.7504	0.904586	7	10	6	0	
36.0930	2.486470	999	4	1	1		80.3129	1.194450	9	7	5	2		118.1334	0.898007	8	11	4	1	
38.1186	2.358870	9	4	2	0		81.5499	1.179440	1	8	4	0		119.5281	0.891570	1	10	6	2	
40.0555	2.249100	259	3	3	2		82.7840	1.164950	20	9	1	0		120.9425	0.885269	2	9	6	5	
41.9195	2.153350	98	4	2	2		84.0139	1.151010	8	8	4	2		122.3780	0.879100	2	12	0	0	
43.7174	2.068870	148	5	1	0		85.2410	1.137550	19	7	6	1		123.8368	0.873058	13	9	7	4	
47.1483	1.926010	17	5	2	1		86.4661	1.124550	7	6	6	4		125.3209	0.867139	1	12	2	0	
48.7934	1.864050	3	4	4	0		87.6901	1.111980	33	9	3	0		126.8327	0.861339	13	10	7	1	
50.3981	1.809170	12	4	3	3		90.1339	1.088070	5	9	3	2		128.3752	0.855653	1	12	2	2	
51.9663	1.758200	9	6	0	0		91.3566	1.076670	4	8	4	4		129.9512	0.850079	17	12	3	1	
53.5017	1.711310	11	6	1	1		92.5789	1.065630	8	8	5	3		133.2190	0.839249	3	10	7	3	
55.0075	1.667970	2	6	2	0		93.8027	1.054920	1	8	6	0		134.9198	0.833987	2	12	4	0	
56.4856	1.627780	5	5	4	1		95.0279	1.044530	2	10	1	1		136.6724	0.828823	1	11	5	4	
57.9393	1.590350	17	6	2	2		96.2467	1.034430	3	10	2	0		138.4838	0.823754	5	12	4	2	
59.3702	1.555390	4	6	3	1		97.4868	1.024630	3	9	4	3		140.3522	0.818777	4	9	9	2	
60.7797	1.522650	43	4	4	4		98.7209	1.015100	3	10	2	2		142.3186	0.813888	4	10	8	2	
62.1708	1.491880	60	5	5	0		99.9592	1.005830	16	9	5	2		144.3650	0.809087	4	12	5	1	
63.5439	1.462910	1	6	4	0		102.4511	0.988023	16	7	7	4		146.5194	0.804369	1	10	6	6	
64.9010	1.435560	210	7	2	1		103.7055	0.979489	6	10	4	0		148.8038	0.799733	1	11	7	2	
66.2427	1.409000	39	6	4	2		104.9667	0.971133	20	9	6	1								

Figure A.17. XRD reference card for Mg<sub>17</sub>Al<sub>12</sub> crystal structure.



## A.4.2. Aluminium (Al)

04-0787		Wavelength= 1.54184				
Al	2 $\theta$	Int	h	k	l	
Aluminum	38.505	100	1	1	1	
	44.778	47	2	0	0	
	65.194	22	2	2	0	
Aluminum, syn [NR]	78.305	24	3	1	1	
	82.519	7	2	2	2	
Rad.: CuK $\alpha$ 1 $\lambda$ : 1.54056 Filter: Ni Beta d-sp:	99.189	2	4	0	0	
Cut off: Int.: Diffract. I/Icor.: 3.619	112.183	8	3	3	1	
	116.723	8	4	2	0	
Ref: Swanson, Tatge, Natl. Bur. Stand. (U.S.), Circ. 539, I, 11 (1953)	137.70	8	4	2	2	
Sys.: Cubic	S.G.: Fm3m (225)					
a: 4.0494	b:	c:	A:	C:		
$\alpha$ :	$\beta$ :	$\gamma$ :	Z: 4	mp:		
Ref: Ibid.						
Dx: 2.699	Dm:	SS/FOM: F <sub>g</sub> = 93/(1.0108, 9 )				
Color: Light gray metallic						
Pattern taken at 25 C. CAS #: 7429-90-5. The material used for the NBS sample was a melting point standard sample of aluminum prepared at NBS, Gaithersburg, MD, USA. The chemical analysis (%): Si 0.011, Cu 0.006, Fe 0.007, Ti 0.0001, Zr 0.003, Ga 0.004, Mo 0.00002, S 0.0001, Al 99.9+ (by difference). Mineral species of doubtful validity, Am. Mineral., 65 205 (1980). Cu type. Gold group, gold subgroup. PSC: cF4. Mwt: 26.98. Volume[CD]: 66.40.						



© 1998 JCPDS-International Centre for Diffraction Data. All rights reserved  
PCPDFWIN v. 2.00

Figure A.18. Aluminium XRD reference card.

## A.4.3. XRD cards for Mg<sub>2</sub>Si crystal structure

**Name and formula**

Reference code: 00-034-0458  
 PDF index name: Magnesium Silicon  
 Empirical formula:  $\text{Mg}_2\text{Si}$   
 Chemical formula:  $\text{Mg}_2\text{Si}$

**Crystallographic parameters**

Crystal system: Cubic  
 Space group:  $Fm-3m$   
 Space group number: 225  
 a (Å): 6.3514  
 b (Å): 6.3514  
 c (Å): 6.3514  
 Alpha (°): 90.0000  
 Beta (°): 90.0000  
 Gamma (°): 90.0000  
 Calculated density (g/cm<sup>3</sup>): 1.99  
 Measured density (g/cm<sup>3</sup>): 2.01  
 Volume of cell (10<sup>6</sup> pm<sup>3</sup>): 256.22  
 Z: 4.00  
 RIR: -

**Status, subfiles and quality**

Status: Marked as deleted by ICDD  
 Subfiles: Inorganic  
 Alloy, metal or intermetallic  
 Quality: Star (S)

**Comments**

Deleted by: Deleted by 00-035-0773.  
 General comments: Pattern at 25 C.  
 Analysis: Chemical analysis (wt.%): Mg 62.3, Si 37.2.  
 Additional pattern: To replace 00-001-1192.

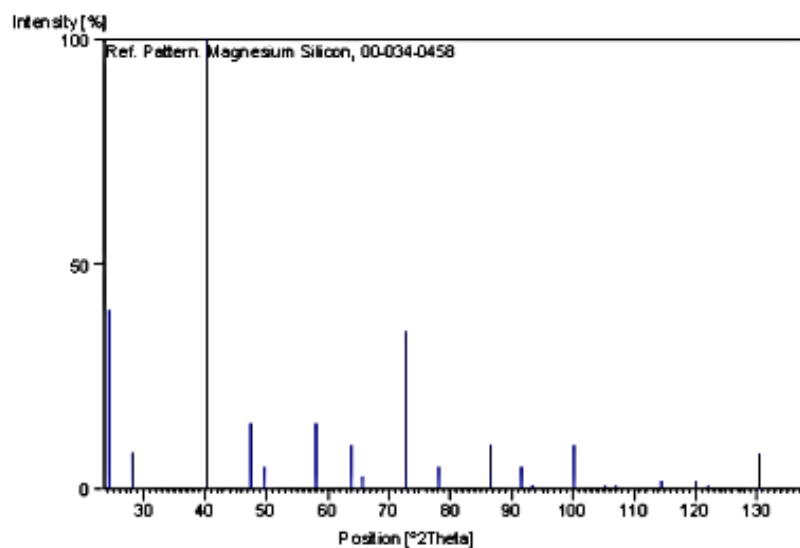
**References**

Primary reference: Friel, J., Bethlehem Steel Corporation, Bethlehem, Pennsylvania, USA., *Private Communication*, (1983)  
 Optical data: *Ibid.*, *Private Communication*  
 Unit cell: *Ibid.*, *Private Communication*

**Peak list**

No.	h	k	l	d [Å]	2Theta[deg]	I [%]
1	1	1	1	3.66000	24.299	40.0
2	2	0	0	3.18000	28.037	8.0

3	2	2	0	2.24500	40.134	100.0
4	3	1	1	1.91500	47.437	15.0
5	2	2	2	1.83400	49.671	5.0
6	4	0	0	1.58800	58.035	15.0
7	3	3	1	1.45700	63.834	10.0
8	4	2	0	1.42000	65.703	3.0
9	4	2	2	1.29650	72.902	35.0
10	3	3	3	1.22240	78.123	5.0
11	4	4	0	1.12280	86.637	10.0
12	5	3	1	1.07370	91.685	5.0
13	4	4	2	1.05860	93.381	1.0
14	6	2	0	1.00440	100.157	10.0
15	5	3	3	0.96970	105.346	1.0
16	6	2	2	0.95760	107.106	1.0
17	4	4	4	0.91680	114.324	2.0
18	5	5	1	0.88940	120.015	2.0
19	6	4	0	0.88070	122.006	1.0
20	6	4	2	0.84870	130.358	8.0
21	7	3	1	0.82680	137.391	2.0

**Stick Pattern****Figure A.19.** XRD reference card for  $\text{Mg}_2\text{Si}$  crystal structure.

The other XRD reference card for  $\text{Mg}_2\text{Si}$  is given as the following.

**Name and formula**

Reference code: 00-035-0773  
 PDF index name: Magnesium Silicon  
 Empirical formula:  $Mg_2Si$   
 Chemical formula:  $Mg_2Si$

**Crystallographic parameters**

Crystal system: Cubic  
 Space group: Fm-3m  
 Space group number: 225  
 a (Å): 6.3512  
 b (Å): 6.3512  
 c (Å): 6.3512  
 Alpha (°): 90.0000  
 Beta (°): 90.0000  
 Gamma (°): 90.0000  
 Volume of cell (10<sup>6</sup> pm<sup>3</sup>): 256.19  
 Z: 4.00  
 RIR: -

**Subfiles and Quality**

Subfiles: Inorganic  
 Alloy, metal or intermetallic  
 Common Phase  
 NBS pattern  
 Quality: Star (S)

**Comments**

Color: Dark blue  
 Sample source: The sample was obtained from CERAC, Incorporated, Milwaukee, Wisconsin, USA. It contained a small amount of MgO.  
 Analysis: Spectrographic analysis (wt%, CERAC, Incorporated): 0.12 Fe; 0.05 Al; 0.01 Mn; 0.001 Ag, Ca, Cr, Cu, Ti.  
 Additional pattern: To replace 00-001-1192 and 00-034-0458.  
 Temperature: The mean temperature of data collection was 23.7 C.

**References**

Primary reference: *Natl. Bur. Stand. (U.S.) Monogr.* 25, **21**, 86, (1985)  
 Structure: Klemm, W., Westlinning, H., *Z. Anorg. Allg. Chem.*, **245**, 365, (1940)  
 Polymorphism: Cannon, P., Conlin, C., *Science*, **145**, 487, (1964)

**Peak list**

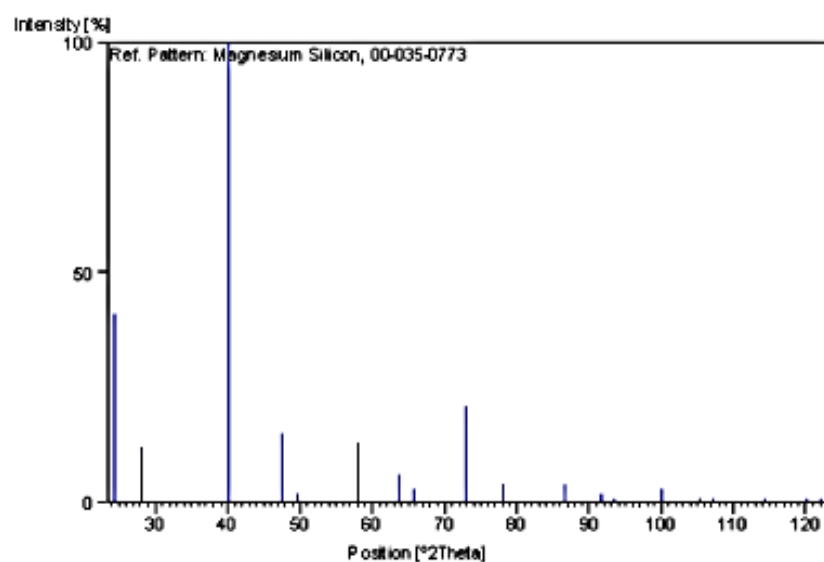
No.	h	k	l	d [Å]	2Theta [deg]	I [%]
1	1	1	1	3.66849	24.242	41.0

Date: 14/05/2013 Time: 17:22:15

File: 6061SSR7-smooth

User: Xia

2	2	0	0	3.17619	28.071	12.0
3	2	2	0	2.24564	40.122	100.0
4	3	1	1	1.91512	47.434	15.0
5	2	2	2	1.83377	49.677	2.0
6	4	0	0	1.58812	58.030	13.0
7	3	3	1	1.45697	63.835	6.0
8	4	2	0	1.42006	65.700	3.0
9	4	2	2	1.29649	72.903	21.0
10	5	1	1	1.22244	78.120	4.0
11	4	4	0	1.12281	86.636	4.0
12	5	3	1	1.07358	91.698	2.0
13	6	0	0	1.05861	93.380	1.0
14	6	2	0	1.00422	100.182	3.0
15	5	3	3	0.96854	105.371	1.0
16	6	2	2	0.95754	107.116	1.0
17	4	4	4	0.91669	114.345	1.0
18	5	5	1	0.88932	120.033	1.0
19	6	4	0	0.88066	122.015	1.0


**Stick Pattern**Figure A.20. XRD reference card for  $\text{Mg}_2\text{Si}$  crystal structure

2 of 2

## Appendix B

### B.1. Engine technical data: Engine tightening torques and piston life

The recommended cylinder mounts and nuts torque value and piston life for the test engine can be in the engine manual in Figures B.1 and B.2 respectively.

TECHNICAL DATA - ENGINE TIGHTENING TORQUES				73
Screw, camshaft gear	M10x1	50 Nm (36.88 lbf ft)	Engine oil (any) (☞ 85)	
Screw, ignition rotor	M10x1	80 Nm (59.01 lbf ft)	Engine oil (any) (☞ 85)	
Plug, oil channel	M10x1	10 Nm (7.38 lbf ft)	–	
Plug, cam lever axle	M10x1	10 Nm (7.38 lbf ft)	–	
Nut, cylinder head	M10x1,25	 Tightening sequence: Tighten in diagonal sequence. Tightening stage 1 10 Nm (7.38 lbf ft) Tightening stage 2 30 Nm (22.13 lbf ft) Tightening stage 3 50°	Engine oil (any) (☞ 85)	

**Figure B.1.** The recommended torque for the cylinder mounts and nuts.

Important maintenance work to be carried out by an authorized KTM workshop. (as additional order)					
	Every 10 service hours / 70 liters of fuel / after each race	Every 20 service hours / 140 liters of fuel	Every 40 service hours / 270 liters of fuel	annually	every 2 years
Carry out a complete fork service.			↑	•	
Carry out a complete shock absorber service.					•
Grease the steering head bearing. (☛ 31)				•	
Clean and adjust carburetor.				•	
Treat electric contacts with contact spray.				•	
Change hydraulic clutch fluid.				•	
Change brake fluid.				•	
Check wear of clutch discs.		•			
Check long clutch springs.		•			
Check clutch slave cylinder for dents.		•			
Check outer clutch hub for dents.		•			
Check cylinder wear and change pistons.			•		
Check camshaft wear. (visual check)			•		
Check wear of valve spring seat.			•		
Check wear of valve guides.			•		
Change valves.			•		
Change valve springs.			•		
Check the timing-chain tensioner function.			•		
Check crankshaft and crankshaft journal for run-out.			•		
Change conrod bearing.			•		
Check piston pin bearing.			•		
Change the crankshaft main bearing.			•		
Check wear of all transmission components including shafts and bearings.			•		
Check long bypass valve spring.			•		
Change glass fiber yarn filling of main silencer. (☛ 59)	•				

**Figure B.2.** The recommended service life for the original piston.

## B.2. Pressure on the cylinder head nuts

To attach the cylinder to the rest of the engine, mounting studs/bolts were used. In the case of the test engine used in the project, the mounting studs/bolts were M10 x 1.25 mm with nominal diameter of 9.96 mm. The washer/nuts had outer and inner diameters of 20 mm and 10 mm respectively. The dry frictional coefficient between steel nuts and aluminium engine casing was assumed to be 0.61 as suggested by (Edge, 2018a). Equation 5.1 was used to find the tension/axial load in the mounting studs which was then converted into pressure using the nuts surface area.

$$T = cDF \quad (5.1)$$

Where T, c, D and F are torque, coefficient of friction constant, nominal bolt diameter and F was bolt tension (axial load).

Substituting into 5.1 and rearranging gave

$$F = (30)/(0.61 \times 10/1000) = 4918 \text{ N}$$

Area of the washer on which the torque/load was acting was calculated as the following.

$$\text{Area of a circle} = \pi r^2$$

$$\text{Area of a washer} = [0.02^2 - (0.01^2)] = 0.0009425 \text{ m}^2$$

Knowing the surface area on the washer and the load acting on it, the pressure was calculated as the following

$$P = F/A = 4918/0.0009425 = 5.22 \text{ MPa}$$

### **B.3. Engineering drawings of the different engine components**

The 2D engineering drawings for the different components included in the FE analyses are given as the following.



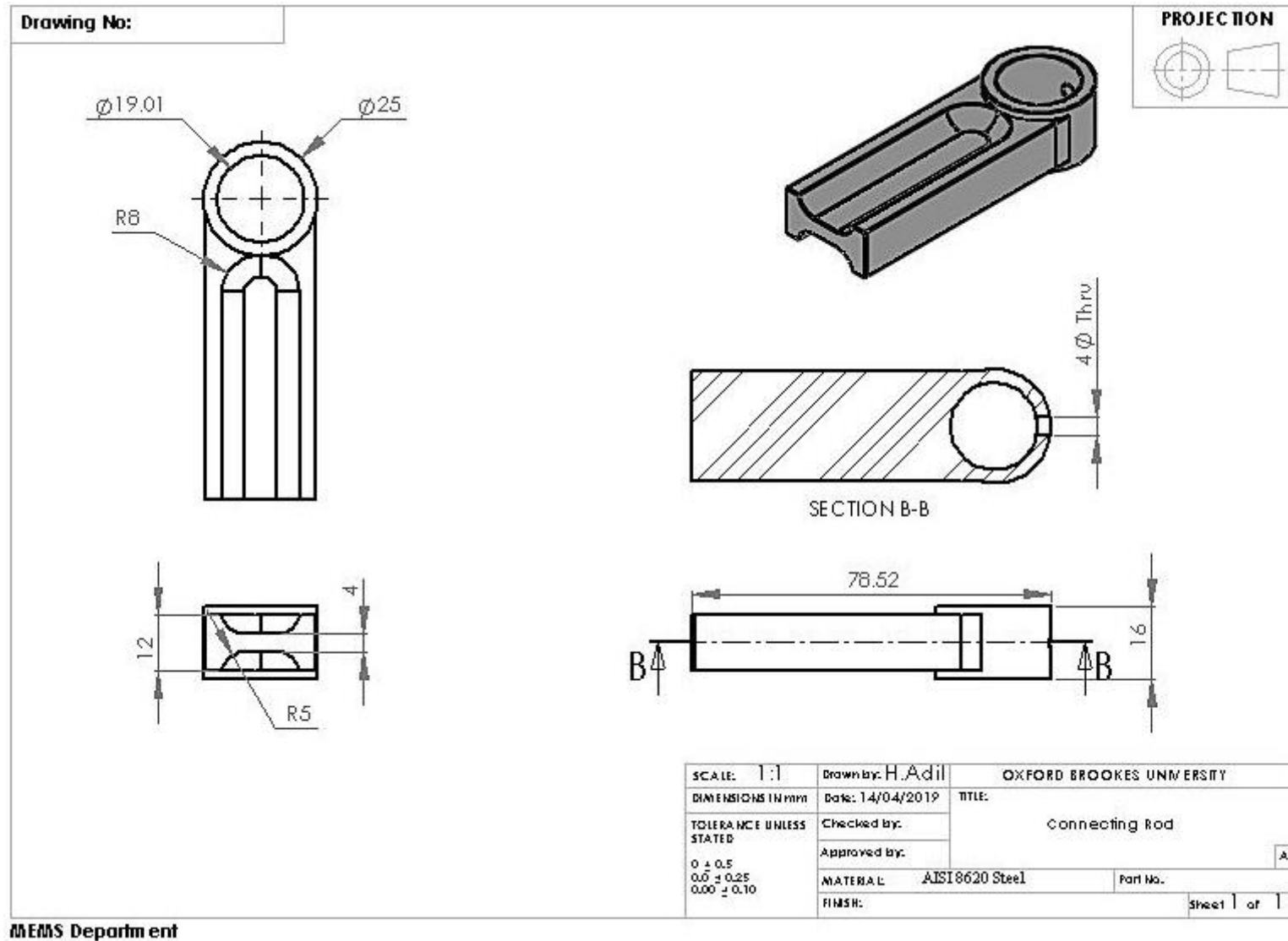


**Figure B.3.** A 2D engineering drawing of the connecting rod small end for the piston FEA.

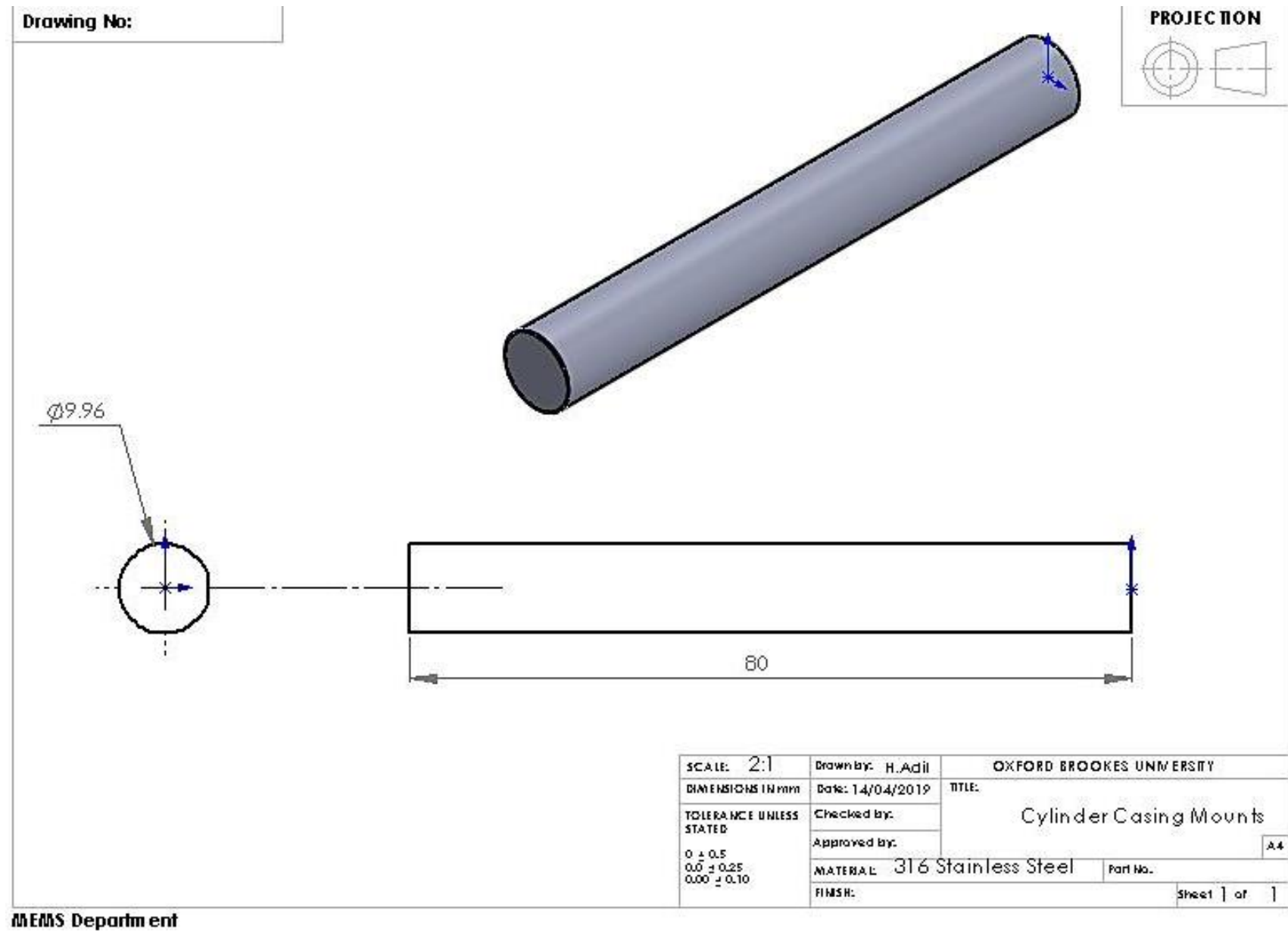


**Figure B.4.** A 2D engineering drawing of the cylinder mounts for the piston FEA.

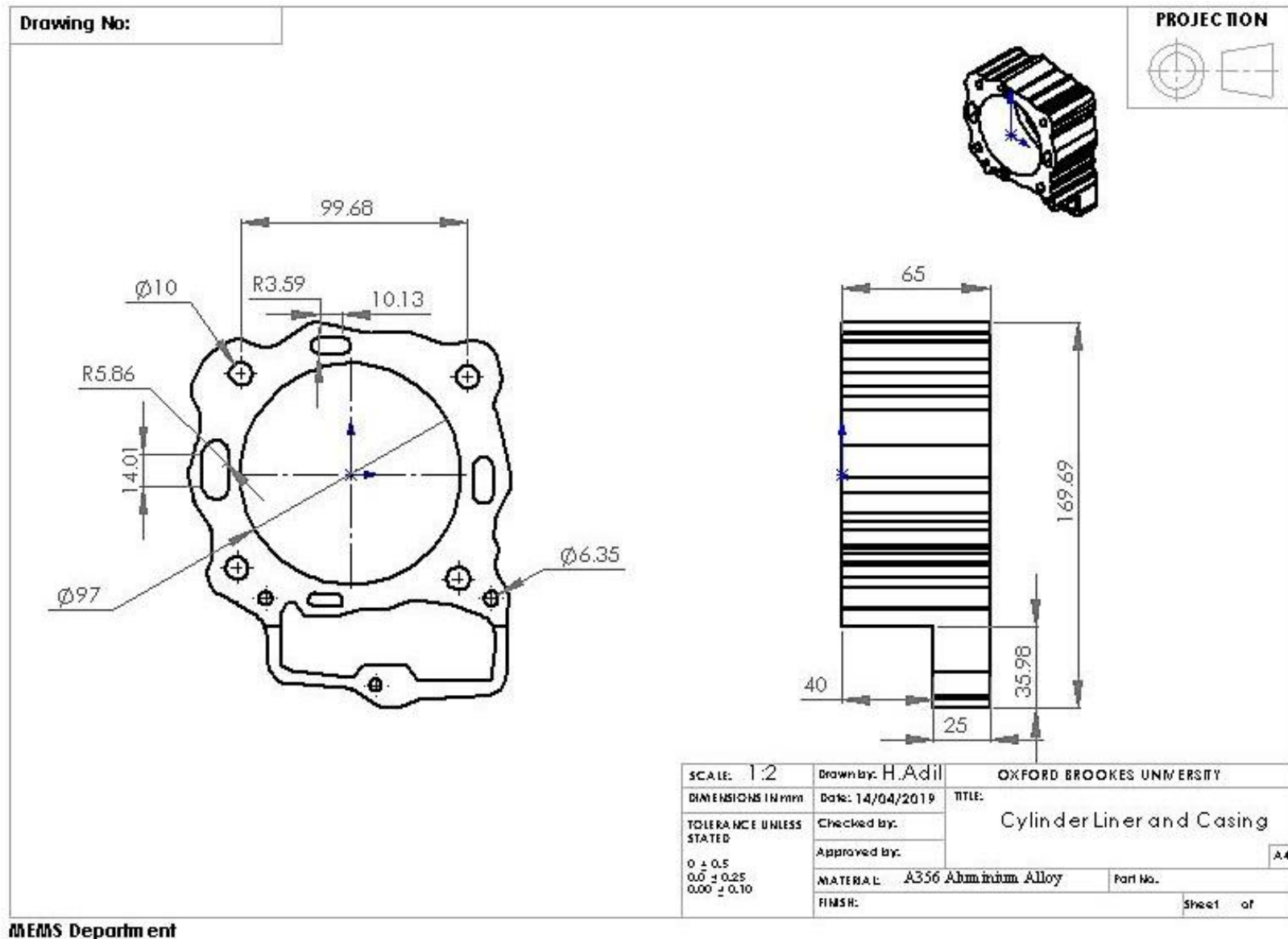


Figure B.5. A 2D engineering drawing of the cylinder liner and casing for the piston FEA.

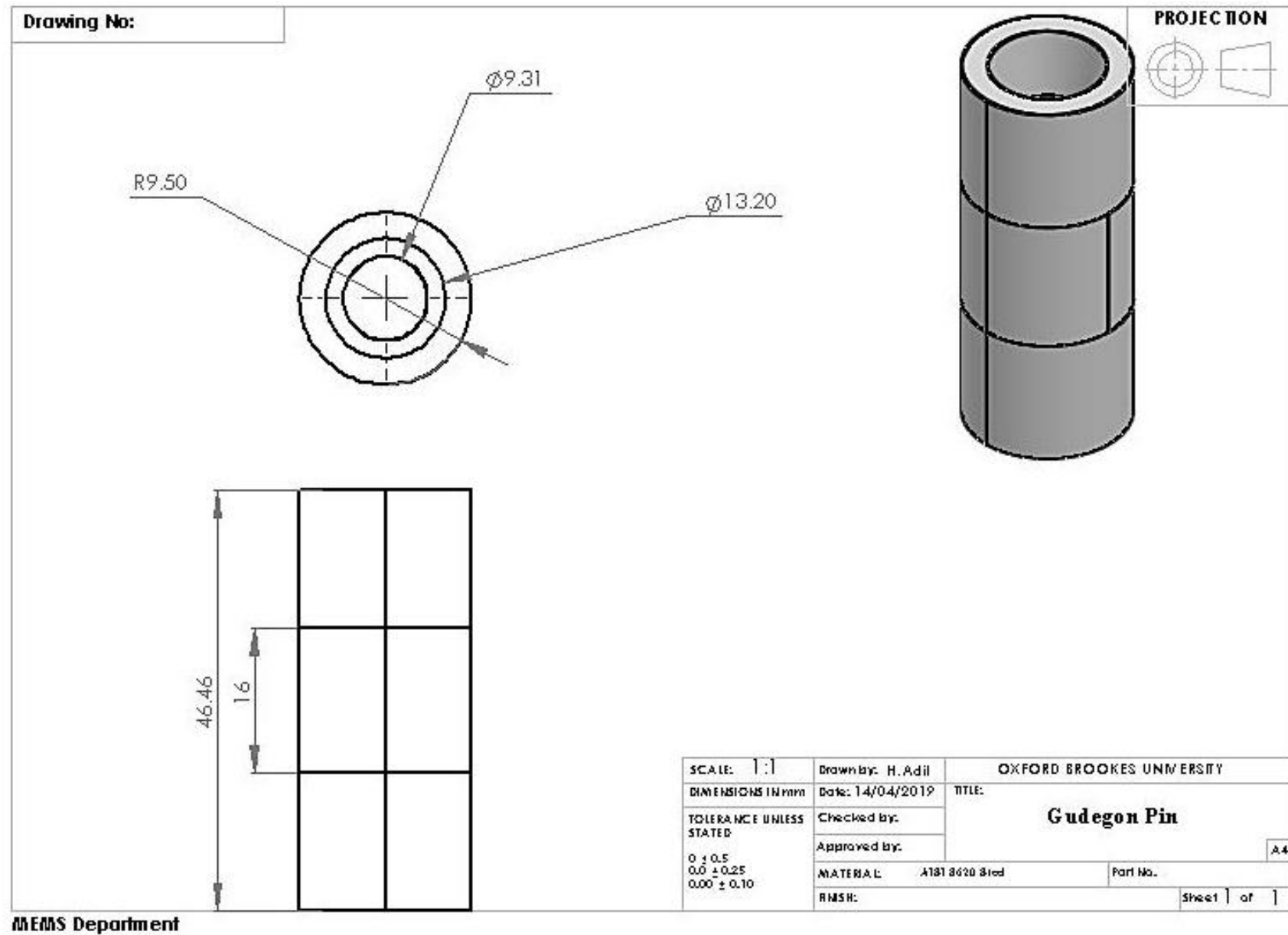
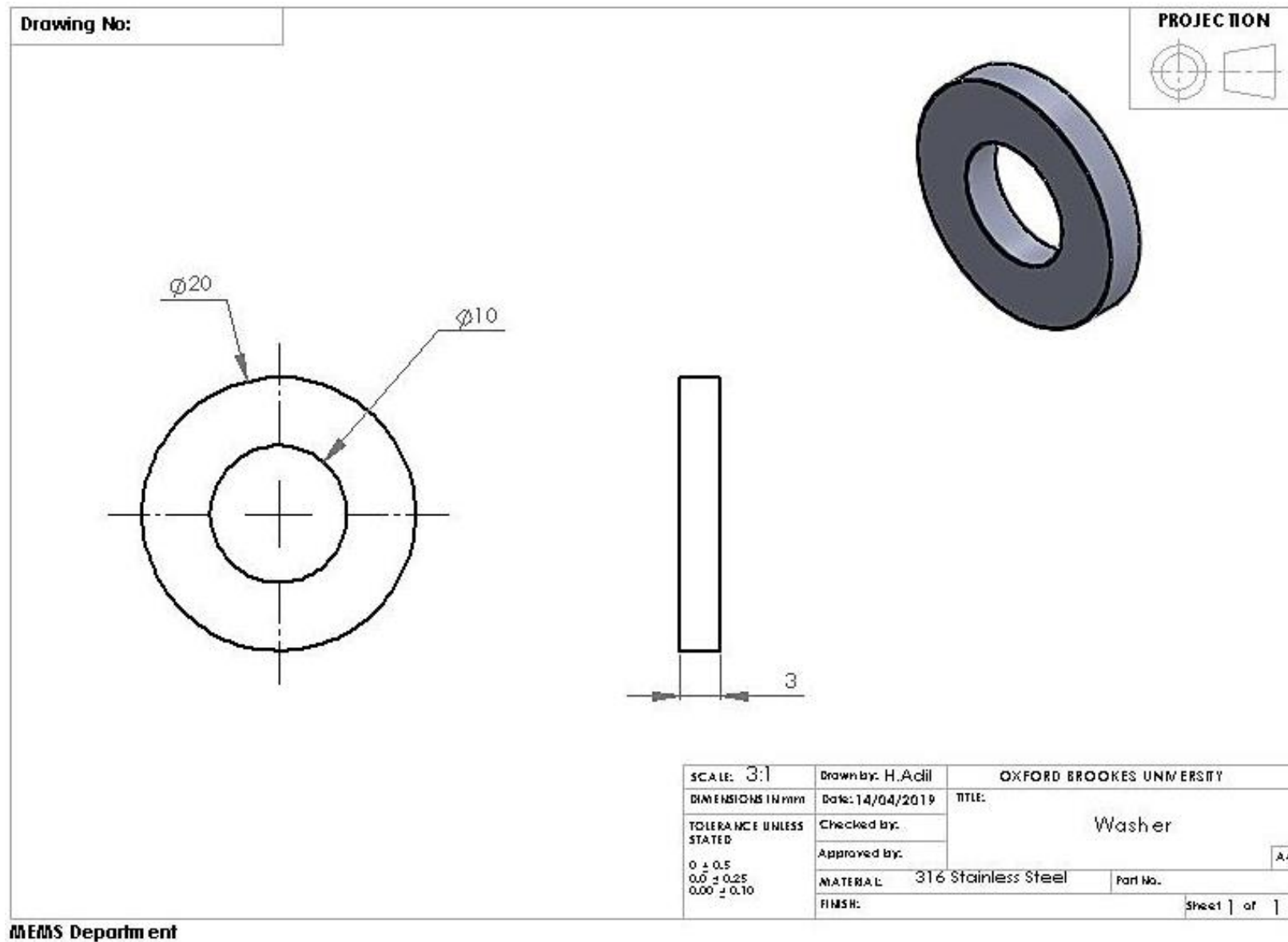
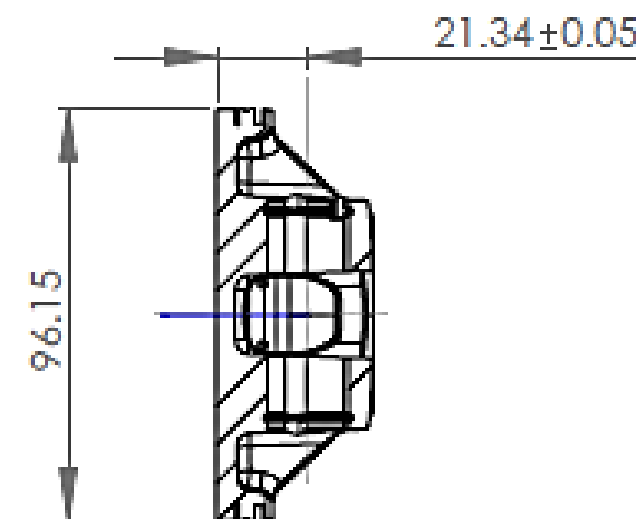
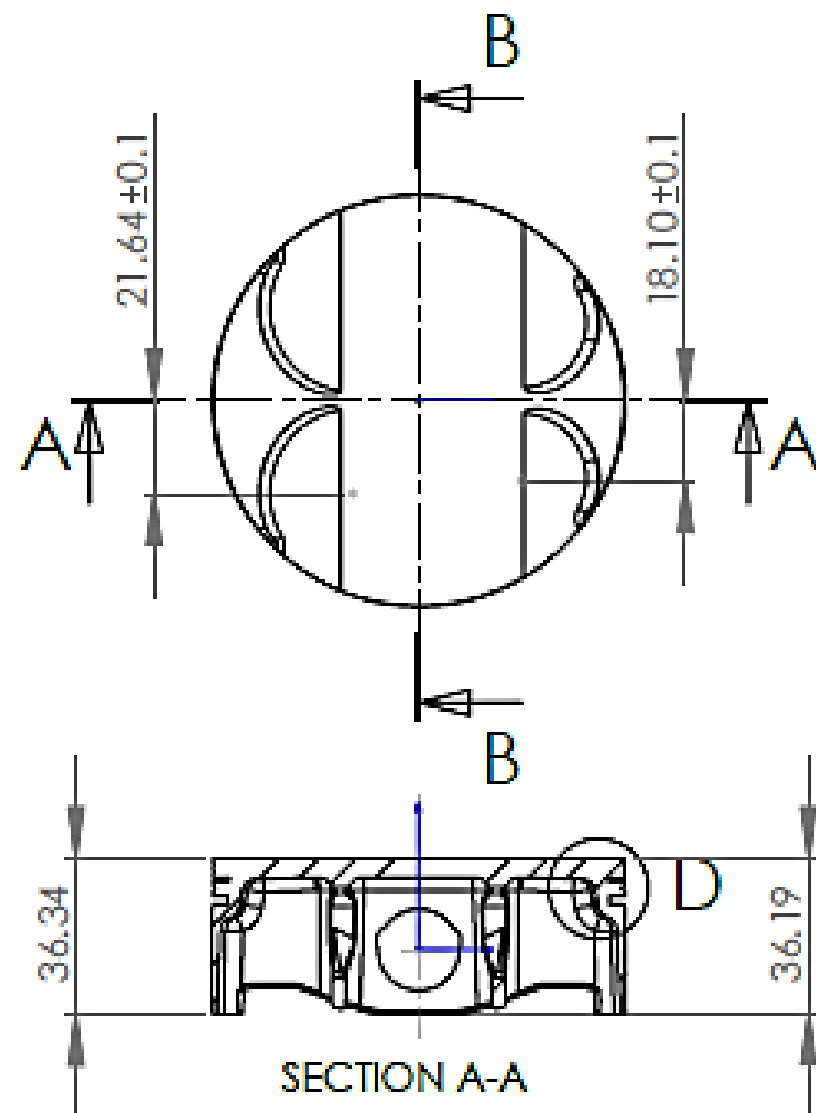


Figure B.6. A 2D engineering drawing of the gudgeon pin for the piston FEA.

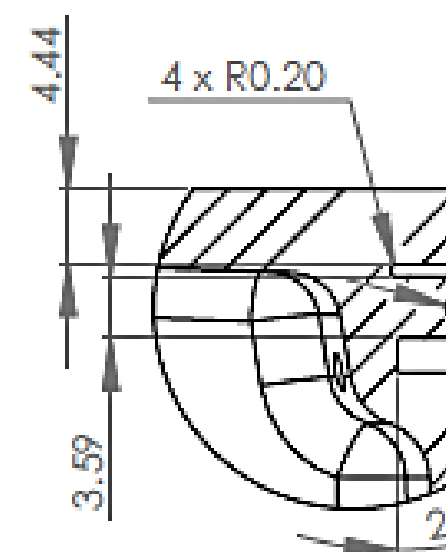


**Figure B.7.** A 2D engineering drawing of the washer for the piston FEA.

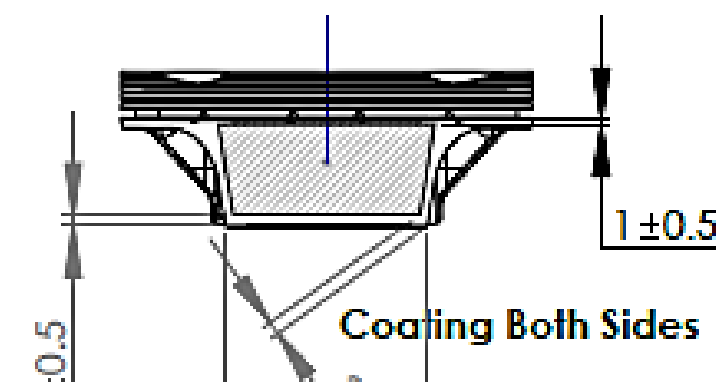
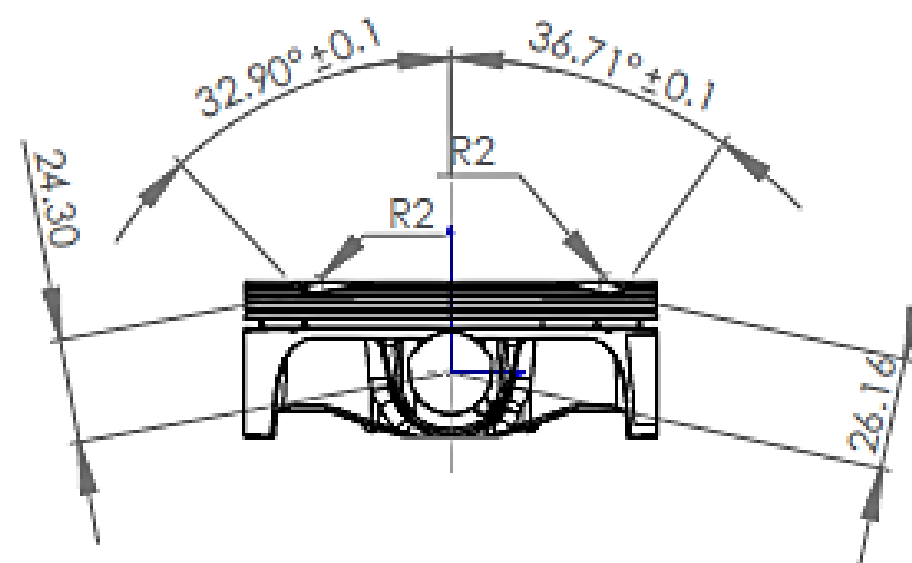
Drawing No:



SECTION B-B



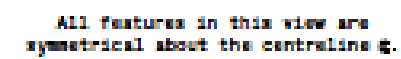
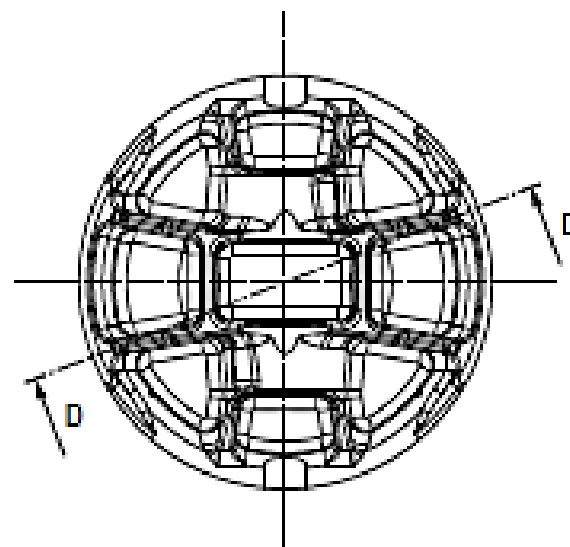
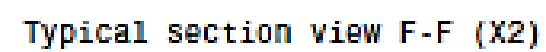
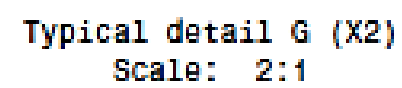
DETAIL D  
SCALE 2 : 1



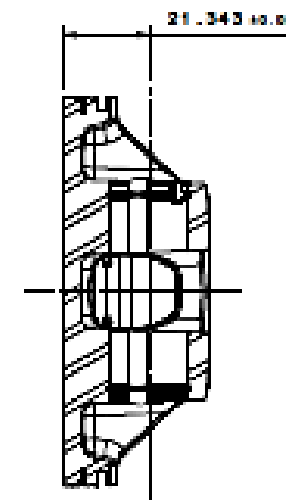
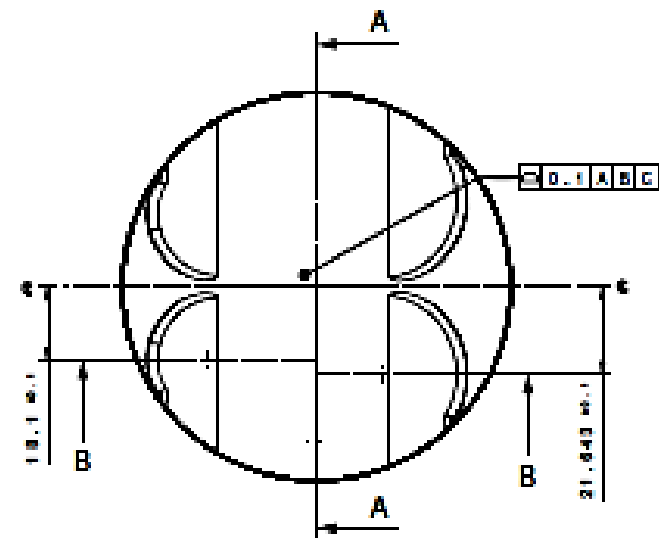
# NOTES:

- 1 - ALL FEATURES ( ) ABOUT THE CEN
  - 2 - MACHINE CROW
  - 3 - ALL SKIRT PROF
  - 4 - COAT SKIRT WIT
- COATING THICKNE

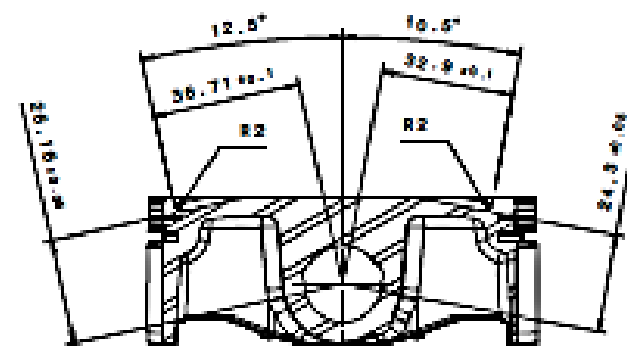




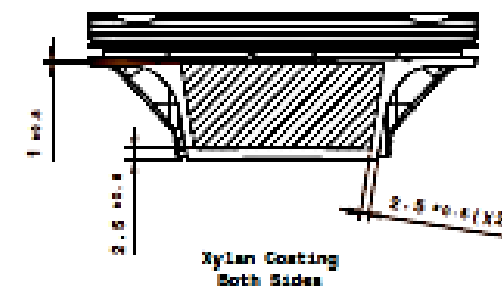
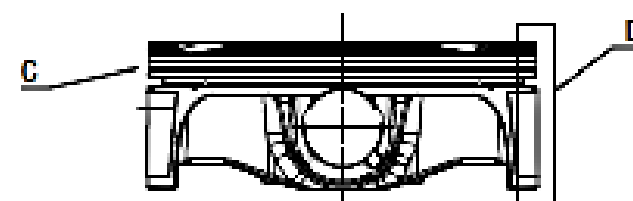




Section view A-A

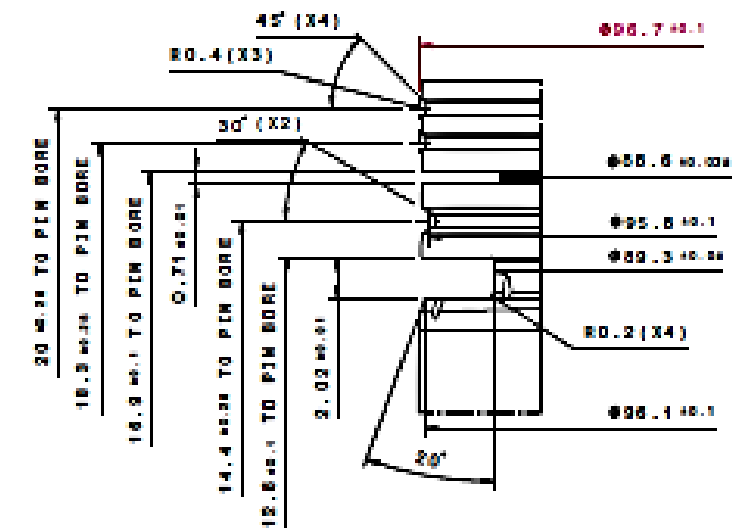


Section view B-B



NOTES:

- 1 - ALL FEATURES ON THIS DRAWING ARE SYMMETRICAL ABOUT THE CENTRELINE SHOWN  $\phi$ .
- 2 - MACHINE CROWN FROM CAD DATA.
- 3 - ALL SKIRT PROFILE DATA IS BEFORE XYLAN COATING.
- 4 - COAT SKIRT WITH BLACK XYLAN 1010 AS SHOWN.  
COATING THICKNESS TO BE 10-20  $\mu$ m PER FACE.  
COATING TO BE APPLIED VIA SPRAY AND CURED AT 220 °C FOR 15 MINUTES MIN.



Detail C  
Scale: 5:1

	HEIGHT FROM PIN BORE	NOMINAL RADIUS	RADIAL QUALITY	INSPECTION DIAMETER $\pm 0.005$	NOTES
A					REF
B					REF
C					
D					
E					
F					
G					
H					REF
J					
K					
L					
M					
N					PIN BORE
P					
R					
S	-8	48.445		36.620	UPPER GRADE DIA
T	-8	48.445		36.620	
U	10	48.445		36.620	LOWER GRADE DIA

## B.4. Material properties for FEA

The mechanical properties and some further information about the different material used for the various components in piston FEA are given as the following.

### B.4.1. Connecting rod and gudgeon pin

Connecting rods are normally drop forged out of steel alloys followed by case hardening. The typical steel alloys used are 42CrMo4, 43CrMo4, 44csr4, 8620 AISI etc. The connecting rod for the test engine (KTM 450 XCF 2008) was made of 8620 AISI by Hot Rods (FullThrottleTahoe, 2017; Racing, 2017; Vertex, 2017; Sales, 2018). Furthermore, the connecting rod for the test engine undergoes a process of double forging which helps to improve the grain flow as well as dimensional consistency (Vertex, 2017).

However, the connecting rod is as good as its supporting/related parts such as wrist/gudgeon pin etc. The wrist pin for test engine was also made of 8620 AISI steel (Interalloy, 2011) and coated with DLC (Diamond Like Carbon). Furthermore, the wrist pin was case hardened. The temperatures dependent mechanical properties of the 8620 AISI steel required for FEA are given in Table B.1.

Property	AISI 8620 Steel	
Density, $\rho$ ( $\frac{Kg}{m^3}$ )	Temp (°C), 25	$\rho$ 7872
Poisson Ratio, $\nu$	Temp (°C), 25	$\nu$ 0.287
	100	0.29
	150	0.291
	200	0.293
	250	0.294
	300	0.295
	350	0.296
Thermal Conductivity, k (W/m°C)	Temp (°C), 25	k 42.5
	100	42
	150	41.5
	200	41
	250	40
	300	39

	350	37.5
Young's Modulus, E GPa	<b>Temp (°C),</b>	<b>E</b>
	25	206
	100	203
	150	200
	200	197
	250	193
	300	189
	350	183
Ultimate Tensile Strength (UTS) (MPa)	<b>Temp (°C),</b>	<b>UTS</b>
	25	560
Yield Strength (YS) (MPa)	<b>Temp (°C),</b>	<b>YS</b>
	25	385
Thermal Expansion Coefficient (TEC) (μm/m.K)	<b>Temp (°C),</b>	<b>TEC</b>
	25	11.4
	100	12.5
	150	13.2
	200	13.5
	250	14.1
	300	14.4
	350	14.7

**Table B.1.** Mechanical properties of AISI 8620 steel used in the connecting rod and pin of the test engine.

#### B.4.2. Cylinder block

Cylinder block, (Figure B.10) also known as engine block is the main housing for the different parts found in engines and constitutes 20 – 25% of the engine's total weight. As it is the main housing, it has to include a number of requirements. These requirements include the wear resistance, long lasting maintenance, and withstand the pressure created when combustion take place. It also has to withstand high temperature, vibration when the engine is in the running condition. For many of the requirements the main feature is its material used and the commonly used material is aluminium alloys (Bloggers, 2014). The aluminium alloys widely used are 319 and A356 and for the test engine cylinder block A356 was used (Tsuyoshi and Sasaki, 2010). The alloy's properties required for FEA are given in Table B.2.

Nickel silicon carbide plating is used on the cylinder bore as opposed to cast iron or chrome plating, and the reason is that nickel silicon carbide allows for tighter tolerances between the piston and cylinder in large bores, provides a low friction surface. It is very durable and allows for greater heat dissipation to the water jacket (Vertex, 2017).



**Figure B.10.** A picture of the cylinder block for the test engine (Vertex, 2017).

Property	A356 Aluminium Alloy	
Density, $\rho$ ( $\frac{Kg}{m^3}$ )	Temp (°C), 25	$\rho$ 2685
Poisson Ratio, $\nu$	Temp (°C), 25-350	$\nu$ 0.33
Thermal Conductivity, k (W/m°C)	Temp (°C), 25	k 151
Young's Modulus, E GPa)	Temp (°C), 25	E 72
	100	70
	150	68
	200	65
	250	57
	300	47
	350	29
Ultimate Tensile Strength (UTS) (MPa)	Temp (°C), 25	UTS 230
	150	160
	200	85
	250	50
	300	30
Yield Strength (YS) (MPa)	Temp (°C), 25	YS 165
	150	140
	200	60
	250	35
	300	25

Thermal Expansion Coefficient (TEC) ( $\mu\text{m/m.K}$ )	Temp ( $^{\circ}\text{C}$ ),	TEC
	25	21.5
	100	21.5
	150	22.5
	200	22.5
	250	23.5
	300	23.5

**Table B.2.** Mechanical properties of aluminium alloy 356-T6-T-T61 used in the cylinder block of the test engine.

#### B.4.3. Cylinder threaded studs and nuts

Threaded fasteners are the vital links that secure everything together in an engine and are often taken for granted. Studs are preferred over bolts because they provide the ability to obtain much more accurate torque values and clamping force as they do not twist during nut tightening and stay stationary. All these result in less wear in block's threads and extends the life of threaded holes and engine block (Mavrigian, 2011). Engine cylinder studs are made of different materials, but the ones used in test engine were made stainless steel 316. The stainless steel properties required for FEA are given in Table B.3. It is also assumed that nuts used with studs are also made of the same material.

Property	316 Stainless Steel	
Density, $\rho$ ( $\frac{\text{Kg}}{\text{m}^3}$ )	Temp ( $^{\circ}\text{C}$ ),	$\rho$
	25	7950
Poisson Ratio, $\nu$	Temp ( $^{\circ}\text{C}$ ),	$\nu$
	25	0.26
	150	0.26
	250	0.29
	350	0.37
Thermal Conductivity, $k$ ( $\text{W/m}^{\circ}\text{C}$ )	Temp ( $^{\circ}\text{C}$ ),	$k$
	25	16.3
Young's Modulus, $E$ GPa	Temp ( $^{\circ}\text{C}$ ),	$E$
	25	200
	100	194
	200	185
	300	177
Ultimate Tensile Strength (UTS) (MPa)	Temp ( $^{\circ}\text{C}$ ),	UTS
	25	560
	200	560
	300	540

Yield Strength (YS) (MPa)	<b>Temp (°C),</b>	<b>YS</b>
	25	240
	200	240
	300	215
Thermal Expansion Coefficient (TEC) ( $\mu\text{m/m.K}$ )	<b>Temp (°C),</b>	<b>TEC</b>
	25	15.7
	100	16.5
	200	16.9
	300	17.3

**Table B.3.** Mechanical properties of stainless steel 316 used in studs and nuts of the test engine.

### **B.5. Instantaneous combustion gas temperature and heat transfer coefficient**

The instantaneous combustion gas temperature and heat transfer coefficient results for the two engine speeds are in Sections B.5.1 and B.5.2.

#### **B.5.1. 6000 RPM**

The instantaneous combustion gas temperature and heat transfer coefficient results for one engine cycle at 6000 rpm are given in Figures B.11 and B.12.

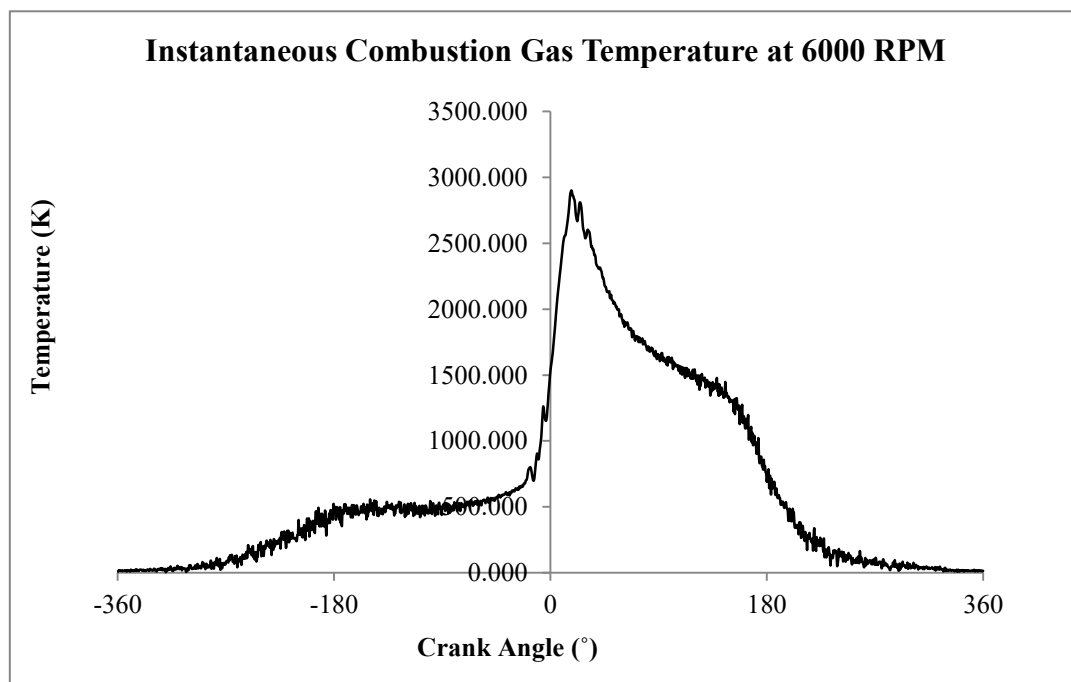


**Figure B.11.** Instantaneous combustion gas temperature for one engine cycle at 6000 rpm.

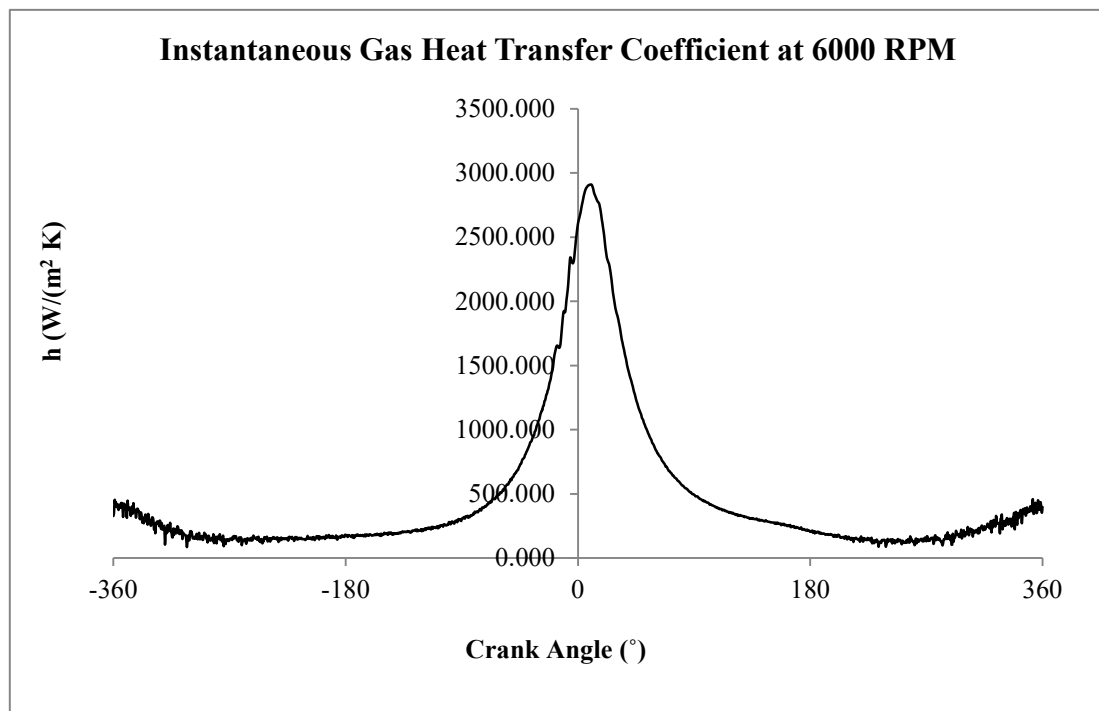


**Figure B.12.** Instantaneous combustion heat transfer coefficient for one engine cycle at 6000 rpm.

#### B.5.2. 7000 RPM

The instantaneous combustion gas temperature and heat transfer coefficient results for one engine cycle at 7000 rpm are given in Figures B.13 and B.14.

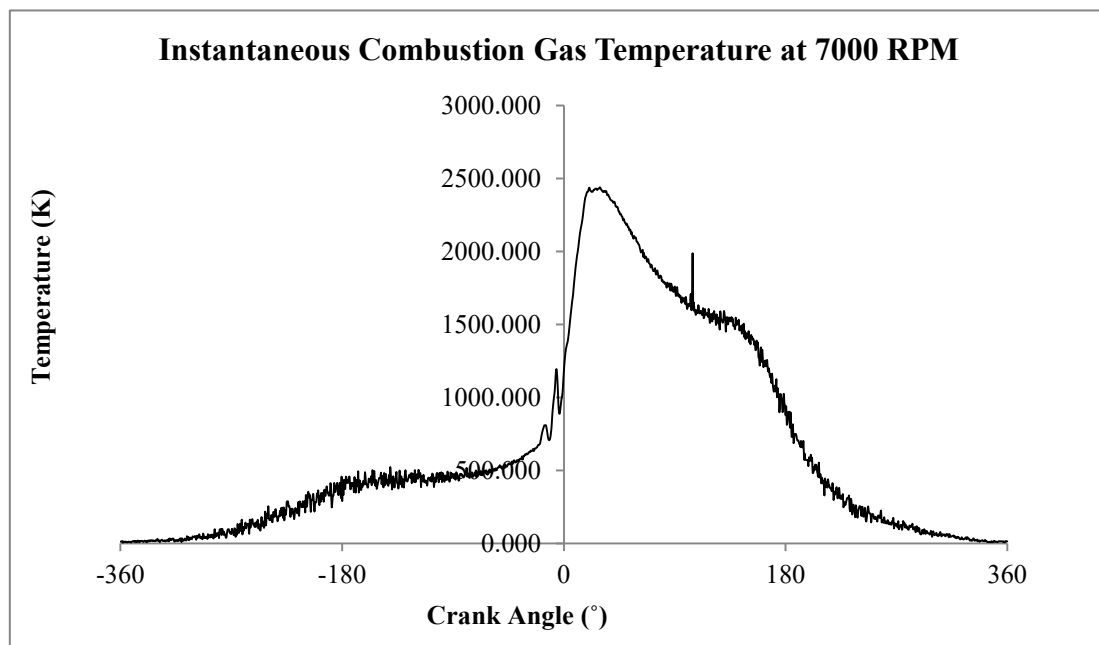


**Figure B.13.** Instantaneous combustion gas temperature for one engine cycle at 7000 rpm.

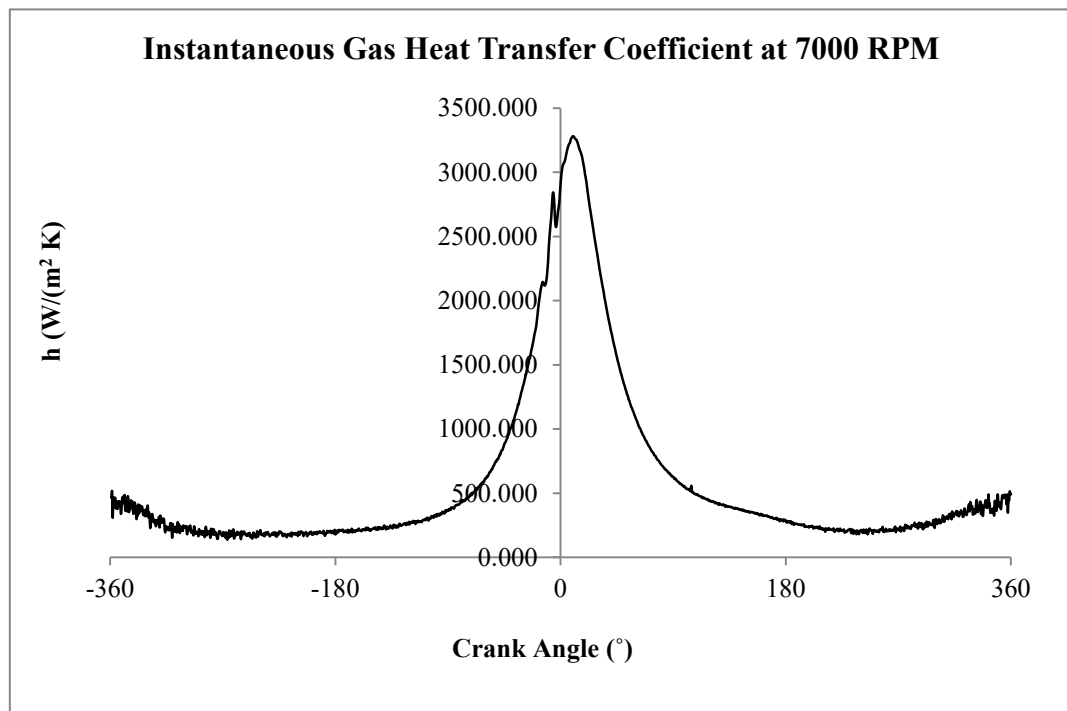


**Figure B.14.** Instantaneous combustion heat transfer coefficient for one engine cycle at 7000 rpm.



## Appendix C

### Appendix C.1. Dynamometer specification and torque, power speed curves

Criteria	Value
Power (kW)	130
Rated Torque (Nm)	400
Minimal speed for rated torque (rpm)	1250
Maximal Speed (rpm)	10000
Minimal speed for maximal power (rpm)	3104
Moment of Inertia (Kgm <sup>3</sup> )	0.14
Maximal share of mass to be coupled at N max (Kg)	2.0
Maximum exciting current (A)	6.1
Weight (Kg)	270
Operating Temperature (°C)	0...+70 without cooling water addition -25...+70 with antifreezer and power reduction of 10-20%
Transporting and storage temperature (°C)	-50 ... +85
Cooling water supply	See page 26 of the dyno manual
Measuring accuracy speed (rpm)	± 1, not lower than 0.025% of rating
Measuring accuracy torque (%)	0.2, referring to rating
Control accuracy speed (rpm)	± 10
Control accuracy torque (%)	± 1, referring to rating

**Table C.1.** Performance specification of Schenck, type W130 dynamometer used in this project.

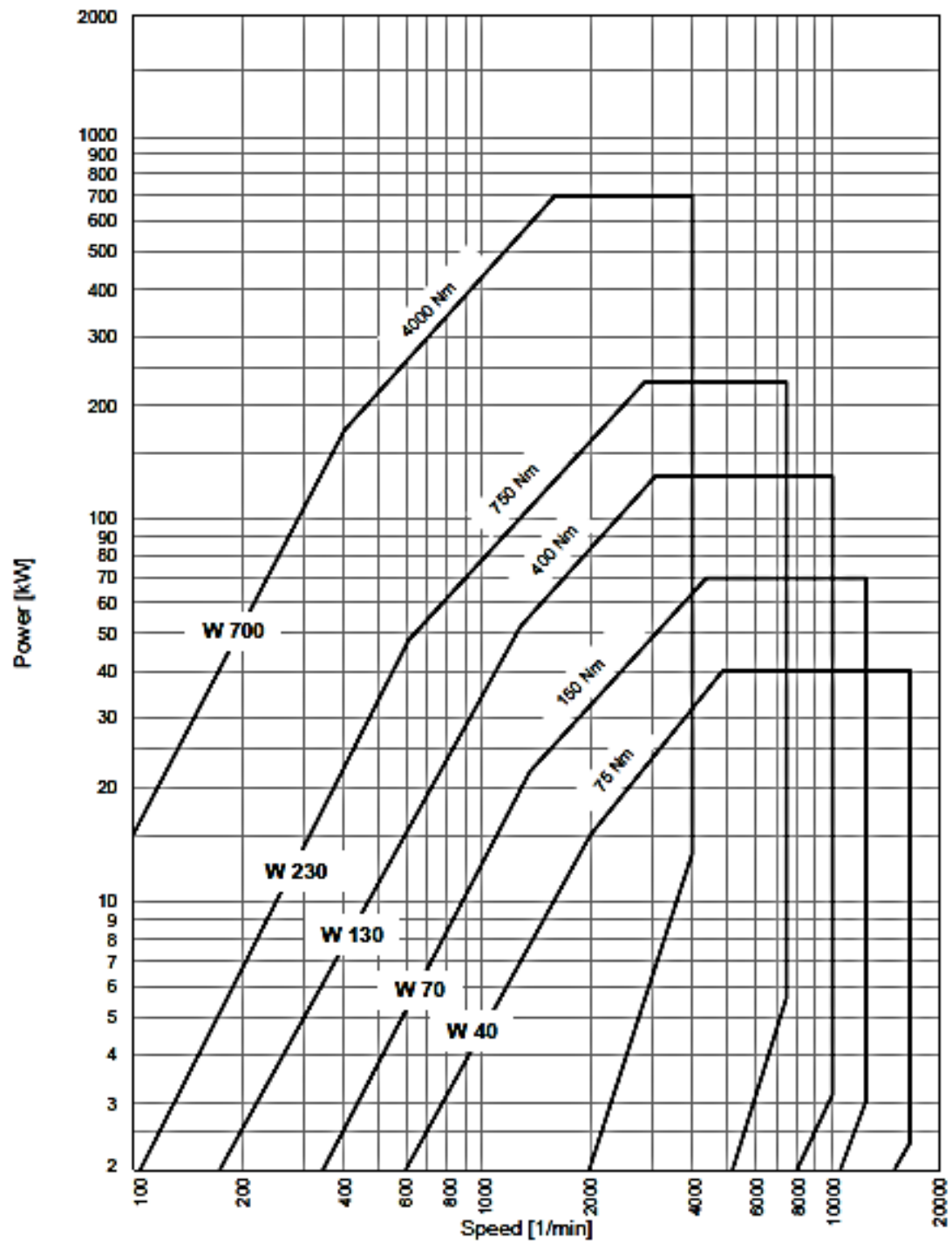


**Figure C.1.** The torque and power speed curves of Schenck, type W130 dynamometer used in this project.

## Appendix C.2. 2D engineering drawings of engine mount and other components

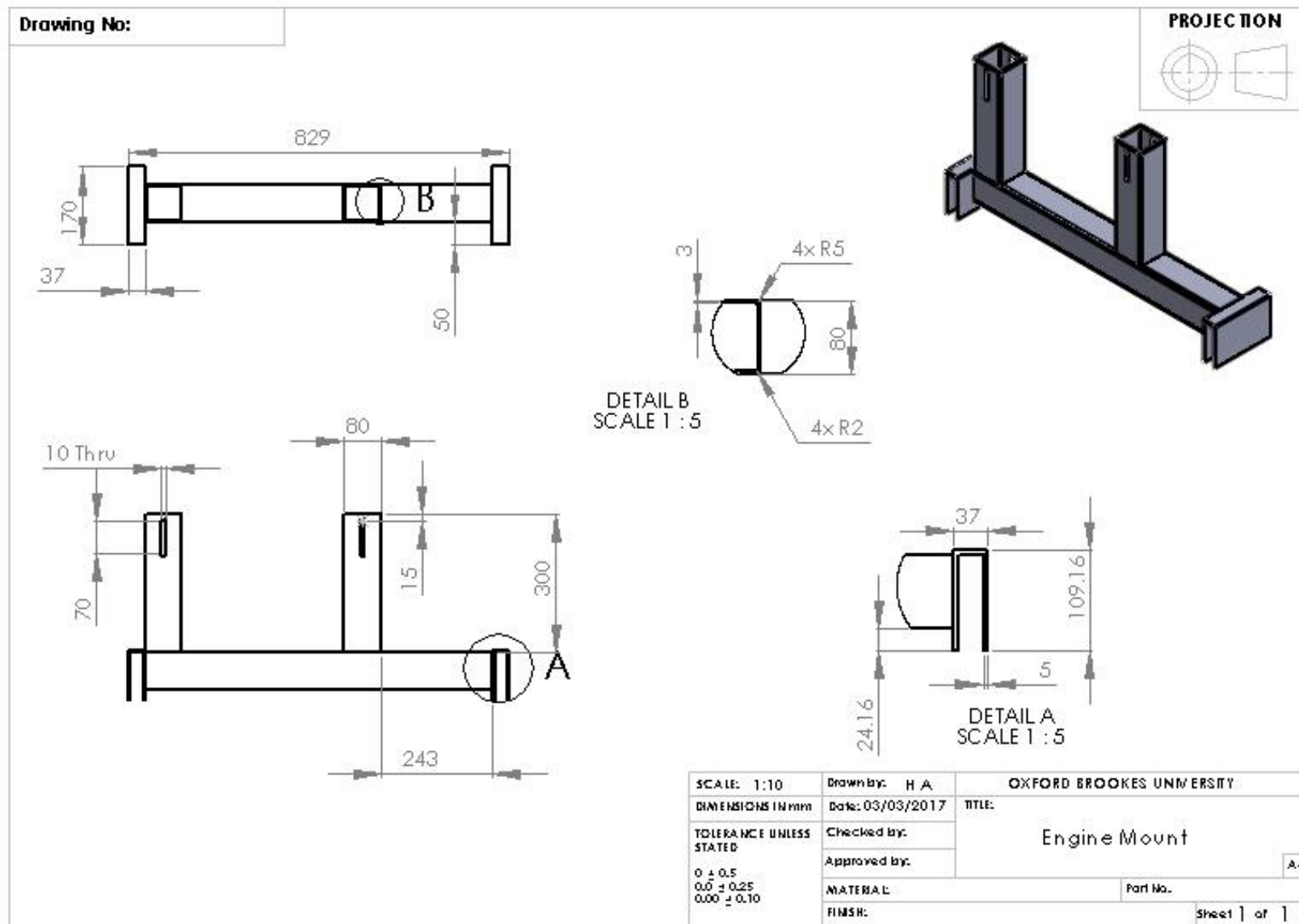
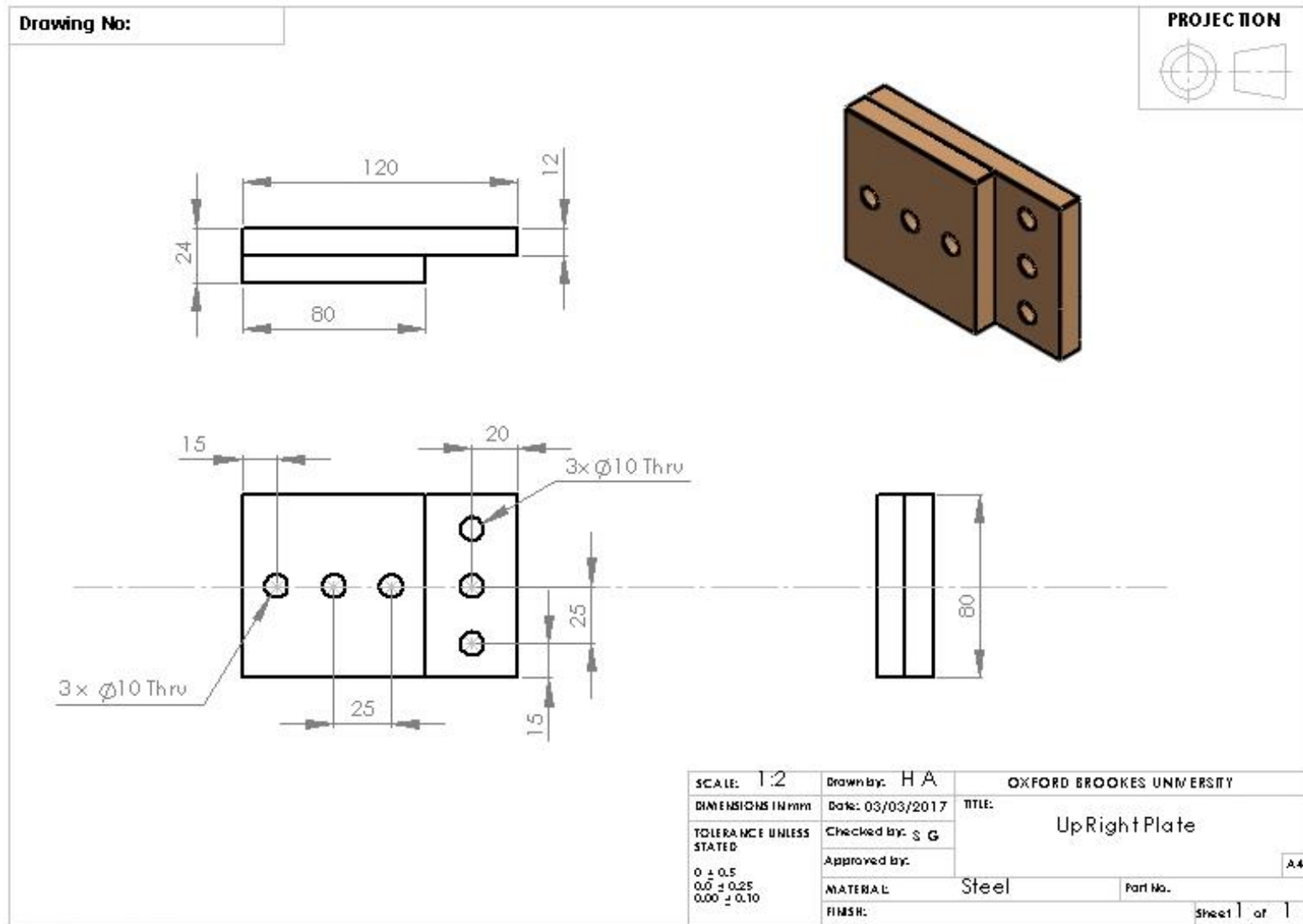
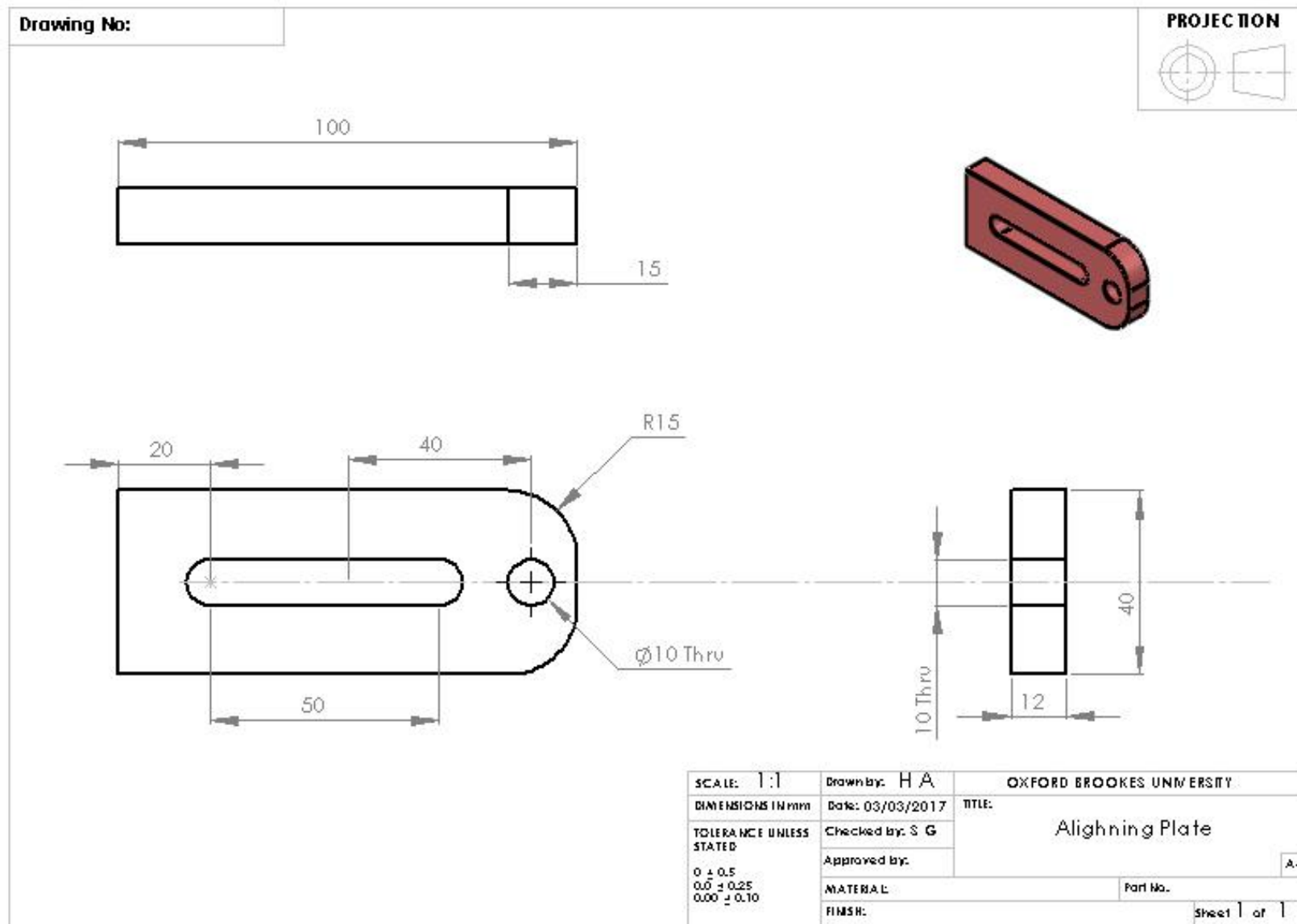


Figure C.2. A 2D engineering drawing of the engine mount.



MEMS Department

Figure C.3. A 2D engineering drawing of the upright plate.



MEMS Department

Figure C.4. A 2D engineering drawing of the engine aligning plate.

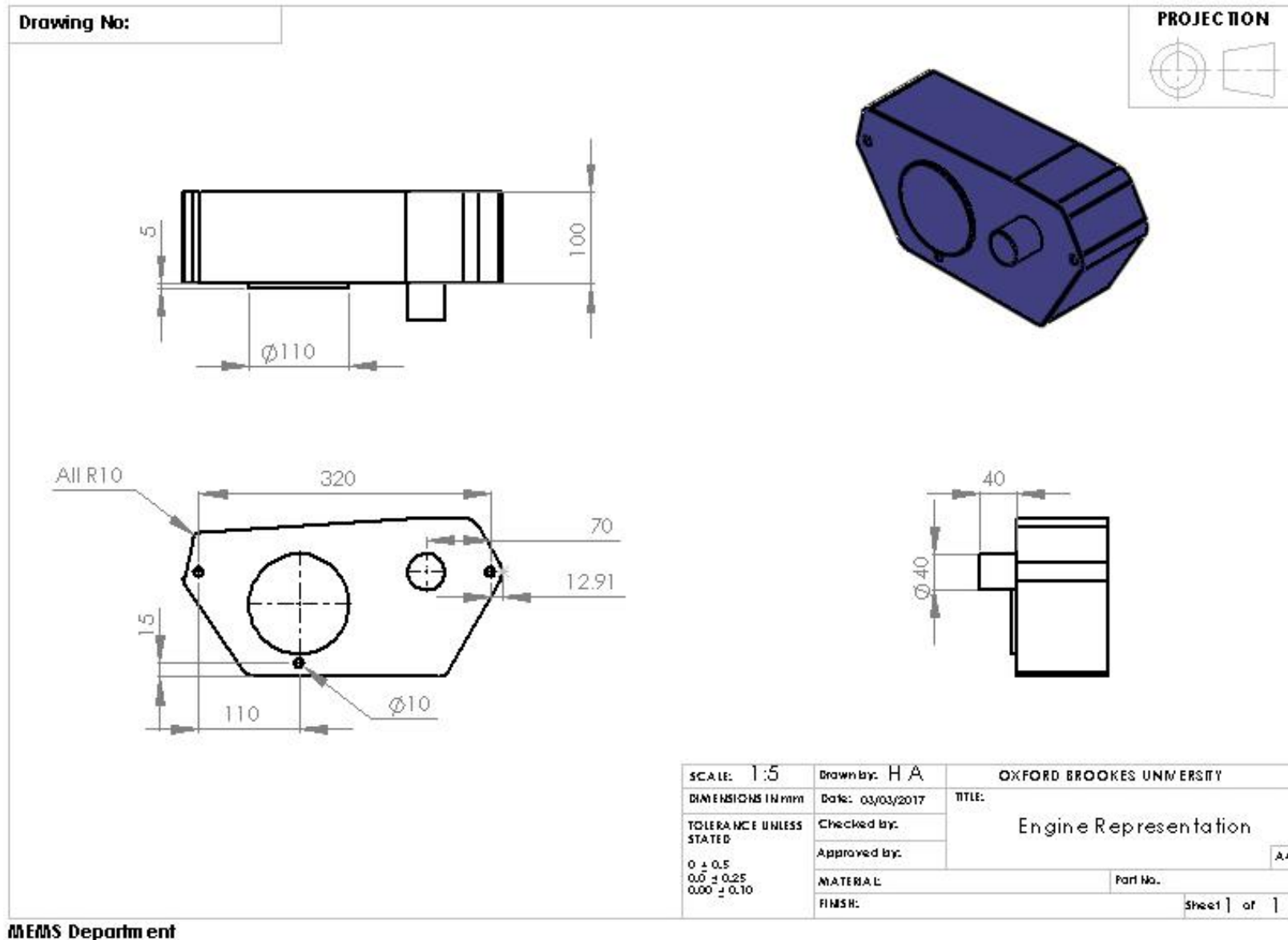
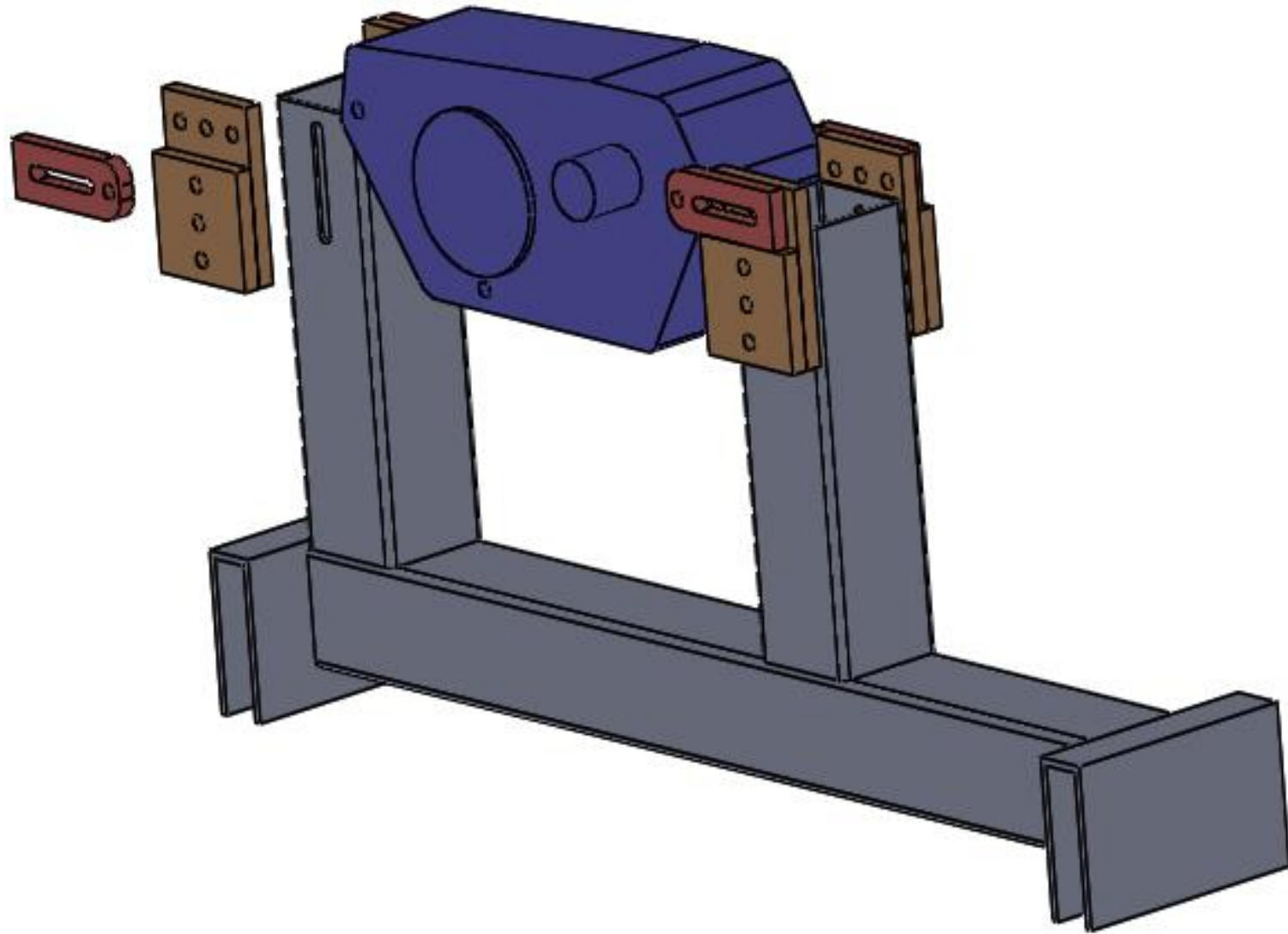


Figure C.5. A 2D engineering drawing of the engine representation.



**Figure C.6.** An exploded view of the engine mount assembly setup

### Appendix C.3. In-cylinder pressure sensor specification

Criteria	Values
Pressure Range	0 – 100 bar (1500 Psi)
Over Pressure	2 x Pressure Range (typical)
Non-Linearity and Hysteresis	±0.1 – 0.5%
Sensitivity Factor Value	2.73 mV/Psi at 200 °C
Vibration	100 G
Pressure Media	Gaseous or Liquid
Current Draw	85 mA Max, 50 mA Typical
Power Supply Voltage	9 – 18V DC
Cable Bending Radius	5 mm or 3/16"
Fibre Optic Cable Length	1.5 m
Cable Operating Temperature	-40 – 200 °C
Sensor Housing Temperature Range	-40 – 380 °C
Frequency Range	1.0 Hz to 25 kHz
Installation Torque	8 in-lbs or 0.9 Nm

**Table C.2.** Performance specification of the in-cylinder pressure sensor used in this project.

### Appendix C.4. Calculation for cutting the bar

In order to determine what length the available material bar should be cut to, so the required billet with diameter of 103 mm and length of 50 mm could be forged. First the volume of the required billet was determined, and then using the cylinder volume equation, the length of the cut bar was determine using the diameter of available material bar.

A billet is a cylinder hence volume of the billet can be determined using the following equation

$$V = \pi r^2 h$$

where V, r and h are the volume, radius and height of the required billet. Substituting the values in the above equation gives



$$V = \pi \left( \frac{103}{2} \text{ mm} \right)^2 \times 50 \text{ mm} = 416614.5 \text{ mm}^3$$

Now that we know the volume of the required billet and diameter of the current bar (60 mm), we can use the same equation rearranged for h to determine the length of the cut.

$$h = V/\pi r^2 \quad h = \frac{416614.5}{\pi \times \left( \frac{60}{2} \right)^2} = 147.3 \text{ mm}$$

The theoretical length needed to make a billet of the required size is 147.3 mm, however the bar was cut in length of 155 mm to account of any material shrinkage and loss during forging.

### Appendix C.5. Tabulated engine results

The averaged engine test results at different engine speeds for both configurations are presented in table forms below.

Torque (Nm)	Fuel Consumption (g/sec)		Air Fuel Ratio	
	Original Piston	New Piston	Original Piston	New Piston
6	0.51	0.50	11.30	11.97
9	0.58	0.57	11.27	11.60
12	0.67	0.65	11.53	11.57
15	0.84	0.83	11.27	11.63
18	0.96	0.96	11.20	11.47

**Table C.3.** Averaged engine test results in two configurations at engine speed of 3000 rpm.

Torque (Nm)	Fuel Consumption (g/sec)		Air Fuel Ratio	
	Original Piston	New Piston	Original Piston	New Piston
6	0.80	0.65	11.20	11.83
9	0.87	0.85	11.10	11.30
12	1.06	1.11	10.63	10.70
15	1.17	1.31	10.37	10.73
18	1.36	1.44	10.53	11.13
21	1.57	1.64	10.70	11.63

**Table C.4.** Averaged engine test results in two configurations at engine speed of 4500 rpm.

Torque (Nm)	Fuel Consumption (g/sec)		Air Fuel Ratio	
	Original Piston	New Piston	Original Piston	New Piston
6	1.17	1.08	10.80	11.17
9	1.44	1.34	10.37	10.47
12	1.54	1.50	10.30	10.40
15	1.61	1.72	10.50	10.37
18	1.82	1.86	10.77	10.43
21	2.02	2.06	10.90	10.73
24	2.21	2.30	11.1	10.80

**Table C.5.** Averaged engine test results in two configurations at engine speed of 6000 rpm.

## **Appendix D**

The design and failure mode effect analysis (DFMEA) carried out to find the root causes of new piston seizure is given below.

DFMEA Design Failure Mode and Effects Analysis												
Product Part	Piston Assembly	Team:										FM
Project:		Responsible:	Habibullah Adil		Manager:							Orig
Item	Function(s)	Potential Failure Mode	Potential Effect(s) of Failure	Severity	Potential Causes(s) of Failure	Control Methods				RPN	Recommended Action	
						Current Design Controls (Prevention)	Occurrence	Current Design Controls (Detection)	Detection		Recommended Action(s)	Resp
Piston	Transfers the combustion energy/load to the connecting rod at pressures of up to 100 bar.	Insufficient clearance	Piston scuffing	6	incorrect dimensioning	FMEA was used to ensure the deformation of new piston design during operation does not exceed the original piston	7	Coolant temperature at exit from engine will be monitored and ensured to stay between 110 - 120 C to avoid overheating of the piston so it does not deform too much or the cylinder not expanding enough to allow for piston expansion. In-cylinder pressure will be monitored and measured to ensure it does not exceed 100 bar. Increase engine speeds in small increments of 500 rpm during engine speeds.	4	168	Use prevention and detection design controls	HA

						carburettor (set needle to fourth position from top) not to put too much fuel into combustion chamber		loads (range of 10.5 to 15). Increase engine speeds in small increments of 500 rpm during engine speeds.				
			total engine seizure	9	incorrect dimensioning	FMEA was used to ensure the deformation of new piston design during operation does not exceed the original piston	7	Coolant temperature at exit from engine will be monitored and ensured to stay between 110 - 120 C to avoid overheating of the piston so it does not deform too much or the cylinder not expanding enough to allow for piston expansion. In-cylinder pressure will be monitored and measured to ensure it does not exceed 100 bar. Increase engine speeds in small increments of 500 rpm during engine speeds.	4	252	Use prevention and detection design controls	HA
				9	excessive thermal loads	The new piston was designed and simulated in the maximum engine loading condition to ensure it can withstand the thermo-mechanical loads of the engine. Coolant temperature monitor guidelines to ensure it stays between 110 - 120 C. Adjust	6	In-cylinder pressures will be monitored to ensure they do not go above 100 bar which can cause excess thermal loads. Coolant temperature will be monitored and ensured to stay between 110 - 120 C. Air fuel ratio (lambda) will be measured and monitored to ensure the mixture does not get too lean or rich to	4	216	Use prevention and detection design controls	HA

			reduced piston/engine life/reliability	7	incorrect dimensioning	FMEA was used to ensure the deformation of new piston design during operation does not exceed the original piston	7	Coolant temperature at exit from engine will be monitored and ensured to stay between 110 - 120 C to avoid overheating of the piston so it does not deform too much or the cylinder not expanding enough to allow for piston expansion. In-cylinder pressure will be monitored and measured to ensure it does not exceed 100 bar. Increase engine speeds in small increments of 500 rpm during engine speeds.	4	196	Use prevention and detection design controls	HA
				7	excessive thermal loads	The new piston was designed and simulated in the maximum engine loading condition to ensure it can withstand the thermo-mechanical loads of the engine. Coolant temperature monitor guidelines to ensure it stays between 110 - 120 C. Adjust carburettor (set needle to fourth position from top) not to put too much fuel into combustion chamber	6	In-cylinder pressures will be monitored to ensure they do not go above 100 bar which can cause excess thermal loads. Coolant temperature will be monitored and ensured to stay between 110 - 120 C. Air fuel ratio (lambda) will be measured and monitored to ensure the mixture does not get too lean or rich to cause excess thermal loads (range of 10.5 to 15). Increase engine speeds in small increments of 500 rpm during engine speeds.	4	168	Use prevention and detection design controls	HA
								Coolant temperature at exit from engine will be				

								during engine speeds.				
				6	excessive thermal loads	The new piston was designed and simulated in the maximum engine loading condition to ensure it can withstand the thermo-mechanical loads of the engine. Coolant temperature monitor guidelines to ensure it stays between 110 - 120 C. Adjust carburettor (set needle to fourth position from top) not to put too much fuel into combustion chamber	6	In-cylinder pressures will be monitored to ensure they do not go above 100 bar which can cause excess thermal loads. Coolant temperature will be monitored and ensured to stay between 110 - 120 C. Air fuel ratio (lambda) will be measured and monitored to ensure the mixture does not get too lean or rich to cause excess thermal loads (range of 10.5 to 15). Increase engine speeds in small increments of 500 rpm during engine speeds.	4	144	Use prevention and detection design controls	HA
			piston and compression ring micro-	8	incorrect dimensioning	FMEA was used to ensure the deformation of new piston design during operation	7	Coolant temperature at exit from engine will be monitored and ensured to stay between 110 - 120 C to avoid overheating of the piston so it does not deform too much or the cylinder not expanding enough to allow for piston expansion. In-	4	224	Use prevention and detection design controls	HA

						thermo-mechanical loads of the engine. Coolant temperature monitor guidelines to ensure it stays between 110 - 120 C. Adjust carburettor (set needle to fourth position from top) not to put too much fuel into combustion chamber		monitored and ensured to stay between 110 - 120 C. Air fuel ratio (lambda) will be measured and monitored to ensure the mixture does not get too lean or rich to cause excess thermal loads (range of 10.5 to 15). Increase engine speeds in small increments of 500 rpm during engine speeds.				
		Lack of lubrication, dry running	Piston scuffing	6	fuel flooding	Adjust carburettor (set needle to fourth position from top) not to put too much fuel into combustion chamber. Ensure to run the engine in idle for long enough (approx. 5 minutes) after just starting so any excess fuel is burnt and the strong gasoline smell from exhaust disappears.	5	Run the engine idle for awhile until the strong gasoline smell from exhaust disappear. Listen for fast cranking when starting the engine. Look out for abnormal fuel consumption using the Fuel Measuring System.	5	150	Use prevention and detection design controls	HA
				6	excessive use of choke	Ensure the test cell is not too cold so there is not much need of using choke. If there is need for using choke then run the engine for long enough (approx. 5	7	Physically check to ensure choke is closed. Look out for abnormal fuel consumption using the Fuel Measuring System. Reduced engine performance. Coolant temperature at exit from engine will be monitored and ensured to stay between 110 -	5	210	Use prevention and detection design controls	HA



						in idle for long enough (approx. 5 minutes) after just starting so any excess fuel is burnt and the strong gasoline smell from exhaust disappears.		Fuel Measuring System. Run the engine idle for awhile until the strong gasoline smell from exhaust disappears.				
				6	oil dilution caused by short-distance driving	Adjust carburettor (set needle to fourth position from top) not to put too much fuel into combustion chamber. Ensure to run the engine in idle for long enough (approx. 5 minutes) after just starting so any excess fuel is burnt and the strong gasoline smell from exhaust disappears.	6	Test oil sample to confirm oil dilution	5	180	Use prevention and detection design controls	HA
				6	incomplete combustion	Ensure the air flow in the test cell is not interrupted and it can provide enough air for the engine operation. Adjust carburettor not to put too much fuel into combustion chamber. Ensure to run the engine in idle for long enough (approx. 5 minutes) after just starting so any excess fuel is burnt and the	6	Measure and monitor the air fuel ratio (AFR) or lambda and ensure it stays within 10.5 - 14.5 by adjusting carburettor jets. Look out for abnormal fuel consumption using the Fuel Measuring System. Run the engine idle for awhile until the strong gasoline smell from exhaust disappears	4	144	Use prevention and detection design controls	HA

						starting so any excess fuel is burnt and the strong gasoline smell from exhaust disappears.						
				9	excessive use of choke	Ensure the test cell is not too cold so there is not much need of using choke. If there is need for using choke then run the engine for long enough (approx. 5 minutes) after just starting so any excess fuel is burnt and the strong gasoline smell from exhaust disappears.	7	Physically check to ensure choke is closed. Look out for abnormal fuel consumption using the Fuel Measuring System. Reduced engine performance. Coolant temperature at exit from engine will be monitored and ensured to stay between 110 - 120 C. Air fuel ratio (lambda) will be measured and monitored to ensure the mixture does not get rich to cause excess thermal loads (range of 10.5 to 15).	5	315	Use prevention and detection design controls	HA
				9	overly rich mixture	Adjust carburettor (set needle to fourth position from top) not to put too much fuel into combustion chamber. Ensure to run the engine in idle for long enough (approx. 5 minutes) after just starting so any excess fuel is burnt and the strong gasoline smell from exhaust	6	Measure and monitor the air fuel ratio (AFR) or lambda and ensure it stays within 10.5 - 14.5 by adjusting carburettor jets. Look out for abnormal fuel consumption using the Fuel Measuring System. Run the engine idle for awhile until the strong gasoline smell from exhaust disappears.	4	216	Use prevention and detection design controls	HA

						strong gasoline smell from exhaust disappears.						
				9	incomplete combustion	Ensure the air flow in the test cell is not interrupted and it can provide enough air for the engine operation. Adjust carburettor (set needle to fourth position from top) not to put too much fuel into combustion chamber. Ensure to run the engine in idle for long enough (approx. 5 minutes) after just starting so any excess fuel is burnt and the strong gasoline smell from exhaust disappears. Use the correct ECU for engine.	6	Measure and monitor the air fuel ratio (AFR) or lambda and ensure it stays within 10.5 - 14.5 by adjusting carburettor jets. Look out for abnormal fuel consumption using the Fuel Measuring System. Run the engine idle for awhile until the strong gasoline smell from exhaust disappears.	4	216	Use prevention and detection design controls	HA
			reduced engine performance due to increased	6	fuel flooding	Adjust carburettor (set needle to fourth position from top) not to put too much fuel into combustion chamber. Ensure to run the engine in idle for long enough (approx. 5 minutes) after just	5	Run the engine idle for awhile until the strong gasoline smell from exhaust disappears. Listen for fast cranking when starting the engine. Look out for abnormal fuel	5	150	Use prevention and detection design controls	HA

						minutes) after just starting so any excess fuel is burnt and the strong gasoline smell from exhaust disappears.		to stay between 110 - 120 C. Air fuel ratio (lambda) will be measured and monitored to ensure the mixture does not get rich to cause excess thermal loads (range of 10.5 to 15).				
				6	overly rich mixture	Adjust carburettor (set needle to fourth position from top) not to put too much fuel into combustion chamber. Ensure to run the engine in idle for long enough (approx. 5 minutes) after just starting so any excess fuel is burnt and the strong gasoline smell from exhaust disappears.	6	Measure and monitor the air fuel ratio (AFR) or lambda and ensure it stays within 10.5 - 14.5 by adjusting carburettor jets. Look out for abnormal fuel consumption using the Fuel Measuring System. Run the engine idle for awhile until the strong gasoline smell from exhaust disappears.	4	144	Use prevention and detection design controls	HA
				6	oil dilution caused by short-distance driving	Adjust carburettor (set needle to fourth position from top) not to put too much fuel into combustion chamber. Ensure to run the engine in idle for long enough (approx. 5 minutes) after just starting so any excess fuel is burnt and the strong gasoline smell from exhaust disappears.	6	Test oil sample to confirm oil dilution	5	180	Use prevention and detection design controls	HA
						Ensure the air flow						

						starting so any excess fuel is burnt and the strong gasoline smell from exhaust disappears. Use the correct ECU for engine.						
			reduced piston/engine life/reliability	7	fuel flooding	Adjust carburettor (set needle to fourth position from top) not to put too much fuel into combustion chamber. Ensure to run the engine in idle for long enough (approx. 5 minutes) after just starting so any excess fuel is burnt and the strong gasoline smell from exhaust disappears.	5	Run the engine idle for awhile until the strong gasoline smell from exhaust disappears. Listen for fast cranking when starting the engine. Look out for abnormal fuel consumption using the Fuel Measuring System.	5	175	Use prevention and detection design controls	HA
				7	excessive use of choke	Ensure the test cell is not too cold so there is not much need of using choke. If there is need for using choke then run the engine for long enough (approx. 5 minutes) after just starting so any excess fuel is burnt and the strong gasoline smell from exhaust disappears.	7	Physically check to ensure choke is closed. Look out for abnormal fuel consumption using the Fuel Measuring System. Reduced engine performance. Coolant temperature at exit from engine will be monitored and ensured to stay between 110 - 120 C. Air fuel ratio (lambda) will be measured and monitored to ensure the mixture does not get rich to cause excess thermal loads (range of 10.5 to 15).	5	245	Use prevention and detection design controls	HA

						disappears.						
				7	oil dilution caused by short-distance driving	Adjust carburettor (set needle to fourth position from top) not to put too much fuel into combustion chamber. Ensure to run the engine in idle for long enough (approx. 5 minutes) after just starting so any excess fuel is burnt and the strong gasoline smell from exhaust disappears.	6	Test oil sample to confirm oil dilution	5	210	Use prevention and detection design controls	HA
				7	incomplete combustion	Ensure the air flow in the test cell is not interrupted and it can provide enough air for the engine operation. Adjust carburettor not to put too much fuel into combustion chamber. Ensure to run the engine in idle for long enough (approx. 5 minutes) after just starting so any excess fuel is burnt and the strong gasoline smell from exhaust disappears. Use the correct ECU	6	Measure and monitor the air fuel ratio (AFR) or lambda and ensure it stays within 10.5 - 14.5 by adjusting carburettor jets. Look out for abnormal fuel consumption using the Fuel Measuring System. Run the engine idle for awhile until the strong gasoline smell from exhaust disappears.	4	168	Use prevention and detection design controls	HA

						smell from exhaust disappears.						
				8	excessive use of choke	Ensure the test cell is not too cold so there is not much need of using choke. If there is need for using choke then run the engine for long enough (approx. 5 minutes) after just starting so any excess fuel is burnt and the strong gasoline smell from exhaust disappears.	7	Physically check to ensure choke is closed. Look out for abnormal fuel consumption using the Fuel Measuring System. Reduced engine performance. Coolant temperature at exit from engine will be monitored and ensured to stay between 110 - 120 C. Air fuel ratio (lambda) will be measured and monitored to ensure the mixture does not get rich to cause excess thermal loads (range of 10.5 to 15).	5	280	Use prevention and detection design controls	HA
				8	overly rich mixture	Adjust carburettor (set needle to fourth position from top) not to put too much fuel into combustion chamber. Ensure to run the engine in idle for long enough (approx. 5 minutes) after just starting so any excess fuel is burnt and the strong gasoline smell from exhaust disappears.	6	Measure and monitor the air fuel ratio (AFR) or lambda and ensure it stays within 10.5 - 14.5 by adjusting carburettor jets. Look out for abnormal fuel consumption using the Fuel Measuring System. Run the engine idle for awhile until the strong gasoline smell from exhaust disappears.	4	192	Use prevention and detection design controls	HA



						disappears.						
				8	incomplete combustion	Ensure the air flow in the test cell is not interrupted and it can provide enough air for the engine operation. Adjust carburettor not to put too much fuel into combustion chamber. Ensure to run the engine in idle for long enough (approx. 5 minutes) after just starting so any excess fuel is burnt and the strong gasoline smell from exhaust disappears. Use the correct ECU for engine.	6	Measure and monitor the air fuel ratio (AFR) or lambda and ensure it stays within 10.5 - 14.5 by adjusting carburettor jets. Look out for abnormal fuel consumption using the Fuel Measuring System. Run the engine idle for awhile until the strong gasoline smell from exhaust disappears.	4	192	Use prevention and detection design controls	HA
		Seizure due to overheating	Piston scuffing	6	Extended high loads on the engine before it has been fully run in	Run the engine under light load condition (approx. 1 hour in increments of 20 minutes) before the actual testing.	4	Look out for reduced engine performance due to increased friction i.e. lower torque than expected	6	144	Use prevention and detection design controls	HA
					Faults in	Ensure the air flow in the test cell is not interrupted and it can provide enough air for the engine operation. Adjust carburettor		Look out for reduced engine performance due to increased friction i.e. lower torque than expected			Use prevention	



						have minimum capacity of 1.20 litre. The coolant should be constantly pumped/circulated.						
			total engine seizure	9	Extended high loads on the engine before it has been fully run in	Run the engine under light load condition (approx. 1 hour in increments of 20 minutes) before the actual testing.	4	Look out for reduced engine performance due to increased friction i.e. lower torque than expected	6	216	Use prevention and detection design controls	HA
				9	Faults in combustion process	Ensure the air flow in the test cell is not interrupted and it can provide enough air for the engine operation. Adjust carburettor (set needle to fourth position from top) not to put too much/less fuel into combustion chamber. Use the correct ECU for engine.	6	Look out for reduced engine performance due to increased friction i.e. lower torque than expected. Measure and monitor the air fuel ratio (AFR) or lambda and ensure it stays within 10.5 - 14.5 by adjusting carburettor jets	6	324	Use prevention and detection design controls	HA
				9	Faults in engine cooling system	Ensure the coolant pump and the coolant system in the test cell are in good working condition, the coolant should have minimum capacity of 1.20 litre. The coolant should be constantly pumped/circulated.	4	Coolant temperature at exit from engine will be monitored and ensured to stay between 110 - 120 C.	4	144	Use prevention and detection design controls	HA
			reduced engine performance		Extended high loads on the engine	Run the engine under light load condition (approx.		Look out for reduced engine performance			Use prevention	

						chamber. Use the correct ECU for engine.						
				6	Faults in engine cooling system	Ensure the coolant pump and the coolant system in the test cell are in good working condition, the coolant should have minimum capacity of 1.20 litre. The coolant should be constantly pumped/circulated.	4	Coolant temperature at exit from engine will be monitored and ensured to stay between 110 - 120 C.	4	96	Use prevention and detection design controls	HA
			reduced piston/engine life/reliability	7	Extended high loads on the engine before it has been fully run in	Run the engine under light load condition (approx. 1 hour in increments of 20 minutes) before the actual testing.	4	Look out for reduced engine performance due to increased friction i.e. lower torque than expected	6	168	Use prevention and detection design controls	HA
				7	Faults in combustion process	Ensure the air flow in the test cell is not interrupted and it can provide enough air for the engine operation. Adjust carburettor (set needle to fourth position from top) not to put too much/less fuel into combustion chamber. Use the correct ECU for engine.	6	Look out for reduced engine performance due to increased friction i.e. lower torque than expected. Measure and monitor the air fuel ratio (AFR) or lambda and ensure it stays within 10.5 - 14.5 by adjusting carburettor jets	6	252	Use prevention and detection design controls	HA
						Ensure the coolant pump and the coolant system in the test cell are in good working		Coolant temperature at				

				8	Faults in combustion process	Ensure the air flow in the test cell is not interrupted and it can provide enough air for the engine operation. Adjust carburettor (set needle to fourth position from top) not to put too much/less fuel into combustion chamber. Use the correct ECU for engine.	6	Look out for reduced engine performance due to increased friction i.e. lower torque than expected. Measure and monitor the air fuel ratio (AFR) or lambda and ensure it stays within 10.5 - 14.5 by adjusting carburettor jets	6	288	Use prevention and detection design controls	HA
				8	Faults in engine cooling system	Ensure the coolant pump and the coolant system in the test cell are in good working condition, the coolant should have minimum capacity of 1.20 litre. The coolant should be constantly pumped/circulated.	4	Coolant temperature at exit from engine will be monitored and ensured to stay between 110 - 120 C.	4	128	Use prevention and detection design controls	HA
		Fracture due to mechanical contact between piston crown and cylinder head	Total engine failure	10	Excessive clearances in the connecting rod bearing or worn out connecting rod bearing	Check the connecting rod for wear before installation. Design the new piston with same clearance between connecting rod bearing	2	Listen for rattling sound during engine operation	5	100	Use prevention and detection design controls	HA
				10	Too small gap between piston crown and cylinder head	Check the gap between piston and cylinder head before installation. Design the new piston with same clearance between	2	Listen for any abnormal sounds during engine operation	5	100	Use prevention and detection design controls	HA

				7	Too small gap between piston crown and cylinder head	Check the gap between piston and cylinder head before installation. Design the new piston with same clearance between piston and cylinder head	2	Listen for any abnormal sounds during engine operation	5	70	Use prevention and detection design controls	HA
Piston Skirt	Keeps the whole piston assembly aligned with cylinder lines while resisting lateral force of up to 7 kN	Insufficient clearance	Piston scuffing	6	incorrect dimension by design	FMEA was used to ensure the deformation of new piston skirt design during operation does not exceed the original piston	7	Coolant temperature will be monitored and ensured to stay between 110 - 120 C to avoid overheating of the piston so it does not deform too much. In-cylinder pressure will be monitored and measured to ensure it does not exceed 100 bar. Increase engine speeds in small increments of 500 rpm during engine speeds.	4	168	Use prevention and detection design controls	HA
				6	distortion during operation	FMEA was used to ensure the deformation of new piston skirt design during operation does not exceed the original piston	7	Coolant temperature will be monitored and ensured to stay between 110 - 120 C to avoid overheating of the piston so it does not deform too much. In-cylinder pressure will be monitored and measured to ensure it does not exceed 100 bar. Increase engine speeds in small increments of 500 rpm during engine speeds.	4	168	Use prevention and detection design controls	HA
				6	cylinder head over-tightened or unevenly	Ensure 10 and then 30 Nm torque is applied as recommended by the	4	Look out for reduced engine performance due to increased	6	144	Use prevention and detection design controls	HA

				6	unsuitable head gasket	Use the head gasket recommended by the manufacturer (KTM) and purchase from manufacturer's approved suppliers	3	Look out for reduced engine performance due to increased friction	6	108	Use prevention and detection design controls	HA
				6	uneven sealing of the cylinder head or gasket	Use KTM approved workshop to carry out engine assembly	5	Look out for reduced engine performance due to increased friction	6	180	Use prevention and detection design controls	HA
				6	dirty or distorted threads in the threaded bores or on the cylinder head bolts	Inspect the threads and bores before installation of the head bolts	3	Look out for reduced engine performance due to increased friction	6	108	Use prevention and detection design controls	HA
			total engine seizure	9	incorrect dimension by design	FMEA was used to ensure the deformation of new piston skirt design during operation does not exceed the original piston	7	Coolant temperature will be monitored and ensured to stay between 110 - 120 C to avoid overheating of the piston so it does not deform too much. In-cylinder pressure will be monitored and measured to ensure it does not exceed 100 bar. Increase engine speeds in small increments of 500 rpm during engine speeds.	4	252	Use prevention and detection design controls	HA
				9	distortion during operation	FMEA was used to ensure the deformation of new piston skirt design during operation does not	7	Coolant temperature will be monitored and ensured to stay between 110 - 120 C to avoid overheating of the piston so it does not deform too much. In-cylinder pressure will be monitored and	4	252	Use prevention and detection design controls	HA

				9	uneven distortion of the cylinder due to problems in cooling system	Ensure the coolant pump and the coolant system in the test cell are in good working condition, the coolant should have minimum capacity of 1.20 litre. The coolant should be constantly pumped/circulated.	4	Look out for reduced engine performance due to increased friction. Monitor and measure the coolant temperature at exit from engine and ensure it stays between 110 - 120 C	4	144	Use prevention and detection design controls	HA
				9	unsuitable head gasket	Use the head gasket recommended by the manufacturer (KTM) and purchase from manufacturer's approved suppliers	3	Look out for reduced engine performance due to increased friction	6	162	Use prevention and detection design controls	HA
				9	uneven sealing of the cylinder head or gasket	Use KTM approved workshop to carry out engine assembly	5	Look out for reduced engine performance due to increased friction	6	270	Use prevention and detection design controls	HA
				9	dirty or distorted threads in the threaded bores or on the cylinder head bolts	Inspect the threads and bores before installation of the head bolts	3	Look out for reduced engine performance due to increased friction	6	162	Use prevention and detection design controls	HA
			reduced engine performance due to increased friction	6	incorrect dimension by design	FMEA was used to ensure the deformation of new piston skirt design during operation does not exceed the original piston	7	Coolant temperature will be monitored and ensured to stay between 110 - 120 C to avoid overheating of the piston so it does not deform too much. In-cylinder pressure will be monitored and measured to ensure it does not exceed 100	4	168	Use prevention and detection design controls	HA



								speeds in small increments of 500 rpm during engine speeds.				
				6	cylinder head over-tightened or unevenly tightened	Ensure 10 and then 30 Nm torque is applied as recommended by the manufacturer and the tightened diagonally	4	Look out for reduced engine performance due to increased friction	6	144	Use prevention and detection design controls	HA
				6	uneven distortion of the cylinder due to problems in cooling system	Ensure the coolant pump and the coolant system in the test cell are in good working condition, the coolant should have minimum capacity of 1.20 litre. The coolant should be constantly pumped/circulated.	4	Look out for reduced engine performance due to increased friction. Monitor and measure the coolant temperature at exit from engine and ensure it stays between 110 - 120 C	4	96	Use prevention and detection design controls	HA
				6	unsuitable head gasket	Use the head gasket recommended by the manufacturer (KTM) and purchase from manufacturer's approved suppliers	3	Look out for reduced engine performance due to increased friction	6	108	Use prevention and detection design controls	HA
				6	uneven sealing of the cylinder head or gasket	Use KTM approved workshop to carry out engine assembly	5	Look out for reduced engine performance due to increased friction	6	180	Use prevention and detection design controls	HA
				6	dirty or distorted threads in the threaded bores or on the cylinder head bolts	Inspect the threads and bores before installation of the head bolts	3	Look out for reduced engine performance due to increased friction	6	108	Use prevention and detection design controls	HA

				7	distortion during operation	FMEA was used to ensure the deformation of new piston skirt design during operation does not exceed the original piston	7	Coolant temperature will be monitored and ensured to stay between 110 - 120 C to avoid overheating of the piston so it does not deform too much. In-cylinder pressure will be monitored and measured to ensure it does not exceed 100 bar. Increase engine speeds in small increments of 500 rpm during engine speeds.	4	196	Use prevention and detection design controls	HA
				7	cylinder head over-tightened or unevenly tightened	Ensure 10 and then 30 Nm torque is applied as recommended by the manufacturer and the tightened diagonally	4	Look out for reduced engine performance due to increased friction	6	168	Use prevention and detection design controls	HA
				7	uneven distortion of the cylinder due to problems in cooling system	Ensure the coolant pump and the coolant system in the test cell are in good working condition, the coolant should have minimum capacity of 1.20 litre. The coolant should be constantly pumped/circulated.	4	Look out for reduced engine performance due to increased friction. Monitor and measure the coolant temperature at exit from engine and ensure it stays between 110 - 120 C	4	112	Use prevention and detection design controls	HA
				7	unsuitable head gasket	Use the head gasket recommended by the manufacturer (KTM) and purchase from manufacturer's approved suppliers	3	Look out for reduced engine performance due to increased friction	6	126	Use prevention and detection design controls	HA



			piston and compression ring micro-welding	8	incorrect dimension by design	FMEA was used to ensure the deformation of new piston skirt design during operation does not exceed the original piston	7	Coolant temperature will be monitored and ensured to stay between 110 - 120 C to avoid overheating of the piston so it does not deform too much. In-cylinder pressure will be monitored and measured to ensure it does not exceed 100 bar. Increase engine speeds in small increments of 500 rpm during engine speeds.	4	224	Use prevention and detection design controls	HA
				8	distortion during operation	FMEA was used to ensure the deformation of new piston skirt design during operation does not exceed the original piston	7	Coolant temperature will be monitored and ensured to stay between 110 - 120 C to avoid overheating of the piston so it does not deform too much. In-cylinder pressure will be monitored and measured to ensure it does not exceed 100 bar. Increase engine speeds in small increments of 500 rpm during engine speeds.	4	224	Use prevention and detection design controls	HA
				8	cylinder head over-tightened or unevenly tightened	Ensure 10 and then 30 Nm torque is applied as recommended by the manufacturer and the tightened diagonally	4	Look out for reduced engine performance due to increased friction	6	192	Use prevention and detection design controls	HA
					uneven distortion of the cylinder	Ensure the coolant pump and the coolant system in the test cell are in good working condition, the		Look out for reduced engine performance due to increased friction. Monitor and			Use prevention	

				8	uneven sealing of the cylinder head or gasket	Use KTM approved workshop to carry out engine assembly	5	Look out for reduced engine performance due to increased friction	4	160	Use prevention and detection design controls	HA
				8	dirty or distorted threads in the threaded bores or on the cylinder head bolts	Inspect the threads and bores before installation of the head bolts	3	Look out for reduced engine performance due to increased friction	4	96	Use prevention and detection design controls	HA
		Lack of lubrication	Piston scuffing	6	lack of engine oil	Visually inspect and check for engine oil before running the engine. Top up the engine with KTM recommended engine oil in sufficient quantity	1	Visually inspect and check for engine oil before running the engine. Look out for reduced engine performance due to increased friction	3	18	Use prevention and detection design controls	HA
				6	oil pressure is low	Inspect engine oil pump and ensure it is in good condition before running the engine. Top up the engine with KTM recommended engine oil in sufficient quantity	2	Inspect engine oil pump and ensure it is in good condition before running the engine. Look out for reduced engine performance due to increased friction	3	36	Use prevention and detection design controls	HA
			total engine seizure	9	lack of engine oil	Visually inspect and check for engine oil before running the engine. Top up the engine with KTM recommended engine oil in sufficient quantity	1	Visually inspect and check for engine oil before running the engine. Look out for reduced engine performance due to increased friction	3	27	Use prevention and detection design controls	HA
						Inspect engine oil pump and ensure it is in good condition before		Inspect engine oil pump and ensure it is in good condition before			Use prevention	

				6	oil pressure is low	Inspect engine oil pump and ensure it is in good condition before running the engine. Top up the engine with KTM recommended engine oil in sufficient quantity	2	Inspect engine oil pump and ensure it is in good condition before running the engine. Look out for reduced engine performance due to increased friction	3	36	Use prevention and detection design controls	HA
			reduced piston/engine life/reliability	7	lack of engine oil	Visually inspect and check for engine oil before running the engine. Top up the engine with KTM recommended engine oil in sufficient quantity	1	Visually inspect and check for engine oil before running the engine. Look out for reduced engine performance due to increased friction	3	21	Use prevention and detection design controls	HA
				7	oil pressure is low	Inspect engine oil pump and ensure it is in good condition before running the engine. Top up the engine with KTM recommended engine oil in sufficient quantity	2	Inspect engine oil pump and ensure it is in good condition before running the engine. Look out for reduced engine performance due to increased friction	3	42	Use prevention and detection design controls	HA
			piston and compression ring micro-welding	8	lack of engine oil	Visually inspect and check for engine oil before running the engine. Top up the engine with KTM recommended engine oil in sufficient quantity	1	Visually inspect and check for engine oil before running the engine. Look out for reduced engine performance due to increased friction	3	24	Use prevention and detection design controls	HA
				8	oil pressure is low	Inspect engine oil pump and ensure it is in good condition before running the engine. Top up the	2	Inspect engine oil pump and ensure it is in good condition before running the engine. Look out for reduced	3	48	Use prevention and detection design controls	HA

						pumped/circulated.						
			total engine seizure	9	Overheating of the engine due to issues with cooling system	Ensure the coolant pump and the coolant system in the test cell are in good working condition, the coolant should have minimum capacity of 1.20 litre. The coolant should be constantly pumped/circulated.	4	Look out for reduced engine performance due to increased friction. Monitor and measure the coolant temperature at exit from engine and ensure it stays between 110 - 120 C	4	144	Use prevention and detection design controls	HA
			reduced engine performance due to increased friction	6	Overheating of the engine due to issues with cooling system	Ensure the coolant pump and the coolant system in the test cell are in good working condition, the coolant should have minimum capacity of 1.20 litre. The coolant should be constantly pumped/circulated.	4	Look out for reduced engine performance due to increased friction. Monitor and measure the coolant temperature at exit from engine and ensure it stays between 110 - 120 C	4	96	Use prevention and detection design controls	HA
			reduced piston/engine life/reliability	7	Overheating of the engine due to issues with cooling system	Ensure the coolant pump and the coolant system in the test cell are in good working condition, the coolant should have minimum capacity of 1.20 litre. The coolant should be constantly pumped/circulated.	4	Look out for reduced engine performance due to increased friction. Monitor and measure the coolant temperature at exit from engine and ensure it stays between 110 - 120 C	4	112	Use prevention and detection design controls	HA
						Ensure the coolant						

	withstanding pressures up to 100 bar and transfers heat to cylinder walls with convection of .....							friction. Check engine oil level regularly for increased oil consumption				
				5	inappropriate cylinder finish	Use KTM approved workshop to inspect and measure cylinder finish before engine assembly	3	Look out for reduced engine performance due to compression loss or increased friction. Check engine oil level regularly for increased oil consumption	5	75	Use prevention and detection design controls	HA
			increased friction	6	ring not fitted properly	Use KTM approved workshop to fit the ring	3	Look out for reduced engine performance due to compression loss or increased friction	5	90	Use prevention and detection design controls	HA
				6	inappropriate cylinder finish	Use KTM approved workshop to inspect and measure cylinder finish before engine assembly	3	Look out for reduced engine performance due to compression loss or increased friction	5	90	Use prevention and detection design controls	HA
			reduced engine performance	6	ring not fitted properly	Use KTM approved workshop to fit the ring	3	Look out for reduced engine performance due to compression loss or increased friction	5	90	Use prevention and detection design controls	HA
				6	inappropriate cylinder finish	Use KTM approved workshop to inspect and measure cylinder finish before engine assembly	3	Look out for reduced engine performance due to compression loss or increased friction	5	90	Use prevention and detection design controls	HA
						Visually inspect and check for engine oil before		Check engine oil level			Use prevention	

						chamber. Use the correct ECU for engine.						
				6	cylinder temperature was too high	Ensure the coolant pump and the coolant system in the test cell are in good working condition, the coolant should have minimum capacity of 1.20 litre. The coolant should be constantly pumped/circulated. Adjust carburettor (set needle to fourth position from top) not to put too much/less fuel into combustion chamber.	7	In-cylinder pressures will be monitored to ensure they do not go above 100 bar which can cause excess thermal loads. Coolant temperature will be monitored and ensured to stay between 110 - 120 C. Air fuel ratio (lambda) will be measured and monitored to ensure the mixture does not get too lean or rich to cause excess thermal loads (range of 10.5 to 15).	4	168	Use prevention and detection design controls	HA
				6	unsuitable lubricating oil	Use the engine oil recommended by the manufacturer (KTM) and purchase from manufacturer's approved suppliers	1	Look out for reduced engine performance due to compression loss or increased friction	5	30	Use prevention and detection design controls	HA
				6	excessive engine loads	Coolant temperature monitor guidelines to ensure it stays between 110 - 120 C. Adjust carburettor (set needle to fourth position from top)	7	Coolant temperature will be monitored and ensured to stay between 110 - 120 C to avoid overheating of the piston so it does not deform too much. In-cylinder pressure will	4	168	Use prevention and detection design controls	HA



			piston skirt seizure	8	Insufficient oil supply	Visually inspect and check for engine oil before running the engine and top up with recommended oil if needed.	1	Check engine oil level regularly for increased oil consumption	3	24	Use prevention and detection design controls	HA
				8	abnormal combustion	Ensure the air flow in the test cell is not interrupted and it can provide enough air for the engine operation. Adjust carburettor (set needle to fourth position from top) not to put too much/less fuel into combustion chamber. Use the correct ECU for engine.	7	Listen for abnormal engine noise. Look out for reduced engine performance due increased friction i.e. lower torque than expected. Measure and monitor the air fuel ratio (AFR) or lambda and ensure it stays within 10.5 - 14.5 by adjusting carburettor jets	5	280	Use prevention and detection design controls	HA
				8	cylinder temperature was too high	Ensure the coolant pump and the coolant system in the test cell are in good working condition, the coolant should have minimum capacity of 1.20 litre. The coolant should be constantly pumped/circulated. Adjust carburettor (set needle to fourth position from top) not to put too much/less fuel into combustion chamber.	7	In-cylinder pressures will be monitored to ensure they do not go above 100 bar which can cause excess thermal loads. Coolant temperature will be monitored and ensured to stay between 110 - 120 C. Air fuel ratio (lambda) will be measured and monitored to ensure the mixture does not get too lean or rich to cause excess thermal loads (range of 10.5 to 15).	4	224	Use prevention and detection design controls	HA
						Use the engine oil recommended by		Look out for reduced				

						combustion chamber		bar.				
				8	imperfect honed cylinder which is not good for oil adhesion	Use KTM approved workshop to inspect and measure cylinder finish before engine assembly	3	Look out for reduced engine performance due to compression loss or increased friction	5	120	Use prevention and detection design controls	HA
			reduced engine performance	6	Insufficient oil supply	Visually inspect and check for engine oil before running the engine and top up with recommended oil if needed.	1	Check engine oil level regularly for increased oil consumption	3	18	Use prevention and detection design controls	HA
				6	abnormal combustion	Ensure the air flow in the test cell is not interrupted and it can provide enough air for the engine operation. Adjust carburettor (set needle to fourth position from top) not to put too much/less fuel into combustion chamber. Use the correct ECU for engine.	7	Listen for abnormal engine noise. Look out for reduced engine performance due to increased friction i.e. lower torque than expected. Measure and monitor the air fuel ratio (AFR) or lambda and ensure it stays within 10.5 - 14.5 by adjusting carburettor jets	5	210	Use prevention and detection design controls	HA
				6	cylinder temperature was too high	Ensure the coolant pump and the coolant system in the test cell are in good working condition, the coolant should have minimum capacity of 1.20 litre. The coolant should be constantly	7	In-cylinder pressures will be monitored to ensure they do not go above 100 bar which can cause excess thermal loads. Coolant temperature will be monitored and ensured to stay between 110 - 120 C. Air fuel ratio (lambda) will be	4	168	Use prevention and detection design controls	HA



				6	excessive engine loads	Coolant temperature monitor guidelines to ensure it stays between 110 - 120 C. Adjust carburettor (set needle to fourth position from top) not to put too much fuel into combustion chamber	7	Coolant temperature will be monitored and ensured to stay between 110 - 120 C to avoid overheating of the piston so it does not deform too much. In-cylinder pressure will be monitored and measured to ensure it does not exceed 100 bar.	4	168	Use prevention and detection design controls	HA
				6	imperfect honed cylinder which is not good for oil adhesion	Use KTM approved workshop to inspect and measure cylinder finish before engine assembly	3	Look out for reduced engine performance due to compression loss or increased friction	5	90	Use prevention and detection design controls	HA
			reduced piston/engine life/reliability	7	Insufficient oil supply	Visually inspect and check for engine oil before running the engine and top up with recommended oil if needed.	1	Check engine oil level regularly for increased oil consumption	3	21	Use prevention and detection design controls	HA
				7	abnormal combustion	Ensure the air flow in the test cell is not interrupted and it can provide enough air for the engine operation. Adjust carburettor (set needle to fourth position from top) not to put too much/less fuel into combustion chamber. Use the correct ECU for engine.	7	Listen for abnormal engine noise. Look out for reduced engine performance due to increased friction i.e. lower torque than expected. Measure and monitor the air fuel ratio (AFR) or lambda and ensure it stays within 10.5 - 14.5 by adjusting carburettor jets	5	245	Use prevention and detection design controls	HA
						Ensure the coolant pump and the		In-cylinder pressures will be monitored to				

						into combustion chamber.						
				7	unsuitable lubricating oil	Use the engine oil recommended by the manufacturer (KTM) and purchase from manufacturer's approved suppliers	1	Look out for reduced engine performance due to compression loss or increased friction	5	35	Use prevention and detection design controls	HA
				7	excessive engine loads	Coolant temperature monitor guidelines to ensure it stays between 110 - 120 C. Adjust carburettor (set needle to fourth position from top) not to put too much fuel into combustion chamber	7	Coolant temperature will be monitored and ensured to stay between 110 - 120 C to avoid overheating of the piston so it does not deform too much. In-cylinder pressure will be monitored and measured to ensure it does not exceed 100 bar.	4	196	Use prevention and detection design controls	HA
				7	imperfect honed cylinder which is not good for oil adhesion	Use KTM approved workshop to inspect and measure cylinder finish before engine assembly	3	Look out for reduced engine performance due to compression loss or increased friction	5	105	Use prevention and detection design controls	HA
Cylinder Liner		Lack of lubrication	increased friction	6	Fuel flooding	Adjust carburettor (set needle to fourth position from top) not to put too much fuel into combustion chamber. Ensure to run the engine in idle for long enough (approx. 5 minutes) after just starting so any excess fuel is burnt and the	5	Run the engine idle for awhile until the strong gasoline smell from exhaust disappears. Listen for fast cranking when starting the engine. Look out for abnormal fuel consumption using the Fuel Measuring System.	5	150	Use prevention and detection design controls	HA

						burnt and the strong gasoline smell from exhaust disappear.						
			increased wear	6	Fuel flooding	Adjust carburettor (set needle to fourth position from top) not to put too much fuel into combustion chamber. Ensure to run the engine in idle for long enough (approx. 5 minutes) after just starting so any excess fuel is burnt and the strong gasoline smell from exhaust disappears.	5	Look out for reduced engine performance due to compression loss or increased friction	5	150	Use prevention and detection design controls	HA
		Mechanical damage to the honing structure of the cylinder liner due to carbon deposit on piston top land	Damage to piston, rings	9	Excessive pressure in the crankcase due to blow by	Use KTM approved workshop to install compression ring etc. so the likelihood of blow by is decreased. Adjust carburettor (set needle to fourth position from top) so it does not put too much fuel into combustion chamber not to cause pressure more than 100 bar.	3	In-cylinder pressure will be monitored and measured to ensure it does not exceed 100 bar.	4	108	Use prevention and detection design controls	HA
				9	use of non-approved engine oil	Use the engine oil recommended by the manufacturer (KTM) and purchase from	1	Look out for reduced engine performance due to compression loss or increased friction. Listen for	5	45	Use prevention and detection design controls	HA

						diagonally (Picture 2)						
				6	incorrect cylinder head gasket	Use the head gasket recommended by the manufacturer (KTM) and purchase from manufacturer's approved suppliers	3	Look out for reduced engine performance due to increased friction or compression loss	5	90	Use prevention and detection design controls	HA
				6	Distorted cylinder bores	Use KTM approved workshop to inspect and measure cylinder before engine assembly	2	Look out for reduced engine performance due to increased friction or compression loss	5	60	Use prevention and detection design controls	HA
				6	dirty or distorted threads in the threaded bores or on the cylinder head bolts	Inspect the threads and bores before installation of the head bolts	3	Look out for reduced engine performance due to increased friction or compression loss	5	90	Use prevention and detection design controls	HA
			Engine performance loss due to compression ring not providing proper seal	6	Uneven or incorrect tightening of the head bolts	Ensure 10 and then 30 Nm torque is applied as recommended by the manufacturer and the tightened diagonally (Picture 2)	4	Look out for reduced engine performance due to increased friction or compression loss	5	120	Use prevention and detection design controls	HA
				6	incorrect cylinder head gasket	Use the head gasket recommended by the manufacturer (KTM) and purchase from manufacturer's approved suppliers	3	Look out for reduced engine performance due to increased friction or compression loss	5	90	Use prevention and detection design controls	HA
						Use KTM						

		Crack esp. at the top of the cylinder inner	Damages other piston assembly components i.e. piston or compression ring	9	Material erosion due to knocking	Visually inspect and check for erosion before engine assembly	3	Listen for abnormal engine sound during operation	3	81	Use prevention and detection design controls	HA
				9	foreign bodies underneath sealing surfaces	Clean all the surfaces before engine assembly	2	Listen for abnormal engine sound during operation	3	54	Use prevention and detection design controls	HA
				9	improper handling of the cylinder liner esp. during transport	Visually inspect and check the cylinder before engine assembly	1	Listen for abnormal engine sound during operation	3	27	Use prevention and detection design controls	HA
Oil Ring	Provides lubrication between piston skirt and cylinder wall.	Loss of tension in the spring	Increased oil consumption as the ring no longer scraps the oil effectively and more oil goes into the combustion chamber which gets burnt	6	improper installation	Use KTM approved workshop to install piston and the carry out the whole engine assembly	2	Look out for reduced engine performance due to increased friction. Regularly check for engine oil consumption	5	60	Use prevention and detection design controls	HA
		Loss of tension in the spring	The oil ring can get stuck to one side in the cylinder and increases friction	6	improper installation	Use KTM approved workshop to install piston and the carry out the whole engine assembly	2	Look out for reduced engine performance due to increased friction	5	60	Use prevention and detection design controls	HA
						Coolant temperature monitor guidelines to ensure it stays		In-cylinder pressures will be monitored to ensure they do not go above 100 bar which				

						carburettor.		increments of 500 rpm during engine speeds. Abnormal engine noise				
				9	Improper handling when inserting the circlips	Use KTM approved workshop to install circlips and the carry out the whole engine assembly	2	Look out for reduced engine performance due to compression loss or increased friction. Abnormal engine noise	5	90	Use prevention and detection design controls	HA
				9	Piston running at an angle due to bent connecting rod	Visually inspect and check the connecting rod before engine assembly	2	Look out for reduced engine performance due to compression loss or increased friction. Abnormal engine noise	5	90	Use prevention and detection design controls	HA
		Jump or knocked out of their grooves	Damage to the piston assembly	9	Excessive Loads	Coolant temperature monitor guidelines to ensure it stays between 110 - 120 C. Adjust carburettor (set needle to fourth position from top) not to put too much fuel into combustion chamber. In-cylinder pressure will be monitored and ensured it does go exceed 100 bar by adjusting carburettor.	5	In-cylinder pressures will be monitored to ensure they do not go above 100 bar which can cause excess thermal loads. Coolant temperature will be monitored and ensured to stay between 110 - 120 C. Air fuel ratio (lambda) will be measured and monitored to ensure the mixture does not get too lean or rich to cause excess thermal loads (range of 10.5 to 15). Increase engine speeds in small increments of 500 rpm during engine speeds. Abnormal engine noise	4	180	Use prevention and detection design controls	HA
					Improper	Use KTM		Look out for reduced				



						engine operation. Adjust carburettor (set needle to fourth position from top) not to put too much/less fuel into combustion chamber. Use the correct ECU for engine.		lower torque than expected. Measure and monitor the air fuel ratio (AFR) or lambda and ensure it stays within 10.5 - 14.5 by adjusting carburettor jets				
				6	Faults in engine cooling system	Ensure the coolant pump and the coolant system in the test cell are in good working condition, the coolant should have minimum capacity of 1.20 litre. The coolant should be constantly pumped/circulated.	4	Coolant temperature at exit from engine will be monitored and ensured to stay between 110 - 120 C.	4	96	Use prevention and detection design controls	HA
				6	faults in oil supply	Check the oil pump is in good working condition, top up the engine with approved oil. Visually inspect and check for engine oil before running the engine and top up with recommended oil if needed.	3	Look out for reduced engine performance/behaviour. Check engine oil level regularly for increased oil consumption	5	90	Use prevention and detection design controls	HA
				6	Extended high loads on the engine before it has been fully run in	Run the engine under light load condition (approx. 1 hour in increments of 20 minutes) before the actual testing.	4	Look out for reduced engine performance due to increased friction i.e. lower torque than expected	5	120	Use prevention and detection design controls	HA
						Ensure the air flow in the test cell is		Listen for abnormal				

				9	Faults in engine cooling system	Ensure the coolant pump and the coolant system in the test cell are in good working condition, the coolant should have minimum capacity of 1.20 litre. The coolant should be constantly pumped/circulated.	4	Coolant temperature at exit from engine will be monitored and ensured to stay between 110 - 120 C.	4	144	Use prevention and detection design controls	HA
				9	faults in oil supply	Check the oil pump is in good working condition, top up the engine with approved oil. Visually inspect and check for engine oil before running the engine and top up with recommended oil if needed.	3	Look out for reduced engine performance/behaviour. Check engine oil level regularly for increased oil consumption	5	135	Use prevention and detection design controls	HA
				9	Extended high loads on the engine before it has been fully run in	Run the engine under light load condition (approx. 1 hour in increments of 20 minutes) before the actual testing.	4	Look out for reduced engine performance due to increased friction i.e. lower torque than expected	5	180	Use prevention and detection design controls	HA
		Radial Impact	Engine noise	5	Excessive installation clearances between piston and cylinder liner	Design new piston with the same amount of clearance between the piston and cylinder liner as the original piston.	4	Listen for abnormal engine noises	3	60	Use prevention and detection design controls	HA
				5	Tight connection or not enough clearance between	Design new piston with the same amount of clearance between the piston and the	4	Listen for abnormal engine noises	3	60	Use prevention and detection	HA



					piston and cylinder liner	the piston and cylinder liner as the original piston						
				9	Tight connection or not enough clearance between piston and connecting rod at small end	Design new piston with the same amount of clearance between the piston and the connecting rod at small end as the original piston	4	Reduced engine performance/behaviour, abnormal engine noise	3	108	Use prevention and detection design controls	HA
				9	Connecting rod not aligned	Use KTM approved workshop to carry out engine assembly and check for connecting rod alignment	3	Reduced engine performance/behaviour, abnormal engine noise	3	81	Use prevention and detection design controls	HA
			Reduced piston fatigue life	7	Excessive installation clearances between piston and cylinder liner	Design new piston with the same amount of clearance between the piston and cylinder liner as the original piston	4	Reduced engine performance/behaviour, abnormal engine noise	3	84	Use prevention and detection design controls	HA
				7	Tight connection or not enough clearance between piston and connecting rod at small end	Design new piston with the same amount of clearance between the piston and the connecting rod at small end as the original piston	4	Reduced engine performance/behaviour, abnormal engine noise	3	84	Use prevention and detection design controls	HA
				7	Connecting rod not aligned	Use KTM approved workshop to carry out engine assembly and check for connecting rod	3	Reduced engine performance/behaviour, abnormal engine noise	3	63	Use prevention and detection design controls	HA

					end							
				6	Connecting rod not aligned	Use KTM approved workshop to carry out engine assembly and check for connecting rod alignment	3	Reduced engine performance/behaviour, abnormal engine noise	3	54	Use prevention and detection design controls	HA
		Overheating	Piston scuffing	6	Extended high loads on the engine before it has been fully run in	Run the engine under light load condition (approx. 1 hour in increments of 20 minutes) before the actual testing.	4	Look out for reduced engine performance due to increased friction i.e. lower torque than expected	5	120	Use prevention and detection design controls	HA
				6	Faults in combustion process	Ensure the air flow in the test cell is not interrupted and it can provide enough air for the engine operation. Adjust carburettor (set needle to fourth position from top) not to put too much/less fuel into combustion chamber. Use the correct ECU for engine.	6	Look out for reduced engine performance due to increased friction i.e. lower torque than expected. Measure and monitor the air fuel ratio (AFR) or lambda and ensure it stays within 10.5 - 14.5 by adjusting carburettor jets	5	180	Use prevention and detection design controls	HA
				6	Faults in cooling system	Ensure the coolant pump and the coolant system in the test cell are in good working condition, the coolant should have minimum capacity of 1.20 litre. The coolant should be	4	Coolant temperature at exit from engine will be monitored and ensured to stay between 110 - 120 C.	5	120	Use prevention and detection design controls	HA

			Total engine seizure	9	Extended high loads on the engine before it has been fully run in	Run the engine under light load condition (approx. 1 hour in increments of 20 minutes) before the actual testing.	4	Look out for reduced engine performance due to increased friction i.e. lower torque than expected	5	180	Use prevention and detection design controls	HA
				9	Faults in combustion process	Ensure the air flow in the test cell is not interrupted and it can provide enough air for the engine operation. Adjust carburettor (set needle to fourth position from top) not to put too much/less fuel into combustion chamber. Use the correct ECU for engine.	6	Look out for reduced engine performance due to increased friction i.e. lower torque than expected. Measure and monitor the air fuel ratio (AFR) or lambda and ensure it stays within 10.5 - 14.5 by adjusting carburettor jets	5	270	Use prevention and detection design controls	HA
				9	Faults in cooling system	Ensure the coolant pump and the coolant system in the test cell are in good working condition, the coolant should have minimum capacity of 1.20 litre. The coolant should be constantly pumped/circulated.	4	Coolant temperature at exit from engine will be monitored and ensured to stay between 110 - 120 C.	5	180	Use prevention and detection design controls	HA
				9	Use of improper compression ring	Use the compression ring recommended by the engine's manufacturer (KTM) and purchase from manufacturer's approved suppliers	3	Look out for reduced engine performance due to increased friction i.e. lower torque than expected	5	135	Use prevention and detection design controls	HA

						from top) not to put too much/less fuel into combustion chamber. Use the correct ECU for engine.		by adjusting carburettor jets				
				6	Faults in cooling system	Ensure the coolant pump and the coolant system in the test cell are in good working condition, the coolant should have minimum capacity of 1.20 litre. The coolant should be constantly pumped/circulated.	4	Coolant temperature at exit from engine will be monitored and ensured to stay between 110 - 120 C.	4	96	Use prevention and detection design controls	HA
				6	Use of improper compression ring	Use the compression ring recommended by the engine's manufacturer (KTM) and purchase from manufacturer's approved suppliers	3	Look out for reduced engine performance due to increased friction i.e. lower torque than expected	5	90	Use prevention and detection design controls	HA
			Reduced piston/engine life and reliability	7	Extended high loads on the engine before it has been fully run in	Run the engine under light load condition (approx. 1 hour in increments of 20 minutes) before the actual testing.	4	Look out for reduced engine performance due to increased friction i.e. lower torque than expected	5	140	Use prevention and detection design controls	HA
				7	Faults in combustion process	Ensure the air flow in the test cell is not interrupted and it can provide enough air for the engine operation. Adjust carburettor (set needle to fourth position	6	Look out for reduced engine performance due to increased friction i.e. lower torque than expected. Measure and monitor the air fuel ratio (AFR)	5	210	Use prevention and detection design controls	HA

[illegible]





## **Appendix D.1. Failure mechanisms in new lightweight piston**

Based on the DFMEA results and expert opinions from KTM mechanic and piston designer, the first new piston might have failed in the following 2 manners.

### **D.1.1. Lack of lubrication caused by fuel flooding due to excessive use of choke**

The top 8 or highest risk priority numbers (RPNs) from DFMEA were (324, 315, 288, 280 and 270) and these are highlighted in Red. They all refer to excessive use of choke or faults in combustion process which could have caused fuel flooding due to excessive use of choke. The fuel washes away oil film from piston and cylinder liner, thus mix friction occurs which leads to seizure.

It can be seen in Figure D.1 that piston crown is all covered in un-burnt fuel while some is even collected in valve pockets (in red).



**Figure D.1.** Fuel flooded piston

### **D.1.2. Less cylinder deformation due to lower coolant temperature**

The high risk priority number (270) also points to overheating of the piston top land due to faults in combustion process which could have been as a result of fuel flooding. The overheating would have expanded the piston much more than it would have been during normal combustion process. This problem would have been made worse due to lower temperature of the coolant. The cylinder liner did not expand much due to lower coolant temperature and hence there was no space for piston to expand into. Furthermore, the cylinder liner is made of cast iron which has more than twice thermal expansion coefficient compared to aluminium alloy that piston is made of. This would have led to increased friction and then to seizure. The engine manufacturer recommended coolant temperature is 110 – 120 °C, while coolant temperature of 80 °C was used for testing. The coolant temperatures of 80 °C and 120 °C have been simulated in piston FEA and it can be seen that it makes significant difference when the coolant temperature is 120 °C instead of 80 °C.

Figures D.2 and D.4 give cylinder deformations in X direction while Figures D.3 and D.5 give cylinder deformations in Y direction for 80 °C and 120 °C respectively. The cylinder deformed 25.3% and 24% more in X and Y directions with coolant temperature 120 °C. Therefore coolant temperature of 110-120 °C should be used instead of 80 °C.



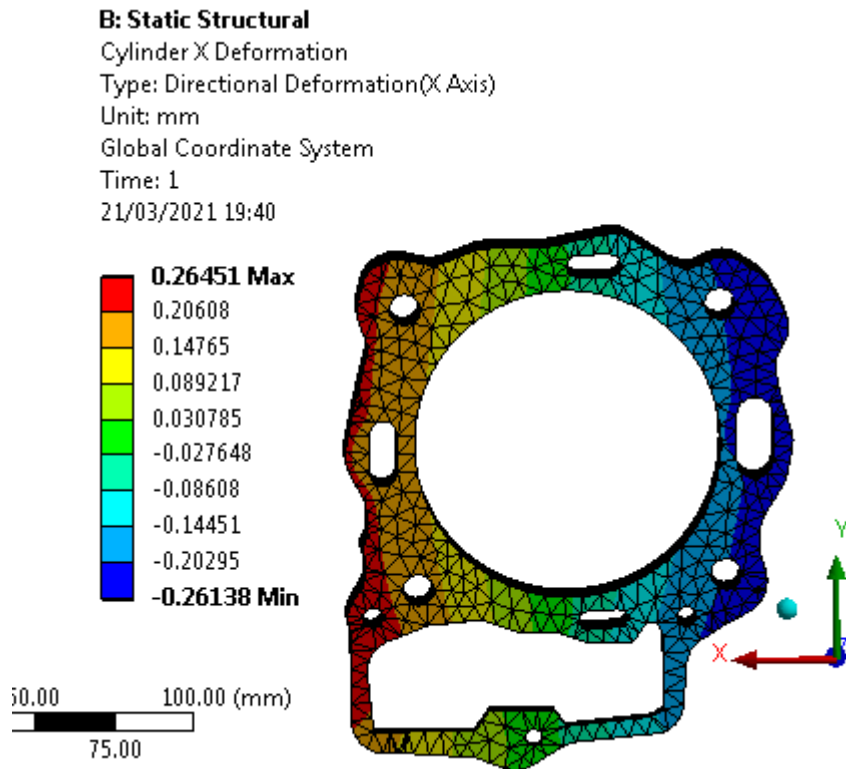


**Figure D.2.** Cylinder deformation in X direction (along pin direction) with coolant temperature of 80 °C

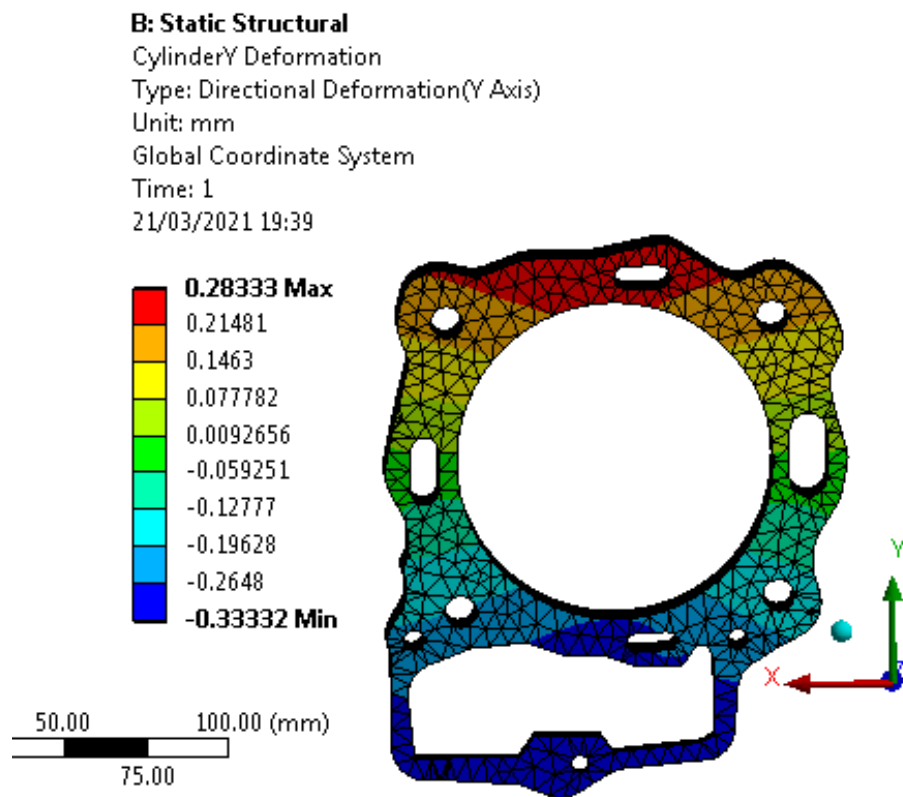


**Figure D.3.** Cylinder deformation in Y direction (perpendicular to pin direction) with coolant temperature of 80 °C.

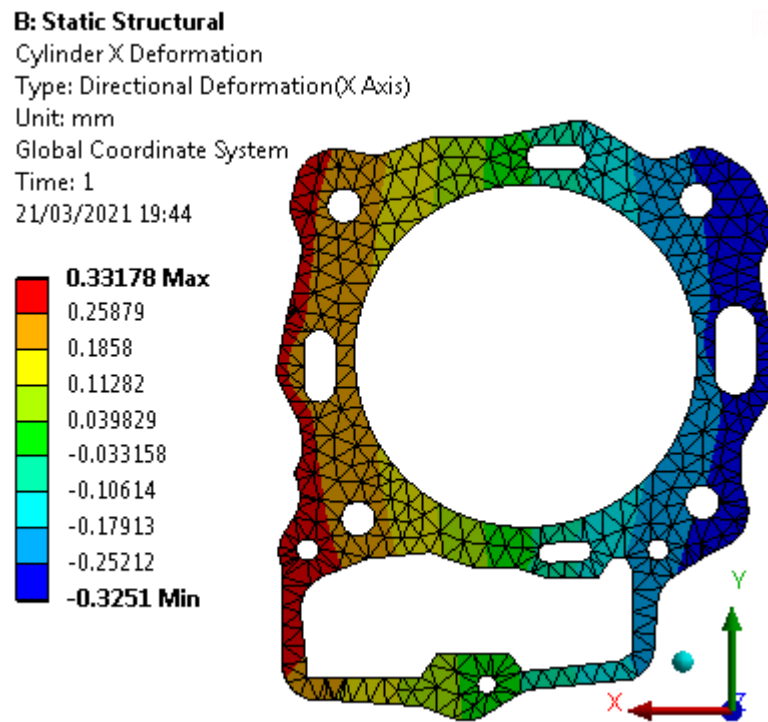


**Figure D.4.** Cylinder deformation in X direction (along pin direction) with coolant temperature of 120 C

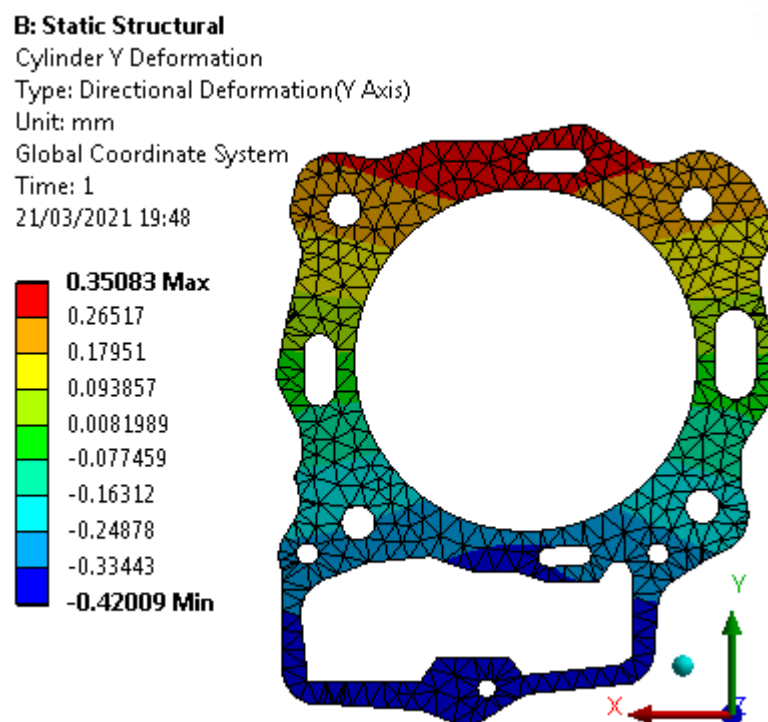


**Figure D.5.** Cylinder deformation in Y direction (perpendicular to pin direction) with coolant temperature of 120 °C.

## **Appendix D.2. Checklist for new piston assembly and testing**

Based on design failure mode and effect analysis (DFMEA) findings, a check list was created. The check list was divided into the following three areas for effective actions to be taken.

### **D.2.1. Assembly, disassembly and piston installation**

- ✓ Check the connecting rod for wear especially the small end before installation.
- ✓ Check the gap between piston and cylinder head before installation
- ✓ Ensure 10 and 30 Nm torque is applied to the cylinder head nuts in stage 1 and 2 and the tightened diagonally as recommended by the manufacturer (KTM).
- ✓ Check the correct head gasket is used. Purchase from KTM.
- ✓ Inspect the threads and bores before installation of the head bolts
- ✓ Top up the engine with the correct quality (SAE 10W50) and quantity (1.2 litre) of engine oil
- ✓ Inspect the coolant pump and ensure it is in working condition.
- ✓ Inspect engine oil pump and ensure it is in good condition before running the engine
- ✓ Inspect and measure cylinder finish before engine assembly.
- ✓ Ensure the rings are fitted correctly
- ✓ Visually inspect and check cylinder for erosion before engine assembly
- ✓ Clean all the surfaces before engine assembly
- ✓ Use KTM approved workshop to install circlips and the carry out the whole engine assembly
- ✓ Use KTM approved workshop to carry out engine assembly and check for connecting rod alignment

### **D.2.2. Just before testing the engine**

- ✓ Adjust the carburettor (set needle to fourth position from top) before testing the engine so it does not put in too much or too little fuel into the combustion chamber.
- ✓ To bed the new piston in, run the engine under light load condition for an hour in increments of 20 minutes.
- ✓ Ensure the coolant pump and test cell coolant system is in working condition.
- ✓ Visually inspect and check for engine oil before running the engine
- ✓ Ensure the correct ECU is used.
- ✓ Ensure the air and fuel flow into the engine is not interrupted
- ✓ Ensure the test cell is not too cold so there is not much need of using choke

### **D.2.3. During engine operation**

- ✓ Ensure to run the engine in idle for long enough after just starting so any excess fuel is burnt and the strong gasoline smell from exhaust disappears.
- ✓ Monitor and measure coolant temperature at exit from engine and ensure it stays between 110 – 120 °C.
- ✓ Monitor and measure in-cylinder pressure and ensure it does not exceed 100 bar.
- ✓ Monitor and measure air fuel ratio (AFR)/lambda and ensure it stays between 10.5 – 15.
- ✓ Ensure to change engine speeds in increments of 500 rpm NOT 1000 rpm.
- ✓ Ensure to keep the engine in new rpm for 5 minutes to reach thermal stability.
- ✓ Ensure air flow is not interrupted
- ✓ Listen out for rattling or any other abnormal sound during engine operation.
- ✓ Listen for fast cranking when starting the engine, this is sign of fuel flooding.
- ✓ Look out for abnormal fuel consumption using the Fuel Measuring System, excess fuel can cause fuel flooding, overheating and other problems.